Dissertation zur Erlangung des Doktorgrades
der Fakultät für Chemie und Pharmazie
der Ludwig-Maximilians-Universität München

Synthetic Investigations in Rare-Earth Borates, Gallates, Oxides, and Gallium Oxonitrides at Extreme Conditions

Dipl.-Chem. Stefanie Alexandra Hering

aus

Rosenheim

2009

Erklärung

Diese Dissertation wurde im Sinne von § 13 Abs. 3 bzw. 4 der Promotionsordnung vom 29. Januar 1998 von Herrn Prof. Dr. H. Huppertz betreut.

Ehrenwörtliche Versicherung

Diese Dissertation wurde selbständig, ohne unerlaubte Hilfe erarbeitet.

München, den 21.12.2009

Stefanie A. Hering

Dissertation eingereicht am: 21.12.2009

1. Gutachter: Prof. Dr. H. Huppertz
2. Gutachter: Prof. Dr. W. Schnick

Mündliche Prüfung am: 18.02.2010

Acknowledgments

First of all, I would like to express my gratitude to my thesis advisor Univ.-Prof. Dr. H. Huppertz for giving me the opportunity to do scientific work in his group, for the enthusiastic interest in my studies and the constant encouragement and guidance offered during the course of this work.

I am also very grateful to Prof. Dr. W. Schnick, head of the inorganic solid-state chemistry and materials research group, for providing the laboratory facilities and excellent research conditions, the unhesitant acceptance in his group, and for his invaluable support.

I am happy to acknowledge my debt to Prof. Dr. W. Schnick for being the second referee of this thesis.

I also thank the other members of my thesis committee, Prof. Dr. W. Schnick, Prof. Dr. Dres. h. c. J. Straus, Prof. Dr. D. Johrendt, Prof. Dr. K. Karaghiosoff, and PD Dr. K. Müller-Buschbaum for their attendance as examiners in my *viva voce*.

In particular, I thank Prof. Dr. Dres. h. c. J. Straus who serves as the "external" member of this committee. His dedicated advocacy of IP protection made the field of intellectual property fascinating for me as an undergraduate student and still continues to inspire and propel me forward in my own career today.

Special thanks go to my cooperation partners Carmen Zvoriste (Tu Darmstadt) and Dr. Isabel Kinski (Fraunhofer-Institut für Keramische Technologien und Systeme, IKTS Dresden) and to Prof. Dr. Ralf Riedel from the Institute of Materials Science at the Darmstadt University of Technology! Thanks a lot for the fruitful discussions and the support over the last few years! The best for you: Carmen Zvoriste and Dr. Isabel Kinski!

Special gratitude goes to my comrades of the laboratories D2.103 and D2.110! I would like to thank Yamini Avadhut, Cordula Braun, Cora Hecht, Sophia Makowski, Christian Minke, Florian Pucher, Tobias Rosenthal, Andreas Sattler, Sebastian Schneider, Stefan Sedlmaier, and Dr. Johannes Weber.

Special thanks go out to the press team! Thanks for collegial and cooperative work with lots of interesting discussions and the press festivities! Thank all of you, Cordula Braun, Almut Haberer, Dr. Gunter Heymann, Dr. Johanna Knyrim, Stephanie Neumair, Florian Pucher, Stefan Sedlmaier, Matthias Schneider, Sebastian Schneider, and Wolfgang Wünschheim for your friendly cooperation and the excellent team work.

Above all, I am truly grateful to my boyfriend for his loving support and the continuous encouragement throughout the course of my studies. Thank you so much, Ali.

For MIK.

Wenn man die Natur einer Sache durchschaut hat,
werden die Dinge berechenbar.
(Blade)

Contents:

1 Introduction

For industry and research, light materials of extraordinary hardness are of high interest. Such materials are challenged to resist mechanical strains. However, it is well known that cutting, grinding, or drilling tasks are solved by diamond-studded devices [1,2]. The ideal physical properties of diamonds (named due to the ancient greek word adámas, meaning "proper" or "unalterable") are low weight beside extraordinary hardness (10, corresponding to the Mohs scale of mineral hardness), high density, ranging between 3.5 to 3.53 g/cm^3 [3], electrical isolation, thermal conductivity (900–2320 W m^{-1} K^{-1}), wide bandgap, resistance to corrosion and radioactive radiation, combined with optical features, such as complete transparency [4,5]. Not only because of its clear colorless appearance and high optical dispersion, but also due to its high durability, diamonds are the most popular of all gemstones applied in jewelry (Figure 1-1).

Figure 1-1. Rough diamonds [6,7], diamond in brilliant cut [8], and colored diamonds [9].

The contamination of the extremely rigid structure with small impurities (about 1 ppm) results in colored diamonds (Figure 1-1). Doping leads to color changes to blue (boron) [5], yellow (nitrogen) while other colored diamonds, like green, purple, pink, orange, black, red, or even brown, are realized as a result of structure defects [10,11].

The crystal structure exhibits tetrahedrally coordinated carbon atoms (sp^3) forming an inflexible three-dimensional structure (Figure 1-2), in contrast to graphite, which is build up from easily sliding sheets. The so called diamond-structure, space group $Fd\overline{3}m$ (no. 227) can be seen
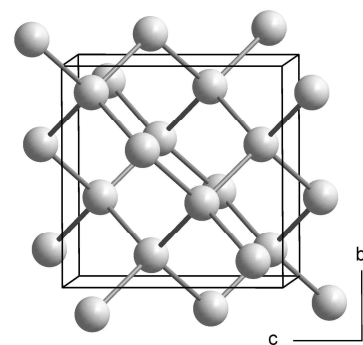
Figure 1-2. Crystal structure of diamond [12].

as a variation of the cubic fcc-type in which half of the tetrahedral voids are filled with carbon [12].

In nature, diamonds are formed in the lithospheric mantle of the Earth´s crust. More precisely, diamonds are formed under high-pressure / high-temperature conditions in the cratonic lithosphere in depths estimated between 140 and 190 km up to 300 km of the Earth´s core [13].

The first successful synthesis of artificial diamonds was performed by General Electric in 1954, winning the international race against time and their Swedish opponent, the ASEA-team (Allmänna Svenska Elektriska Aktiebolaget). Starting in 1941, General Electric (GE), Norton, and the Carborundum companies agreed on continuing in research on diamond synthesis. Interrupted by the World War II, experiments were resumed 10 years later. However, by forming a high-pressure task force, including F. P. Bundy, H. M. Strong, and T. Hall [14], the first commercially access to synthetic diamonds was approached [15,16]. With the help of a belt apparatus, pressures of 10 GPa at temperatures of 2000 °C were achieved [17].

Approximately 130 million carats (26 t) are mined per year, to satisfy the global demand for diamonds. Supporting the industry, 100 t of man-made diamonds are synthesized annually [18]. In priority, artificial diamonds are used mostly for industrial purposes. Therefore, high-pressure / high-temperature processes, starting from graphite, are required at conditions of typically 6 GPa at 1500 °C [19,20]. Another important synthetic strategy for diamond synthesis is chemical vapor deposition (CVD). Chemical reaction of active radicals in a plasma lead to diamonds under low pressure conditions. The reaction is initiated by ignition *via* microwaves or lasers [21]. Catalysts (*e.g.* Co, Ni, Mn, Cr) simplified the required synthetic conditions, but the optimization of the synthetic processes still continues [22].

The successful diamond synthesis pushed developments in high-pressure devices forward. Up to now, three different types of static press designs are known: The belt press, the cubic press and the split-sphere presses. The belt apparatus works with an upper and lower anvil, pressing the load in a cylindrical inner cell. The anvils also provide electrical current to the compressed cell for heating up the sample.

Cubic or multianvil presses provide isotropic pressure simultaneously onto all faces of a cube-shaped volume [24]. The first multianvil high-pressure device,

Figure 1-3. T. Hall with tetrahedral press [23].

the tetrahedral press, developed by T. Hall, worked with four anvils, applying pressure on a tetrahedrally shaped sample [25] (Figure 1-3). For an increase of the sample volume, the design had to be changed as tetrahedral presses cannot easily be scaled up to larger volumes. However, the pressurized volume can be increased by using larger anvils in combination with increasing force required upon the anvils to achieve the same pressure. The alternative way is a decrease of the surface area of the pressurized volume by using more anvils to converge upon a different platonic solid, such as an octahedron, as it is realized in the Walker-type multianvil apparatus.

Split-spheres are the most efficient pressure devices. Equipped with a centered ceramic and cylindrical "synthesis capsule", these devices work with an octahedral cavity which is compressed by eight outer anvils, like the present Walker-type multianvil high-pressure device [26]. The sample is placed into a cube of pressure-transmitting material, compressed by inner tungsten carbide anvils (or VK10 hard alloy), while the whole setup is placed in a disc-shaped barrel filled with oil to pressurize upon heating.

Due to the great efforts made in developing different designs of press devices, the benefits achieved in high-pressure / high-temperature chemistry must not be left unhonored. Super hard materials, such as nitrides and carbides, or C/N- and B/C/N-phases doped with different elements are still in the scientific scope concerning hardness, molecular weight, and conductivity. Cubic boron nitride, counted as second hardest material after diamond, is widely known as abrasive [27,28] or can be applied for building and cutting tools besides construction purposes, such as rods, step-bearing, bearings, and slider bearings [29]. The behavior under pressure was theoretically investigated based on first-principles method [30]. Starting from amorphous BN (mechanically milled hexagonal BN) the phase transformation into the cubic compound starts at 5.5 GPa and temperatures exceeding 2200 °C or 7.7 GPa and above 1500 °C, respectively, depending on treatment with or without H_2O as catalyst [31]. When transformed, c-BN shows extraordinary hardness and pressure stability [32,33]. It can be applied in high-pressure / high-temperature chemistry as reactor for the synthesis of hard materials [34].

Within the class of super hard materials, McMillan *et al*. investigated also borides which exhibit structures in analogy to *α*-rhombohedral boron. Under the applied high-pressure / high-temperature conditions the compound B_6O_{1-x} [35-38] was obtained, using the Walker-type multianvil technique.

Further investigations offered new synthesis routes to compounds exceeding the hardness of c-BN [39]. BC_2N and BC_4N are therefore promising materials [40-42]. Nevertheless, working

groups were able to synthesize BC_2N in a diamond anvil cell (18 GPa, 2480 °C). The investigation of the physical and structural properties showed a high hardness ranging between c-BN and diamond.

Continous research on nitrides led to the compound "C_3N_4", which is one of the most intensly studied systems of all. Even though α-, β-, and γ-C_3N_4 are only theoretically predicted by Cohen *et al*., the hardness of γ-C_3N_4 is estimated to be comparable or even exceeding that of diamond [43-45]. Therefore, research still continues, although Solozhenko *et al*. recently stated that efforts in finding harder materials than diamond might be for naught [46]. Approaches on hard materials still generate new different compounds. High-pressure / high-

temperature synthesis led to the high-pressure modification γ-Si_3N_4, crystallizing in the cubic spinel-type structure ($Fd\bar{3}m$, no. 227) [47,48]. The structure of the ambient pressure modifications α- and β-Si_3N_4 consist exclusively of SiN_4-tetrahedra. According to the pressure coordination rule, the coordination numbers in high-pressure phases increase under extreme conditions. γ-Si_3N_4 exhibits two different types of polyhedra, SiN_4-tetrahedra besides SiN_6-units (Figure 1-4). Although the modification β-Si_3N_4 already plays an important role as ceramic material,

Figure 1-4. Crystal structure of the high-pressure modification of γ-Si_3N_4. Green: SiO_6-tetrahedra, yellow: SiN_4-tetrahedra [47].

the synthesis of the new cubic modification was sensational [49].

Investigations showed a considerable hardness of the cubic phase γ-Si_3N_4, exceeding that of the polymorphs α- and β-Si_3N_4 and even of the hardest oxide (SiO_2, *stishovite*) known so far. The theoretical calculations of another high-pressure polymorph of Si_3N_4 became true when static pressure experiments up to 34 GPa and shock pressures up to 40 GPa led to the modification of c-Si_3N_4 [50].

As industry always strives to improve existing materials, current research in high-pressure chemistry on nitride-compounds expanded to the field of phosphorous nitrides. The binary high-pressure compound γ-P_3N_5 was synthesized under high-pressure / high-temperature conditions of 11 GPa and 1530 °C [51]. The interesting crystal structure represents a novel structural feature as it comprises a
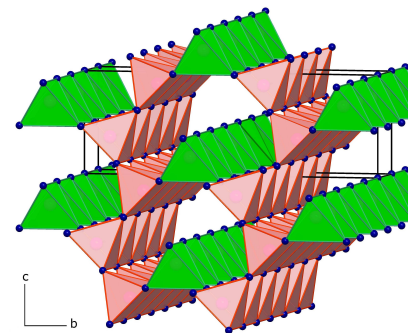
Figure 1-5. Crystal structure of γ-P_3N_5 [51].

three-dimensional network, composed of corner-sharing PN_4-tetrahedra besides distorted PN_5-square pyramids (Figure 1-5). Theoretical investigations on the structure performed by Kroll and Schnick predicted a pressure induced transformation at pressures exceeding 43 GPa of γ-P_3N_5 into the δ-P_3N_5 modification, which would crystallize in the *kyanite*-type structure ($P\overline{1}$, no. 2) [52].

Enlarging the elemental composition in phosphorous nitrides, lithium phosphorus nitrides with the composition of $LiPN_2$ and Li_7PN_4 were synthesized. Due to lithium ion conductivity found in the compounds, these structures are highly appreciated for technical applications [53,54].

Other ternary P-N-compounds were also obtained *via* high-pressure / high-temperature synthesis. At conditions of 11 GPa and 600 °C, the first nitridic clathrate $[P_4N_4(NH)_4](NH_3)$ could be synthesized by Karau *et al.*, using a multianvil high pressure device [55]. Thermolysis of NH_4N_3 provided *in-situ* a high N_2 partial pressure and led to nitridophosphates mixed with P_3N_5. As phosphates are considered as advanced materials for the application as ionic conductors [56], catalysts in organic syntheses [57], or even as NLO-materials [58,59], research intensified.

In addition to the interesting technical applications, oxonitridophsphates comprise also interesting metastable structures only accessible *via* high-pressure conditions. The compound $Sr_3P_6O_6N_8$ could be synthesized by Sedlmaier *et al.* under high-pressure / high-temperature conditions of 6 GPa and 920 °C. The highly condensed layered structure consists of PON_3-tetrahedra connected among each other *via* corner-sharing, exhibiting threefold coordinated nitrogen atoms [60]. Interestingly, the linkage of the PON_3-tetrahedra resulted in *vierer* and *sechser* rings in analogy to layered silicates, which was never observed before.

The parameter pressure was not only useful for nitrides, phosphorous nitrides, and oxonitrides, but also to find access to new high-pressure modifications in intermetallic phases. At ambient pressure conditions, different rare-earth stannides exist with the composition of *RE*PtSn (*RE* = La - Nd, Sm) [61-66], *RE*PdSn (*RE* = La; Ce, Pr, Nd) [66], and *RE*NiSn (*RE* = La - Nd, Sm) [66-68]. Remarkably, the ZrNiAl structure-type can only be found for small rare-earth elements. Heymann *et al.* were able to stabilize the hexagonal ZrNiAl-structure [69-71] for large rare-earth ions [72-75], although the rare-earth compounds crystallize normally in the orthorhombic TiNiSi-type
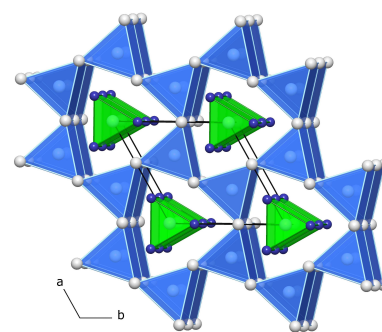
Figure 1-6. TiNiSi crystal structure [76].

structure [76] according to their ionic radii (Figure 1-6). The parameter pressure enabled the transformation of the stannide ErAgSn into the ZrNiAl structure, although NP-ErAgSn adopts the NdPtSb structure-type.

While intermetallic phases are highly appreciated due to their various physical properties and applications, borates are in the scientific focus owing to their NLO qualities. In our working group, high-pressure chemistry as a tool to explore new scientific fields led to new interesting compounds with promising properties. The parameter pressure allowed the synthesis of various new crystalline borates with extraordinary structures and physical properties.

Silicates are known for their multitude of different structures, arranged in isolated and double tetrahedra, rings, single and double chains, sheets, or three dimensional framework. As in borates BO_4- and BO_3-units occur, the structural diversity is exceedingly high. The trigonal BO_3- and tetrahedral BO_4-units can exist isolated or can be distributed in the structure arranged in groups, rings, chains, bands, layers, or entire networks. The BO-units can be connected among each other *via* one, two, or three common corners.

Rare-earth oxoborates were in the focus of Huppertz *et al*. Owing to his great efforts research has led to a plethora of new compounds, synthesized under high-pressure / high-temperature conditions. Even the interesting structural characteristic of edge-sharing BO_4-tetrahedra was found first in the compounds $RE_4B_6O_{15}$ (RE = Dy, Ho) [77-79], obtained *via* high-pressure / high-temperature synthesis (8 GPa, 1000 °C).

Due to the scientific success of rare-earth oxoborates, research was enlarged into transition metal and main group metal borates, recently also in oxofluoroborates. Extraordinary borate compounds, bearing transition metal cations were synthesized by Knyrim during her Ph. D. thesis. The borates β-MB_2O_5 (M = Zr, Hf) were obtained from high-pressure / high-temperature synthesis (7.5 GPa, 1100 °C) resulting in corner-sharing BO_4-tetrahedra interconnected to layers, which were only separated by the metal cations [80,81].

The composition β-MB_4O_7 (M = Mn, Co, Ni, Cu) was obtained under pressure conditions of 7.5 GPa and temperatures ranging in between 550 and 1250 °C, respectively. The crystal structure shows tetrahedrally coordinated boron, connected *via* common corners, forming three-dimensional networks of BO_4-groups. Interestingly, the structure is isotypic to the compound β-ZnB_4O_7 which was also obtained *via* high-pressure / high-temperature synthesis (10.5 GPa, 1000 °C, multianvil device) [82].

Further compounds were also obtained *via* high-pressure / high-temperature chemistry, *e.g.* MB_2O_4 (M = Fe, Ni, Cd), or β-BaB_4O_7, or δ-BiB_3O_6. The high-pressure modification α-

FeB_2O_4 was derived from synthetic conditions of 7.5 GPa and 1100 °C, in a multianvil high pressure device. The crystal structure represents only corner-sharing BO_4-groups, interconnected to *sechserrings*. Six of these rings are condensed to borate layers [83]. Enlarging the composition, the compound HP-NiB_2O_4 was synthesized under high-pressure / high-temperature conditions of 7.5 GPa and 680 °C. Its crystal structure consists of distorted tetrahedral BO_4-groups, which are connected among each other, resulting in planar layers [84]. The compound CdB_2O_4 was obtained *via* high-pressure / high-temperature synthesis of 7.5 GPa and 1000 °C. The crystal structure is built of corner-sharing BO_4-tetrahedra, linked to layers, forming *sechserrings*, which are interconnected to a three-dimensional network. High-pressure / high-temperature conditions of 7.5 GPa and 1100 °C led to the β-modification of BaB_4O_7. The crystal structure revealed isotopy to the mineral $BaBe_2Si_2O_7$ (*barylite*) [85], as it is composed of corner-sharing BO_4-tetrahedra, interconnected to a network.

Beside these interesting new structure, one of the most important borates BiB_3O_6 was already known from the literature und highly appreciated due to its NLO-properties. High-pressure / high-temperature synthesis of 5.5 GPa and 820 °C led to the new modification δ-BiB_3O_6. The crystal structure shows exclusively corner-sharing BO_4-tetrahedra, forming layers, interconnected *via* zickzack-chains of BO_4-groups [86].

A new field of borate-chemistry was approached when A. Haberer started investigating quaternary oxofluoroborates. Recently, the synthesis of $Yb_5(BO_3)_2F_9$, $Gd_4B_4O_{11}(F,H)_2$, and $Pr_4B_3O_{10}F$ was successfully performed under high-pressure conditions of 7.5 GPa at 1100 °C ($Yb_5(BO_3)_2F_9$) [87], 7.5 GPa at 1100 °C $Gd_4B_4O_{11}F_2$ [88], and 3 GPa at 800 °C ($Pr_4B_3O_{10}F$) [89], using a Walker-type high-pressure device. The structure of $Yb_5(BO_3)_2F_9$ can be described in relation to the gadolinium fluoride borates $Gd_3(BO_3)_2F_3$ and $Gd_2(BO_3)F_3$ as an alternating layer with the composition "$YbBO_3$" and "YbF_3", spreading into the *bc*-plane. Chapter 4.3 gives a detailed view over the results in borates obtained in the last few years in our working group.
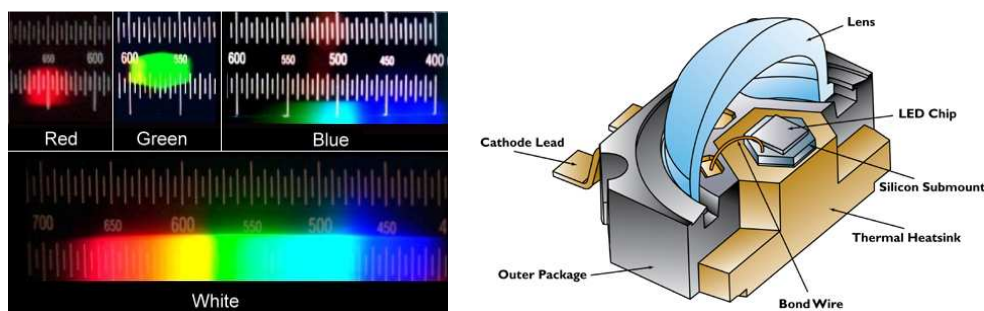
Figure 1-7. Spectra of LED [90], besides an assemblage of LED [91].

As high-pressure chemistry offers the possibility to synthesize metastable compounds, new fields can be explored. Concerning the questions of daily and future life, these compounds have the potential to advance energy saving technologies such as fuel cells, compact fluorescent lamps (CFLs) and light emitting diodes (LEDs), hybrid technology, or electric motors. In the scope of research are therefore promising materials for technical applications.

As research continued in the last few years, improvements on luminescence led to new structures in the field of nitridosilicates, derived by the HF-furnace technique or under high-pressure / high-temperature conditions. The working group of Schnick focuses on nitridosilicates as these materials are stil in the scientific scope. Nitridosilicates in the stoichiometric ratio of $Sr_2Si_5N_8$ or $SrSi_2O_2N_2$ show outstanding luminescence properties when doped with Eu^{2+} [92-96]. As research continued, in the last years new compounds were obtained, *e.g.* $SrAlSi_4N_7:Eu^{2+}$ [97] and $Sr_5Al_{5+x}Si_{21-x}N_{35-x}O_{2+x} : Eu^{2+}$ [98]. As nitridosilicates show extraordinary luminescence properties, the application as LED materials is obvious. Besides different nitridosilicates, other compounds are therefore also used. Nitrides are also important, *e.g.* gallium nitride enables promising applications [99,100], as well as ternary compounds like InGaN or quaternary nitrides like AlGaInN, phosphorous-compounds such as AlGaInP, or arsenic-compounds as GaInNAs.

Gallium nitride, as basis for high-efficient fc-LED (flip-chip light emitting diodes), provides a combination of reduced operation voltage with low junction temperature [101]. Moreover, GaInNAs-based high-power laser diodes can be used for the pumping of Raman amplifiers as they show emissions in the range of 1220 to 1240 nm wavelength, and exhibit very low internal losses of only 0.5 cm^{-1} [102].

Finally, one can say, high-pressure chemistry comprises a diversity of different chemical fields. Pressure can be successfully applied for the synthesis of super-hard materials such as diamonds and analogue materials, like nitrides, carbides, or borides. Borates,

containing main group ions, transition metal cations, or rare-earth elements are accessible just as well as intermetallic compounds.

In this thesis, high-pressure / high-temperature investigations on different systems were performed. First of all, synthesis of crystalline gallium oxonitrides lay in the focus, besides exploring the ideal high-pressure / high-temperature conditions for a successful synthesis of ideal gallium oxonitrides. The stability field of gallium oxonitrides was investigated and experiments were performed under variation of pressure, temperature, and molar ratio of the starting mixture and heating segments, to learn more about formation and decomposition of the spinel-type material.

In addtition to that, rare-earth gallates were investigated. The question for new rare-earth gallates derived under high-pressure / high-temperature conditions was another main point in this work. The field of the rare-earth compounds still enlarges, based on interesting properties and applications.

Investigations on rare-earth compounds enlarged to the field of rare-earth oxoborates. However, these compounds exhibit interesting structures and properties, so research under high-pressure / high-temperature conditions still continues. Based on the versatile new borates, synthesized in our working group, the main goal of high-pressure / high-temperature chemistry is to stabilize new metastable compounds to expand the existing limits of a normal pressure chemistry to find new interesting advanced materials.

2   Experimental Methods

2.1   High-Pressure Multianvil Synthesis

The experiments in this work were performed under high-pressure / high-temperature conditions, in 1000 t presses applying the multianvil technique. The presses are shown in Figure 2-1.

Syntheses were performed in modified Walker-type modules (all devices from Voggenreiter, Mainleus, Germany). The pressure conditions in this setup are nearly hydrostatic, as the pressure is constantly induced to the sample from all sides. A detailed description of the press construction, pressure, and temperature calibration as well as sample preparation are given in the following chapters [2.1.1 - 2.1.8].

Figure 2-1. Frontal view of the old (left) [109] and new (right) 1000 t presses.

2.1.1   The Multianvil Technique

The combination of extreme conditions, reasonable costs for the experiments and reasonable large sample volumes at the same time, is realized in Walker-type multianvil synthesis. The experiments under high-pressure / high-temperature conditions were performed in a modified Walker-type multianvil apparatus. This technique was developed in 1990 by Walker *et al*. [103,104], improved and modified by Frost *et al*. [105,106]. An upscale to 1000 t was done with the help of the company Voggenreiter (Mainleus, Germany), which allows working with an almost hydrostatic pressure up to 25 GPa.

2.1.2   The 1000 t Presses

Both 1000 t high-pressure devices are identical in construction, except a few insignificant details. The high-pressure facilities consist of hydraulic down stoking presses, with a predefined maximum load of 1000 t, which comes up to 700 bar oil pressure.

The presses can be divided into three main parts. First, the main pressure cylinder (CCR-10002, Enerpac, Columbus, WI, USA, for the old model; the new model works with equipment of Voggenreiter, Mainleus, Germany), secondly, the regulation cylinder with a worm gear screw jack driven by a servomotor, and last, of the main engine with the oil reservoir (Figure 2-2).
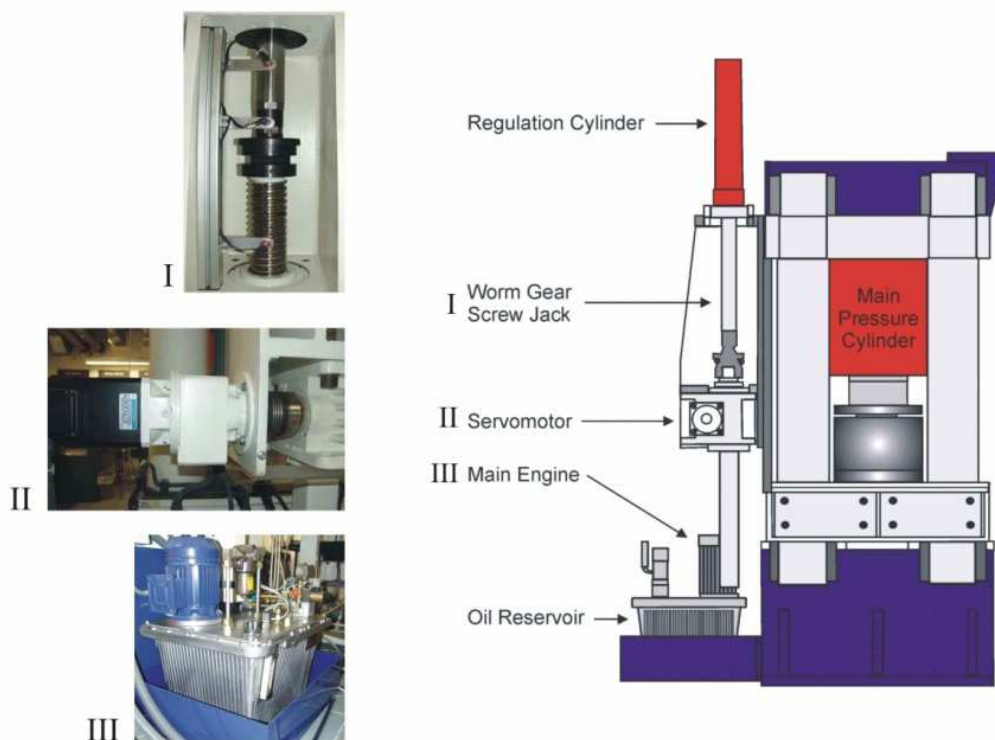
Figure 2-2. Schematic view of the 1000 t press with the hydraulic unit. **I:** Worm gear screw jack. **II:** Servomotor for pressure regulation. **III:** Main hydraulic unit and oil reservoir [109].

Figure 2-2 shows the old press with a systematic description of the different parts. The main valve for the main pressure cylinder and the lock valves for the regulation cylinder are placed under the top covering above the top plate. Figure 2-3 presents the valves and oil pipes, besides the diagram of the oil circuit used in the press. The diagram separates the three main pressure parts by a red line.

Before an experiment is started, the Walker-type module is centered underneath the main pressure cylinder. Between the cylinder and the module, a remaining small gap of about 1 cm

has to be closed when the pressure program is started. The ram is driven fast within 10 seconds onto the top plate of the module.
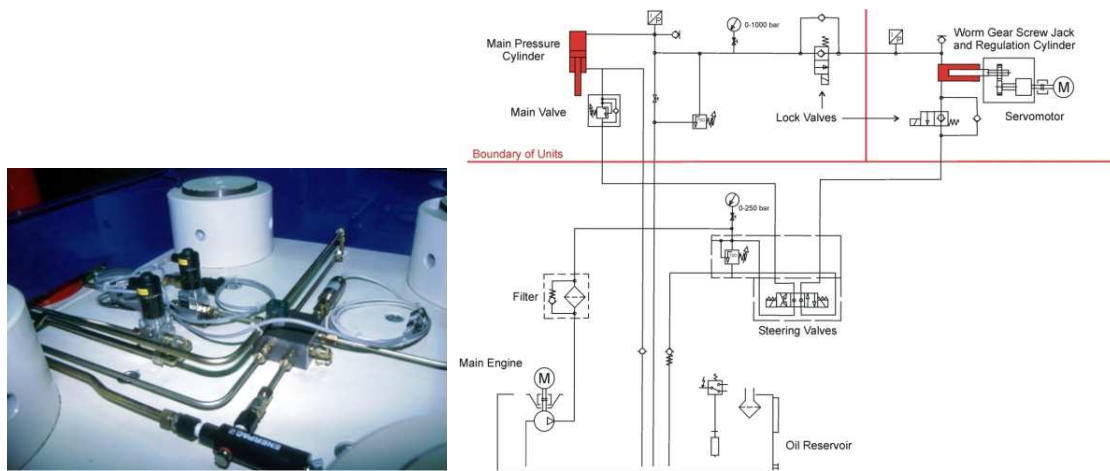
Figure 2-3. Left: Hydraulic valves and oil pipes on the top plate of the 1000 t press. **Right:** Oil circuit diagram of the press, divided into the main parts [109].

Induction switches (see Figure 2-4) control the lowering of the press cylinder onto the top plate. A hard put down is avoided, by controlling and stopping the driving ram just before the distance piece touches the top of the module. After the press is closed, the main segment of the program is started. The servomotor regulates and controls the oil pressure in the main cylinder by moving the worm gear screw jack into the outer regulation cylinder (Figure 2-2, Part I). The adjustment of the oil pressure is more precisely carried out by the servomotor than with the help of the main engine. After reaching an oil pressure of 14 bar, which corresponds to a load of 19.5 t, the predetermined pressure protocol was started. In this segment, all gaps in the assembly were closed, (more details are available in chapter 2.1.1).

Figure 2-4. Iduction switches [109].

A technical limit for an increasement of the pressure is a maximum compression rate of 1 bar per minute, which corresponds to a load of 86 t per hour, while the pressure release (decompression period) takes threefold the time (86 t / 3 h).

The controlling of the main engine, servomotor, and the valves was formerly executed by a PLC unit (<u>P</u>rogrammable <u>L</u>ogic <u>C</u>ontroller (SPS <u>S</u>peicher<u>p</u>rogrammierbare <u>S</u>teuerung)) (Simatic S7-300, Siemens AG, Germany) equipped with a serial RS232C interface. Essential information about the experimental profile was accomplished by a second control unit (Windows PC), for transferring the pressure ramps to the PLC device, reading the actual system pressure and inspecting all actions with the PLC unit, while the new version of the press program is only controlled by the PC, without a secondary control unit. To control the

actual run, the programs "PRESSCONTROL I" and "PRESSCONTROL II" [107,108] were developed and programmed with Visual C++ (Microsoft) for communication, monitoring, and calibration of the 1000 t press and the adjusted heating unit. The program controls the experiments, reports about malfunctions, or records measurements and is used for pressure and temperature calibration experiments. In Figure 2-5 the graphical working surface is shown.

For a successful program run, experimental parameters and setups must be entered, information about the assembly size (*e.g*. 18/11, 14/8), type of the furnace material (graphite or lanthanum chromite), and in detail the exact heating and pressure ramps.
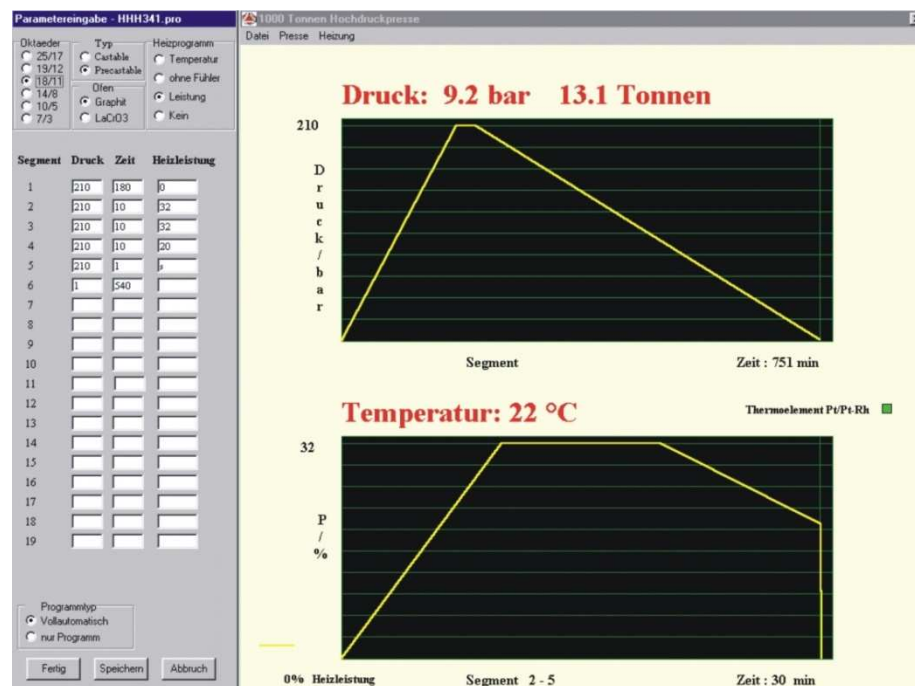
Figure 2-5. Graphical surface of the program "PRESSCONTROL I" [107].
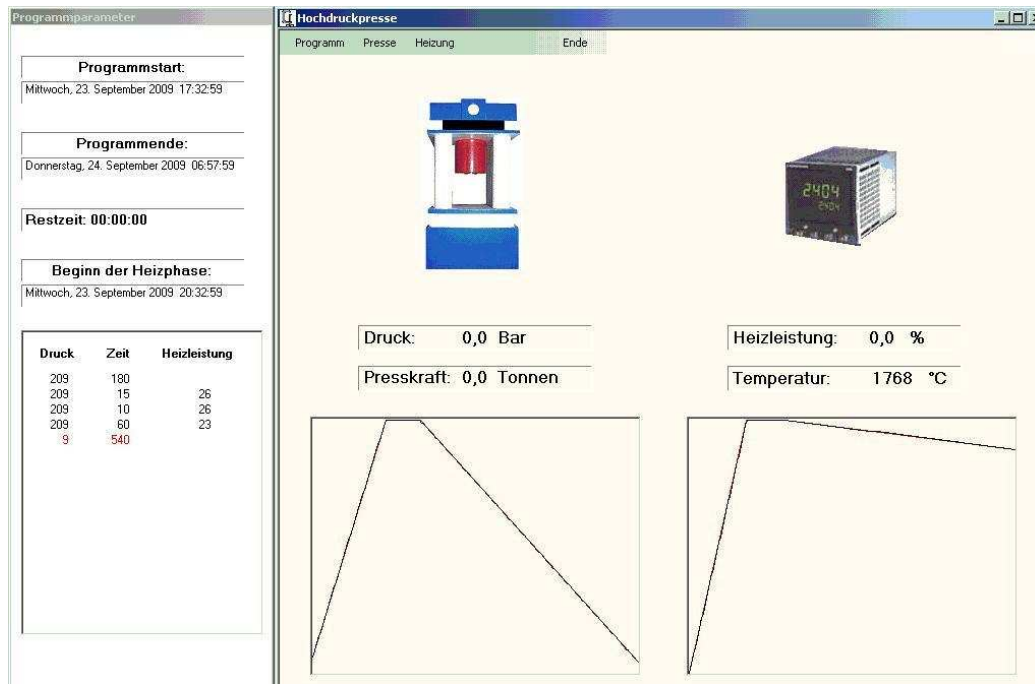
Figure 2-6. Graphical surface of the program "PRESSCONTROL II" [108].

The program distinguishes between a temperature-controlled heating *via* a thermocouple (*e.g.* Pt-Pt$_{87}$Rh$_{13}$ or W$_3$Re$_{97}$-W$_{25}$Re$_{75}$) or the predetermined power / temperature calibration curves. The curves are determined for the corresponding assembly in dependence of the applied pressure. The synthesis temperature is limited by the applied furnace material (graphite up to 1400 °C; LaCrO$_3$ up to 2700 °C).

Besides the experimental setup, the pressure and the temperature ramps have to be defined, including intended times for each step, given in minutes. The pressure ramp consists of three main parts, the compression, up to the designated pressure, given as oil pressure in correspondence for the intended load, the holding segment, in which the heating proceeds, followed by the decompression period down to ambient pressure. The heating is also divided into several heating segments: increase of the temperature, the static dwell, a tempering phase, and quenching or a slow cooling phase down to room temperature.

After entering the experimental details, the program was saved and the pressure and temperature ramps are displayed on the screen (Figure 2-5).

Starting the press is accomplished *via* the task line of the program, by sending the parameters to the PC. During the experiment, the actual oil pressure and temperature is displayed on the screen (Figure 2-5). The implementation of security functions in case of a sudden pressure loss in the assembly (blow-out) stops the program. The experiment is automatically cancelled and the decompression segment is initiated, followed by the press opening.

2.1.3 The Walker-type Module

To realise high pressures and high temperatures in combination with a relatively high experimental volume at the same time, probably the best setup is the high-pressure system developed by Walker *et al.* [103] in 1990. The here applied press setup is based on the multianvil-apparatus, connecting the advantages of a nearly hydrostatic pressure, combined with large sample volumes at reasonable costs. An enhancement of the Walker-type technique

was done by Frost *et al.* [105] in 1998 at the Bayerisches Geoinstitut (Bayreuth, Germany), followed by a scale-up to a maximum load of 1000 t, which was fabricated by the company Voggenreiter (Mainleus, Germany).
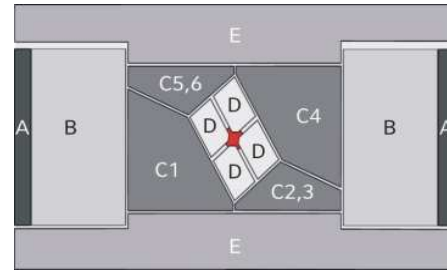
Figure 2-7.   Schematic setup of the Walker-type module [109].

Figure 2-7 demonstrates the schematic setup of the module. Six tool steel wedges (C1-6; outer anvils) including eight tungsten carbide cubes (D; inner anvils), besides the centered octahedral pressure medium (highlighted in red) are positioned in the containment ring, which is made of hardened tool steel (B; module). The latter is surrounded by a safety ring (A; module). The loading of the module is accomplished through pressure-distribution plates on top and bottom of the module (E). For security reasons, the stability range of the containment ring (HSM, 1.2343, $R_c = 52$, 17.8 cm (inner diameter), 33.8 cm (outer diameter), total height 19.4 cm) and the surrounding safety ring (Höver, 1.4541, 33.8 cm (inner diameter), 37.8 cm (outer diameter) total height 19.4 cm) are dimensioned with a factor of 2.5, which means that the module holds a load of 2500 t without any failure [109].

The applied material for the wedges is tool steel (HSM, 1.3343) hardened to $R_c = 62$ and exhibits a square face with the dimensions of 6.0 cm × 6.0 cm (for 32.0 mm tungsten carbide cubes), with an angle of 35°26' to the axis of the module. The lowest corner of the square face has a distance of 2.0 cm from the basis. Figure 2-8 gives a view of one of the 98.0 mm high wedges with the square face in front and wiring channels on both sides. The three assembled wedges fit perfectly into the 17.8 cm diameter cylindrical cavity of the containment ring, while a small gap of approximately 1 mm remains in between. Figure 2-9 shows a photograph of the massive containment ring surrounded by the safety ring, which incorporates three wedges with wiring ports.

Figure 2-8. Single tool steel wedge with wiring channels for calibration [109].
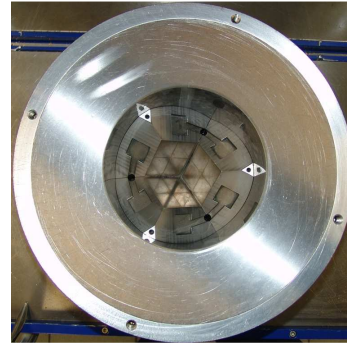
Figure 2-9. Containment ring with three wedges [109].

The containment ring is covered by two pressure-distribution plates at its top and bottom (37.8 cm in diameter, 3.9 cm thickness). These plates are made from an aluminium alloy (Alimex, AMP 8000, Willich, Germany) except the raised part in the middle of the plate. This part contacts directly the wedges, and is therefore substituted by tool steel (Höver, 1.4548.4) to avoid deformations of the plate. Both, top and bottom distribution plates comprise cooling spirals for a water cooling system, during the heating segment. Figure 2-10 (left) shows the spiral cooling lines applied into the pressure-distribution plates, and sealed by the tool steel plates (Figure 2-10 (right)).
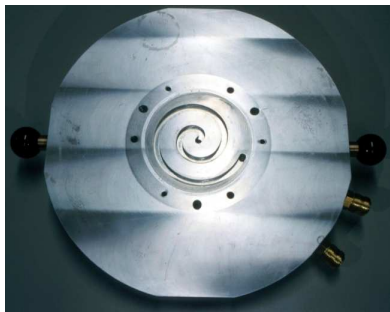
Figure 2-10. Left: Cooling spiral inside the pressure distribution plate [109].
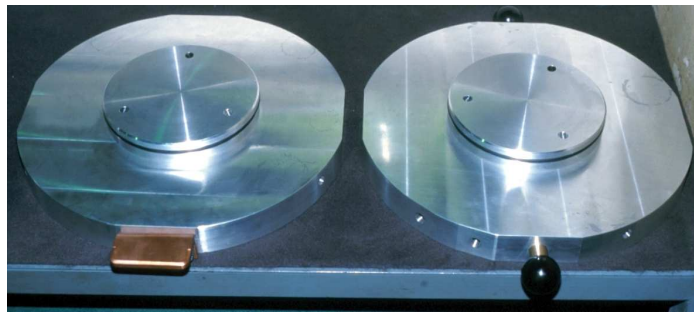
Right: Pressure distribution plates (left: bottom plate, right: top plate) [109].

In addition to that, several tunnels and shafts are added to the pressure-distribution plates as well as to the six wedges, which are necessary for pressure and temperature calibration or monitoring of experiments.

2.1.1   The Preparation of the High-pressure Experiment

The Walker-type multianvil module (section 2.1.3) works with six wedges compressing a cubic arrangement of eight inner anvils. The inner anvils consist of equilateral tungsten carbide cubes, with an edge length of 32 mm and truncated corners shaped to triangular faces. An octahedral cavity is generated by arranging the eight cubes to a big cube and facing the truncated corners to the center of an octahedral array. The pressure cell is located in this octahedral space. The existing different assemblies are defined by their octahedral edge length (OEL) and truncation edge length (TEL) of the corresponding tungsten carbide cubes. For instance, an 18/11-assembly describes an octahedron with an edge length of 18 mm, whereas the eight tungsten carbide cubes exhibit truncated triangular faces with an edge length of 11 mm. In this work mainly 18/11- and 14/8-assemblies were used. Furthermore for higher pressures than 13 GPa a 10/5-assembly can be used as a matter of routine.

The achievable maximum pressure and maximum of sample volume are both determined and limited by the size of the octahedron. These values range typically from ~35 mm^3 at a maximum pressure of 10 GPa (18/11), ~9 mm^3 at a maximum pressure of 13 GPa (14/8), and ~4 mm^3 at a maximum pressure of 16 GPa (10/5-assembly).

As pressure transmitting medium MgO-octahedra, prefabricated, sintered, and doped with 5 % magnesium chromite (Ceramic Subtrates & Components Ltd.; Newport, Isle of Wight) are applied.

Table 2-1 shows the utilized different MgO-octahedra and tungsten carbide cubes, displaying the different sizes with octahedral edge length of 18 mm (left), 14 mm (middle) and the 10 mm-assembly (right). The edge lengths of the truncated tungsten carbide cubes are also shown in Table 2-1. The limits of sample volume for each experiment are also given.

Table 2-1. The three different assemblies, showing the sizes of tungsten carbide cubes (mm) with the corresponding octahedral pressure medium, listing the maximum achievable pressures [109].

Assembly Sizes		
18/11	14/8	10/5
18 mm OEL	14 mm OEL	10 mm OEL
11 mm TEL	8 mm TEL	5 mm TEL
max. Synthesis pressure		
10 GPa, 100 kbar	13 GPa, 130 kbar	16 GPa, 160 kbar
Sample volume		
ca. 35 mm^3	ca. 9 mm^3	ca. 4 mm^3
ca. 30 – 50 mg	ca. 20 – 30 mg	ca. 10 – 15 mg
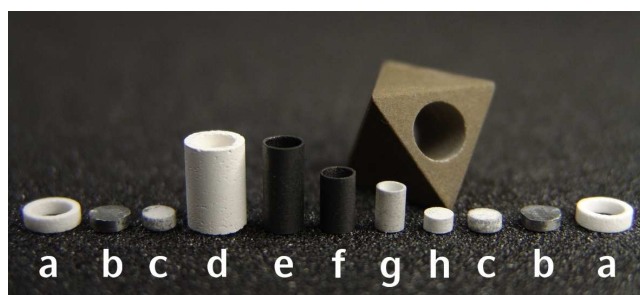
Figure 2-11. Survey of the assembly parts; a: MgO rings, b: Mo-plates, c: MgO-plates, d: zirconia sleeve, e: long graphite tube, f: short graphite tube, g: h-BN crucible, h: h-BN plate [109].

The different parts for assembly setup are shown in Figure 2-11. A hole is drilled into the octahedra along its $\bar{3}$ axis from face to face, to put in the sample.

The sample is positioned into a hexagonal boron nitride crucible (Henze BNP GmbH, HeBoSint® S10, Kempten, Germany) (g) while filled and closed with a hex. BN plate (h) and centered in the octahedron. An advantage of the crucible material is the chemical inertness under high-pressure / high-temperature conditions. Nevertheless, some materials will still react with the crucible material depending on the chemical system and especially the applied synthesis conditions. Beside BN, the application of different capsule materials like copper, molybdenum, platinum, or gold are also possible. Here, for samples in the In-O-N-system, copper crucibles, fitting into the BN-crucible were used for the syntheses, beside Mo-crucibles in some Ga-O-N syntheses.

Sample heating is realized by cylindrical graphite tubes (RW 403, SGL Carbon, Bonn, Germany) (e) surrounding the h-BN capsule used as resistance furnaces. Graphite has a natural limit for its application under high-pressure / high-temperature conditions. It can be used as heating material without check its function up to pressures of 10 GPa and temperatures of 1500 °C. Increasing the pressure and the temperature the material starts to convert to diamond and its performance of a resistance furnace collapses. As an alternative, LaCrO$_3$ (Cherry-O, Amagasaki-City, Japan) or tantalum foil (Sigma Aldrich, Munich, Germany) can be used to heat up the sample. With those materials, temperatures up to 2727 °C can be generated. The thermal gradient along the sample length is reduced by two telescoped furnaces, with a stepped wall thickness [110]. The crucible is centered inside the furnaces using MgO-plates (Magnorite MN399CX, Saint-Gobain Industrial Ceramics, Worcester, MA, USA) (c) at the bottom and the top of the furnaces. Thermal isolation of the octahedra is realized by a zirconia sleeve (d) (Ceramic Substrates & Components Ltd., Newport, Isle of Wight) surrounding the inner assemblage. The electric contact to the furnace is assured by two molybdenum plates (Mo007905, Goodfellow, Bad Nauheim, Germany) (b) at the top and the bottom, fitting into the MgO-rings (a). For experiments performed under less extreme conditions, longer zirconia sleeves can be applied instead of MgO-rings. Then the Mo-plates are directly positioned into the sleeve. Figure 2-12 and Figure 2-13 show the dimensions of the described pieces of the 18/11- and 14/8-assembly, used in this thesis. Further information can be found in Ref. [109,111,112].
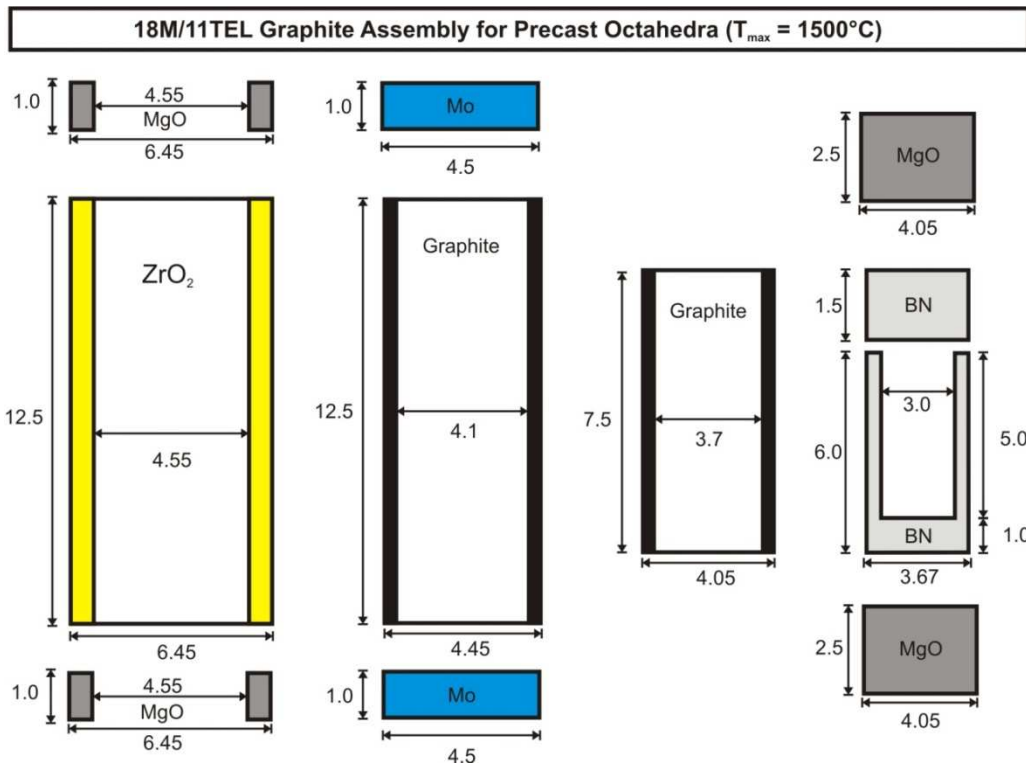
Figure 2-12. Dimensions (mm) of the pieces used for the 18/11-assembly (precastable MgO-octahedron, pyrophillite gaskets) [109].

Figure 2-13. Dimensions (mm) of the pieces used for the 14/8-assembly (precastable MgO-octahedron, pyrophyllite gaskets) [109].

The applied parts of the assembly, like h-BN, graphite, and MgO pieces were manufactured using a lathe (Opti D480, Collrep GmbH, Maintal, Germany). After insertion of the pieces into the octahedron, the eight tungsten carbide cubes are arranged around it as seen schematically in Figure 2-14 (left). To guarantee pressure increasement, the octahedral cavity has to be sealed. The triangular faces of the truncated cubes fit onto the faces of the octahedron, kept on distance *via* pyrophyllite gaskets. In Figure 2-14, four tungsten carbide cubes are shown bearing the half octahedral cavity in the center of it. On the left side, the schematic setup is shown, beside the completed cubic (Figure 2-14, right).

Figure 2-14. Insertion of the octahedron into the eight tungsten carbide cubes (inner anvils) [66,109].

Figure 2-15 demonstrates the setup for the pyrophyllite gaskets on the tungsten carbide cubes. Four cubes are applied with gaskets, one supplied with three short and no long gaskets, the next with two short and one long gasket, a third one with a short and two long gaskets and finally one cube with no short and three long gaskets, as shown in Figure 2-15.
The gaskets are mounted and fixed parallel to the edge of the cubes with small dots of instant adhesive (UHU GmbH & Co. KG, Bühl, Germany; Ropid 100, 150, and 200, Conrad, Hirschau, Germany). An important advice is, to use the adhesive as scarcely as possible for fixing the gaskets, as it can react as lubricant at elevated temperatures. Behind the gaskets, cardboards (Bristol cardboard, 369 g / m^2) are fixed by instant adhesive to inhibit the gaskets from sliding when pressure is applied.

Furthermore, one half of the cubes are covered with gaskets and cardboards, the other half has to be laminated with PTFE-tape (SKAP 130, Beichler & Grünwald GmbH, Löchgau, Germany; Vitaflon, Bad Kreuznach, Germany; Ammerflon, Diessen a. Ammersee, Germany). The function of the PTFE-foil lies in fixing the gasket on its designated position, inhibiting the extruding of the crushed gaskets.

Figure 2-15. Arrangement of the pyrophyllite gaskets on four tungsten carbide cubes [66].

Quality, technical specifications, and suitability of the tungsten carbide cubes used as inner anvils are highly variable depending on the production of different manufactures [113]. At the moment, the best material in quality, concerning stability and lifetime, are cubes of Toshiba grade "F" (Langenfels, Germany), Kennametal "THM-U", "THM-F" (Mistelgau, Germany), and Ceratizit "TSM-10" and "TSM-20" (Reutte, Austria).

For this work, the following sorts of cubes were applied: "THM-U", "THM-F"and Ceratizit "TSM-10" and "TSM-20". The stabilization of the assembled cubes is realized by fixed epoxy-pads of fiber-glass reinforced (Type 2372.4, Menzel & Seyfried, Gröbenzell, Germany), thickness of 0.8 mm (Figure 2-15, left).

Moreover, the top and bottom plate of the assembled cube are prepared with incisions, wherein thin copper stripes (1.5 cm x 3.0 cm, thickness 0.2 mm) are positioned. The flow of the electrical current is ensured by the contacts of the copper pads, leading from the pressure-distribution plates to the wedges and further *via* copper pads to the tungsten carbide cubes. The molybdenum plates in the octahedron contact the cubes directly. Finally, the cube is completed and ready for the experiment, and can be inserted into the nest of wedges, as shown in Figure 2-16.
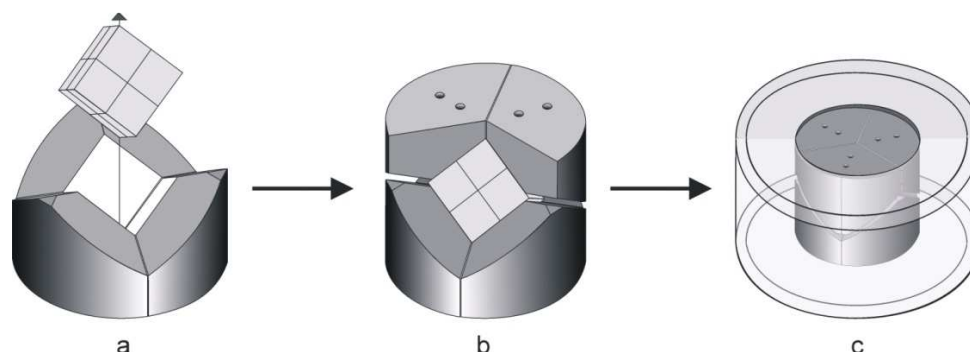
Figure 2-16. Schematic illustration of the assemblage of the anvils in the Walker-type module [109].
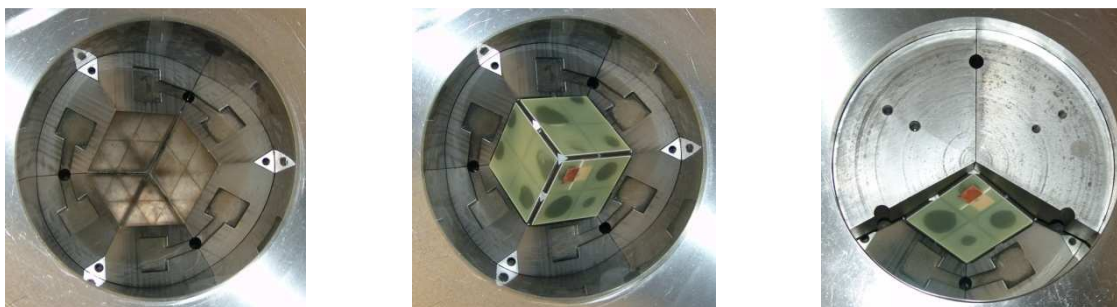
Figure 2-17. Illustration of the assemblage of the anvils in the Walker-type module [109].

In Figure 2-17 the schematic loading of the Walker-type module is shown. Before loading the module with the wedges and the cube, two layers of PET-foil (BO-PET IA, D-K Kunststoff-Folien GmbH, Dessau, Germany) (thickness 0.75 mm) are inserted, to isolate the containment ring from the wedges. Another aspect is the filling of the gap (0.125 mm) between the wedges and the containment ring. Therefore, one large PET-sheet covers the complete inner part and isolates also the top, by sticking ca. 1.5 cm out of the containment ring. The outer surface of the foil is covered with PTFE-spray, to cling it to the module. The inner small sheets of the foil cover the outer part of the wedges, also adhered by small amounts of PTFE-spray. The foils fulfil the function of an isolator for the wedges and the module, besides acting as lubricant, to allow movements of the wedges.

The experiment can be started, when the module is closed by the top distribution plate, and positioned under the hydraulic ram. For successful heating, connection to the water cooling system must be guaranteed.

2.1.2   Recovering of the Sample

After the decompression protocol, the Walker-type module is removed from the hydraulic ram to the preparation plate. When the top pressure-distribution plate is lifted, the module can be unpacked. The upper three wedges are removed, and the cube which comprises the eight inner cubic anvils and contains the octahedron, are carefully raised out of the nest.

Figure 2-18. Cube of inner anvils opened after a high-pressure / high-temperature experiment [66].

Figure 2-18 gives a view of the opened cube after a successful experiment, revealing the octahedron containing the sample. The function of the cardboard, PTFE-tape and gaskets is clearly demonstrated, when two cubes are carefully removed to

reveal the centered octahedron. The recovered octahedron is broken apart with the help of a center punch and a hammer. Finally, the surrounding graphite furnaces and the boron nitride crucible are removed to obtain the sample. Nevertheless, if the sample material showed reactions with the boron nitride crucible, a surrounding part of different color and hardness around the "real" sample can be found. Figure 2-19 show typical crucibles containing the samples.
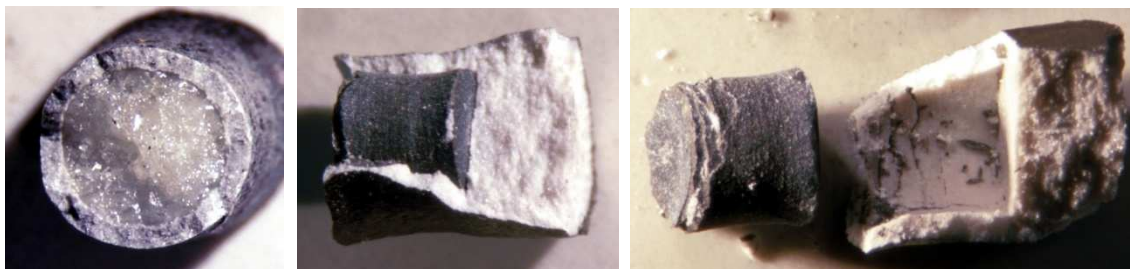
Figure 2-19. Typical BN crucibles containing the imbedded sample after the experiment. **Left:** borate sample, **Right:** intermetallic phase [66].

2.1.3   Experimental Dangers and Problems

Due to the robustness of the two Walker-type modules, with containment rings scaled up to a 2.5-fold stability (up to a maximal load of 2500 t), there exists no reason for experimental dangers with regard to ruptures. Nevertheless, during the heating period of an experiment, ear protectors are required owing to the risk of a blowout (spontaneous loss of pressure in the assembly, *e.g.* after a gasket failure, in combination with an explosion noise due to the reassembling of the wedges).

Figure 2-20 shows an octahedron after a blowout. A second danger is caused by the eight tungsten carbide anvil cubes. Especially when the experiment needs extended high-pressure / high-temperature conditions, the cubes can build up inner tensions. These tensions are the reason for cracks or even explosive destructions under normal

Figure 2-20. Octahedron after blow-out [109].

pressure conditions (Figure 2-21). Therefore, it is necessary to keep used cubes under a shield, to protect the environment from explosive shreds and wear goggles while working with them.
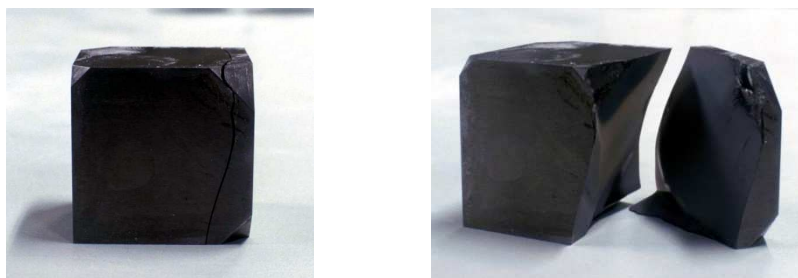
Figure 2-21. Cracked and destroyed tungsten carbide cubes.

2.1.4 Pressure Calibration

The program "PRESSCONTROL II" [107] provides an application for automatic pressure calibration. As pressure calibration is basic for repeatability and reproducibility of experiments and results.

Due to the multitude of factors which are colluding in a multianvil setup, calibration of the exact pressure inside a sample is required and essential. Pressure induced phase transformations of well-known systems are the basis for it. These results are established from investigations in diamond anvil cells (DAC), when actual pressure changes are detected by the shift of the fluorescence lines of ruby, which is added to the sample as reference.

Figure 2-23. Circuit for calibration with bismuth.

For press calibration, changes in the electric resistance are investigated due to phase transitions caused by the applied pressure. Typically Bi and ZnTe are used for pressure calibration, based on the well-established phase transitions up to pressures of 13 GPa. A constant current flow through the octahedron, and therefore through the bismuth piece is ensured. The shift in the electric resistance caused by the phase transformation is very small. Therefore detection is enabled, *via* electrical amplification. Figure 2-23 shows the schematic circuit for the pressure calibration for bismuth, carried out *via* measuring the resistance change due to the phase transformation.

Figure 2-22. Schematic octahedron for bismuth calibration [109].

The phase transition of Bi belongs to the best studied at all and starts at 2.55 GPa (I-II), when phase I transforms into phase II. At 3.15 GPa the transition II-III occurs and finally at 7.7 GPa

a last structural change starting from phase III to phase V is caused [114-125]. Figure 2-24 shows a typical diagram of the relative resistance of Bi for a 14/8 assembly (precastable assemblage) in correlation with applied oil pressure. The three phase transformations of Bi are identifiable as sharp changes in resistance, due to phase transitions of I-II, II-III, and III-V. The first structural change starts from rhombohedral Bi-I (isostructural to α-As) to monoclinic Bi-II, transforming into Bi-III, composed of a tetragonal host structure and an interpenetrating guest component, incommensurate with the host [125]. Increasing the pressure, leads to the cubic body-centered Bi-V phase at 7.7 GPa.

ZnTe shows a semiconductor to metal transition initiated by applying high-pressure (6 GPa – anomaly –, LPP-HPP1 at 9.6 GPa, and HPP1-HPP2 at 12.1 GPa) [126-129] followed by phase transformations.

The preparation of a Bi calibration experiment takes several different steps. First a hole was drilled along the $\bar{3}$ axis of the octahedral pressure medium (diameter 1.7 mm), then stuffed with a cylindrical piece of Bi metal (length ca. 3.8 mm). The remaining space on top and bottom of the Bi piece was filled with copper electrodes to complete with either side of the octahedron. Both copper electrodes were provided with Cu wires, wrapped by another fine, curled Cu wire, to assure electrical communication between the bismuth and the resistance measuring circuit outside the press. The schematic octahedron prepared for a calibration experiment is shown in Figure 2-22.
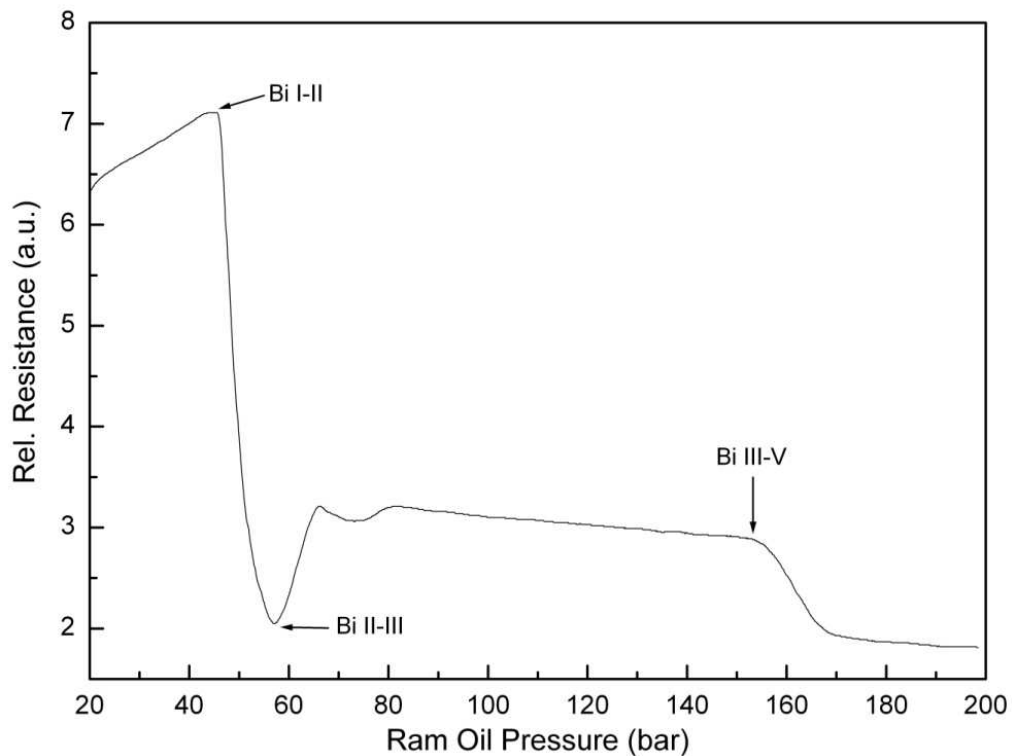
Figure 2-24. Relative resistance diagram of bismuth in dependence of the ram oil pressure (14/8 assembly).

For pressure calibration with ZnTe (99.998 %, Alfa Aesar), fine powders were filled in the centered borehole of an octahedron (thickness 1.9 mm, diameter 1.6 mm). As the resistance of ZnTe (semiconductor) is larger compared to the resistance of bismuth, the build-up is simplified. It requires only the filling of the bore-hole in the octahedron with the ZnTe powder. Figure 2-25 shows the resistance changes of ZnTe, (phase transformations at 6, 9.6, and 12 GPa) in correlation with the applied hydraulic oil pressure.

The anomaly at an applied pressure of approximately 6 GPa results from a change in the bandgap of the zinc blende structured ZnTe, followed by a phase transformation to a semiconducting cinnabar-type phase at approximately 9.5 GPa [128,129]. The last resistance change at ~12 GPa is caused by the transition to a metallic orthorhombic phase (*Cmcm*, no. 63), which is related to a distorted rock salt structure [130].
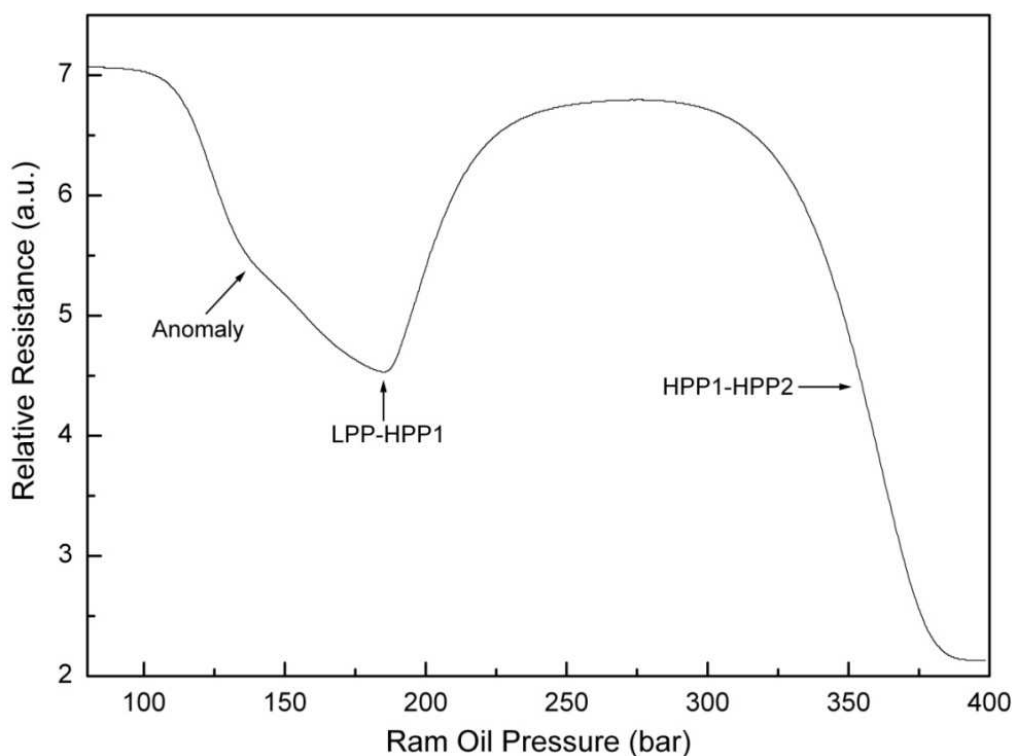
Figure 2-25. Typical relative resistance diagram of ZnTe depending on the ram oil pressure (14/8 assembly).

Other systems which can be used for pressure calibrations are the metals cerium (phase transition at 0.77 GPa [131-133]), besides thallium (phase transition at 3.65 GPa [134]) and barium (phase transition at 5.5 GPa [135-137]). ZnS is useful for the calibration of pressures up to 15.5 GPa, required for experiments performed in the smallest assembly setup (10/5) [138-142].

In Figure 2-26 the pressure calibration curves for the 18/11, 14/8, and the 10/5-assembly are shown. In dependence on the applied press load, the resulting pressures for the three different assemblies are shown. Furthermore, the discrepancies between the two calibration materials (Bi and ZnTe) are also given.
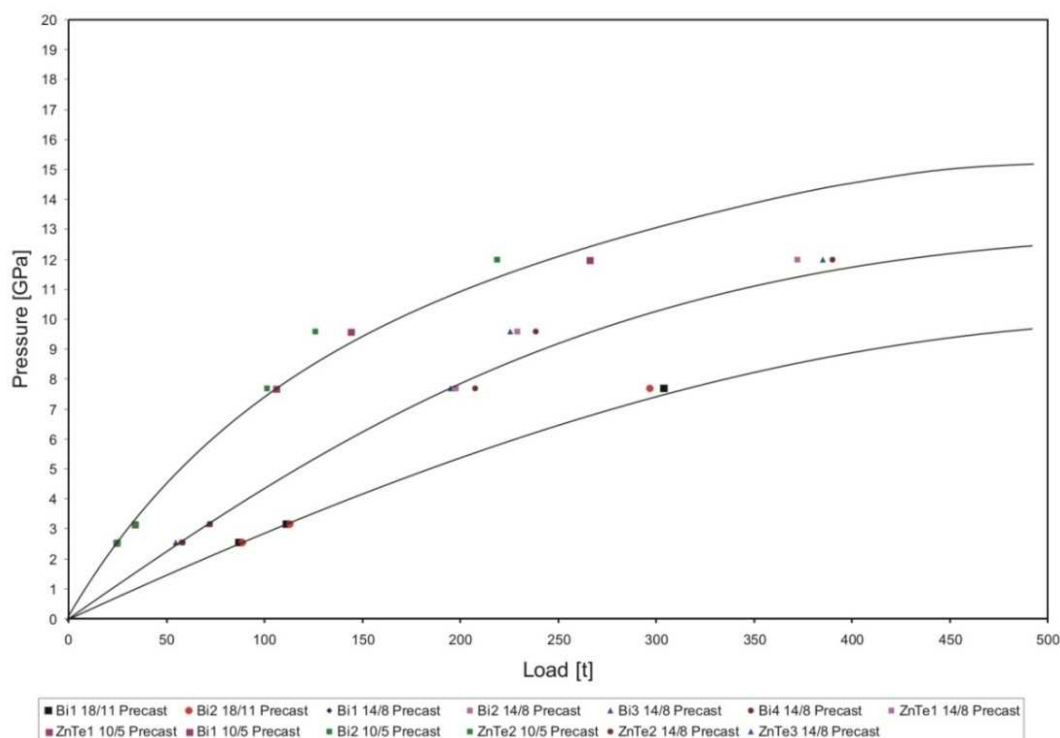
Figure 2-26. Pressure calibration curves for the 18/11, 14/8, and the 10/5-assembly [109].

2.1.5   Temperature Calibration

Reproducible experiments require an exact knowledge of the applied pressure and temperature. For temperature calibration, thermocouples are used. Figure 2-27 (left) shows the thermocouple with copper coil and Mo-ring which can be inserted perpendicular to the heater or along the axis as shown in Figure 2-27 (right). The thermocouple is directly connected to an Eurotherm 2404 temperature controller (Limburg a. d. Lahn, Germany).

The material used as thermocouple was Pt-Pt$_{87}$Rh$_{13}$ for temperatures up to 1500 °C besides W$_3$Re$_{97}$-W$_{25}$Re$_{75}$ for temperature calibration above 1500 °C (SPPL-010, SP13RH-010, W3W25-010, Newport Omega, Deckenpfronn, Germany).
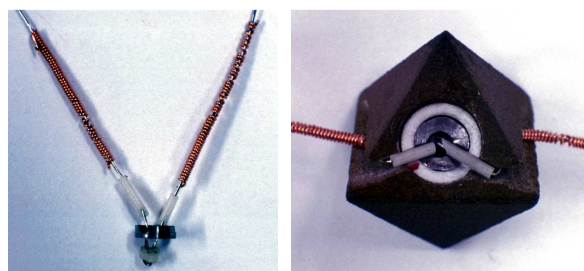
Figure 2-27. Left: Thermocouple with copper coils, alumina sleeves, and molybdenum ring. **Right:** MgO-octahedron prepared for temperature calibration with inserted thermocouple [109].

The preparation of a temperature calibration experiment differs from the usual assembly setup. The insertion of the thermocouple into the MgO-octahedron requires the replacement of the MgO and Mo-plate at one side of the octahedron by corresponding rings, to put in the

wiring of the thermocouple. The use of a thermocouple in combination with a sample is also possible, when measured along the heater axis. But this offers a source of uncertainty, due to the thermal gradient existing primarily along the sample axis. As the temperature is not measured directly in the sample, the actual temperature exceeds the measured result. Another uncertainty and deviation concerning the precision of measurements result from the pressure effect on the thermocouple electromotive force (emf) [143], which can not be interpreted up to now. Therefore, the recorded temperatures are always affected by several effects. Diagrams of the recorded temperatures in correlation to the applied heating power were

Figure 2-28. Prepared octahedron for the temperature calibration.

established for every assembly at different pressures (*e.g.* 18/11-assembly, at 3 - 9 GPa). As a result of the different influences affecting the temperature during an experiment, the actual synthesis temperature varies in a roughly estimated temperature range ($\pm 50\,^{\circ}$C), without fitting a thermocouple in every applied assembly.

There exists another method for measuring the temperature inside the sample (Figure 2-28). Preparation requires an assembly in the normal setup, but instead of a BN nitride crucible a solid BN cylinder is used. After assemblage, a hole is drilled from edge to edge through the octahedron (see Figure 2-29) (diameter 0.8 - 0.9 mm, for Pt-Pt$_{87}$Rh$_{13}$ thermocouple, 1.0-1.1 mm for W$_3$Re$_{97}$-W$_{25}$Re$_{75}$ thermocouple) and the thermocouple wires are centered in the octahedron, contacted ideally in the middle of the BN solid body (Figure 2-29).

The outer arrangements are in accordance to the normal assembly (detailed information in chapter 2.1.1). This bears the big advantage of comparable results to experimental use, in combination with a simplified assemblage.

Figure 2-30 gives a view of a typical temperature calibration curve (for an 18/11-assembly), showing the heating pressure in dependence of the temperature at a

Figure 2-29. Schematic view of the assembly for temperature calibration.

given heating power. The heating capacity is given in %, in correlation to a maximum of 3000 W.
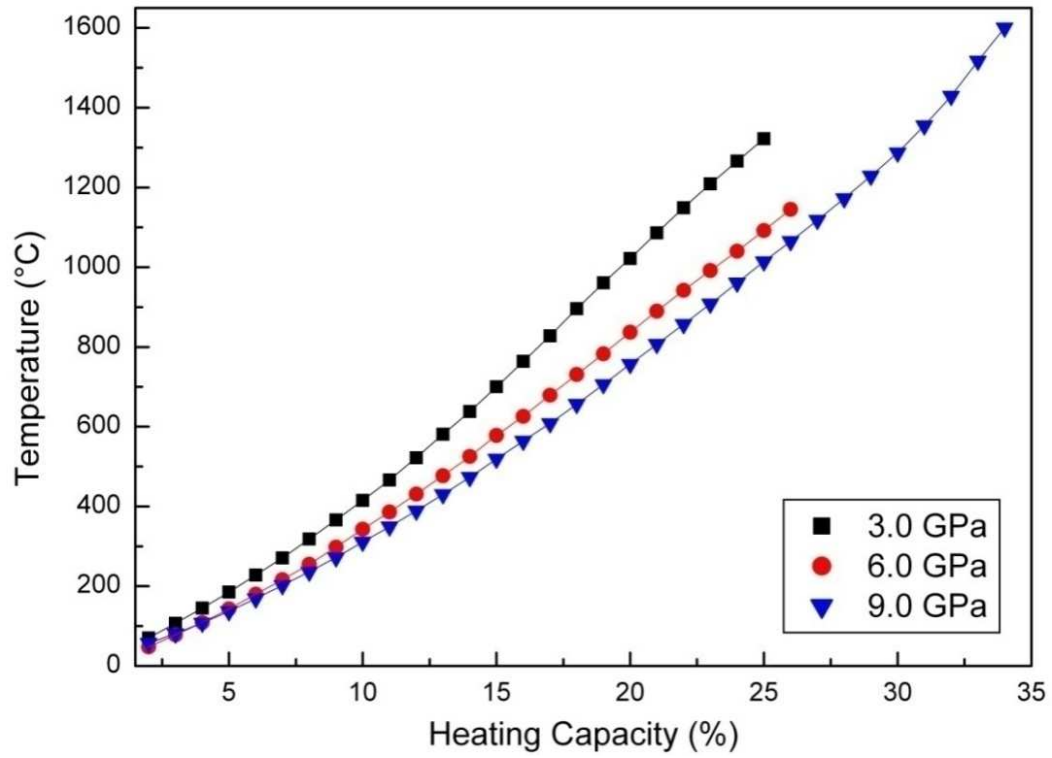
Figure 2-30. Temperature calibration curves measured at different pressures (3.0, 6.0 and 9.0 GPa) for 18/11-assembly.

3   Analytical Methods

3.1   X-Ray Diffraction

X-Ray powder diffraction enhanced phase analysis, determination of crystal parameters, and reaction- and product-control. Structure determination was accomplished by single crystal X-ray diffraction.

3.1.1   Basic Principles of X-Ray Diffraction

Diffraction phenomena can be observed, when the applied radiation ranges in the same order of magnitude as the interplanar spacing of the lattice (0.03-0.05 nm) [144-146]. The suitable radiation is X-rays, preferable $CuK_{\alpha1}$ ($\lambda = 154.18$ pm) and $MoK_{\alpha1}$ ($\lambda = 71.073$ pm) for powder measurements. For single crystal X-ray diffraction $MoK_{\alpha1}$ ($\lambda = 71.073$ pm) radiation is applied. Dispersion of the X-rays is caused by the periodically arranged atoms or ions in the three dimensional diffraction grating. To achieve constructive interference, the retardation between two waves must be an integer multiple of the wavelength. Due to the three dimensional periodicities in a crystal the dispersed waves show angle intensity maxima resulting in sharp reflections. A description of this phenomenon can be found in the three Laue-equations Eq. 3-1, which all have to be fulfilled to observe a reflection.

$$a\ cos\ \mu_a + a\ cos\ \nu_a = n_1\ \lambda$$
$$b\ cos\ \mu_b + a\ cos\ \nu_b = n_2\ \lambda$$
$$c\ cos\ \mu_c + a\ cos\ \nu_c = n_3\ \lambda \qquad \textbf{(3-1)}$$

a, b, c: lattice period (x-, y-, z-direction)
μ_a, μ_b, μ_c: angle of incidence
ν_a, ν_b, ν_c: diffraction angle
n_1, n_2, n_3: diffraction order

The atoms or ions can be assigned as parts of lattice planes. As a result of periodicity, there exists a family of parallel planes to every lattice plane. The Bragg equation Eq. 3-2 describes the diffraction of X-rays as a partial reflection (angle of incidence = diffraction angle) of the waves at the lattice planes of a crystal, which belongs to the same family.

$$2\ d_{hkl}\ sin\ \theta_{hkl} = n\ \lambda$$

$$\textbf{(3-2)}$$

d_{hkl}: interplanar spacing
θ_{hkl}: angle of incidence (= diffraction angle)
n: diffraction order
λ: wavelength

A correlation of the interplanar spacing d_{hkl} of the lattice planes belongs to the same family with the diffraction angle θ_{hkl} (Figure 3-1).
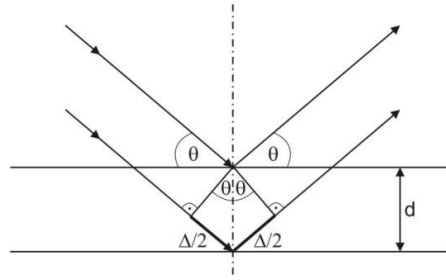
Figure 3-1. Reflection of X-rays of two lattice planes, from the same family. (d = interplanar spacing).

For X-rays, the total intensities I_{hkl} of the scattered beam, is proportional to the square of the structure amplitude, considering several correction terms during data reduction Eq. 3-3.

$$I_{hkl} \propto L \cdot P \cdot \left| F_{hkl} \right|^2$$

(3-3)

(L = Lorentz factor, P = polarization factor, F_{hkl} = structure amplitude)

The interaction of X-rays with the electron shell of the corresponding atoms and ions result in reflections of specific intensity, as it depends on the number of electrons and therefore on the chemical element. The scattered total intensities I_{hkl} Eq. 3-4 are in proportion with the square of the structure amplitude, taking into account several correction terms during data reduction.

$$F_{hk} = \sum_{j} f_{j} e^{2\pi i (hx_{j} + ky_{j} + lz_{j})}$$

(3-4)

The structure amplitude F_{hkl} depends on the atom position as well as on its scattering factor f_j. Therefore, a summation over all atoms j in a cell is allowed according to Eq. 3-5.

$$\rho_{xyz} = \frac{1}{V} \sum_{hkl} F_{hkl} \cdot e^{-2\pi i (hx + ky + lz)}$$

(3-5)

x_j, y_j, z_j: atomic positions

From Eq. 3-3 it can be seen that F_{hkl} is directly proportional to the total intensities I_{hkl}. If the structure factors are known in the modulus and phase, the atomic positions are definitely determinable. According to Eq. 3-4 the electron density function ρ_{xyz} and therefore the crystal structure can finally be calculated by a Fourier-transformation of F_{hkl}.

As a result of Eq. 3-3, only the moduli of F_{hkl} can be obtained from the diffraction intensity data, though the corresponding phase information is lost (crystallographic phase problem). The problem of identifying the atomic positions, starting only from $|F_{hkl}|$, can be solved by means of the *Direct methods* or the *Patterson method* [147,148]. Optimization of the model on full-matrix least squares on F^2 lead to the data refinement. Additional atoms are assigned to residual peaks by difference Fourier synthesis with an associated refinement of the electronic density until no significant residual peak remains.

3.1.2 Powder Diffractometric Methods

For identification of the synthesized samples X-ray powder diffraction was used. Required crystal parameters could be obtained by determination from powder measurements.

For powder diffractometry a STOE Stadi P diffractometer (STOE & Cie, Darmstadt, Germany) was applied. The STOE Stadi P diffractometer is constructed in focussing geometry using a Ge(111)-monochromatized $CuK_{\alpha1}$ ($\lambda = 154.18$ pm) and $MoK_{\alpha1}$ ($\lambda = 71.073$ pm) radiation.

Most samples were measured in transmission geometry, while placing the powdered sample between two thin acetate films. Moisture or air-sensitive samples were prepared under argon atmosphere in a glove box (MBraun, MB150-GI and UniLab, $O_2 < 1$ ppm, $H_2O < 1$ ppm, Garching) and measured in Debye-Scherrer geometry in a glass capillary (Hilgenberg, Malsfeld, Germany,). The intensities were collected by a PSD (position sensitive detector) with an opening angle of $2\theta = 5$ °.

3.1.2.1 High-Temperature Powder Diffractometry

High-temperature programmed *in-situ* powder diffractograms were measured on a STOE Stadi P diffractometer (STOE & Cie, Darmstadt, Germany) with Ge(111)-monochromatized $MoK_{\alpha1}$ ($\lambda = 71.073$ pm) radiation. The temperature was induced with a computer controlled STOE furnace. The measurements were performed in Debye-Scherrer geometry (silica glass capillary, Hilgenberg, Malsfeld, Germany, $\emptyset_{ext.}$ 0.1–0.5 mm). An electrical heated graphite tube held the sample vertical with respect to the scattering plane. Holes in the graphite tube permitted unobstructed pathway for the primary beam as well as for the scattered radiation. The temperature was controlled by a thermocouple, and kept constant within 0.2 degrees. The samples were heated up to 1100 °C starting at room temperature in steps of 50 °C. The heating rate was set to 50 °C / min, while measurement started directly after reaching the

designated temperature. After heating up, the sample was cooled to 500 °C in steps of 50 °C, and further on in steps of 100 °C down to room temperature. Due to the construction of the heating device, the data collection is limited to a 2θ-range of approximately 3 - 21°.

3.1.2.2 Single Crystal Diffraction Data

Small single crystals were isolated by mechanical fragmentation using a polarization microscope MZ12 (Leica, Bensheim, Germany). Therefore, a bulk of crystals covered with a thin film of paraffin oil was placed on a glass carrier. Small crystals were selected and fixed on top of thin glass fibers by means of beeswax. The quality of the crystals was checked on a Buerger precession camera (Precession camera 205, Huber Diffraktionstechnik GmbH, Rimsting, Germany) in Laue mode, using white Mo radiation (X-ray generator Kristalloflex 760, Siemens, Germany). The camera was equipped with an imaging plate system [149] consisting of image plates coated with photosensitive material (BaBrF: Eu^{2+}). The system was applied for recording the dispersed X-ray diffraction pattern and a laser scanner (BAS-2500 Bio Imaging Analyser, Fuji Photo Film Corporation, Japan) for readout.

Single crystal intensity data were collected at room temperature on a STOE IPDS-I diffractometer equipped with an area detector (STOE & Cie GmbH, Darmstadt, Germany) or on a Kappa CCD diffractometer (BRUKER AXS / Nonius, Karlsruhe, Germany) equipped with a rotating anode, for small crystals. In both diffractometers graphite monochromatized Mo$K_{\alpha 1}$ radiation ($\lambda = 71.07$ pm) was applied. Generally, the raw data reduction was performed with specific instrumental depending software. A multi-scan absorption correction Scalepack [150] was applied to the intensity data.

3.1.3 Computer Programs for X-Ray Diffraction Experiments

For scanning and viewing the Laue diagrams, the programs BASREAD [151] and TINA [152] were used, respectively. Powder diffractograms were recorded and handled with the STOE program package WinXPOW [153,154]. The included programs TREOR [155-157], ITO [158], DICVOL [159], and THEO [160] allowed indexing of recorded powder diffractograms and simulation of powder patterns on the basis of single crystal data. For phase analyses the integrated search routine "search match" [161], referring to the JCPDS-database [162], was used. Furthermore, confirmation of the sample composition was performed on the basis of

powder diffraction patterns using GSAS [163] and EXPGUI [164] for Rietveld refinements, to determine the by-products and the product to educt ratio in the sample.

The programs X-RED [165], X-SHAPE [166], and HABITUS [167] were used for data reduction as well as absorption correction on single crystal data. The data sets were analyzed by the program X-PREP [168] which can also be applied for determination of fitting space groups, besides semi-empirical absorption correction. Crystal structures were solved by *Direct-* or *Patterson-methods* using the program SHELXS-97 [169] or SIR2004 (Semi-Invariants Representation) [170]. Structure refinement, based on F^2 (full-matrix least-square method), was carried out using the program SHELXL-97 [171,172]. Both programs, SHELXS-97 and SHELXL-97, are combined in the user interface X-STEP32 [173] and WinGX [174,175]. Structure evaluation and verification including the selected space groups, was done *via* the program PLATON including the ADDSYMM routine [176].

Crystal structure visualization was performed with the program DIAMOND [177].

3.2   Spectroscopic Methods

3.2.1   Energy Dispersive Analysis of X-Rays

Investigations concerning the morphology and elemental composition of crystals and bulk compounds were examined with an electron scanning microscope (JSM-6500F with field emission source, Jeol, USA; with a maximum resolution of 1.5 nm). The EDX-technique (Energy Dispersive Analysis of X-rays) allows a qualitative and semi-quantitative analysis of the composition based on the characteristic X-ray emission of the elements (EDX detector: 7418 Oxford Instruments, Abingdon, Oxfordshire, OX13 5QX, UK). Electrons are accelerated by high voltage and focussed on the sample. While hitting the electronic shell, K-, L-, or M-shell electrons are expelled, if the energy of the electronic beam is higher than the ionization energy of the element. An electronic hole in the shell is instantly filled and occupied by an electron from a higher shell while losing the difference in energy by emitting characteristic X-ray radiation, which is unique for every element. Beside determination of the elements, the morphology and topology of the sample is investigated. Elastic and inelastic scattering of the electrons in the sample yields information of the sample surface.

The composition of the sample can only be determined in a semi-quantitative way, as sample orientation is random. Improvement could be achieved by imbedding the sample in resin or an orientation to plain surfaces.

The samples were provided as fine powders, bulk material or single crystals, placed on a brazen sample holder and fixed with self-adhesive carbon plates (Plano, Wetzlar, Germany). Prior to the measurement, the samples were sputtered with carbon (Sputter device: BAL-TEC MED 020, BAL-TEC AG, Balzers, Netherlands) to avoid charge effects and to ensure conductivity. Collection and evaluation of the data was performed with the INCA [178] program package.

3.2.1   Transmission Electron Microscope

Transmission electron microscopes (TEM) allow viewing of samples, realized by focussing and transmitting a beam of electrons through ultra thin specimens to learn more about the structural properties. The energy of the electronic beam requires high energetic electrons of 100-400 keV.

A beam of electrons is transmitted through crystalline samples interacting with the specimen as it passes through. Based on the duality of electrons (wave-particle), scattering on the atomic diffraction lattice occurs, due to the wavelength. Diffraction of the electrons results in specific angles, determined by the crystal structure of the sample. Some electrons may pass through the specimen unobstructed. Recording the spots on a screen results in selected area diffraction pattern (SADP) on which each spot stands for a specific diffraction condition due to the crystal structure. Recording different diffraction conditions require tilting and moving of the sample.

By selected-area electron diffraction (SAED), further information on the crystallographic structure of the sample is provided. A specific area of a polycrystalline sample is chosen and investigated by a focussed electron beam, from which diffraction patterns are measured. Although similar to X-ray diffraction investigations, the advantage lies in the high resolution of small areas. SAD patterns represent a projection of the reciprocal lattice, with resulting reflections shown as sharp diffraction spots, which allow the measurement of lattice parameters and identification of crystal structures, or determination of lattice matching, interfaces, twinning, and certain crystalline defects [179].

3.2.2   Electron Energy Loss Spectroscopy

Elemental composition, chemical bonding, electronic, and surface properties, besides element-specific couple distance distribution functions can be determined with electron energy loss spectroscopy (EELS). In contrast to EDX, EELS achieves best results at relatively low elements (carbon to zinc), due to sharp excitation edges and well-defined and detectable energy losses ($< 3\,keV$) [180]. Another advantage is the possibility of determining the oxidation state of the elements. The samples were exposed to an electron beam of known energy to induce interaction with the specimen due to inelastic scattering of the electrons. The energy loss of the electrons is measurable by an electron spectrometer due to inelastic interactions like phonon excitations, inter and intra band transitions, plasmon excitations and ionization of the inner shell beside Čerenkov radiation [181]. The elemental composition is determined by interactions of electrons with the inner shell of the sample. Besides the elemental composition, EEL-spectroscopy allows also the quantification of the atomic content. Information about the dispersion relation of the material can be given by measuring the scattering angle due to inelastic scattering [182]. There are different types of EELS-facilities, most common is the transmission EELS, with kinetic energies typically in the range of 100 up to 300 keV, to enable the electrons to pass through the material. In addition to that, other methods like RHEELS, (reflection high-energy electron energy-loss spectroscopy) typically in the range of 10 to 30 keV, or valence EELS (for plasmons and interband transitions) besides inner-shell ionization-EELS.

3.2.3   Vibrational Spectroscopy

Vibrational spectroscopy is a versatile technique for the characterization of molecular arrangements and compounds. Measured spectra are usually analyzed with the help of databases, to assign typical vibrations to peaks. Although the method works easily for organic compounds, difficulties arise when vibrations of solid state compounds are to be assigned to measured peaks. Nevertheless, vibrational spectroscopic investigations are useful for distinguishing between BO_3- and BO_4-groups.

Infrared spectra were recorded on a Spektrum BX II FTIR-spectrometer (Perkin Elmer, USA), equipped with a Dura sampler diamond-ATR, scanning in the range from 650 to 4500 cm^{-1}, or on a Bruker IFS66/v FTIR spectrometer (Bruker Analytik GmbH, Ettlingen, Germany). The

latter handled the sample in an evacuated cell scanning the range of 400-4000 cm^{-1} (DLATGS detector). The samples were dried and thoroughly mixed with dry KBr (5 mg sample, 500 mg KBr) in a glove box (MBraun, MB150-GI and UniLab, $O_2 < 1$ ppm, Garching, Germany) before measurement. Preparation requires pressed samples, by using a hand press with a press capacity of 10 kN. Measurement on air required only fine powdered dry samples, without adding KBr.

Raman spectra were measured on single crystals applying a Raman-microscope (Horiba Jobin yvon HR800, x50LWD), using green laser light (Melles Griot ion laser) with a wavelength of 514 nm. The preparation required testing on a Buerger precession camera and fixing the single crystals on glass fibers as described in chapter 3.1.2.2.

3.3   Theoretical Calculations

3.3.1   Lattice Energy Calculation according to the Maple Concept

Calculations according to the MAPLE concept (Madelung Part of Lattice Energy) [183-185] are an appropriate method to prove the plausibility of crystal structures. The computations are based on the electrostatic interactions in ionic crystals, depending on the distances, their charge, as well as the coordination number. Partial MAPLE-values are determined for every single ion in the structure, summarized in a total MAPLE-value of the whole compound. MAPLE-values are additive in high accuracy, which means that the sum of the total MAPLE-values are comparable to the calculated MAPLE-value of the respective structure.

3.3.2   The Bond-Length Bond-Strength Concept

For solid state compounds bond distances play an important role. The correlation of Bond-Length and Bond-Strength permits the interpretation and evaluation of bond distances. Based on Pauling´s defined bond-grade [186], which was mainly applied for metallic or intermetallic compounds, Brown [187] extended the concept, as well as Brese and O'Keeffe [188] to generalize it to a multitude of different compounds.

Contrary, it is possible to calculate backwards the valence sums from bond distances derived from crystal structure determinations. This method is a helpful tool to check crystal structure

determinations on their plausibility. Bond valences v_{ij} of bonds between atoms i and j are calculated according to Eq. 3-6.

$$v_{ij} = \exp\left[\frac{(R_{ij} - d_{ij})}{b}\right]$$

(3-6)

v_{ij} = bond valence
R_{ij} = bond valence parameter
d_{ij} = bond distance
b = constant (37 pm)

The constant b was determined by Brown and Altermatt [187] and stated for a value of 37 pm. R_{ij} is characteristically for each element combination and was determined from known compounds [187,189]. The total valence sum V_i summarizes the bond valences v_{ij} of all bonds starting from atom i according to Eq. 3-7.

$$V_i = \sum_j v_{ij}$$

(3-7)

3.3.3   Calculations of the Charge Distribution according to the Chardi Concept

The CHARDI Concept (Charge Distribution in Solids) [190,191] is a combination of Pauling´s bond grade [186] and the effective coordination number (ECoN). In contrast to the MAPLE concept which is based on an ionic approach, CHARDI considers beside the ionic contribution anion-anion- and cation-cation interactions as well.

The ECoN contribution $\Delta E(ij \rightarrow k)$ is based on the averaged distance $d(ij \rightarrow k)$ between the cations K_{ij} (crystallographic site j) and the anions A_k in the structure. The summation of all contributions provides a partial effective coordination number $\Delta(\text{ECoN})$ for every anion A_k counted as ligand of a cation K_{ij}. Parts of the charge distribution $\Delta q(ij \rightarrow k)_{\text{cation}}$ result from considering the number of the anions A_k, surrounding K_{ij}. The charges of the cations K_{ij} and A_k were calculated according to the Eq. 3-8 and Eq. 3-9, respectively.

$$Q_{\text{cation}} = - \sum_i \sum_j \Delta q(ij \rightarrow k)_{\text{cation}}$$

(3-8)

$$Q_{\text{anion}} = - \sum_k \Delta q(ij \rightarrow k)_{\text{anion}}$$

(3-9)

$\Delta q(ij \rightarrow k)_{\text{cation}}$ = charge distribution of cation K_{ij} with respect to anion A_k, $\Delta q(k \rightarrow ij)_{\text{anion}}$ = charge distribution of anion A_k with respect to cation K_{ij}, $i = i^{\text{th}}$ cation, j = crystallographic layer, $k = k^{\text{th}}$ anion

4 Experimental Section

4.1 Rare-Earth Gallates

4.1.1 Introduction

In nature, rare-earth gallates can be found in different stoichiometric compositions, like RE_3GaO_6, $RE_3Ga_5O_{12}$, $RE_4Ga_2O_9$, or $REGaO_3$. Beside gallium, deposits of aluminium, gallium, iron, manganese, or even silica are also accessible.

Taking a closer look at the ternary system RE-Ga-O, several compounds are known. Compounds in the stoichiometric composition RE_3GaO_6 (RE = Nd, Sm - Er) [192-194] were synthesized by several working groups. Liu *et al*. obtained the compounds *via* solid state reactions at temperatures of 1400-1800 °C starting from the corresponding rare-earth oxides RE_2O_3 (RE = Nd, Sm - Er) [192] and Ga_2O_3 powder in high purity (>99.9%). Antic-Fidancev *et al*. [193] and Nicholas *et al*. [194] also succeeded in synthesizing the compounds RE_3GaO_6. Structural refinement showed that the lattice parameters and cell volumes of the non-centrosymmetric orthorhombic structures (space group $Cmc2_1$, no. 36) decrease along the series (RE = Nd, Sm - Er) due to the lanthanide contraction. The first structural results on gallates with the composition $RE_3Ga_5O_{12}$ were achieved by Menzer [195,196] and Weidenborner [197]. Structural refinement revealed a cubic system and the space group $Ia\overline{3}d$ (no. 230). The crystal structure can be described as two repetitive chain-arrangements, formed by the anions. The coordination results in tetrahedra, octahedra, and dodecahedra, all connected *via* edge-sharing among eacht other. The dodecahedral sites are occupied by rare-earth cations, while the cations (M = Al, Si, Fe, Ga) are coordinated tetrahedrally and octahedrally.

Linares *et al*. was the first group working on garnet structures with the composition $RE_3Ga_5O_{12}$ (RE = Y, Nd, Sm, Eu, Gd, Dy, Ho, Yb, Lu) [198-205]. While reporting about the crystal growth of $Gd_3Ga_5O_{12}$, the corresponding aluminium-compound $Y_3Al_5O_{12}$ was obtained by using the Czochralski technique for crystal growth [198,203]. Doped with rare-earth elements or chromium [202], these garnets find application in lasers facilities.

Interestingly, a direct synthetic access to those compounds *via* solid state reactions starting from the corresponding oxides seemed impossible. Euler *et al*. reported about the synthesis of the compounds $RE_3Ga_5O_{12}$ (RE = Y, Yb, Lu) in fluxes of PbO or PbO-PbF$_2$ including the single crystal structure determination of the three compounds [199].

Another experimental approach was made by Carruthers *et al*. by preparing ceramic compounds in the ternary system Gd_2O_3-Ga_2O_3 by sinter-processes at temperatures of 1100-1500 °C, which led to crystalline garnets [204]. Sawada *et al*. [201] investigated also garnets with the composition $RE_3Ga_5O_{12}$ (RE = Nd, Sm, Gd, Tb). Not only gallium garnets are shown, but also compounds with the composition $RE_3M_5O_{12}$ with other cations (M = Al, Si, Fe, Ga) and rare-earth ions (RE = Y, Sm, Gd, Dy, Yb, Lu) are found in some natural minerals, like in $Ca_3Al_2Si_3O_{12}$ (*grossularite*) which structure was determined in 1958 by Abrahams and Geller [206]. Furthermore other Al-compounds such as $Al_2Si_3Fe_3O_{12}$ (*almandite*) was examined by Euler and Bruce [199], or $Ga(OH)_3$ (*söhngeite*) found by Strunz [207].

Research on rare-earth garnets continued, enlarging into magnetic properties [208]. $Nd_3Ga_5O_{12}$ doped with different rare-earth elements (RE = Yb, Tm, Er, Ho, Dy) was investigated in dependency of the temperature (ranging in between -195 up to +27 °C), showing paramagnetism with Curie-Weiss-behavior. But no evidence for long-range ordering has been found, which should prove ferrimagnetism, ferromagnetism, or antiferromagnetism of the compounds [209]. Different working groups are focused on magnetoelastic properties, though examination of the specific behavior at low temperatures showed that the electronic structure of the RE-ion is determined by the surrounding crystal field, which results in the corresponding spectroscopic and magnetic properties, and magneto optical phenomena of the compounds. This stands in the focus, as the magnetoelastic phenomena effects *e.g.* the anomalies in the lattice parameters and provides more information about the interaction of rare-earth cations and their environment. Therefore, magnetostriction and thermal expansion of rare-earth gallium and aluminium garnets $RE_3Ga_5O_{12}$ and $RE_3Al_5O_{12}$ (RE = Gd - Yb) were investigated [210,211]. Referring to a garnet structure with rare-earth cations on different crystallographic sites, the differential longitudinal magnetostriction can be expressed in terms of field-induced changes of quadrupole moments.

Another different composition $RE_4M_2O_9$ within the group of rare-earth gallates is known. The monoclinic compounds $RE_4Al_2O_9$ (RE = Y, Sm, Eu, Gd, Tb, Dy, Ho, Er, Tm, Yb) and $RE_4Ga_2O_9$ (RE = La, Pr, Nd, Sm- Gd) crystallize in the space group $P2_1/c$ (no. 14) and were examined by Yamane *et al*. [212] and other working groups [192,194,213]. The determinations of the structures were performed with Rietveld methods. Distinguished by the

metal cation, the preparation of the different ternary oxides required different synthesis conditions. As Al-compounds required extended temperatures of 1600 up to 1800 °C, the gallium analogue compounds were obtained at lower temperatures around 1400 up to 1600 °C. The compounds display reversible phase transitions due to heating (>1000 °C) accompanied with a thermal hysteresis and a volume contraction of 0.5 - 0.7 %. Within the row of the rare-earth elements, the temperatures required for the phase transformations increase.

The last composition, REGaO$_3$, within the group of rare-earth gallates described here, exhibits an equal content of rare-earth- and metal-cations in the structure [214]. The chemistry of perovskite like gallates REMO$_3$ (M = Cr, Mn, Fe, Al, Ga) was in the focus of the experimental work of Geller *et al.* [215]. Furthermore, Marezio *et al.* [216] succeeded in synthesizing crystalline REGaO$_3$ compounds (RE = La, Pr, Nd, Sm - Lu) under high-pressure / high-temperature conditions in the presence of a NaOH flux, *via* decomposition of the related garnets RE_3Ga$_5$O$_{12}$ (RE = Sm - Tb) obtained under atmospheric pressure [217]. Only partial decomposition occured, when garnet compounds like RE_3Ga$_5$O$_{12}$ within the row of (RE = Dy - Lu) were applied. The reaction led to samples containing REGaO$_3$, beside the starting material.

A various number of different rare-earth compounds with aluminium REAlO$_3$ (RE = Y, Eu, Gd, Yb, Lu) [218], gallium, REGaO$_3$, (RE = La, Pr, Nd, Sm - Lu) [194,216,217,219-228], and iron, REFeO$_3$ (RE = Lu, Yb, Y, Dy, Sm) [229,230] were synthesized applying different experimental routes. The compounds were characterized by structural refinement based on Rietveld methods on powder diffraction data or single crystal data. Due to interesting properties of these materials, such as ferrimagnetism in yttrium iron garnets [199,231,232] research intensified. Spontaneous magnetization can occur, when identical magnetic ions occupy different crystallographic sites in the structure. This phenomenon can be observed in perowskite-like materials, when gallium is substituted for iron.

Table 4-1 summarizes the different compositions within the rare-earth gallates.

Table 4-1. Overview of the different rare-earth compositions.

Composition	Space group	Author
RE_3GaO_6	$Cmc2_1$, no. 36	Liu [192], Antic-Fidancev [193], Nicholas [194]
$RE_3Ga_5O_{12}$	$Ia\bar{3}d$, no. 230	Menzer [195,196], Weidenborner [197], Linares [198], Euler [199], Brandle [200], Sawada [201], Patzke [202], Czochralski [203], Carruthers [204], Kim [205], Abrahams [206], Belov [208]
$RE_4Ga_2O_9$	$P2_1/c$, no. 14	Liu [192], Nicholas [194], Yamane [212], Gesing [213]
REGaO$_3$	$Pnma$, no. 62	Nicholas, [194], Schneider [214], Geller [215], Marezio [216,217], Geller [219], Guitel [220], Brandle [221], Sallavuard [222], Schäfer [223], Geller [224], Angel [225], Vasylechko [226,227], Hering [228]

All these compounds are accessible under ambient pressure conditions. Only few attempts (Marezio *et al*. [216,217]) were made, to synthesize new rare-earth gallates under elevated pressures.

First results on rare-earth gallates derived from high-pressure / high-temperature synthesis were obtained within a previous work. Single crystals of HoGaO$_3$ were synthesized under high-pressure / high-temperature conditions of 7.5 GPa and a temperature of 1250 °C, starting from a mixture of monoclinic β-Ga$_2$O$_3$ and cubic C-Ho$_2$O$_3$ in the molar ratio of 1 : 1 [228]. Even though, the compound was already characterized from powder by Marezio *et al.*, the crystal structure was confirmed by single crystal data, for the first time. Remarkably, most of the rare-earth gallium garnets are known from the literature, but only a few were obtained as single crystals, so far (RE = La, Pr, Nd, Gd, Ho) [219,225-228].

A comparison of both lattice parameters showed that the single crystal data for HoGaO$_3$ (a = 553.0(2), b = 753.6(2), c = 525.4(2) pm (standard setting: *Pnma*)) [228] correspond well to the original values of Marezio *et al*. (a = 525.1(2), b = 553.1(2), c = 753.6(2) pm (setting: *Pbnm*)) [216].

4.1.2   DyGaO$_3$

Previous experimental work, performed within the diploma thesis, led to a crystalline sample of HoGaO$_3$, synthesized under high-pressure / high-temperature conditions of 7.5 GPa and 1250 °C [228]. Although, HoGaO$_3$ was already known from the literature, only powdered samples were obtained so far. From this sample, a single crystal structure determination was possible for the first time. The single crystal data confirmed the orthorhombic structure and the space-group *Pnma* (no. 62).

Within this work, the previously started investigation on rare-earth gallates was continued. Additional experiments were accomplished, starting from other rare-earth oxides (*RE* = La, Ce, Tb, Dy, Ho, Er, Tm, Yb, Lu) mixed with *β*-Ga$_2$O$_3$, under variation of the molar ratio of the educts, as well as of the applied pressures and temperatures. Although, experiments led to rare-earth gallates, new compositions were not obtained so far.

The existing stoichiometric compositions *RE*GaO$_3$ or *RE*$_3$Ga$_5$O$_{12}$ are also accessible under different high-pressure / high-temperature conditions. Experiments starting from the binary oxides of C-*RE*$_2$O$_3$ and *β*-Ga$_2$O$_3$ resulted in the compound *RE*$_3$Ga$_5$O$_{12}$ (*RE* = Dy, Ho, Tm, Yb, Lu), mostly obtained as by-product with other gallates. Additionally, the composition *RE*GaO$_3$ (*RE* = La, Ce, Tb, Dy, Ho, Er, Tm, Yb, Lu) was obtained. Unfortunately, not all of them could be measured *via* single crystal structure determination, as the grade in crystallinity was not sufficient for all of them.

Continuous investigations on rare earth gallates under high-pressure / high-temperature conditions led finally to the crystalline dysprosium orthogallate DyGaO$_3$ [233], on which we managed to determine the single crystal structure for the first time.

4.1.2.1   Starting Materials for the Synthesis of DyGaO$_3$

For the preparation of rare-earth gallates, the following commercially available substances were used as listed in Table 4-2. Additionally, the corresponding ICSD numbers are listed. The starting materials for the syntheses were all air-and humidity resistant. The analysis and characterization of the crystalline educts and products were executed with powder diffractometry comparing the measured educts to the ICSD-database.

Table 4-2: List of applied substances.

Substance	State	Source of Supply	Purity [%]	ICSD-PDF
C-Dy_2O_3	Powder	Alfa Aesar, Emmerich, Germany,	99.995	[00-088-2164]
C-Tm_2O_3	Powder	Alfa Aesar, Emmerich, Germany,	99.995	[00-082-2416]
β-Ga_2O_3	Powder	Fluka, Seelze, Germany	99.99	[00-087-1901]

4.1.2.2   Synthesis of DyGaO$_3$

The synthesis of the orthorhombic compound DyGaO$_3$ started from cubic C-Dy_2O_3 (Alfa Aesar, Emmerich, Germany, 99.995 %) and monoclinic β-Ga_2O_3 (Fluka, Seelze, Germany, 99.99 %) in a stoichiometric ratio of C-Dy_2O_3 : β-Ga_2O_3 = 1 : 1, as seen in Eq. 4-1. Both compounds were closely ground and filled into a hex. boron nitride crucible, which was inserted into the experimental setup of an 18/11-assembly [103,104,111].

$$Dy_2O_3 + Ga_2O_3 \quad \xrightarrow[1250\ °C]{7.5\ GPa} \quad 2\ DyGaO_3 \tag{4-1}$$
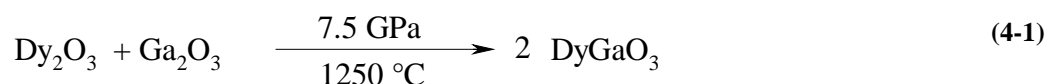
The reaction of the oxides leading to the formation of the rare-earth gallate DyGaO$_3$ occurred at a pressure of 7.5 GPa and a temperature of 1250 °C. Therefore, the assembly was compressed within 3 h up to the intended pressure, followed by a heating period, in which the sample was heated within 15 min up to 1250 °C. The temperature was hold there for 15 min and afterwards decreased to 650 °C within 20 min. Finally, the heating was stopped to cool the sample down to room temperature. When the heating was switched off, the decompression protocol was started. The decompression segment to ambient pressure took 9 h.

After the experiment, the cube was removed from the module and the sample preparation followed (see chapter 2.1.2). For further analytical characterization, the boron nitride crucible, containing the sample, was mechanically separated, and the sample was obtained as a greyly gleaming, crystalline product. The sample was insensitive against air or moisture.

4.1.2.1   Analytical Investigations and Crystal Structure Analysis of DyGaO$_3$

The product was analyzed with a X-ray powder diffractometer and therefore prepared and analyzed on a Stoe Stadi P powder diffractometer equipped with monochromatized Cu$K_{\alpha 1}$ ($\lambda = 154.051$ pm) radiation. Figure 4-1 gives a view of the powder diffraction pattern, exhibiting DyGaO$_3$, beside a small amount of Dy$_3$Ga$_5$O$_{12}$ [202].

A single crystal was isolated and selected by mechanical fragmentation from the bulk sample. The crystal was tested on a Buerger precession camera in Laue mode, equipped with an image plate system (Fujifilm BAS-1800). The suitable crystal allowed a successful single crystal structure determination.

The single crystal data were collected at room temperature from a small regular crystal on a Stoe IPDS-I diffractometer with Mo$K_{\alpha 1}$ radiation ($\lambda = 71.073$ pm). A numerical absorption correction (HABITUS [166,167]) was applied to the intensity data. The systematic reflection conditions led to the space groups *Pna*2$_1$ (no. 33) and *Pnma* (no. 62). The structure solution and the parameter refinement with anisotropic displacement parameters for all atoms (full-matrix least squares against F^2) were successfully achieved in the space group *Pnma,* using the SHELX-97 software suite [169,171,172]. All relevant information and details concerning the data collection of orthorhombic DyGaO$_3$ are listed in Table 4-3. The positional parameters (Table 4-4), anisotropic displacement parameters (Table 4-5), interatomic distances (Table 4-6), and interatomic angles (Table 4-7) of DyGaO$_3$ are listed in the following.
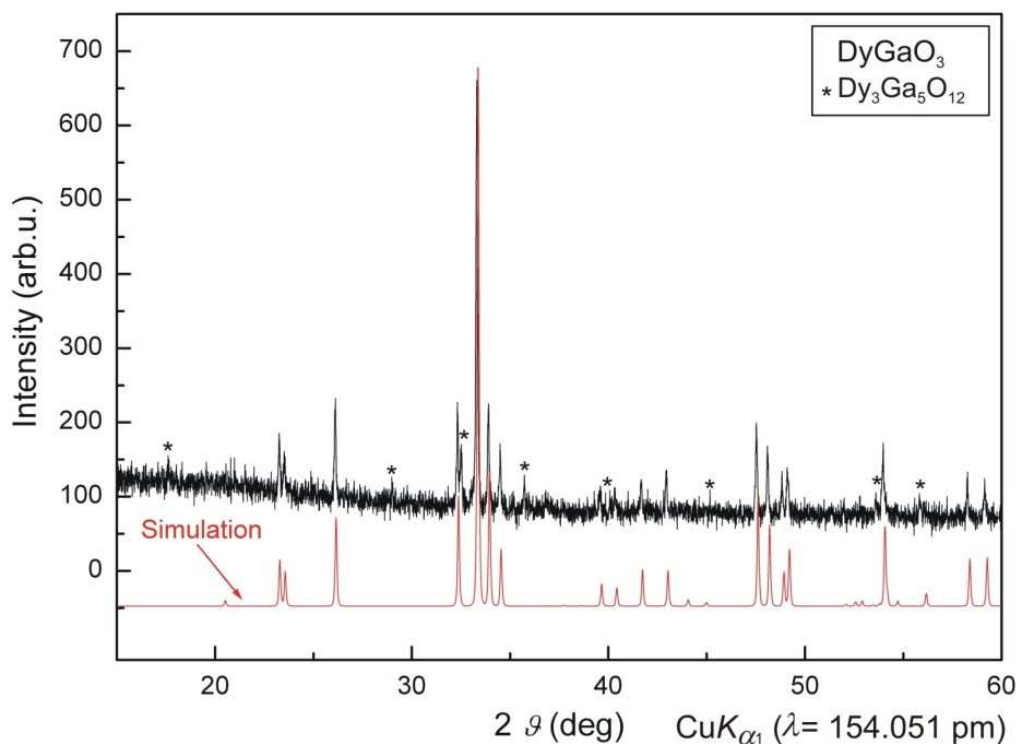
Figure 4-1. Powder diffraction pattern of the reaction product $DyGaO_3$ starting from $C-Dy_2O_3$ and $\beta-Ga_2O_3$. The simulation of the powder diffraction pattern is positioned underneath. As by-product, cubic $Dy_3Ga_5O_{12}$ occurred, marked in the pattern (*) [202].

The simulated pattern derived from single crystal data is consistent with the measured powder diffractogram. Indexing of the powder diffraction pattern resulted in an orthorhombic cell, displaying lattice parameters of $a = 554.11(4)$, $b = 756.0(2)$ and $c = 527.75$ pm (Table 4-3).

High-pressure / high-temperature synthesis led to the orthorhombic dysprosium orthogallate $DyGaO_3$, synthesized in a Walker-type multianvil apparatus at conditions of 7.5 GPa and 1250 °C. The single crystal data were collected from a $DyGaO_3$ single crystal. The compound crystallizes in the space group *Pnma* (no. 62) (Z = 4), displaying lattice parameters of $a = 552.5(2)$, $b = 754.4(2)$, and $c = 527.7(2)$ pm. The single crystal data refinement resulted in values of $R1 = 0.027$ and $wR2 = 0.0309$ (all data).

Table 4-3. Crystal data and structure refinement of orthorhombic $DyGaO_3$.

Empirical formula	$DyGaO_3$
Molar mass, g mol^{-1}	280.22
Crystal system	orthorhombic
Space group	*Pnma* (no. 62)
Single crystal diffractometer	Stoe IPDS
Radiation	Mo$K_{\alpha 1}$ ($\lambda = 71.073$ pm) (graphite monochromator)
Single crystal data	
a, pm	552.5(2)
b, pm	754.4(2)
c, pm	527.7(2)
V, nm^3	0.22002(8)
Powder diffractometer	Stoe Stadi P
Radiation	Cu$K_{\alpha 1}$ ($\lambda = 154.051$ pm)
Powder data	
a, pm	554.11(4)
b, pm	756.0(2)
c, pm	527.75(9)
V, nm^3	0.22107(4)
Formula units per cell	$Z = 4$
Calculated density, g cm^{-3}	8.460
Crystal size, mm^3	$0.08 \times 0.04 \times 0.04$
Temperature, K	293(2)
Detector distance, mm	50.0
Exposure time, min	18.0
Absorption coefficient, mm^{-1}	45.5
$F(000)$, e	484
θ range, deg	4.71-30.39
Range in *hkl*	$\pm 7; \pm 10; \pm 7$
Reflections total / independent	2123 / 350
R_{int}	0.0464
Reflections with $I \geq 2\sigma(I)$	302
R_σ	0.0255
Data / ref. parameters	350 / 29
Absorption correction	multi-scan (HABITUS [167])
Final $R1$ / $wR2$ [$I \geq 2\sigma(I)$]	0.027 / 0.0654
Final $R1$ / $wR2$ (all data)	0.0309 / 0.0662
Goodness-of-fit on F^2	1.023
Largest diff. peak and hole, e Å^{-3}	2.2 / -1.7

Table 4-4. Atomic coordinates and isotropic equivalent displacement parameters U_{eq} (Å^2) of DyGaO$_3$ (space group: *Pnma*) (standard deviations in parentheses). U_{eq} is defined as one third of the trace of the orthogonalized U_{ij} tensor.

Atom	Wyckoff position	x	y	z	U_{eq}
Dy	4*c*	0.56388(8)	1/4	0.01609(7)	0.0084(2)
Ga	4*a*	0	1/2	0	0.0072(3)
O1	4*c*	0.033(2)	3/4	0.102(2)	0.010(2)
O2	8*d*	0.1965(8)	0.5526(7)	0.6958(8)	0.0093(9)

Table 4-5. Anisotropic displacement parameters U_{ij} (Å^2) of DyGaO$_3$ (space group *Pnma*) (standard deviations in parentheses).

Atom	U_{11}	U_{22}	U_{33}	U_{23}	U_{13}	U_{12}
Dy	0.0078(3)	0.0087(3)	0.0087(3)	0.000	0003(2)	0.000
Ga	0.0080(6)	0.0068(5)	0.0069(5)	0.9999(3)	0.0003(3)	0.0002(4)
O1	0.015(3)	0.002(3)	0.013(3)	0	0.002(3)	0
O2	0.010(2)	0.009(2)	0.009(2)	0.910(2)	0.003(2)	0.001(2)

Table 4-6. Interatomic distances (pm) of DyGaO$_3$ (space group *Pnma*) based on single crystal data (standard deviations in parentheses).

Dy–O1	225.4(7)	Ga–O1	197.0(2) 2×
Dy–O2	227.8(5) 2×	Ga–O2	197.8(4) 2×
Dy–O1	230.5(7)	Ga–O2	201.0(4) 2×
Dy–O2	250.7(5) 2×	**Ø = 198.6**	
Dy–O2	264.6(5) 2×		
Ø = 242.8			

Table 4-7. Interatomic angles of orthorhombic DyGaO$_3$.

O1–Dy–O1	88.2(2)	O1–Ga–O1	180.0(3)
O1–Dy–O2	67.5(2) 2×	O1–Ga–O2	88.2(2) 2×
O1–Dy–O2	69.7(2) 2×	O1–Ga–O2	88.6(2) 2×
O1–Dy–O2	69.8(2) 2×	O1–Ga–O2	91.4(2) 2×
O1–Dy–O2	104.6(2) 2×	O1–Ga–O2	91.8(2) 2×
O1–Dy–O2	135.6(2)		
		O2–Ga–O2	89.93(8) 2×
O2–Dy–O1	136.1(2) 2×	O2–Ga–O2	90.07(8) 2×
		O2–Ga–O2	180.0(3) 2×
O2–Dy–O2	66.25(6) 2×	O2–Dy–O2	81.7(2)
O2–Dy–O2	72.0(2)	O2–Dy–O2	118.02(9) 2×
O2–Dy–O2	72.10(12)	O2–Dy–O2	119.3(2)
O2–Dy–O2	72.9(2)	O2–Dy–O2	128.52(8) 2×
O2–Dy–O2	77.7(2) 2×	O2–Dy–O2	156.1(2) 2×

4.1.2.2   Results and Discussion on $DyGaO_3$

In the ternary system RE-Ga-O, four compositions are known: $RE_3Ga_5O_{12}$ (RE = Y, Sm, Gd, Dy, Ho, Yb, Lu) [198-202], RE_3GaO_6 (RE = Nd, Sm - Er) [192-194], $RE_4Ga_2O_9$ (RE = La, Pr, Nd, Sm - Gd) [192,194,212,213], and REGaO$_3$ (RE = La, Pr, Nd, Sm - Lu) [217,219,224-228]. The latter compounds were synthesized under atmospheric pressure or *via* decomposition of the related garnets $RE_3Ga_5O_{12}$ (RE = Sm - Lu) under high-pressure / high-temperature conditions in the presence of a NaOH flux [217]. In this context, $DyGaO_3$ was synthesized for the first time by Marezio *et al.* and characterized with the lattice parameters a = 528.2(2), b = 553.4(2), and c = 755.6(2) pm (setting: *Pbnm*) received from powder data [216].

The structure of $DyGaO_3$ was described as isostructural with the rare-earth orthoferrites, possessing an orthorhombic perovskite-like structure (GdFeO$_3$-type [234]). The single crystal data for $DyGaO_3$ (a = 552.5(2), b = 754.4(2), and c = 527.7(2) pm [(standard setting: *Pnma*) (Table 4-3)] correspond well to the original values of Marezio *et al*. [216]. Further single crystal data exist only for the rare-earth orthogallates REGaO$_3$ (RE = La, Pr, Nd, Gd, Ho) [219,225-228]. The structure was investigated and described by Geller *et al.* [229,235], Will [236], and Marezio *et al*. [237]. Figure 4-2 shows the structure of the dysprosium orthogallate with a view along [010].
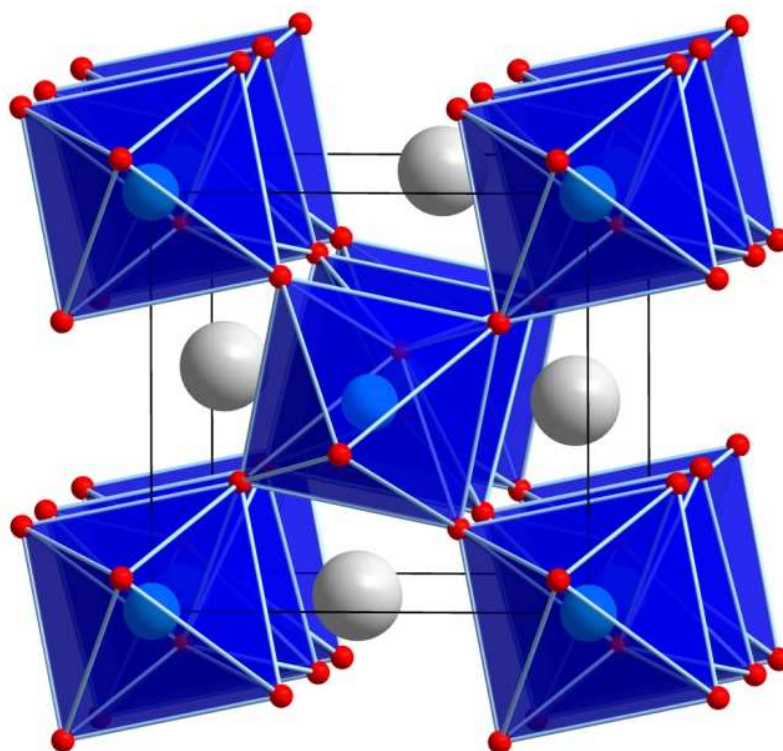
Figure 4-2. View approximately along the [010] axis of the orthorhombic DyGaO$_3$, illustrating the GaO$_6$ octahedra. The Dy-atoms are positioned in the resulting channels.

Like in cubic perovskite-structures, the oxygen and rare-earth ions form a face-centered cubic structure, in which the Ga^{3+}-ions occupy ¼th of the octahedrally coordinated positions. In difference to the cubic perovskite structure, the GaO$_6$ octahedra are distorted along the *c* axis and tilted among each other, resulting in an angel of 146.7 ° (diverging from 180 °).

The Ga-O bond lengths in DyGaO$_3$ range from 197.0(2) to 201.0(4) pm (av. = 198.6 pm) (Table 4-6). The distances correspond to values found for octahedrally coordinated gallium atoms in *α*-Ga$_2$O$_3$ (192-208 pm [238]) and *β*-Ga$_2$O$_3$ (193.5(2) - 207.4(1) pm [239]). The dysprosium cations show a 4+4-coordination, displaying Dy-O bond lengths of 225.4(7) to 230.5(7) pm (the first four) and 250.7(5) to 264.6(5) pm (the second four). The experimental average value of (242.8 pm) is in good accordance to the average bond length of 236 pm, found in Dy$_3$GaO$_6$ [192]. The comparison with the anologue holmium gallate shows that the values obtained for DyGaO$_3$ agree well with those derived from single crystal data for HoGaO$_3$ (224.6(4) to 229.2(5) pm (the first four) and 248.9(4) to 264.8(4) pm (the second four)). Also the average bond lengths of 242.0 pm (HoGaO$_3$) is almost equal to the average value for DyGaO$_3$ of 242.8 pm.

Figure 4-3 shows a comparison of the different lattice parameters *a*, *b,* and *c* of all known rare-earth gallates in the standard setting (space group: *Pnma*, no. 62) including the values of DyGaO$_3$. The three axes show a different behavior: while the *b* and *c* parameters smoothly

decrease in going from La to Lu, the parameter *a* exhibits an unexpected behavior in showing a maximum at about Gd. This phenomenon was already observed by Marezio *et al.* for the rare-earth gallates [216] and also by Eibschütz for the corresponding orthoferrites [230]. This effect is commonly interpreted as consequence of the size of the rare-earth cations: as the size of the RE^{3+}-cations decreases, the average RE^{3+}-O distance of the first nearest oxygen atoms decreases as well (first effect), whereas the average RE^{3+}-O of the second nearest oxygen atoms increases (second effect). Only the parameter *a* is affected by this double effect, leading to an increase by going from La to Gd, because in this region, the second effect is the predominant one, whereas it decreases within the row starting at Gd to Lu, because here the first effect is predominant. This rather unsatisfying explanation has to be checked in the future, when the missing single crystal data in the rare-earth gallates series will be available.
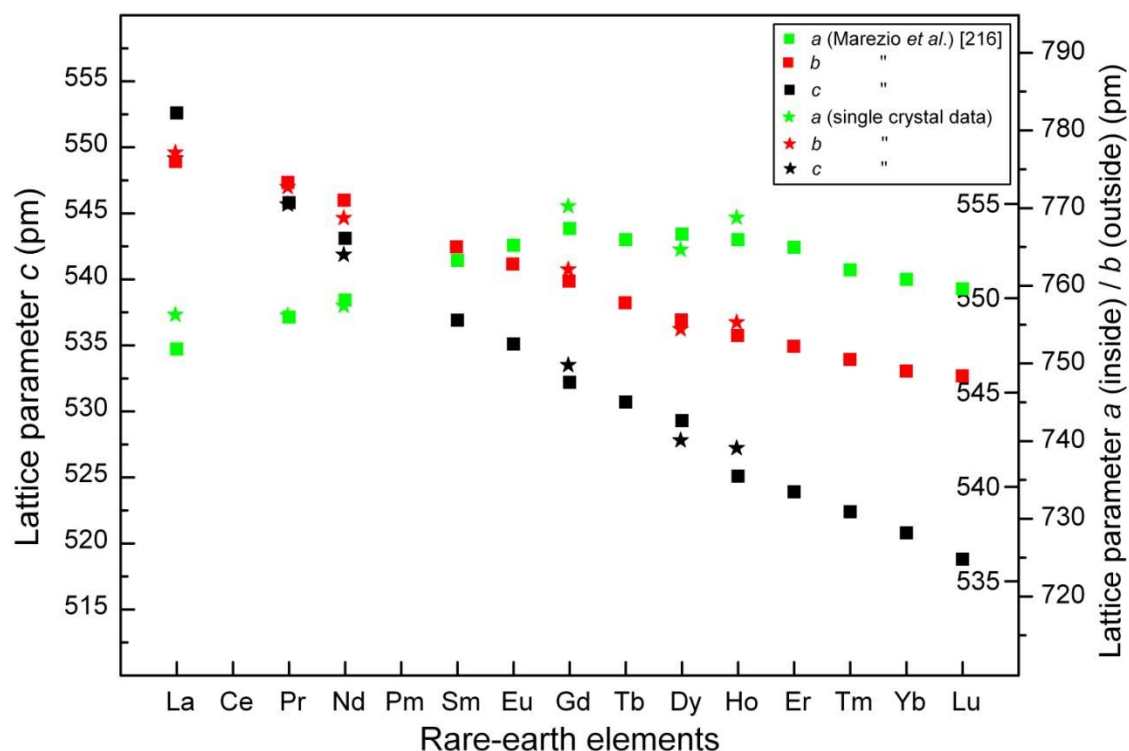
Figure 4-3. Lattice parameters *a*, *b,* and *c* of the different rare-earth gallates REGaO$_3$ (RE = La, Pr, Nd, Sm - Lu; standard setting *Pnma*). The square stands for the literature values of Marezio *et al*. [216] and the star (*) for the single crystal data.

Similar observations were described by Berkowski *et al.*, who investigated single crystals of the solid solution La$_{1-x}$Nd$_x$GaO$_3$ [240]. It was found that the volume of the unit cell decreases linearly with an increasing Nd concentration according to Vegard´s law. This agrees with the general behavior of all ternary rare-earth gallates, showing decreasing volumes due to the lanthanide contraction (Figure 4-4).
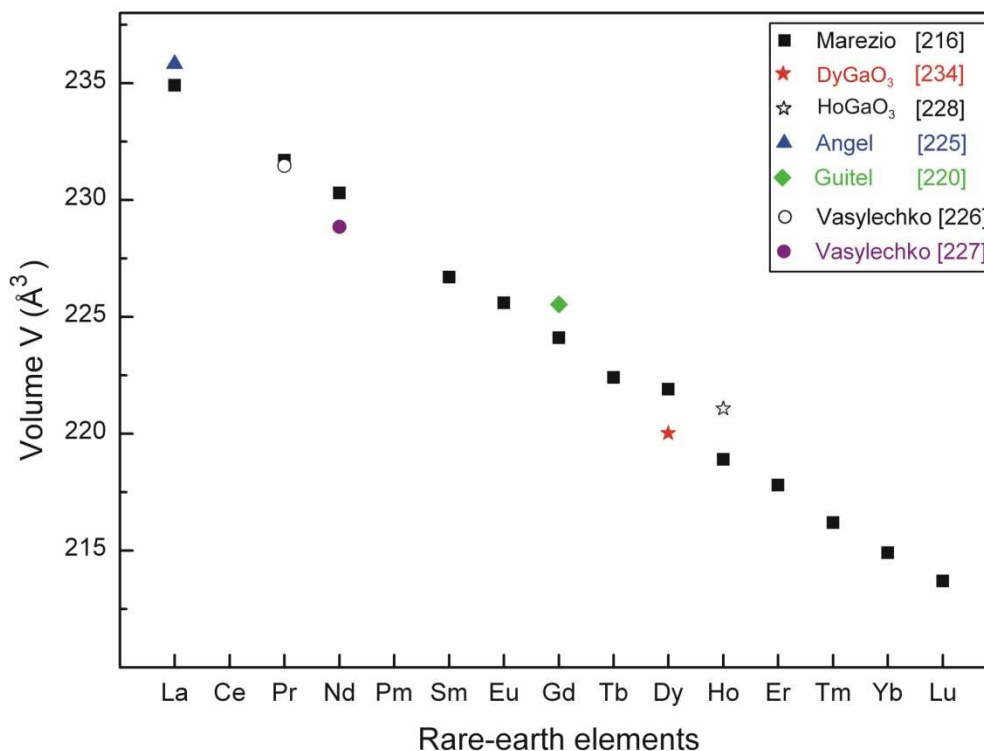
Figure 4-4. Volume of the different rare-earth gallates REGaO$_3$ (RE = La, Pr, Nd, Sm-Lu; standard setting *Pnma*).

With increasing Nd concentration x in La$_{1-x}$Nd$_x$GaO$_3$, the lattice parameters a and c decrease (setting of space group *Pbnm*), whereas b increases. At $x = 0.32$, the parameters a and b become equal and the crystal adopts a pseudo-tetragonal structure. Due to the preferred tendency for twinning, these solid solutions were characterized by powder X-ray diffraction.

4.1.2.3   Theoretical Calculations for DyGaO$_3$

The calculation of the charge distribution of the atoms in DyGaO$_3$ *via* bond-valence sums with the Bond-Length / Bond-Strength concept (ΣV) [186-188] and with the CHARDI concept (ΣQ) (Charge Distribution in Solids) [186,190,191] confirmed the formal valence states in the rare-earth gallate (Table 4-8). For the calculation of the bond-valence parameters of R$_{ij}$ = 203.6 for Dy-O bonds and R$_{ij}$ = 173.0 for Ga-O bonds were applied [188]. The values for dysprosium and gallium stand in good accordance with the expected values of +3, so do the results for the oxygen atoms.

Table 4-8. Charge distribution in DyGaO$_3$, with the calculated Bond-Length / Bond-Strength concept (ΣV) and the CHARDI concept (ΣQ).

	Dy	Dy	Ga	O(1)	O(2)
ΣV	+3.0	+3.1	+3.0	-2.1	-2.0
ΣQ	+3.0	+3.0	+3.0	-2.11	-1.94

The additive potential of the Madelung part of the lattice energy values (MAPLE) [183-185] allows to calculate hypothetical values for the compound DyGaO$_3$ starting from the end members dysprosium oxide C-Dy$_2$O$_3$ [258] and gallium oxide β-Ga$_2$O$_3$ [241]. The calculation of the MAPLE values for DyGaO$_3$ allowed the comparison with the calculated MAPLE contributions of the educts.

$$Dy_2O_3 + Ga_2O_3 \quad \xrightarrow[1250\ °C]{7.5\ GPa} \quad 2\ DyGaO_3 \qquad \text{(4-2)}$$
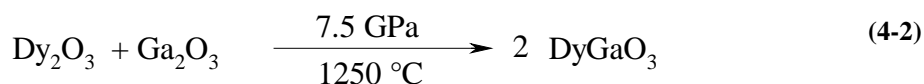
According to Eq. 4-2 the calculations for DyGaO$_3$ resulted in a value of 32714 kJ/mol compared to 32697 kJ/mol [C-Dy$_2$O$_3$ (15184.4 kJ/mol) + β-Ga$_2$O$_3$ (17513 kJ/mol)] (deviation 0.05 %) derived from the binary oxides. Therefore the crystal structure solution can be seen as electrostatical consistent.

4.1.2.4   Conclusion

According to the observations that pressure can induce crystallisation, as often seen in the field of borates, investigations on rare-earth gallates were continued. Although rare-earth gallates are well investigated, only few results led to crystalline samples, so far. Within this and previous experimental work, crystalline compounds in the system *RE*GaO$_3$ (*RE* = Dy, Ho) were obtained.

Recently, the first crystalline HoGaO$_3$ was obtained derived from high-pressure / high-temperature conditions of 7.5 GPa and 1250 °C, wherefrom the typical orthogallate structure was confirmed. Continous work under extreme conditions on the field or rare-earth gallates, resulted now in the first crystalline sample of DyGaO$_3$.

Applying high-pressure / high-temperature conditions of 7.5 GPa and 1250 °C to a mixture of the binary educts C-Dy$_2$O$_3$ and β-Ga$_2$O$_3$, resulted in a highly crystalline sample. The obtained

structural results correspond well with those, derived from powdered samples (Marezio *et al*. [216]), as well as with the single crystal data for HoGaO$_3$ [228].

Further investigations on rare-earth gallates led to interesting results concerning the phase transformations of the applied starting materials (C-rare-earth oxides).

4.2 Rare-Earth Oxides

4.2.1 Introduction

About 80 years ago, Goldschmidt *et al*. [242] commenced to examine the chemistry of rare-earth elements, investigating the chemical behavior, stability, and phase transformations. They classified these oxides in three groups A-RE_2O_3, B-RE_2O_3, and C-RE_2O_3 with respect to the different crystal structures.

Figure 4-5 gives an overview of the rare-earth sesquioxides classified in the three different structure types A, B, and C.

La	Ce	Pr	Nd	Pm	Sm	Eu	Gd	Tb	Dy	Ho	Er	Tm	Yb	Lu
A-RE_2O_3														
					B-RE_2O_3									
			C-RE_2O_3											

Figure 4-5. Overview of the three different rare-earth sesquioxide structure classifications: type A, B, and C.

Other working groups, like Iandelli, Shafer *et al*., or Foex *et al*. tried to find out, which parameters (ionic radius of the RE^{3+}-ion, temperature, pressure) cause the formation of the specific structure-type in the row of the lanthanide ions [243-245].

They recognized that the phase transformations between the structure types are reversible and can be initiated at high temperatures. However, the required heating temperature increased within the row of the lanthanide ions.

In detail, type A sesquioxides (high-temperature form) include the rare-earth oxides from La to Pm, characterized by large ionic radii and are therefore often called the "early" elements in the rare-earth alignment. The structural characterization, based on single crystal data, led to a trigonal symmetry crystallizing in the space group $P\bar{3}m1$ (no. 164) [246]. Often, this structure-type is named the "lanthanum oxide-type". In Figure 4-6, the crystal structure of A-Nd_2O_3 is shown with a view along along [$\bar{1}00$] [247].

The structure exhibits seven-fold coordinated RE^{3+}-cations. Remarkable are the different bond-lengths in the coordination sphere, resulting in a 4+3-coordination for the rare-earth ions, separating into four short RE-O-bonds (av. 234.29 pm) and three extended ones (av. 269.49 pm).
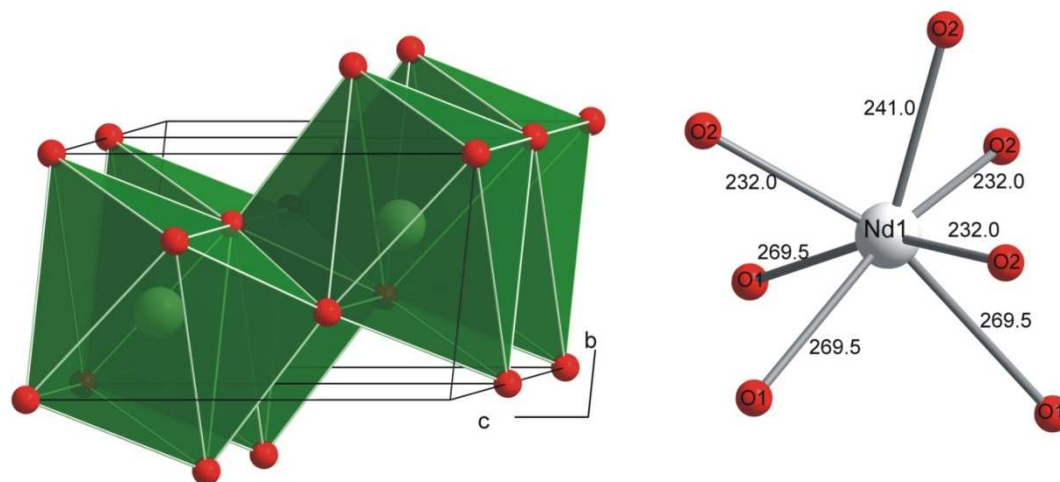
Figure 4-6. Left: Crystal structure of A-Nd$_2$O$_3$ with a view along along [$\bar{1}$00]; **Right:** Coordination sphere of the 4+3-coordination of Nd1 in A-Nd$_2$O$_3$.

The monoclinic type B sesquioxides crystallize in the space group *C*2/*m* (no. 12). Rare-earth elements starting at samarium to terbium belong to that group. The *RE*$^{3+}$-ions are surrounded by six and seven oxygen anions, forming six-fold coordinated polyhedra (distorted octahedra) and capped trigonal-prismatic coordination polyhedra, respectively. Due to the coordination numbers, the structure can be described as an intermediate form between the trigonal A-phase (only *RE*O$_7$-units) and the cubic C-phase (only *RE*O$_6$-units) [248]. Figure 4-7 gives a detailed view of the structure of monoclinic B-*RE*$_2$O$_3$. The capped trigonal prisms (light green) are connected to each other *via* shared faces, while the distorted octahedra (dark green) are linked *via* edge-sharing among each other, forming linear strings along [0$\bar{1}$0].
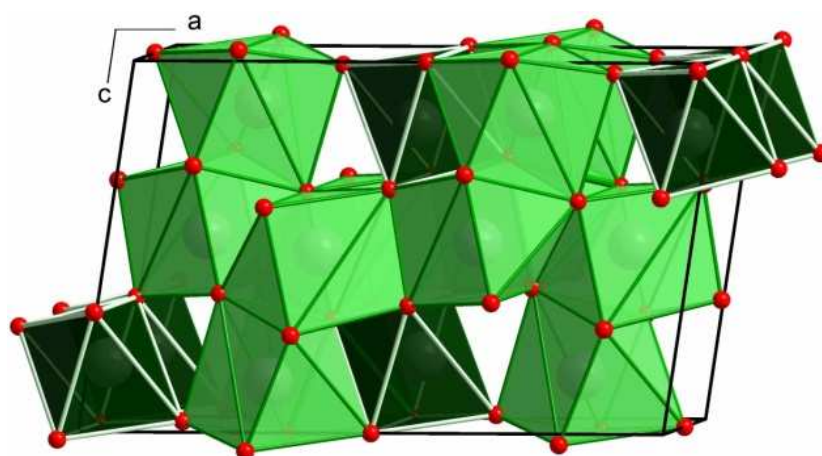
Figure 4-7. Crystal structure of monoclinic B-*RE*$_2$O$_3$ with a view along [0$\bar{1}$0]. The light green polyhedra correspond to the capped trigonal prismatically and the dark green polyhedra to the octahedrally coordinated *RE*$^{3+}$-ions, respectively.

The so-called C-type sesquioxides (low-temperature form) crystallize in a cubic form, and can be found for the rare-earth elements from neodymium to lutetium. The structure can be described in analogy to the bixbyite-structure (Mn_2O_3-type, defective fluorite structure), crystallizing in the space group $Ia\overline{3}$ (no. 206). The structure exhibits only distorted octahedrally coordinated RE^{3+}-cations, connected *via* edge- and corner-sharing [249]. Structural investigations into the cubic fluorite structure of the lanthanide oxides REO_2 showed that vacancies in the lattice lead to the composition of C-type RE_2O_3 [250]. Industrial applications *e.g.* in automobile exhaust catalysts, intensified research on these material [251-253]. Additionally, several studies were performed on high-pressure modifications of REO_2 (RE = Ce, Pr). The parameter pressure can induce transformations, as observed for the cubic fluorite structure of CeO_2, which transforms into the orthorhombic α-$PbCl_2$-type (*cotunite*). Although several different high-pressure modifications are known for Ce, the element Pr is only scarcely investigated. Recently, synthetic conditions of 5.5 GPa and 1000 °C led to a new high-pressure modification, HP-PrO_2, which could be determined by single crystal data [254].

Other stoichiometric compounds like intermediate phases were obtained, investigating the system REO_x (RE = Ce, Pr, Tb). The experiments started from their melts, and showed structural relations and similarities to other substance classes like fluorite-type dioxides. These structures presented relations to the crystallographic positions of the metal in the structures. Furthermore, a theoretical work of Eyring *et al*. showed that RE_2O_3-homologues with the general composition REO_{2n-1} are related to the A-type sesquioxides concerning the O-substructure [255].

Figure 4-8 displays the crystal structure type of C-RE_2O_3, indicating edge-sharing of the polyhedra [256]. For a better view, only half of the RE-cations are visualized by the corresponding polyhedra.
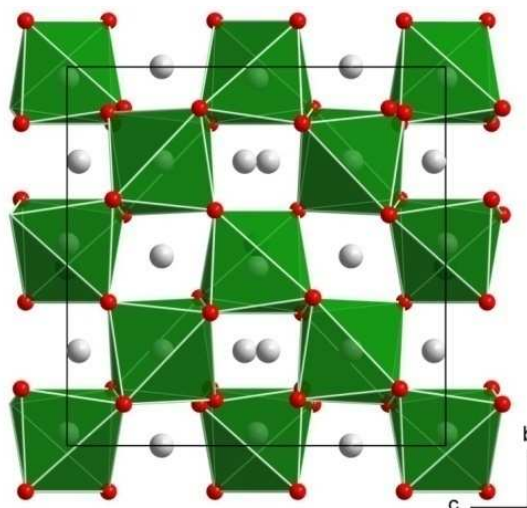
Figure 4-8. Crystal structure of type C-*RE*$_2$O$_3$, with a view along [$\bar{1}$00]. For a better view, only half of the *RE*-cations are shown.

Moreovere, systematic investigations of the transformation temperature for rare-earth oxides were performed by Iandelli [243]. The study confirmed the dependence of the transformation temperature from the atomic radii of the rare-earth ion. One of the first working groups preparing the C-type rare-earth oxides La$_2$O$_3$ and Nd$_2$O$_3$ *via* gently heating processes were Lohberg *et al*. The synthetic route applied the respective nitrate compounds [257]. The phase transformation started already at low temperatures for the C-type *RE*-oxides (*RE* = La, Pr), but the product consisted always of a mixture of type A and C due to an incomplete transformation reaction.

Maslen *et al*. investigated by means of synchrotron studies the magnetic properties and structure factors of the C-type sesquioxides (*RE* = Y, Dy, Ho) [258]. The physical properties are affected by vacant *f*-electron subshells, although the influences on the chemical bonding situation are negligible. Nevertheless, the magnetic properties are of high interest. According to Hund's rule, the vacancies in the shells can be filled, affecting the crystallographic situation, chemical bonds, and electron density.

Continuous work by several working groups [259-266] and expanding the applied conditions led to the formation of B-type sesquioxides. Pressure, as a useful tool to stabilize metastable compounds was successfully applied for the synthesis of B-*RE*$_2$O$_3$. Within investigations of phase transformations in rare-earth oxides, Hoekstra [267,268] obtained several monoclinic *RE*-sesquioxides (*RE* = Y, Sm, Eu, Gd, Tb, Dy, Ho, Er, Tm, Yb, Lu). Shafer *et al*. received also the monoclinic form B-*RE*$_2$O$_3$ (*RE* = Y, Sm, Nd, La), prepared by the hydrothermal technique [245]. Further investigations on the phase transformations yielded in transformed parts (~20 %) of the cubic starting material C-Ho$_2$O$_3$. Sawyer *et al*. succeeded in obtaining the monoclinic B-type applying high-pressure impact methods [248].

In contrast to that, the high-pressure / high-temperature experiments of Hoekstra were performed in a tetrahedral anvil high-pressure device developed by T. Hall [269], using pyrophyllite as pressure medium. For the experiments, annealed sesquioxides (at 1000 °C) were applied, filled into Pt-capsules and compressed and heated.

It was figured out that the phase transformations of the cubic rare-earth sesquioxides into the monoclinic compounds (C-B transformation) are reversible under certain high-pressure / high-temperature conditions between 2.5 and 4 GPa at temperatures of 900-1000 °C [267]. Although pressure is known as a tool to enable crystallisation of metastable compounds, the transformed monoclinic rare-earth oxides were unexceptionally obtained as powders.

Within the investigations, Hoekstra received also the monoclinic form of Ho_2O_3. The determination of the cell parameters of the monoclinic compound B-Ho_2O_3 were derived from powder diffraction patterns, leading to lattice parameters of $a = 1390(1)$, $b = 349.2(3)$, $c = 859.2(8)$ pm, and $\beta = 99.98(5)°$ [268]. The results of the indexed cell and the intensities of the reflections from the X-ray powder diffraction pattern directed to the conclusion that this phase was isotypic to the structure type of monoclinic B-Sm_2O_3, published earlier by Cromer [270].

Although pressure was useful in synthesis of these compounds, heating processes at ambient pressure did not lead to a phase transformation of C-RE_2O_3. Hoekstra [268] and Sawyer [248] were able to prove that the monoclinic phase of B-RE_2O_3 is affected by heating. In case of B-Ho_2O_3, the phase disappears caused by temperature treatment. The re-transformation into the cubic C-phase was successful, which supported the assumption of a metastable high-pressure phase [268].

It is noteworthy that there exist several ways of inducing phase transformations between the three different rare-earth oxide phases, depending on the applied temperature and pressure conditions [271,272]. Additional compounds added to the sample during the experiment can help to transform the sesquioxides under pressure and temperature treatment. For example, Foex et al. achieved a transformation from the C-type to the B-type sesqioxides structure by adding an amount of lime [243], but also supported by other oxides like SrO [273] or NaF [264].

In the last few years several attempts were made to transform sesquioxides into the monoclinic form. The transformed compounds were always obtained as nanocrystalline powder. For every element in the late row, the transformation was reported so far, but the compounds suffered always in crystallinity, probably due to the applied synthetic conditions.

Therefore, single crystal data for the late rare-earth elements have not been reported, yet. Our high-pressure / high-temperature investigations applying multianvil-devices on rare-earth compounds led to crystalline compounds of monoclinic B-type rare-earth sesquioxides (*RE* = Dy, Ho, Er, Tm). First experiments resulted in crystalline samples, but the crystals were too small for single crystal data collection. The improvement of the applied synthetic conditions increased the crystallinity. Therefore, the structure of B-Ho_2O_3 could be solved by single crystal determination, for the first time.

4.2.1.1   Starting Materials for the Synthesis of B-Ho_2O_3

The starting materials for the syntheses were all air- and humidity resistant. The analysis and characterization of the crystalline educts were executed with powder diffractometry, comparing the measured educts to the ICSD-database. The applied substances are listed in Table 4-17, provided with the corresponding ICSD numbers.

Table 4-9: List of applied substances.

Substance	State	Source of Supply	Purity [%]	ICSD-PDF
C-Dy_2O_3	Powder	Alfa Aesar, Emmerich, Germany,	99.995	[00-088-2164]
C-Ho_2O_3	Powder	Alfa Aesar, Emmerich, Germany	99.995	[00-088-2163]
C-Tm_2O_3	Powder	Alfa Aesar, Emmerich, Germany,	99.995	[00-082-2416]
β-Ga_2O_3	Powder	Fluka, Seelze, Germany	99.99	[00-087-1901]

4.2.1.2   Synthesis of B-Ho_2O_3

Our original intention was to synthesize rare-earth gallates with new compositions. We started with a stoichiometric ratio of C-Ho_2O_3 : β-Ga_2O_3 = 6 : 1. Starting materials were fine powders of cubic C-Ho_2O_3 (Alfa Aesar, Emmerich, Germany, 99.995 %) and β-Ga_2O_3 (Fluka, Seelze, Germany, 99.99 %). Additional experiments started from different educt mixtures of pure C-Ho_2O_3 besides stoichiometric ratios of C-Ho_2O_3 : β-Ga_2O_3 = 10 : 1, or 1 : 1, which led also to a phase transformed, highly crystalline sample of B-Ho_2O_3. The educts were ground, mixed, and filled into a boron nitride crucible (Henze BNP GmbH, HeBoSint® S10, Kempten, Germany). The boron nitride crucible was positioned inside the center of a 14/8-assembly, which was compressed by eight tungsten carbide cubes (TSM-10 Ceratizit, Reutte,

Austria). The assembly was compressed up to 11.5 GPa in 3½ h, using a multianvil device, based on a Walker-type module, and a 1000 t press (both devices from the company Voggenreiter, Mainleus, Germany). The detailed description of the preparation of the assembly can be found in chapter 2.1.1 and refs. [103,104,111].

The sample was electrically heated up to 1250 °C (cylindrical graphite furnace) in 15 min, kept there for 10 min, and cooled down to 650 °C in 10 min at constant pressure. Afterwards, the sample was quenched to room temperature by switching off the heating, followed by a decompression period of 10½ hours.

The product, a mixture of monoclinic B-Ho_2O_3 and orthorhombic $HoGaO_3$, obtained as by-product, was separated from the surrounding boron nitride crucible. The sample appeared grey-pink while handled in the laboratory (neon lamps) or showed a light beige-orange color, when investigated under natural light sources, caused by the Alexandrite effect [274,275]. This effect was first discovered in 1834 by the Finnish mineralogist N. G. Nordenskjöld [276], though some minerals are changing their color while being exposed to different light sources.

Figure 4-9 gives a view of the powder diffraction pattern exhibiting monoclinic B-Ho_2O_3, orthorhombic $HoGaO_3$ as by-product, weak reflections of hexagonal boron nitride from the crucible, and residual starting material C-Ho_2O_3. Some small air- and water-resistant crystals of B-Ho_2O_3 were isolated from the bulk sample for the single crystal structure determination.

Additional experiments under different high-pressure / high-temperature conditions led to the result that the necessary pressure for the formation of the high-pressure phase B-Ho_2O_3 can be reduced to a minimum of 7.5 GPa at temperatures around 1250 °C. As a side effect of reduced pressure, the degree of crystallinity of the samples suffered, as often seen in the field of borates [277,386-390].

At this point it is important to raise the issue, if pure cubic C-Ho_2O_3 without adding β-Ga_2O_3 can be transformed into the monoclinic form under these conditions. In fact, our experiments showed that it was impossible. The addition of a small amount of β-Ga_2O_3 was necessary to induce this phase transformation. This result corresponds with the observations of Foex and Warshaw *et al.*, who also added flux materials for successful transformations [271,272].
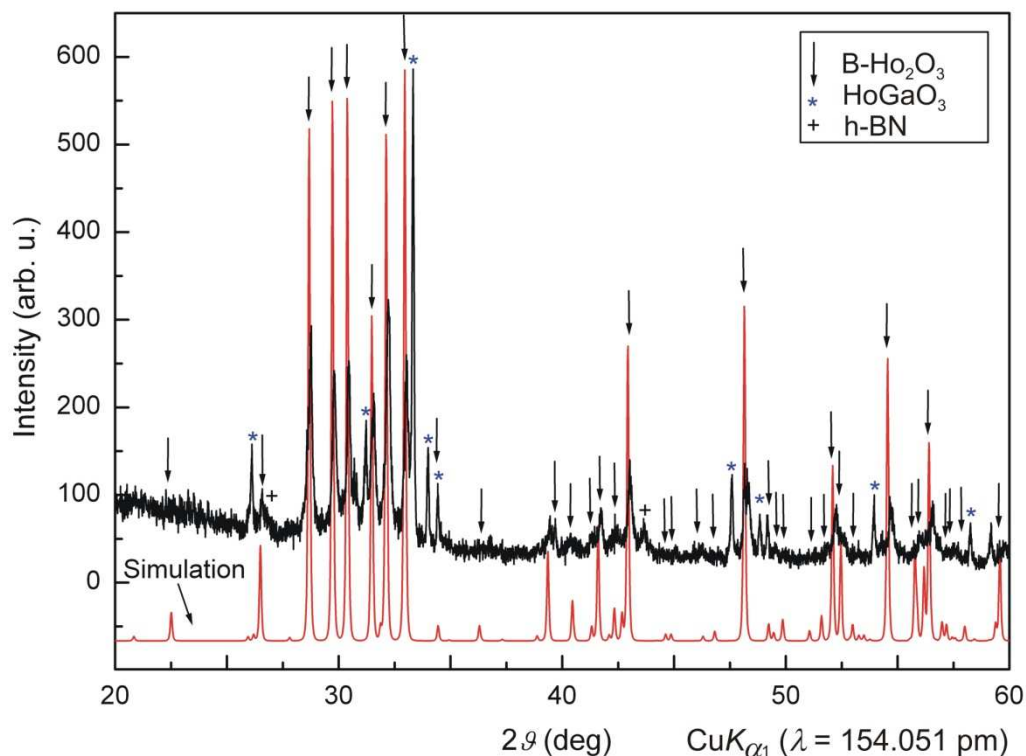
Figure 4-9. Powder diffraction pattern of the reaction product B-Ho$_2$O$_3$, starting from C-Ho$_2$O$_3$: β-Ga$_2$O$_3$ = 6 : 1 (11.5 GPa, 1250 °C). A simulation of a theoretical powder pattern of monoclinic B-Ho$_2$O$_3$, based on the single crystal data, is positioned underneath. The marked reflections refer to HoGaO$_3$, which occurs as a by-product. The remaining reflections correspond to a fraction of the starting material C-Ho$_2$O$_3$ [Radiation: Cu$K_{\alpha 1}$ (λ = 154.051 pm)].

4.2.1.3   Crystal Structure Analysis of B-Ho$_2$O$_3$

To analyse the product of the reaction C-Ho$_2$O$_3$: β-Ga$_2$O$_3$ = 6 : 1, a Stoe Stadi P powder diffractometer with monochromatized Cu$K_{\alpha 1}$ radiation was employed. The reflections of the main phase (monoclinic B-Ho$_2$O$_3$, Figure 4-9) were indexed using the program routine ITO [158]. The results led to a monoclinic cell with the lattice parameters a = 1394.3(7), b = 350.0(3), c = 864.4(8) pm, and β = 100.18(7)° (Table 4-10).

Single crystals of monoclinic B-Ho$_2$O$_3$ were isolated from the sample by mechanical fragmentation. After checking the quality, regarding crystallinity and suitability, the intensity data were collected at room temperature applying an Enraf-Nonius Kappa-CCD single crystal diffractometer with graded multi-layer X-ray optics and Mo$K_{\alpha 1}$ radiation (λ = 71.073 pm) from a small regular crystal with the size of $0.02 \times 0.02 \times 0.02$ mm^3.

The lattice parameters from the single crystal structure determination of monoclinic B-Ho$_2$O$_3$ (a = 1394.7(3), b = 350.83(7), c = 865.6(2) pm, and β = 100.23(3)°) agree well with those of

the powder pattern of the sample (Table 4-10). Furthermore, a multi-scan absorption correction (SCALEPACK [150]) was applied to the intensity data.

According to the systematic reflection conditions, the space groups $C2/m$ (no. 12) and $C2$ (no. 5) were derived. The structure solution and the parameter refinement with anisotropic displacement parameters for all atoms (full-matrix least squares against F^2) were successfully achieved in the space group $C2/m$ by the SHELX-97 software suite [169,171]. All relevant information and details concerning the single crystal data collection are listed in (Table 4-10). Additionally, the positional parameters (Table 4-11), anisotropic displacement parameters (Table 4-12), and interatomic distances (Table 4-13) are listed.

Table 4-10. Crystal data and structure refinement of monoclinic B-Ho_2O_3.

Empirical formula	Ho_2O_3
Molar mass, g mol^{-1}	377.86
Crystal system	monoclinic
Space group	*C*2/*m* (no. 12)
Powder diffractometer	Stoe Stadi P
Radiation	Cu$K_{\alpha 1}$ (λ = 154.051 pm)
Powder data	
a, pm	1394.3(7)
b, pm	350.0(3)
c, pm	864.4(8)
β, deg	100.18(7)
V, nm^3	0.4151(4)
Single crystal diffractometer	Enraf-Nonius Kappa CCD
Radiation	Mo$K_{\alpha 1}$ (λ = 71.073 pm) (graphite monochromator)
Single crystal data	
a, pm	1394.7(3)
b, pm	350.83(7)
c, pm	865.6(2)
β, deg	100.23(3)
V, nm^3	0.4168(2)
Formula units per cell	*Z* = 6
Calculated density, g cm^{-3}	9.03
Crystal size, mm^3	$0.02 \times 0.02 \times 0.02$
Temperature, K	293(2)
Detector distance, mm	40.0
Exposure time, min	20.0
Absorption coefficient, mm^{-1}	56.3
F(000), e	948
θ range, deg	3.5-30.0
Range in *hkl*	$\pm 19; \pm 4; \pm 12$
Reflections total / independent	3514 / 689
R_{int}	0.0744
Reflections with $I \geq 2\sigma(I)$	576
R_σ	0.0505
Data / ref. parameters	689 / 48
Absorption correction	multi-scan (Scalepack [150])
Final *R*1 / *wR*2 [$I \geq 2\sigma(I)$]	0.0425 / 0.1087
Final *R*1 / *wR*2 (all data)	0.0517 / 0.1130
Goodness-of-fit on F^2	1.041
Largest diff. peak and hole, e Å^{-3}	4.2 / -4.0

Table 4-11. Atomic coordinates and isotropic equivalent displacement parameters U_{eq} (Å^2) of B-Ho$_2$O$_3$ (space group: $C2/m$) (standard deviations in parentheses). U_{eq} is defined as one third of the trace of the orthogonalized U_{ij} tensor.

Atom	Wyckoff-Position	x	y	z	U_{eq}
Ho1	$4i$	0.63508(5)	0	0.4880(2)	0.0129(3)
Ho2	$4i$	0.68977(5)	0	0.1369(2)	0.0130(3)
Ho3	$4i$	0.96655(5)	0	0.1869(2)	0.0150(3)
O1	$4i$	0.1282(8)	0	0.282(2)	0.020(3)
O2	$4i$	0.8244(8)	0	0.030(2)	0.018(3)
O3	$4i$	0.7938(8)	0	0.373(2)	0.019(3)
O4	$4i$	0.4695(8)	0	0.343(2)	0.015(2)
O5	$2b$	0	1/2	0	0.012(3)

Table 4-12. Anisotropic displacement parameters U_{ij} (Å^2) of B-Ho$_2$O$_3$ (space group $C2/m$) (standard deviations in parentheses).

Atom	U_{11}	U_{22}	U_{33}	U_{23}	U_{13}	U_{12}
Ho1	0.0079(4)	0.0157(5)	0.0152(5)	0	0.0023(3)	0
Ho2	0.0093(4)	0.0147(5)	0.0154(5)	0	0.0040(3)	0
Ho3	0.0090(4)	0.0162(5)	0.0187(5)	0	-0.0004(3)	0
O1	0.010(5)	0.026(7)	0.023(7)	0	0.000(5)	0
O2	0.013(5)	0.027(7)	0.012(6)	0	-0.001(4)	0
O3	0.021(6)	0.016(7)	0.020(7)	0	0.000(5)	0
O4	0.011(5)	0.019(6)	0.016(6)	0	0.006(4)	0
O5	0.016(8)	0.013(8)	0.006(7)	0	-0.001(6)	0

Table 4-13. Interatomic distances (pm) of B-Ho$_2$O$_3$ (space group $C2/m$) based on single crystal data (standard deviations in parentheses).

Ho1–O4	224(2)		Ho2–O2	224(2)		Ho3–O2	219.7(2)
Ho1–O3	225.6(8)	2×	Ho2–O2	225.7(8) 2×		Ho3–O4	220.8(7) 2×
Ho1–O4	243(2)		Ho2–O3	229(2)		Ho3–O1	226.1(2
Ho1–O1	249(2)	2×	Ho2–O1	240.5(9) 2×		Ho3–O5	248.58(7) 2×
Ho1–O3	258(2)		Ho2–O1	270(2)			

4.2.1.4   Results and Discussion on B-Ho$_2$O$_3$

The monoclinic compound B-Ho$_2$O$_3$ was already synthesized by Hoekstra, obtained as fine powder [267,268]. In order to determine the structure, X-ray powder diffraction pattern were compared to other monoclinic phases, like B-Sm$_2$O$_3$ [270]. Further investigations, as well as

theoretical calculations on rare-earth material were performed [280]. Within the high-pressure / high-temperature investigations of rare-earth compounds, the monoclinic phase B-Ho_2O_3 was obtained as highly crystalline sample. The comparison between the lattice parameter derived from the literature (powder data), the theoretical data, and the experimental data set (single crystal) agree well.

Figure 4-10 gives an overview of the corresponding volumes from literature data. Single crystal data of monoclinic sesquioxides are only available for the oxides RE_2O_3 (RE = Sm - Tb) [263-279]. Figure 4-10 clearly shows a decrease in volume within the row of the rare-earth elements due to the lanthanide contraction. Obviously, our single crystal data agree well with the data from the literature.
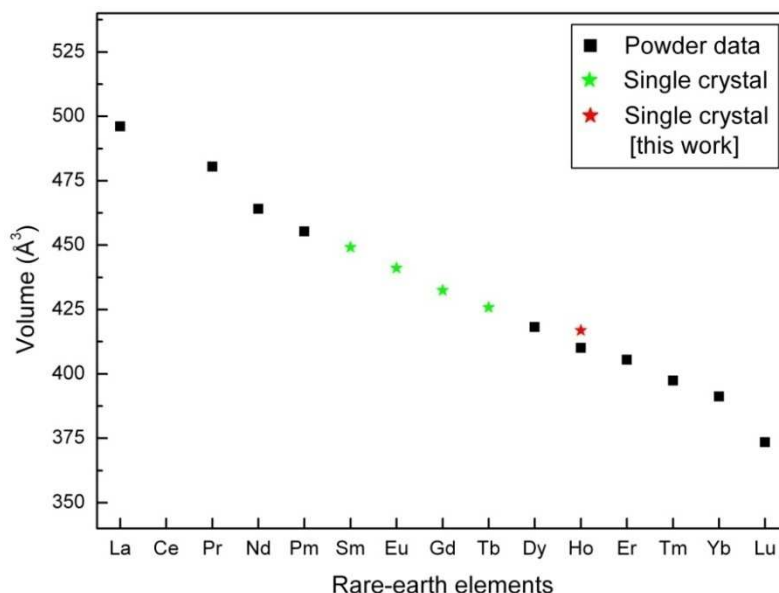
Figure 4-10. Overview of the corresponding volumes of the monoclinic B-type sesquioxides. The square (■) marks experimental powder data from the literature and the star (∗) stands for the single crystal data (green: literature, red: this work).

Recently, theoretical calculations on the basis of DFT and PAW methods, concerning phase transition of the rare-earth sesquioxides RE_2O_3 (RE = La - Lu, Y, Sc) were performed by the working group of Wu *et al*. [280]. The influence on the lanthanide contraction related to the decreasing ionic radii along the series was also investigated. Investigations into the bulk modulus of the compounds RE_2O_3 (RE = La - Lu) showed a continuous decrease with increasing atomic numbers, besides a reduction of the transition pressure and enthalpy for the transformation of monoclinic B-type into the hexagonal A-type structure. The comparison of the calculated data of Wu *et al*. with the experimental single crystal results affirmed the consistency of the data.

The single crystal lattice parameters of B-Ho_2O_3, (a = 1394.7(3), b = 350.83(7), c = 865.6(2) pm, and β = 100.23(3)° (Table 4-14)) and atomic coordinates (Table 4-11) show good accordance with the theoretical values obtained by Wu *et al.* ($a_{calc.}$ = 1399.14, $b_{calc.}$ = 348.87, $c_{calc.}$ = 861.01 pm, and $\beta_{calc.}$ = 100.266° [280]). The theoretical and experimental derived results are listed in Table 4-14.

Table 4-14. Atomic coordinates and isotropic equivalent displacement parameters U_{eq} (Å^2) of B-Ho_2O_3 (space group: $C2/m$) (standard deviations in parentheses). U_{eq} is defined as one third of the trace of the orthogonalized U_{ij} tensor. The corresponding theoretical values (Wu *et al.* [280]) are shown in brackets under the measured values.

Atom	Wyckoff-Position	x	y	z	U_{eq}
Ho1	4i	0.63508(5)	0	0.4880(2)	0.0129(3)
		[0.6347]	[0]	[0.4879]	
Ho2	4i	0.68977(5)	0	0.1369(2)	0.0130(3)
		[0.6916]	[0]	[0.1371]	
Ho3	4i	0.96655(5)	0	0.1869(2)	0.0150(3)
		[0.9679]	[0]	[0.1859]	
O1	4i	0.1282(8)	0	0.282(2)	0.020(3)
		[0.1278]	[0]	[0.2815]	
O2	4i	0.8244(8)	0	0.030(2)	0.018(3)
		[0.8254]	[0]	[0.0302]	
O3	4i	0.7938(8)	0	0.373(2)	0.019(3)
		[0.7935]	[0]	[0.3768]	
O4	4i	0.4695(8)	0	0.343(2)	0.015(2)
		[0.4711]	[0]	[0.3430]	
O5	2b	0	0.5	0	0.012(3)
		[0]	[0.5]	[0]	

Figure 4-11 represents the lattice parameters *a*, *b*, and *c* of the monoclinic B-type sesquioxides derived from experimental powder data of the literature (■), the theoretical work of Wu *et al.* (●) [280], and the experimental data of B-Ho$_2$O$_3$ [single crystal data (*)]. The lattice parameters tally well and decrease almost linearly due to the lanthanide contraction, except for the theoretical values for B-Er$_2$O$_3$ [280]. Unfortunately, some theoretical data are missing (*RE* = Eu, Yb).
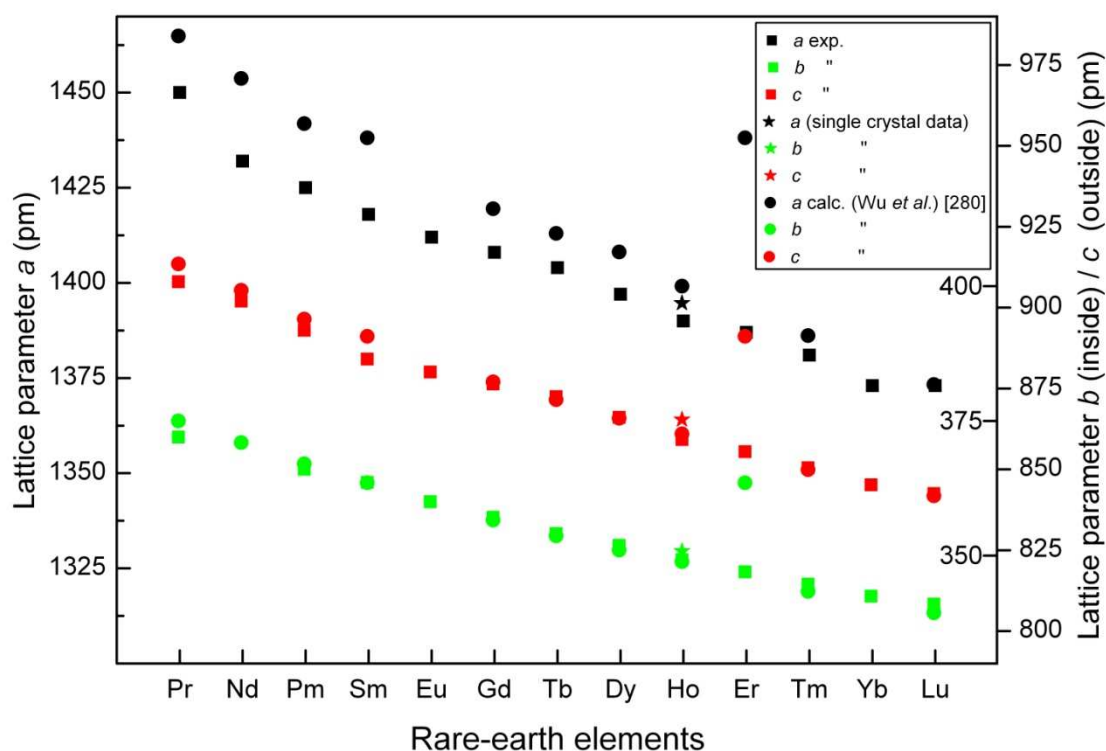
Figure 4-11. Comparison of the lattice parameters *a*, *b*, and *c* of the monoclinic B-type sesquioxides. The square (■) marks experimental values from the literature (powder data), the circle (●) shows data from theoretical calculations [280], and the star (*) marks the experimental data of this work (single crystal data).

Figure 4-12 shows the structure of monoclinic B-Ho$_2$O$_3$ with a view along [0$\overline{1}$0], displaying two different types of polyhedra: distorted octahedrally coordinated Ho^{3+}-ions next to seven-fold coordinated cations forming capped trigonal prisms. A closer look at the coordination sphere of Ho3 reveals six oxygen atom octahedrally arranged in a distance of 219.7(2) to 248.58(7) pm (av. = 230.8 pm) (Table 4-13) and an additional oxygen atom in a distance of 312.7 pm.
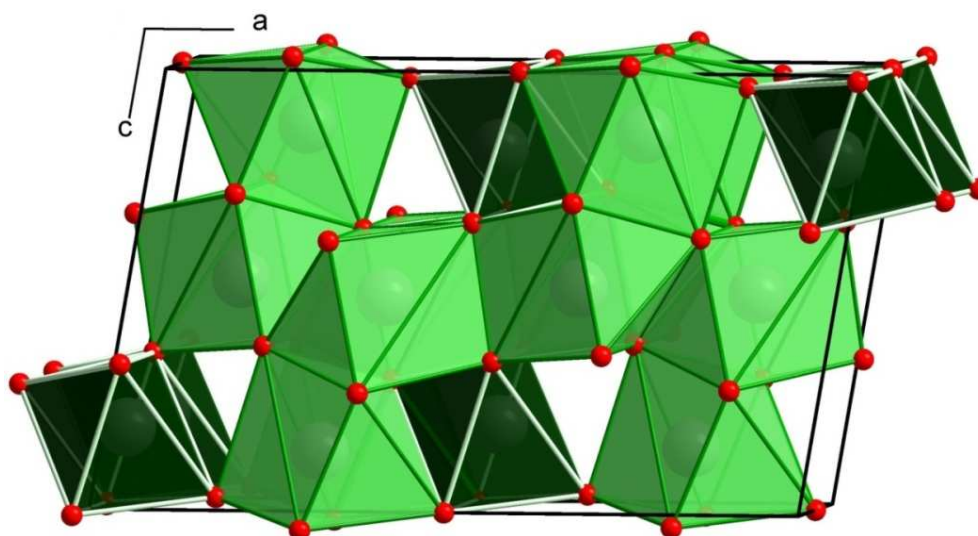
Figure 4-12. Crystal structure of monoclinic B-Ho_2O_3 with view along [0$\bar{1}$0]. The light polyhedra and the dark polyhedra correspond to the capped trigonal prismatically and octahedrally coordinated Ho^{3+}-ions, respectively.

Furthermore, MAPLE calculations (*Ma*delung *p*art of *l*attice *e*nergy) for Ho3 were performed [183-185]. The MAPLE results proved a negligible coordinative contribution of ECoN = 0.003 (*E*ffective *Co*ordination *N*umber) for this ion; so the six-fold coordinated description is reasonable.

The comparison to the cubic C-Ho_2O_3 shows that the average bond length of the octahedrally coordinated Ho3-O (av. = 228.3(3) pm) [258] stands in good accordance to the Ho-O distances in other octahedra.

The Ho-O distances of the capped trigonal prisms (Ho1, Ho2) range between 224-270 pm (av. = 237.8 pm), which corresponds well with the bond lengths of Ho (av. = 236 pm) in Ho_3GaO_6 [192].

In Figure 4-13, the coordination spheres of the three crystallographicaly independent Ho^{3+}-cations with plotted interatomic distances (Ho-O) are shown.
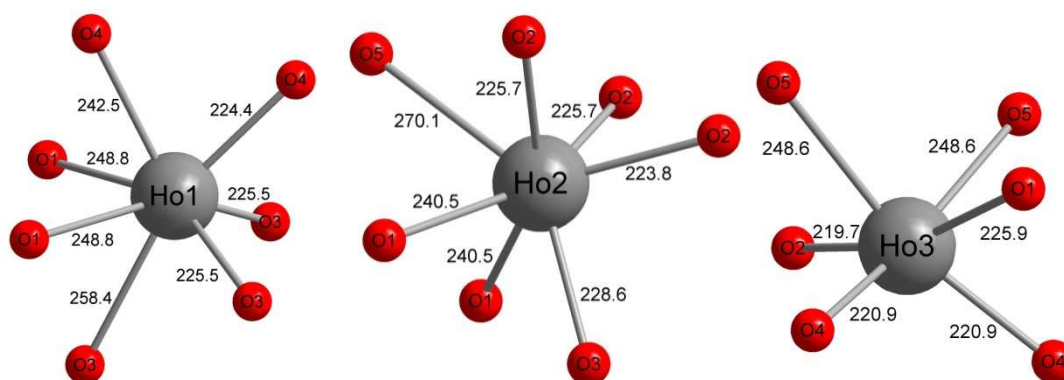
Figure 4-13. Coordination spheres of the three crystallographically independent Ho^{3+}-ions in B-Ho$_2$O$_3$.

At this point the question arises, if it is possible to transform cubic Ho$_2$O$_3$ into the monoclinic form under these conditions, starting from pure C-Ho$_2$O$_3$, without adding β-Ga$_2$O$_3$.

The lowest fraction of β-Ga$_2$O$_3$ and C-Ho$_2$O$_3$ leading to a transformed compound was 1 : 10. In fact further investigations showed that it was not possible to obtain the monoclinic compound without adding flux materials. Therefore we can state that the addition of a small amount of β-Ga$_2$O$_3$ was necessary for a successful transformation.

4.2.1.5   Theoretical Calculations for B-Ho$_2$O$_3$

Bond valence sums were calculated for B-Ho$_2$O$_3$ on the basis of the Bond-Length / Bond-Strenght concept (ΣQ) [186-188] and the CHARDI (ΣV) [190,191] concept (see Table 4-15). The formal ionic charges of the atoms were within the limits of both concepts with the exception of the reduced value for the oxygen atom O5, exhibiting a value of -1.45 (ΣQ), due to a extraordinary long Ho2-O5-bond of 270.1 pm.

Table 4-15. Charge distribution in B-Ho$_2$O$_3$ calculated with the Bond-Length / Bond-Strength concept.

	Ho1	Ho2	Ho3	O1	O2	O3	O4	O5
ΣQ	2.73	2.99	2.94	-2.25	-2.25	-1.78	-2.10	-1.45
ΣV	3.0	3. 0	3.0	-2.0	-2.0	-2. 0	-2.0	-2.0

4.2.2 Conclusion

The successful synthesis and structural characterization of the crystalline compound monoclinic holmium sesquioxide B-Ho_2O_3 started from C-Ho_2O_3 and β-Ga_2O_3 in the molar ratio of 6 : 1 under high-pressure / high-temperature conditions of 11.5 GPa / 1250 °C. The structure was already known, but only from powder data.

For the first time, the successful synthesis of a crystalline compound with a high degree of crystallinity allowed the determination of the structure on the basis of single crystal data. A comparison of the existing structural parameters, based on the experimental data (powder) [267,268] and theoretical work [280] was done, which showed that all data stand in good accordance to each other.

Within our experimental work, the stability region for the metastable rare-earth oxide was investigated at different high-pressure / high-temperature conditions. Applying low fractions of β-Ga_2O_3, the experiments led to monoclinic B-Ho_2O_3. Nevertheless, experiments starting only from the rare-earth oxide (C-type) showed that the transformation into the monoclinic compound did not occur. So, for the transformation of C-Ho_2O_3, the addition of small amounts of β-Ga_2O_3 is necessary and helps to transform the compound, which stands in accordance to results of Foex *et al*. [244] or Pagano *et al*. [281], as flux materials improve crystallinity.

Under variation of the applied fluxes, several experiments were performed. Besides β-Ga_2O_3, mixtures of boron nitride and boron oxide were also added to the rare-earth oxides, as it was already successfully used for other compounds [282]. For Ho_2O_3, we can state that the phase transformation can be initiated by small amounts of β-Ga_2O_3, as well as by adding low fractions of h-BN and B_2O_3.

Additionally, experiments starting from other rare-earth oxides (RE = Dy, Er, Tm) were performed. Interestingly, the phase transformation for other C-type rare-earth oxides (RE = Dy, Er, Tm) under high-pressure / high-temperature conditions was observed (detected and determined by powder diffractometry and compared to the simulated diffraction pattern derived from the single crystal data of B-Ho_2O_3), but samples were obtained with a low degree of crystallinity. To improve crystal growth, other flux materials were applied. Unfortunately, the conditions could not be improved up to now. Therefore, measurable single crystals of these compounds are still not available.

For future work, we should concentrate on a variation of the flux material to improve crystallinity and come to measurable single crystals of the corresponding rare-earth oxides.

Within these investigations, a side reaction between the applied flux material h-BN, B_2O_3, and the rare-earth oxide occurred. The following chapter deals with the new holmium oxide borate obtained under high-pressure / high-temperature conditions, its characterization, crystal structure, stability, and spectroscopic investigations.

4.3 Rare-Earth Borates

4.3.1 Introduction

Boron plays an outstanding role in group 13 elements. Concerning chemical relationships within the Periodic Table, its affinity to silicon is higher than aluminium, gallium, or indium. Boron is often used as additive in organometallic compounds as Lewis acid due to its electron deficiency, and the vacant *p*-orbital. In contrast to that, the resulting structural diversity is appreciated in inorganic chemistry.

Figure 4-14. The minerals *kernite* [283], *ulexite* [284], and *colemanite* [285].

Valued in different natural minerals, boron exhibits a colorful spectra in gemstones, such as *borax* ($Na_2B_4O_5(OH)_4 \cdot 8\,H_2O$), *kernite* ($Na_2B_4O_6(OH)_2 \cdot 3\,H_2O$), *ulexite* ($NaCaB_5O_6(OH)_6 \cdot 5\,H_2O$) or *colemanite* ($Ca_2B_6O_{11} \cdot 5\,H_2O$). Furthermore, in the group of *tourmalines* $AB_3M_6[(OH,F)(OH,O)_3(BO_3)_3Si_6O_{18}]$ with (A = Na, Ca, K), (B = Al, Li, Fe, Mg, Mn, Zn, Cu), and (M = Al, Cr, Fe, Mg, Mn, V) [286] boron plays also an outstanding role.

However, synthesized oxoborates are in the scientific focus for high-tech purposes and industrial applications. Based on their high thermal stability, borates are used for high-temperature devices or utilized for optical glasses, phosphors, and non linear optical materials (NLO) due to their luminescence properties. Doped with europium, *e.g.* SrB_4O_7 : Eu, borates are used as phosphorus material for UV-emitting lamps in medical equipment. Green fluorescent lamps work *e.g.* with $GdMgB_5O_{10}$: (Ce, Tb) while red-emitting components in high-definition television apparatus work with $(Y, Gd)BO_3$: Eu. When the first borate was utilized as laser material, research intensified. Therefore β-BaB_2O_4 (BBO) is highly appreciated [287,288]. Further crystalline borates, like LiB_3O_5 (LBO) [289-292], α-BiB_3O_6 (BIBO) [293-295], and $CsLiB_6O_{10}$ (CLBO) [296-299] allowed the application for laser light of certain wavelengths and power levels, unattainable for solid state facilities in the past

[300,301]. Recently, the new non-centrosymmetric δ-modification of BiB_3O_6 (BIBO) was synthesized in our working group, applying high-pressure / high-temperature conditions of 5.5 GPa at 820 °C to mixtures of Bi_2O_3 and B_2O_3 (1 : 3) [86].

In analogy to the structural diversity of silicates, oxoborates display a diversity of characteristical different structures, based on the chemical relationship of boron and silicon. Silicates offer SiO_4-tetrahedra distributed as isolated units in the structure, bound in pairs, linked in larger clusters, including rings, chains, double chains, sheets, and three-dimensional frameworks as well.

Nevertheless, the BO_3-units and BO_4-groups can also be distributed as isolated units in the structure, linked in groups, chains, bands, sheets or bound in even more complex networks [302,303]. The fundamental principle for the structural diversity of borates is based on the ability of boron to coordinate to three as well as to four oxygen atoms, resulting in triangular BO_3-units and BO_4-tetrahedra.
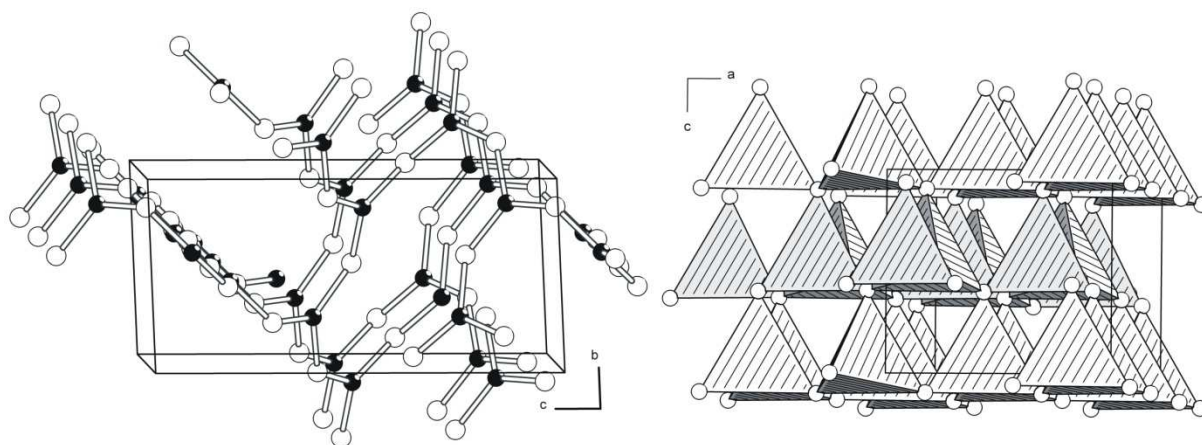
Figure 4-15. Left: Crystal structure of trigonal B_2O_3-I with a view along $[\bar{1}00]$ [305]. **Right**: Crystal structure of orthorhombic B_2O_3-II with a view along $[0\bar{1}0]$ [306].

The coordination number of boron is also affected under high-pressure conditions. According to the pressure coordination rule [304], increasing the pressure leads to higher coordinated ions in the structure. The comparison of the modifications of the normal pressure modification of boron oxide B_2O_3-I [305], and the high-pressure modification B_2O_3-II [306] shows that all trigonal BO_3-units in B_2O_3-I transform under pressure into BO_4-tetrahedra (B_2O_3-II). The crystal structures are shown in Figure 4-15.

A typical structural characteristic, the fundamental building blocks (FBB), was already postulated in 1969 by Edwards and Ross and classified by Burns [307-309]. This structural build-up of triangular BO_3-units and BO_4-tetrahedra linked only *via* common corners and not *via* edge- or face-sharing, can be used within the important class of oxoborates.

Research on borates was mostly conducted under normal pressure conditions. Due to geological interests in gemstones the conditions for synthetic borates were enlarged into a high-pressure approach. Originally, rare-earth oxoborates were in the scientific focus of Meyer, who presented first results in the system REBO$_3$ (RE = Pr, Nd, Sm - Dy, Yb) [310]. Exploring new synthetic fields under high-pressure / high-temperature conditions using belt devices, he investigated the influence of pressure on the high-temperature modifications of rare-earth orthoborates REBO$_3$ and observed pressure-induced transformations at an applied pressure of 2 up to 6.5 GPa, at 850-1000 °C to the λ-modifications (space group: $Pmcn$).

In 1999, Huppertz *et al.* commenced high-pressure / high-temperature research on crystalline borates applying a Walker-type high-pressure device. Continuative research led to a diversity of different rare-earth, transition metal, and main group borates. Recently the field of rare-earth fluorborates was seized.

The first rare-earth borates were obtained from the binary oxides in the following stoichiometric compositions, REBO$_3$, different modifications of REB$_3$O$_6$, and RE_3BO$_6$, enlarging the number with compositions of RE_2B$_4$O$_9$ and RE_4B$_6$O$_{15}$.

Continuous research led to a diversity of new structures. So, the rare-earth oxoborate Dy$_4$B$_6$O$_{15}$ was the first compound exhibiting [BO$_4$]$^{5-}$-tetetrahedra in the structure connected *via* edge-sharing [77]. This extraordinary compound proved linkage *via* common edges, abolishing the postulate of only shared corners in borates.

Up to date, more than 500 oxoborates are known, and still new structures are obtained. In the last decade, the substance class of oxoborates [300,301,311-313] was in the focus of the scientific research in our working group with respect to their structural behavior and new synthetic possibilities under high-pressure / high-temperature conditions. The use of the multianvil technique [111] allowed the access to several new metastable polymorphs and compositions, unattainable under normal pressure conditions. Adjacent to a multitude of new main group [86,277,314,315] and transition metal oxoborates [80-84,316-323], special attention was given to the ternary rare-earth oxoborates with trivalent rare-earth cations [324].

In 1999, at the outset of our research, trivalent rare-earth oxoborates in the composition REBO$_3$ [325-353], REB$_3$O$_6$ [347-376], "RE_3BO$_6$" [324,377], RE_{26}O$_{27}$(BO$_3$)$_8$ [378,379], $RE_{17.33}$(BO$_3$)$_4$(B$_2$O$_5$)$_2$O$_{16}$ [380,381], and $RE_{8.66}$(BO$_3$)$_2$(B$_2$O$_5$)O$_8$ [382] were known. Shortly after, several polymorphs of these compositions were obtained in experiments performed under high-pressure / high-temperature conditions. Continuative research led to the compositions REB$_5$O$_9$ [383,384] and RE_4B$_{14}$O$_{27}$ [385], which were discovered under normal pressure conditions by Li *et al.* and Nikelski *et al.*, respectively. The work group of Huppertz

et al. was able to add four new compositions to the system by applying high-pressure conditions, namely $RE_4B_6O_{15}$ [77,78], $RE_2B_4O_9$ [386-389], $RE_3B_5O_{12}$ [390], and $RE_4B_{10}O_{21}$ [391,392]. In the case of $RE_4B_6O_{15}$, the new structural motive of edge-sharing BO_4 tetrahedra was observed for the first time. Table 4-16 gives a survey of all known compositions (to the best of our knowledge) of ternary rare-earth oxoborates with trivalent rare-earth cations ordered by the ratio $RE_2O_3 : B_2O_3$. So, at the top of Table 4-16, the rare-earth oxoborates *α-/β-RE*B$_5$O$_9$ show the highest fraction of boron, while at the bottom of Table 4-16 the compounds with the lowest boron contents are positioned. In the last place of Table 4-16, the new compound $RE_{31}O_{27}(BO_3)_3(BO_4)_6$ (RE = Ho) can be found, exhibiting the lowest percentage of boron in a trivalent rare-earth oxoborate synthesized so far. In the following, the high-pressure synthesis, the crystal structure, and characterization of the new rare-earth oxide borate $Ho_{31}O_{27}(BO_3)_3(BO_4)_6$ is reported.

Table 4-16. Known phases in the system RE_2O_3/B_2O_3.

Composition	RE_2O_3 : B_2O_3	RE : B	RE	Comments
α-REB$_5$O$_9$	1 : 5	0.2	Sm - Er	Pentaoxoborates [383]
β-REB$_5$O$_9$	1 : 5	0.2	La, Ce	Pentaoxoborates [384]
RE_4B$_{14}$O$_{27}$	1 : 3.5	0.285	La	[385]
α-REB$_3$O$_6$	1 : 3	0.33	La - Nd, Sm - Tb	[354,362,363,366,367,372]
βREB$_3$O$_6$	1 : 3	0.33	Tb-Lu	[350,373-376]
γ-REB$_3$O$_6$	1 : 3	0.33	La-Nd	[368,369]
δ-REB$_3$O$_6$	1 : 3	0.33	La, Ce	[370,371]
RE_4B$_{10}$O$_{21}$	1 : 2.5	0.4	Pr	[391,392]
α-RE_2B$_4$O$_9$	1 : 2	0.5	Eu, Gd, Tb, Dy	[386]
β-RE_2B$_4$O$_9$	1 : 2	0.5	Dy, Gd	[388,389]
RE_3B$_5$O$_{12}$	3 : 5	0.6	Er-Lu	[390]
RE_4B$_6$O$_{15}$	2 : 3	0.66	Dy, Ho	[77,78]
π-REBO$_3$	1 : 1	1	Y, Ce - Nd, Sm - Lu	LT Pseudo hex. phases [332,337]
μ-REBO$_3$	1 : 1	1	Y, Sm - Lu	HT Calcite related structure [332,337]
λ-REBO$_3$	1 : 1	1	La-Eu	Aragonite structure [334,345,351]
β-REBO$_3$	1 : 1	1	Sc, Yb, Lu	Calcite structure [335,338-340]
ν-REBO$_3$	1 : 1	1	Ce - Nd, Sm - Dy	Tric. (H-NdBO$_3$) [333,336,341,343,347,349]
χ-REBO$_3$	1 : 1	1	Dy, Ho, Er	Triclinic phases [352,353]
H-REBO$_3$	1 : 1	1	La, Ce	Monocl. (H-LaBO$_3$) [341,343,344,347]
$RE_{8.66}$O$_8$(BO$_3$)$_2$(B$_2$O$_5$)	8.66 : 4	2.165	Ho	[382]
$RE_{17.33}$O$_{16}$(BO$_3$)$_4$(B$_2$O$_5$)$_2$	~8.7 : 4	2.175	Y, Gd	[380,381]
RE_3BO$_6$	3 : 1	3	Y, La, Pr - Lu	((REO)$_3$BO$_3$) [337]
RE_{26}O$_{27}$(BO$_3$)$_8$	13 : 4	3.25	La, Nd	(8 RE_3BO$_6 \cdot RE_2$O$_3$) [378,379]
RE_{31}O$_{27}$(BO$_3$)$_3$(BO$_4$)$_6$	31 : 9	3.44	Ho	[this work]

4.3.2 Starting Materials for the Synthesis of $Ho_{31}O_{27}(BO_3)_3(BO_4)_6$

The starting materials for the synthesis were all air- and humidity resistant. The analysis and characterization of the crystalline educts and products was executed with powder diffractometry, comparing the measured educts to the ICSD-database. Remarkable is that impurities of less than 3 % cannot be detected. The applied substances are listed in Table 4-17, added with the corresponding ICSD numbers.

Table 4-17: List of applied substances.

Substance	State	Source of Supply	Purity [%]	ICSD-PDF
B_2O_3	Granulate	Strem Chemicals, Newburyport, USA	99.9	amorphous
Ho_2O_3	Powder	Alfa Aesar, Emmerich, Germany	99.995	[00-088-2163]
$C-Dy_2O_3$	Powder	Alfa Aesar, Emmerich, Germany,	99.995	[00-088-2164]

4.3.3 Holmium Oxide Borate $Ho_{31}O_{27}(BO_3)_3(BO_4)_6$

4.3.3.1 Synthesis of $Ho_{31}O_{27}(BO_3)_3(BO_4)_6$

The compound $Ho_{31}O_{27}(BO_3)_3(BO_4)_6$ was synthesized under high-pressure / high-temperature conditions of 7.5-11.5 GPa and 1200 °C in a modified Walker-type module in a multianvil 1000 t press. As starting materials fine powders of $C-Ho_2O_3$ (99.995 %, Alfa Aesar, Emmerich, Germany) and B_2O_3 (99.9 %, Strem chemicals, Newburyport, USA) were applied, mixed and ground together to fill the reactants finally into the BN-crucibles (BNP GmbH, HeBoSint® S10, Germany) (volume: ~9 mm^3 (14/8) up to ~35 mm^3 (18/11)), and sealed with a fitting hex. boron nitride plate. The stoichiometric ratio of $C-Ho_2O_3 : B_2O_3$ was 15.5 : 4.5 as shown in Eq. 4-3.

$$15.5 \ Ho_2O_3 \ + \ 4.5 \ B_2O_3 \ \xrightarrow[1200°C]{7.5 - 11.5 \ GPa} \ Ho_{31}O_{27}(BO_3)_3(BO_4)_6 \qquad \textbf{(4-3)}$$
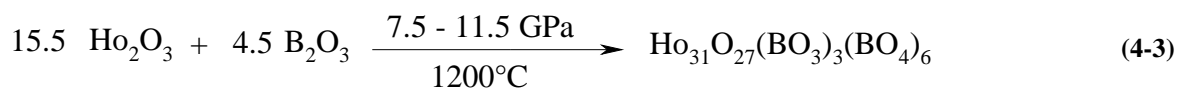
As pressure medium, precastable MgO-octahedra (Ceramic Substrates & Components, Isle of Wight, UK) with edge lengths of 14 or 18 mm (14/8 or 18/11-assembly) were applied. Eight

tungsten carbide cubes (TSM 10, Ceratizit, Austria) with the truncation edge lengths of 8 or 11 mm, compressed the octahedra.

The assemblies were compressed up to 11.5 GPa in 3.5 h followed by a heating period of 15 min, in which the samples were heated up to a temperature of 1200 °C. The temperature was held for 10 min, followed by a tempering segment (10 min) at 450 °C, to quench the sample finally to room temperature within one minute. After decompression (10.5 h), the recovered MgO octahedron was broken apart, to isolate the sample for further analytical investigations.

To estimate the formation region of the compound, with respect to the parameters pressure and temperature, we performed several different high-pressure / high-temperature experiments under variation of the applied pressures and temperatures at constant composition of the starting materials. These experiments led to the finding that the pressure could be reduced to 7.5 GPa at the same synthesis temperature of 1200 °C, still leading to the compound $Ho_{31}O_{27}(BO_3)_3(BO_4)_6$ in good quality.

The surrounding hexagonal boron nitride crucibles were carefully separated from the samples, to obtain the air- and humidity-resistant compound $Ho_{31}O_{27}(BO_3)_3(BO_4)_6$. The crystalline sample was grey to pink (neon lamps) to yellow-orange (naturally light sources), depending on the lighting conditions (Alexandrite effect [274,275]).

After preparation, the sample was examined by powder diffraction data at ambient temperature. In addition to that, as a matter of routine the sample was investigated with an EDX device (Oxford Instruments, Oxfordshire, UK) as semiquantitative method to examine the elemental content, crystal size, and homogeneity of the product. The EDX measurements exhibited high crystallinity and confirmed Ho, B, and O in the compound.

4.3.3.2   Crystal Structure Analysis of $Ho_{31}O_{27}(BO_3)_3(BO_4)_6$

The samples were characterized by powder X-ray diffraction, therefore a small part of the sample was closely ground and analyzed using a STOE Stadi P diffractometer, with monochromatized Cu$K_{\alpha 1}$ ($\lambda = 154.051$ pm) radiation (STOE & Cie, Darmstadt, Germany). Figure 4-16 shows a typical powder diffraction pattern of the sample exhibiting $Ho_{31}O_{27}(BO_3)_3(BO_4)_6$ as well as marked reflections of the starting material C-Ho_2O_3. The experimental powder pattern tallies well with the theoretical powder pattern (Figure 4-16, bottom) simulated from single-crystal data.
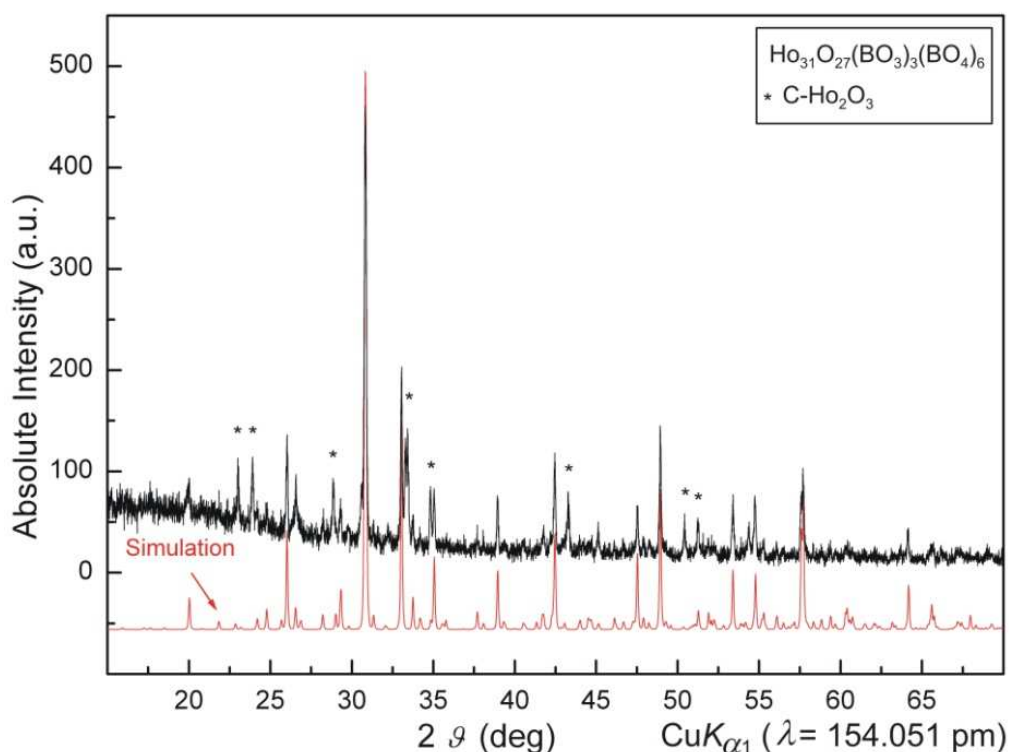
Figure 4-16. Powder diffraction pattern of the trigonal compound $Ho_{31}O_{27}(BO_3)_3(BO_4)_6$ compared to the simulated pattern, derived from single crystal determination. Marked reflections refer to remaining starting material C-Ho_2O_3.

All powder diffractograms were measured and handled with the Stoe program package WinXPOW [154]. The implied programs TREOR [155-157], ITO [158], DICVOL [159], and THEO [160] allowed the handling of the powder patterns. The powder diffraction pattern was indexed on the basis of a trigonal cell with the lattice parameters $a = 2657.9(4)$ and $c = 1146.9(2)$ pm and a volume of $7.001(3)$ nm^3.

Due to its crystallinity, small single crystals of $Ho_{31}O_{27}(BO_3)_3(BO_4)_6$ were mechanically isolated, and tested for symmetry and suitability on a precession camera in Laue mode (Buerger Precession camera 205, Huber Diffraktionstechnik GmBH, Rimsting, Germany) combined with an image plate system (Fujifilm BAS-2500 Bio Imaging Analyser, Fuji Photo Film corporation, Japan). Single crystal intensity data were collected at room temperature from a small, regular crystal with of size $0.01 \times 0.01 \times 0.01$ mm^3, applying an Enraf-Nonius Kappa-CCD single crystal diffractometer (Enraf Nonius, Delft, Netherlands) with graphite monochromatized Mo$K_{\alpha 1}$ ($\lambda = 71.073$ pm) radiation. A multi-scan absorption correction (SCALEPACK [150]) was applied to the intensity data. The crystal structure was solved and refined on the basis of a trigonal cell.

According to the systematic extinctions, the space groups, $R\overline{3}$ (no. 148) and $R3$ (no. 146) were derived. Structure solution and parameter refinement with anisotropic displacement parameters for all atoms (full-matrix least squares against F^2) were successfully achieved in the space group $R\overline{3}$ (no. 148) by the SHELX-97 software set [171,172].

All relevant information and details concerning the single-crystal data collection are listed in Table 4-18. Furthermore, the positional parameters (Table 4-19), anisotropic displacement parameters (Table 4-20), interatomic distances (Table 4-21), and interatomic angles (Table 4-22) are listed.

Table 4-18. Crystal data and structure refinement of $Ho_{31}O_{27}(BO_3)_3(BO_4)_6$.

Empirical formula	$Ho_{31}O_{27}(BO_3)_3(BO_4)_6$
Molar mass, g mol^{-1}	6170.12
Crystal system	trigonal
Space group	$R\bar{3}$ (no. 148)
Powder diffractometer	Stoe Stadi P
Radiation	$CuK_{\alpha1}$ (λ = 154.051 pm)
Powder data	
a, pm	2658.2(6)
c, pm	1145.5(3)
V, nm^3	7.010 (3)
Single crystal diffractometer	Enraf-Nonius Kappa CCD
Radiation	$MoK_{\alpha1}$ (λ = 71.073 pm) (graphite monochromator)
Single crystal data	
a, pm	2657.9(4)
c, pm	1146.9(2)
V, nm^3	7.017(2)
Formula units per cell	$Z = 6$
Calculated density, g cm^{-3}	8.76
Crystal size, mm^3	$0.1 \times 0.1 \times 0.1$
Temperature, K	293(2)
Detector distance, mm	35.0
Exposure time, min	25.0
Absorption coefficient, mm^{-1}	47.9
$F(000)$, e	15612
θ range, deg	3.6-30
Range in hkl	$\pm37; \pm16; \pm37$
Reflections total / independent	4550 / 3434
R_{int}	0.0941
Reflections with $I \geq 2\sigma(I)$	26407
R_σ	0.0624
Data / ref. parameters	4550 / 302
Absorption correction	multi-scan (SCALEPACK [150])
Final $R1$ / $wR2$ [$I \geq 2\sigma(I)$]	0.0319 / 0.0526
Final $R1$ / $wR2$ (all data)	0.0571 / 0.0564
Goodness-of-fit on F^2	1.053
Largest diff. peak and hole, e Å^{-3}	5.9 / -2.6

Table 4-19. Atomic coordinates and isotropic equivalent displacement parameters (U_{eq} / Å^2) for Ho$_{31}$O$_{27}$(BO$_3$)$_3$(BO$_4$)$_6$ (space group: $R\overline{3}$, no. 148). U_{eq} is defined as one third of the trace of the orthogonalized U_{ij} tensor.

Atom	Wyckoff site	x	y	z	U_{eq}
Ho1	18f	0.04045(2)	0.13786(2)	0.24508(4)	0.0074(2)
Ho2	18f	0.09366(2)	0.29530(2)	0.25530(4)	0.0074(2)
Ho3	18f	0.00695(2)	0.33401(2)	0.09479(5)	0.0113(2)
Ho4	18f	0.09250(2)	0.29633(2)	0.92081(4)	0.0082(2)
Ho5	18f	0.95947(2)	0.19489(2)	0.09030(4)	0.0073(2)
Ho6	18f	0.95431(2)	0.19082(2)	0.40076(4)	0.0083(2)
Ho7	18f	0.12112(2)	0.08890(2)	0.42691(4)	0.0099(2)
Ho8	18f	0.90851(2)	0.03104(2)	0.07485(4)	0.0086(2)
Ho9	18f	0.23591(2)	0.35261(2)	0.09477(4)	0.0084(2)
Ho10	18f	0.12334(2)	0.44307(2)	0.38490(4)	0.0101(2)
Ho11	6c	0	0	0.25270(9)	0.0170(2)
O1	18f	0.0857(3)	0.3476(3)	0.4003(5)	0.006(2)
O2	18f	0.0588(3)	0.2083(3)	0.8364(5)	0.006(2)
O3	18f	0.1526(3)	0.2744(3)	0.0279(5)	0.007(2)
O4	18f	0.9482(3)	0.1263(3)	0.2446(6)	0.010(2)
O5	18f	0.9971(3)	0.2626(3)	0.2484(6)	0.011(2)
O6	18f	0.8271(3)	0.9442(3)	0.0306(5)	0.007(2)
O7	18f	0.0700(3)	0.995(3)	0.3979(5)	0.008(2)
O8	18f	0.1760(3)	0.3889(3)	0.8966(5)	0.009(2)
O9	18f	0.0504(3)	0.2053(3)	0.3892(6)	0.011(2)
O10	18f	0.0926(3)	0.3359(3)	0.0884(5)	0.006(2)
O11	18f	0.2186(3)	0.1385(3)	0.3676(5)	0.009(2)
O12	18f	0.9429(3)	0.1253(3)	0.5537(6)	0.013(2)
O13	18f	0.0023(3)	0.2570(3)	0.5430(6)	0.011(2)
O14	18f	0.0923(3)	0.0945(3)	0.2550(5)	0.012(2)
O15	18f	0.1453(3)	0.2832(3)	0.4313(6)	0.014(2)
O16	18f	0.2029(3)	0.4406(3)	0.4522(6)	0.009(2)
O17	18f	0.9928(3)	0.2641(3)	0.8482(6)	0.012(2)
O18	18f	0.2704(3)	0.3571(3)	0.9165(6)	0.010(2)
O19	18f	0.0044(3)	0.0692(3)	0.1042(6)	0.010(2)
O20	18f	0.0511(3)	0.2073(3)	0.0901(6)	0.015(2)
B1	18f	0.2212(5)	0.1167(5)	0.252(2)	0.009(2)
B2	18f	0.2202(5)	0.4457(5)	0.577(2)	0.007(2)
B3	18f	0.1070(5)	0.2232(6)	0.421(2)	0.014(3)

Table 4-20. Anisotropic displacement parameters (U_{ij} / Å^2) for Ho$_{31}$O$_{27}$(BO$_3$)$_3$(BO$_4$)$_6$ (space group $R\bar{3}$, no. 148).

	U_{11}	U_{22}	U_{33}	U_{23}	U_{13}	U_{12}
Ho1	0.0072(2)	0.0068(2)	0.0083(3)	0.0002(2)	0.0010(2)	0.0036(2)
Ho2	0.0071(2)	0.0081(2)	0.0069(2)	0.0007(2)	0.0001(2)	0.0038(2)
Ho3	0.0076(2)	0.0071(2)	0.0191(3)	-0.0023(2)	-0.0025(2)	0.0036(2)
Ho4	0.0084(2)	0.0083(2)	0.0081(2)	-0.0008(2)	-0.0010(2)	0.0043(2)
Ho5	0.0066(2)	0.0074(2)	0.0072(2)	-0.0003(2)	-0.0006(2)	0.0028(2)
Ho6	0.0091(2)	0.0081(2)	0.0088(2)	-0.0009(2)	-0.0007(2)	0.0050(2)
Ho8	0.0086(2)	0.0073(2)	0.0080(2)	0.0005(2)	0.0004(2)	0.0027(2)
Ho9	0.0070(2)	0.0098(2)	0.0069(2)	-0.0003(2)	0.0001(2)	0.0031(2)
Ho10	0.0091(2)	0.0083(2)	0.0134(3)	-0.0007(2)	-0.002(2)	0.0047(2)
Ho11	0.0086(3)	0.0086(3)	0.0339(6)	0.000	0.000	0.0043(2)
O1	0.008(4)	0.005(3)	0.005(4)	-0.001(3)	0.003(3)	0.003(3)
O2	0.009(4)	0.005(3)	0.004(3)	0.000(3)	0.005(3)	0.003(3)
O3	0.009(4)	0.007(3)	0.008(4)	0.003(3)	0.001(3)	0.006(3)
O4	0.003(3)	0.009(4)	0.015(4)	-0.005(3)	-0.003(3)	0.002(3)
O5	0.006(4)	0.016(4)	0.008(4)	-0.002(3)	-0.002(3)	0.004(3)
O6	0.004(3)	0.008(3)	0.007(4)	0.001(3)	0.004(3)	0.001(3)
O7	0.011(4)	0.013(4)	0.005(4)	0.002(3)	0.003(3)	0.010(3)
O8	0.007(4)	0.006(3)	0.008(4)	-0.001(3)	-0.001(3)	-0.002(3)
O9	0.007(4)	0.016(4)	0.011(4)	-0.004(3)	-0.002(3)	0.007(3)
O10	0.006(3)	0.008(3)	0.005(3)	0.001(3)	0.003(3)	0.003(3)
O11	0.008(4)	0.017(4)	0.003(4)	-0.002(3)	-0.001(3)	0.007(3)
O12	0.010(4)	0.017(4)	0.011(4)	0.002(3)	0.001(3)	0.006(3)
O13	0.006(4)	0.011(4)	0.016(4)	0.003(3)	0.001(3)	0.003(3)
O14	0.021(4)	0.017(4)	0.000(4)	0.000(3)	0.001(3)	0.010(3)
O15	0.016(4)	0.014(4)	0.006(4)	-0.004(3)	0.005(3)	0.003(3)
O16	0.008(4)	0.009(4)	0.007(4)	-0.001(3)	0.000(3)	0.003(3)
O17	0.013(4)	0.008(4)	0.010(4)	0.000(3)	0.004(3)	0.001(3)
O18	0.005(3)	0.013(4)	0.014(4)	-0.006(3)	-0.002(3)	0.007(3)
O19	0.008(4)	0.010(4)	0.014(4)	0.000(3)	0.000(3)	0.005(3)
O20	0.012(4)	0.018(4)	0.013(4)	0.006(3)	0.007(3)	0.007(3)
B1	0.015(6)	0.012(6)	0.005(6)	0.003(5)	0.003(5)	0.011(5)
B2	0.005(6)	0.007(6)	0.004(6)	-0.003(5)	-0.008(5)	0.001(5)
B3	0.020(7)	0.025(7)	0.005(6)	0.005(5)	0.005(5)	0.016(6)

Table 4-21. Interatomic distances (pm) derived from single crystal data of $Ho_{31}O_{27}(BO_3)_3(BO_4)_6$.

Ho1-O14	219.8(7)	Ho5-O17	227.9(6)	Ho9-O18	222.0(6)
Ho1-O19	226.0(6)	Ho5-O20	228.8(6)	Ho9-O13	222.8(6)
Ho1-O7	227.4(6)	Ho5-O3	231.0(6)	Ho9-O1	224.6(6)
Ho1-O4	231.4(6)	Ho5-O6	235.1(6)	Ho9-O3	228.2(6)
Ho1-O9	235.4(6)	Ho5-O5	239.3(6)	Ho9-O15	243.5(7)
Ho1-O16	239.4(6)	Ho5-O8	244.1(6)	Ho9-O11	244.2(6)
Ho1-O20	247.4(7)	Ho5-O4	244.9(6)	Ho9-O17	266.4(7)
	Ø = 232.4	Ho5-O18	282.8(6)		Ø = 236.0
			Ø = 241.6		
Ho2-O10	220.5(6)	Ho6-O10	218.5(6)	Ho10-O1	222.1(6)
Ho2-O1	224.4(6)	Ho6-O13	226.7(7)	Ho10-O16	228.3(6)
Ho2-O5	226.3(6)	Ho6-O12	238.3(7)	Ho10-O13	229.1(7)
Ho2-O15a	244.1(7)	Ho6-O9	238.8(6)	Ho10-O2	237.3(6)
Ho2-O16	252.1(6)	Ho6-O5	241.1(6)	Ho10-O18	242.8(6)
Ho2-O15b	254.9(7)	Ho6-O4	242.8(6)	Ho10-O11	258.1(6)
Ho2-O9	257.8(7)	Ho6-O8	261.0(6)	Ho10-O12	271.4(7)
Ho2-O20	277.4(7)	Ho6-O11	276.1(6)	Ho10-O17	296.7(6)
	Ø = 244.7	Ho6-O15	286.7(7)		Ø = 248.1
			Ø = 247.8		
Ho3-O18	220.5(6)	Ho7-O14	214.7(6)	Ho11-O19a	246.6(6)
Ho3-O1	224.0(6)	Ho7-O7a	219.0(6)	Ho11-O19b	246.6(6)
Ho3-O10	225.2(6)	Ho7-O7b	227.5(6)	Ho11-O19c	246.6(6)
Ho3-O13	236.9(6)	Ho7-O11	234.5(6)	Ho11-O14a	248.4(7)
Ho3-O17a	239.3(6)	Ho7-O12a	244.1(6)	Ho11-O14b	248.4(7)
Ho3-O5a	250.6(7)	Ho7-O12b	261.8(7)	Ho11-O14c	248.4(7)
Ho3-O5b	269.8(6)	Ho7-O9	293.4(7)	Ho11-O7a	254.9(6)
Ho3-O17b	288.1(7)	Ho7-O7	293.8(6)	Ho11-O7b	254.9(6)
	Ø = 244.3	Ho7-O4	302.2(6)	Ho11-O7c	255.0(6)
			Ø = 254.6		Ø = 250.0
Ho4-O10	219.0(6)	Ho(8)-O14	223.2(6)		
Ho4-O18	220.1(6)	Ho(8)-O19a	224.8(6)		
Ho4-O2	226.2(6)	Ho(8)-O2	225.8(6)		
Ho4-O3	230.9(6)	Ho(8)-O6a	229.6(6)		
Ho4-O17	236.3(6)	Ho8-O6b	232.8(6)		
Ho4-O8a	236.5(6)	Ho8-O19b	239.3(6)		
Ho4-O8b	265.5(6)	Ho8-O20	278.1(7)		
Ho4-O20	282.5(7)	Ho8-O19c	290.8(6)		
	Ø = 239.5	Ho8-O4	293.9(6)		
			Ø = 248.7		

B1-O11	146.41(3)	B2-O3	146.21(2)	B3-O9	138.11(4)
B1-O8	147.8(2)	B2-O16	148.41(2)	B3-O15	140.41(4)
B1-O2	148.21(3)	B2-O6	149.71(3	B3-O13	142.41(3)
B1-O4	152.21(3)	B2-O20	150.11(2)		Ø = 140.3
	Ø = 148.7		Ø = 148.6		

Table 4-22. Interatomic bond angles (O-B-O) (deg.) for $Ho_{31}O_{27}(BO_3)_3(BO_4)_6$.

O11-B1-O8	112.0(8)	O3-B2-O16	109.9(8)	O9-B3-O15	117.3(10)
O11-B1-O2	108.5(8)	O3-B2-O6	106.5(8)	O9-B3-O12	121.3(10)
O8-B1-O2	111.8(8)	O16-B2-O6	111.5(8)	O15-B3-O12	121.3(10)
O11-B1-O4	109.8(8)	O3-B2-O20	113.8(8)		
O8-B1-O4	103.4(8)	O16-B2-O20	105.9(8		
O2-B1-O4	111.4(8)	O6-B2-O20	109.3(7)		
Ø 109.5		**Ø 109.5**		**Ø 120.0**	

4.3.3.3   Crystal Structure of $Ho_{31}O_{27}(BO_3)_3(BO_4)_6$

Figure 4-17 shows the crystal structure of the holmium oxide borate $Ho_{31}O_{27}(BO_3)_3(BO_4)_6$ displaying isolated BO_4-tetrahedra as dark hatched polyhedra and BO_3-units in form of ball-stick modells, embedded in a complex holmium oxide network. Three crystallographically different boron atoms occur in the structure, from which B1 and B2 are tetrahedrally coordinated, while B3 is coordinated trigonally planar by three oxygen atoms. Eleven crystallographically independent Ho^{3+} cations can be distinguished, which are seven- (Ho1, Ho9), eight- (Ho2 - Ho5, Ho10), and nine-fold coordinated (Ho6 - Ho8, Ho11) by oxygen atoms.
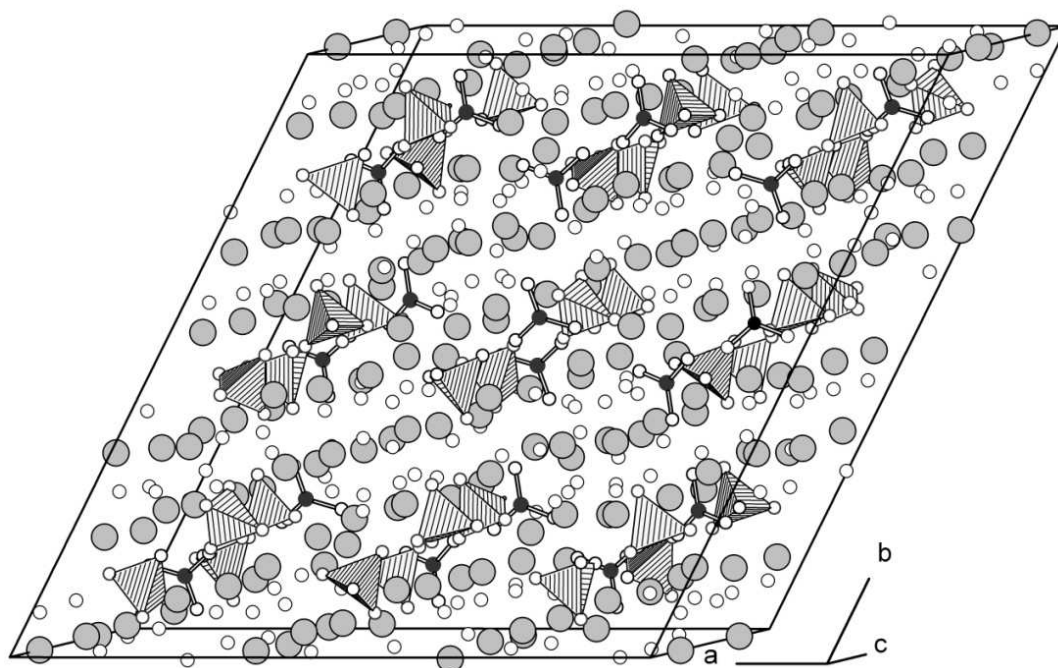
Figure 4-17. Crystal structure of $Ho_{31}O_{27}(BO_3)_3(BO_4)_6$ showing BO_3- and BO_4-units embedded in a complex holmium oxide network.

For a better understanding of the arrangement of the BO_3- and BO_4-units, Figure 4-18 displays only these groups without the holmium ions and oxygen atoms, which are not bonded to boron. In the bottom of Figure 4-18, the unit cell with a view along [001] is shown. In the top area of Figure 4-18, the central area is picked out with a view along [0$\overline{1}$0]. Along the c-direction, a sequence of two BO_4-tetrahedra and one trigonal BO_3-unit can be found, while a corrugated sequence of BO_3-units and BO_4-tetrahedra can be observed along the a-axis. It is noteworthy that all BO_3- and BO_4-groups in the structure of $Ho_{31}O_{27}(BO_3)_3(BO_4)_6$ are isolated, without a linkage among each other.

Screening the literature, several oxoborates with isolated BO_3-groups (*e.g. ludwigite* ($Mg_2FeO_2(BO_3)$ [393]) and a few compounds with isolated BO_4-tetrahedra ((*e.g. sinhalite* ($AlMgBO_4$) [394]) are known. But structures exhibiting both, isolated BO_4-tetrahedra and BO_3-units at the same time are not known so far. From our knowledge, $Ho_{31}O_{27}(BO_3)_3(BO_4)_6$ is the first oxide borate, in which isolated BO_3-groups as well as isolated BO_4-tetrahedra occur in the same structure next to each other.
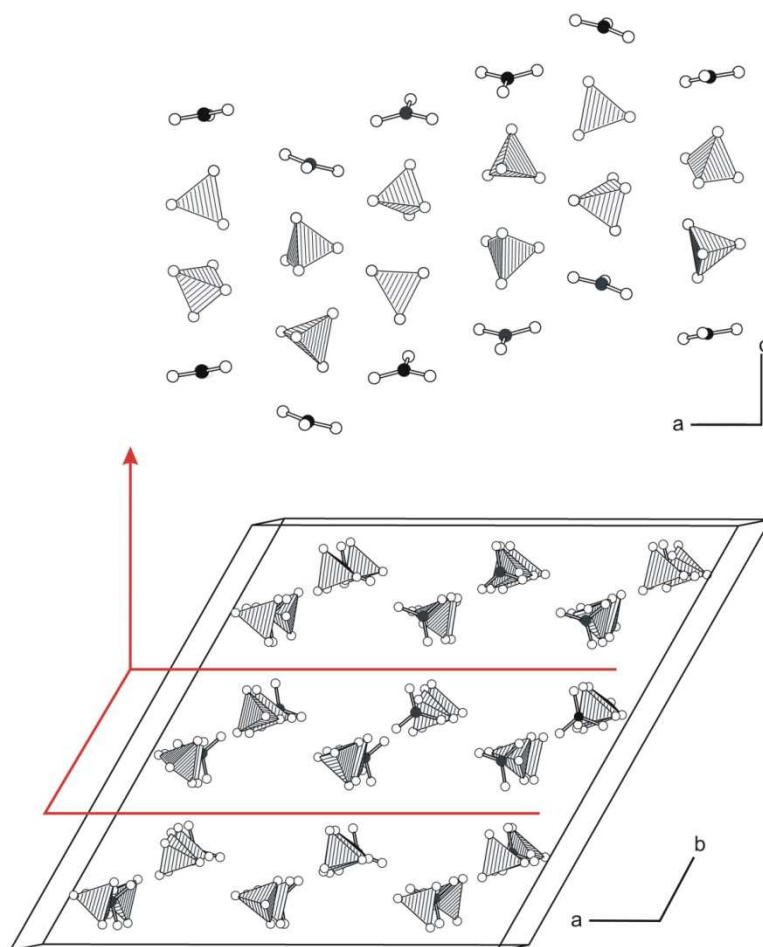
Figure 4-18. Arrangement of the isolated trigonal BO_3-units and BO_4-tetrahedra in the crystal structure of $Ho_{31}O_{27}(BO_3)_3(BO_4)_6$.

The whole structure of $Ho_{31}O_{27}(BO_3)_3(BO_4)_6$ is build-up from the above mentioned Ho-O-polyhedra, which are linked among themselves and additionally *via* the trigonal BO_3- and tetrahedral BO_4-units. The linkage includes corner-, edge-, and face-sharing of the units. Figure 4-19 displays a part of the structure viewing along the *c*-axis, showing the polyhedra of Ho1, Ho2, Ho3, Ho7, and Ho8 and the linkage to the corresponding BO_3-units and BO_4-tetrahedra.
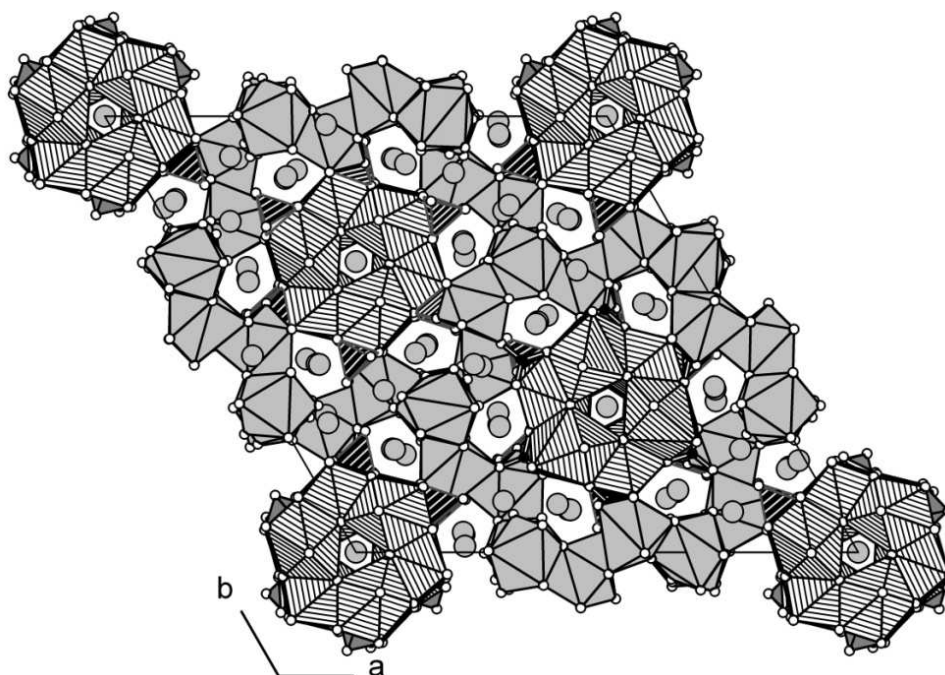
Figure 4-19. Crystal structure of $Ho_{31}O_{27}(BO_3)_3(BO_4)_6$ (view along [00$\bar{1}$] with the coordination polyhedra of Ho1, Ho2, Ho3, Ho7, and Ho8. The BO_4-tetrahedra and BO_3-groups are shown as black tetrahedra and ball-stick model, respectively.

Figure 4-20 displays the structure with the coordination polyhedra of Ho1, Ho4, Ho5, Ho6 Ho10, and Ho11, and their linkage to the BO_3-units and BO_4-tetrahedra. Ho11 (light polyhedra) is surrounded by ring-alike assemblages of Ho1, Ho7, and Ho8.
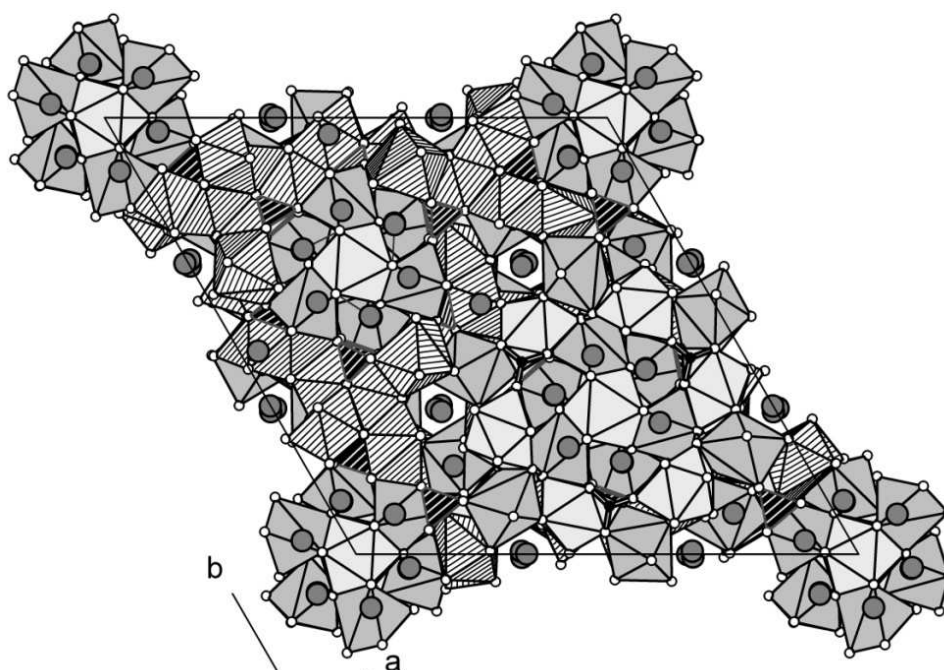
Figure 4-20. Crystal structure of $Ho_{31}O_{27}(BO_3)_3(BO_4)_6$ (view along $[00\bar{1}]$), with the coordination polyhedra of Ho1, Ho4, Ho5, Ho6, Ho9, Ho10, and Ho11.

The average bond distances B-O inside the BO_4-tetrahedra show typical values of 148.7 pm for B1 and 148.6 pm for B2 (Table 4-13). The values stand in good accordance with the ideal bond lengths of 147.6 pm for solitary BO_4-tetrahedra [311]. The nearly planar BO_3-units exhibit an average B3-O bond length of 140.3 pm (Table 4-21), which is slightly longer compared to *e.g.* β-YbBO$_3$ (av. 137.8(4) pm) [340] or β-Gd$_2$B$_4$O$_9$ (av. 137.6(4) pm) [389]. Longer B-O-bonds for trigonal BO_3-units can be found in oxoborates like *tunellite* $SrB_6O_9(OH)_2 \cdot 3\,H_2O$ (av. 151.4 pm) [395], *aristarainite* $Na_2Mg[B_6O_8(OH)_4]_2 \cdot 4\,H_2O$ (av. = 151.7 pm) [396], *aksaite* $MgB_6O_{10} \cdot 5\,H_2O$ (av. = 151.7 pm) [397], B_2O_3-II (av. = 150.8 pm) [306], or ideal values of 150 pm [398]. The average O–B–O angles show ideal values of 109.5° (B1 and B2) for the tetrahedrally coordinated boron atoms and 120.0° in the BO_3-triangles, due to their trigonal planar structure (Table 4-22).

The Ho-O-distances vary between 214.7 and 302.2 pm (Table 4-21), which is in good agreement to the bond lengths found in $Ho_4B_6O_{15}$ (222.4(4)-262.4(4) pm) [382] or $Ho_{8.66}(BO_3)_2(B_2O_5)O_8$ (221.6(6)-286.9(13) pm) [382]. The coordination spheres of the individual Ho^{3+}-cations in $Ho_{31}O_{27}(BO_3)_3(BO_4)_6$ are shown in Figure 4-21. Displaying the three different coordinations of seven- (Ho1, Ho9), eight- (Ho2, Ho3, Ho4, Ho5, Ho10), and nine-fold coordinated Ho-atoms (Ho6, Ho7, Ho8, Ho11).
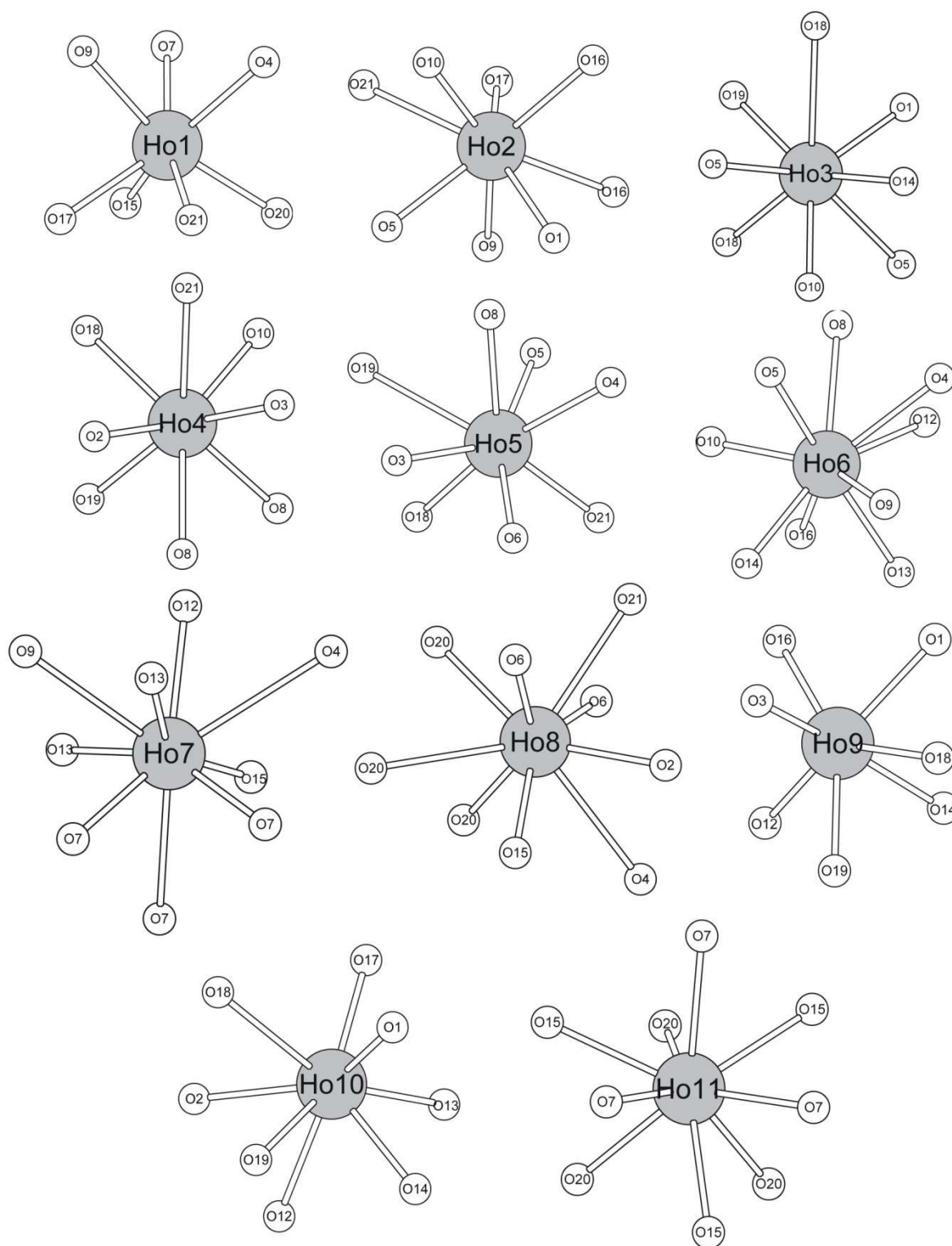
Figure 4-21. Coordination spheres of the Ho-polyhedra in the crystal structure of $Ho_{31}O_{27}(BO_3)_3(BO_4)_6$.

4.3.3.1   Placement of $Ho_{31}O_{27}(BO_3)_3(BO_4)_6$ in the Crystal Chemistry of Oxoborates

Up to date, the compound $Ho_{31}O_{27}(BO_3)_3(BO_4)_6$ represents the rare-earth richest rare-earth oxide borate exhibiting exclusively isolated BO_3- and BO_4-groups next to each other.

On the strengths of our past experiences, the exclusive occurrence of BO_4-tetrahedra for a compound, which was synthesized under extreme pressure conditions of 11.5 GPa, would be expected. Nevertheless, $Ho_{31}O_{27}(BO_3)_3(BO_4)_6$ exhibits trigonal planar coordinated boron atoms, which are exceptional for a material synthesized under these conditons.

In the past, all oxoborate compounds synthesized at pressures exceeding 8 GPa revealed exclusively BO_4-tetrahedra. This behavior is expected and accepted for oxoborates in agreement with the pressure coordination rule [399]. In a few cases, the formation of edge-sharing BO_4-tetrahedra was observed as a new structural motif for oxoborates under high-pressure conditions (*e.g.* HP-NiB_2O_4 [318] or β-FeB_2O_4 [321]) beside $RE_4B_6O_{15}$ (*RE* = Dy, Ho) [77,78] and α-$RE_2B_4O_9$ (*RE* = Eu, Gd, Tb, Dy) [386]).

All the more it is astonishing that the BO_3-group is stable in the structure of $Ho_{31}O_{27}(BO_3)_3(BO_4)_6$, especially in the plethora of oxygen atoms.

4.3.3.2   IR Spectroscopy of $Ho_{31}O_{27}(BO_3)_3(BO_4)_6$

The FTIR spectra of $Ho_{31}O_{27}(BO_3)_3(BO_4)_6$ was recorded on a Spektrum BX II FTIR-spectrometer (Perkin Elmer, USA) equipped with a Dura sampler diamond-ATR, scanning in the range from 650 to 4500 cm^{-1}. The measurement was conducted at room temperature. The sample was dried before measurement, and thoroughly ground. In Figure 4-22 the spectral region in the range from 2700 to 650 cm^{-1} is shown.

Analyzing the spectra, absorptions between 1100 and 800 cm^{-1} are characteristical for tetrahedral BO_4-groups as compared to borates like β-$RE(BO_2)_3$ (*RE* = Dy - Lu) [376] or π-REBO_3 (*RE* = Y, Gd) [332,400] or π-REBO_3 (*RE* = Y, Gd) [400,401], which possess exclusively BO_4-tetrahedra. Typical absorptions for triangular BO_3-groups appear at about 1500 and 1200 cm^{-1}, and below 790 cm^{-1} as found in $LaBO_3$ [342,402] or χ-REBO_3 (*RE* = Dy, Er) [352,353].
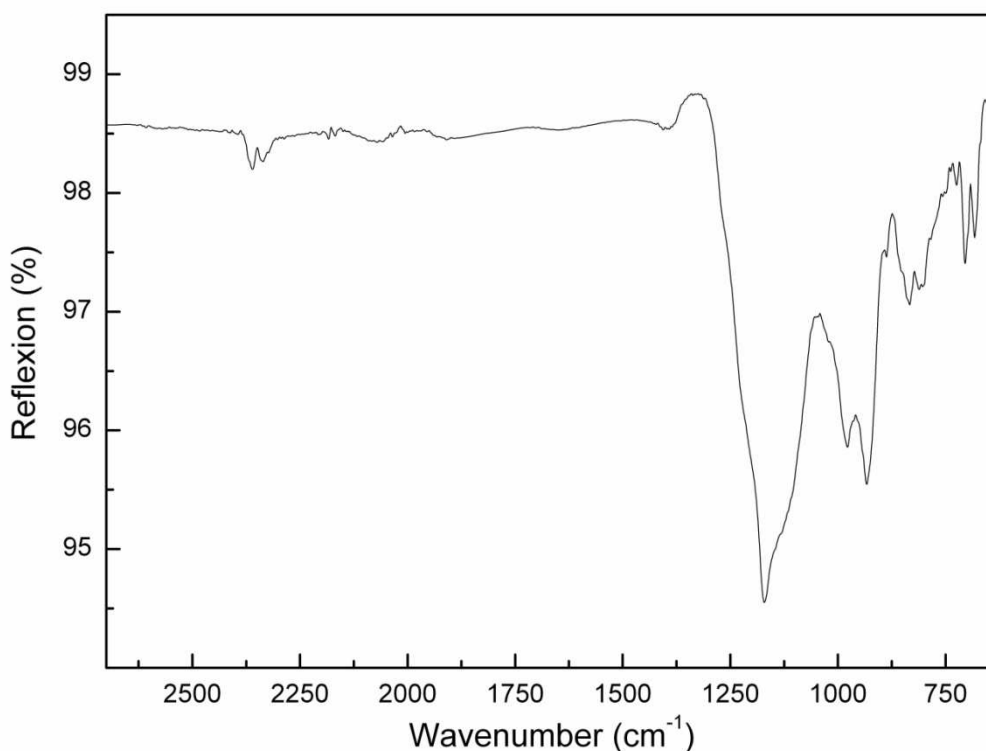
Figure 4-22. IR spectrum of $Ho_{31}O_{27}(BO_3)_3(BO_4)_6$.

For the IR-measurements powdered samples were applied. For more accurate measurements in particular, more investigations on it will follow in the near future.

4.3.3.3   Thermal Behavior of $Ho_{31}O_{27}(BO_3)_3(BO_4)_6$

The thermal stability of the oxide borate $Ho_{31}O_{27}(BO_3)_3(BO_4)_6$ was examined *via* an *in-situ* temperature-programmed X-ray powder diffraction experiment performed in air. Therefore, a Stoe Stadi P powder diffractometer (Mo$K_{\alpha 1}$; $\lambda = 71.073$ pm) with a computer controlled Stoe furnace was used. The sample was enclosed in a silica glass capillary (Hilgenberg, Germany, $\varnothing_{ext.}$ 0.3 mm) and heated up from room temperature to 1100 °C in steps of 50 °C. In the following, the sample was cooled down to 500 °C in steps of 50 °C and further on in steps of 100 °C down to room temperature. Figure 4-23 shows the investigated sample consisting of $Ho_{31}O_{27}(BO_3)_3(BO_4)_6$ besides a small fraction of the high-pressure modification of holmium oxide B-Ho_2O_3 (monoclinic). The latter derived from the transformation of the cubic starting material C-Ho_2O_3 under the applied conditions of 11.5 GPa. The high-temperature powder patterns revealed a temperature stability of the oxide borate $Ho_{31}O_{27}(BO_3)_3(BO_4)_6$ up to a temperature of 700 °C (Figure 4-23). The elevation of the temperature up to 950 °C led to a

complete decomposition of $Ho_{31}O_{27}(BO_3)_3(BO_4)_6$ while the reflections of monoclinic B-Ho_2O_3 also disappeared. The latter transformed *via* an amorphous transition state into cubic C-Ho_2O_3 which crystallized at 1000 °C. Therewith, the high-pressure modification monoclinic B-Ho_2O_3 was retransformed to the cubic normal-pressure modification *via* heating, which is in accordance to the results obtained from Hoekstra *et al.* [267]. At 1050 °C, additional reflections of μ-$HoBO_3$ (high-temperature modification of $HoBO_3$) emerged. It is likely that it resulted from a reaction of C-Ho_2O_3 with the boron-containing decomposition products of $Ho_{31}O_{27}(BO_3)_3(BO_4)_6$. The reflection at 21.3° refers to the Stoe furnace.
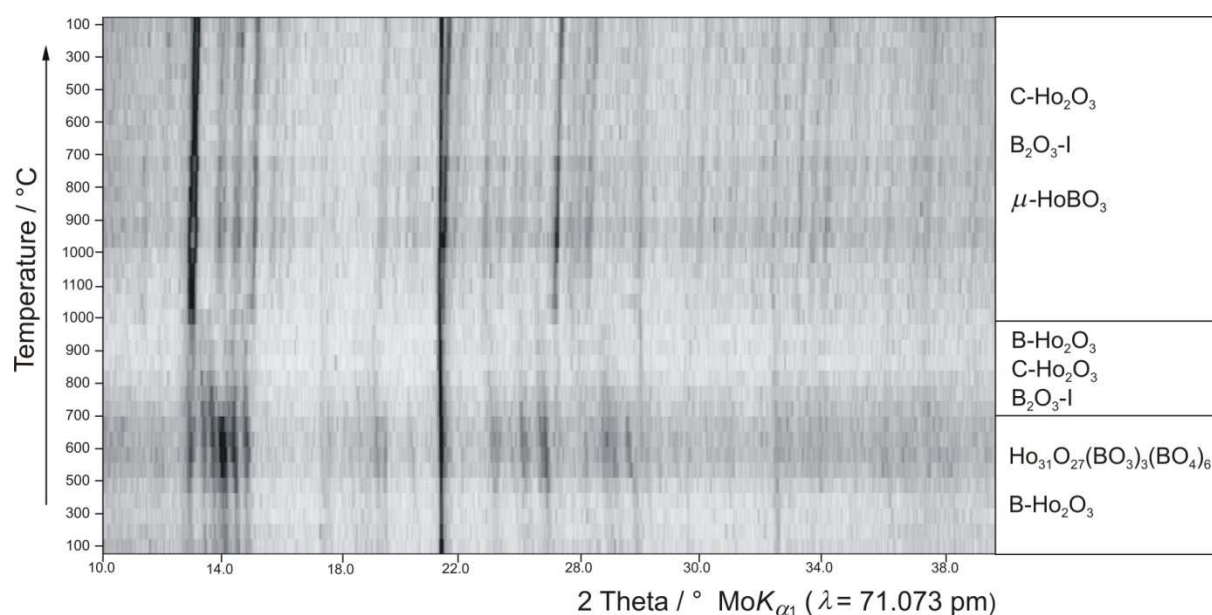
Figure 4-23. High-temperature X-ray powder diffraction pattern of $Ho_{31}O_{27}(BO_3)_3(BO_4)_6$.

4.3.3.4   Theoretical Calculations for $Ho_{31}O_{27}(BO_3)_3(BO_4)_6$

The calculation of the charge distribution of the atoms in $Ho_{31}O_{27}(BO_3)_3(BO_4)_6$ *via* bond valence sums by the bond-length bond-strength-concept (ΣV) [186-189] and with the CHARDI concept (Charge Distribution in Solids) (ΣQ) [190,191] confirmed the formal valence states in the oxide borate. For the calculation, bond-valence parameters of $R_{ij} = 137.1$ for the B-O bonds and $R_{ij} = 202.3$ for Ho-O bonds were applied [306]. The calculated results in Table 4-23 show that the values for holmium and boron are in good accordance with the expected values from the literature. The calculations of the bond valence sums for the oxygen atoms are in the expected range, except the values for O(5) and O(17): Those values O(5) = 1.67 and O(17) = 1.62 differ from the expected contribution of -2.

Table 4-23. Charge distribution in $Ho_{31}O_{27}(BO_3)_3(BO_4)_6$, calculated with the Bond-Length / Bond-Strength concept (ΣV) [186-189] and the CHARDI concept (ΣQ) [190,191]. (Ho-O, $s = \exp[(2.023 - d_i)/0.37]$; B-O, $s = \exp[(1.371 - d_i)/0.37]$)

	Ho1	Ho2	Ho3	Ho4	Ho5	Ho6	Ho7	Ho8	Ho9	Ho10	Ho11
ΣV	3.18	2.86	2.72	3.33	2.98	2.94	3.04	3.23	3.03	2.74	2.49
ΣQ	3.09	2.90	2.93	2.94	3.40	3.00	2.92	2.97	2.82	2.79	2.98

	B1	B2	B3
ΣV	2.93	2.93	2.75
ΣQ	3.15	3.07	3.03

	O1	O2	O3	O4	O5	O6	O7	O8	O9	O10
ΣV	-2.23	-2.18	-2.19	-1.92	-1.67	-2.03	-1.97	-1.85	-2.06	-2.43
ΣQ	-2.42	-2.26	-2.25	-1.76	-1.70	-2.07	-2.06	-1.77	-2.09	-2.46

	O11	O12	O13	O14	O15	O16	O17	O18	O19	O20
ΣV	-1.88	-1.92	-1.97	-2.19	-1.94	-1.87	-1.64	-2.26	-1.83	-2.12
ΣQ	-1.90	-1.90	-2.11	-2.28	-1.95	-1.95	-1.42	-2.25	-1.78	-1.63

The calculation of the Madelung part of the lattice energy (MAPLE) [183-185] for $Ho_{31}O_{27}(BO_3)_3(BO_4)_6$ allowed to compare the results with the corresponding MAPLE calculations starting from the binary educts C-Ho_2O_3 (cubic) [403] and the high-pressure modification of boron oxide B_2O_3-II (orthorhombic) [306]. The additive potential of the MAPLE values allows to calculate hypothetical values for the compound $Ho_{31}O_{27}(BO_3)_3(BO_4)_6$ starting from the educts holmium oxide and boron oxide.

The calculations for $Ho_{31}O_{27}(BO_3)_3(BO_4)_6$ resulted in a value of 333313 kJ/mol compared to 335495 kJ/mol [$15.5 \times$ C-Ho_2O_3 (15276 kJ/mol) + $4.5 \times B_2O_3$-II (21938 kJ/mol)] (deviation 0.65 %) derived from the binary oxides. The MAPLE value calculated for the starting materials monoclinic B-Ho_2O_3 and B_2O_3-II [$15.5 \times$ B-Ho_2O_3 (15133 kJ/mol) + $4.5 \times B_2O_3$-II (21938 kJ/mol)] results to 333291 kJ/mol (deviation 0.01 %).

4.3.4 Conclusion

The first reaction leading to the new holmium oxide borate $Ho_{31}O_{27}(BO_3)_3(BO_4)_6$ started from C-Ho_2O_3 and a mixture of BN with B_2O_3, contaminated with H_3BO_3. The primary question for the formation tendency was the dependence on the phase transformation of the cubic C-Ho_2O_3 into the metastable high-pressure modification B-Ho_2O_3.

Under the high-pressure and high-temperature reaction conditions of 7.5-11.5 GPa and 1200 °C, the C-type modification of holmium oxide normally transforms into the B-type modification. Therewith, the reactivity of the holmium oxide is remarkably increased under these conditions and wherefore it could initiate and support the formation of the holmium oxide borate $Ho_{31}O_{27}(BO_3)_3(BO_4)_6$.

In case of holmium, the foregoing phase transformation enabled the formation of the compound, while the formation was not observed for RE = La, Dy, Er, Tm. It is therefore likely that the key to analogue rare-earth oxide borates could probably lie in the transformation of C-RE_2O_3 to monoclinic B-type rare-earth oxides.

High-pressure research offers new access to diverse new compounds, such as borates, gallates, oxides, or nitrides. In the following chapter, examples are given when the parameter pressure enhanced crystallisation. It is often seen in the field of borates, but was also used to stabilize metastable compounds in adversion to more stable educts. Systematic investigations on the ideal conditions leading to gallium oxonitride compounds are given in the following.

4.4 Gallium Oxonitrides

4.4.1 Introduction

Investigations on ternary crystalline phases of gallium oxonitrides derived from GaN and Ga_2O_3 have intensified in the last years, as the importance of gallium nitride based electroluminescent materials has increased. The research on Ga-O-N phases is also motivated by promising interesting properties for industrial purposes, such as temperature stability, high hardness, and optical transparency as already observed in the corresponding Al_2O_3-AlN system.

With the first investigations on aluminium oxonitrides in the early 1970s, research arose around the globe. When realising that the addition of nitrogen to aluminium oxide leads to new spinel-type compounds, the door to a new synthesis field was opened. These investigations resulted in the Al_2O_3-AlN phase diagram and supported the synthesis of AlON-ceramic material. Up to date, ALON™ materials are applied due to their interesting properties of transparency and hardness [404] for military equipment such as aircraft lenses, missile domes, or transparent armors, but also for appliances on infrared spectroscopy, scanner, or laser windows beside applications for semi-conductor processings. The synthetic access to AlON materials and ceramics was closely examined. First syntheses of AlON-ceramics started from Al_2O_3-AlN mixtures applied in sintering processes by McCauley *et al*. [405]. Other routes used pressure-less sintering, hot pressing, or hot isostatic pressing (HIP) of AlON powders [406-408].

Although AlON materials are well investigated, only little is known about the corresponding Ga-O-N system. Now the scientific focus lies on it [409-414], highly motivated by expected properties found in AlON materials.

In 1976, first results in the Ga-O-N system were achieved by Verdier and Marchand by chance. A phase with the composition $Ga_{1-x/3}\square_{x/3}N_{1-x}O_x$ with x ~ 0.1 ($\square$ = cation vacancy) was obtained as a side product, derived by reactions of ammonia on gallium oxide surfaces at low temperatures [415]. A few years later, in 1979, Grekov and Demidov attempted the first synthesis with the aim to obtain gallium oxonitride phases [416] *via* pyrolytic splitting of a $GaCl_3 \cdot NH_3$ complex leading to amorphous films with variable nitrogen / oxygen ratios.

In the next years, several publications and patents on gallium oxonitrides followed by Shiota and Nishizawa, comprising passivation films and insulating layers [417-419].

Research on GaON-materials continued, although neither the crystal structure nor the phases of the gallium oxonitride layers could be clearly defined. With growing interest in oxonitrides, the usefulness and effectiveness of crystalline gallium oxonitrides as optical and electrical material was noticed. Besides that, the role of manufacturing of these compounds was also well-examined.

In the 1990s, efforts and synthetic approaches towards gallium oxonitrides were undertaken by several research groups. As results led to interesting patents on technical applications for crystalline compounds, the knowledge for new phases was provided [420-424]. Analytical investigations of the formation of GaO_xN_y compounds were not only approached by Schmitz *et al.* [425]. The formation of GaO_xN_y on CaGa (001) layers was investigated by means of different spectroscopic methods. The adsorption of NO on the CaGa layers led to amorphous GaO_xN_y films, confirmed by LEED (Low Energy Electron Diffraction). The measurement of the atomic ratio nitrogen to oxygen in the compound was estimated to N/O ≈ 2/1. The determination of the bandgap resulted in a value of 4.1 ± 0.2 eV, showing that it lies in between β-Ga_2O_3 (4.5 eV) and GaN (3.5 eV).

Structural and electronic properties of a gallium oxonitride compound with an ideal composition of Ga_3O_3N and a lattice parameter of 822.8 pm were investigated by Lowther *et al.* [426]. The calculations of the direct bandgap resulted in a value of 2.16 eV. Experiments of Puchinger *et al.* confirmed the theoretical results with experiments, when synthesizing a cubic spinel structured gallium oxonitride phase with the composition $Ga_{2.8}O_{3.5}N_{0.5}$, derived as thin films, exhibiting a lattice parameter of 820 pm [427]. Small gallium oxonitride spots were obtained as an impurity in surface areas on a thin film of GaN, starting from a gallium dimethylamide-based liquid precursor obtained by chemical solution deposition (CSD) *via* pyrolysis in ammonia atmosphere. The nanocrystalline grain layers were formed at temperatures of 600-700 °C and characterized *via* HRTEM-SAED (High-Resolution Transmission Electron Microscopy - Selected Area Electron Diffraction) coupled with EEL (Electron Energy Loss) and Auger spectroscopy. The cubic structure of the phase was confirmed while exhibiting a lattice parameter of $a_0 = 820.0(7)$ pm and a composition of $Ga_{2.8}O_{3.5}N_{0.5}$.

On the basis of these results, new synthetic approaches were made. Though, only a nitrogen doped oxide material was known, Kinski *et al.* gained access to precursor-derived gallium oxonitride compounds [428]. New precursor-routes were approached, by providing a

dimethylamine adduct of gallium tris-(t-butoxide), $Ga(O^tBu)_3 \cdot HNMe_2$, which was used as molecular precursor. The gallium (t-butoxide) dimethylamine adduct possessed gallium simultaneously bonded to nitrogen and oxygen, and was applied as a molecular single source precursor in high-pressure / high-temperature experiments. Treated under ammonia atmosphere at elevated temperatures, it finally transformed to a nanocrystalline oxonitride compound. Characterising the resulting ceramic *via* X-ray powder diffraction pattern and TEM (Transmission Electron Microscope) investigations, confirmed the formation of nanocrystalline particles. The remaining carbon found in the sample was stated to be 1.8 wt%, while FTIR spectroscopy (Fourier Transformed Infrared Spectroscopy) showed no evidence for hydrogen bonds in the compound. These new results were the basis for an improved synthesis, and eventually led to quite different synthesis routes which resulted both in crystalline $Ga_xO_yN_z$ compounds.

Crystalline gallium oxonitrides were published in 2005 for the first time, by Soignard *et al.* in London and Kinski *et al.* in Darmstadt. Both groups obtained well-characterized crystalline gallium oxonitride phases [429,430] under high-pressure / high-temperature conditions. While Soignard *et al.* used a mixture of α/β-Ga_2O_3 and w-GaN in a molar ratio of 1 : 1, Kinski *et al.* applied an advanced nanocrystalline gallium oxonitride ceramic, obtained from a pyrolysis process of a dimethylamide based precursor [428], with a mean N/O-ratio of 0.86 as starting material.

Soignard *et al.* performed multianvil and DAC (Diamond Anvil Cell) experiments applying high-pressure / high-temperature conditions of 5 GPa and temperatures around 1500-1700 °C and using 1 : 1 mixtures of α/β-Ga_2O_3 and w-GaN in welded Pt capsules [430]. The structure of the gallium oxonitride compound was refined on the basis of Rietveld analysis on X-ray powder diffraction data revealing a cubic, slightly distorted spinel structure with a lattice parameter of $a_0 = 828.1(2)$ pm. The distortion of the polyhedra is caused by anion (O/N) disordering. Due to broad bands in the Raman spectra, the substantial disorder on the O and N site, as well as vacancies on octahedrally coordinated Ga sites were confirmed, which led to the experimental composition of $Ga_{2.8}O_{3.24}N_{0.64}$. In addition to that, electron probe microanalysis of the sample estimated the mean N/O-ratio in the sample to 0.20(1). Furthermore, optical properties were examined. Excitation of the sample with laser light of $\lambda = 325$ nm resulted in a photoluminescence between 400 and 750 nm.

Theoretical calculations showed that the formation of the sample is endothermic at ambient pressure and low temperatures and therefore confirmed the experimental high-pressure / high-temperature conditions for a successful synthesis.

The gallium oxonitride compound obtained by Kinski *et al.* was synthesized in a multianvil high-pressure / high-temperature experiment under conditions of 7 GPa and 1100 °C [429]. As starting material a prestructured gallium oxonitride ceramic was applied, derived from a single-source molecular precursor $[Ga(O^tBu)_2NMe_2]_2$ with a mean N/O-ratio of 0.86 [428,429]. The synthesis yielded a highly crystalline sample with wurtzite-structured gallium nitride and γ-Mo_2N obtained as by-products, which indicates a nitrogen loss during the high-pressure experiment. Rietveld refinement of X-ray powder diffraction data confirmed the cubic structure, exhibiting a lattice parameter of $a_0 = 826.4(1)$ pm. Furthermore, TEM coupled with an electron energy loss spectrometer (EELS) and energy dispersive X-ray spectrometer (EDX) was used to analyze the sample. TEM analysis showed high crystallinity of the whole oxonitride sample, while EEL-spectra allowed the quantification of the N/O-ratio to a mean value of 0.12(2). The cubic face-centered cell was indicated by a SAED pattern with extinctions leading to the space group $Fd\overline{3}m$ (no. 227), confirming the spinel structure of the compound.

The exact stoichiometric composition was estimated in accordance to McCauleys constant anion model (developed for AlONs) [431]. An ideal spinel structure requires 24 cation sites beside 32 anion sites. For maintaining charge balance, the anions are fully occupied, while the cation positions exhibit vacancies. Based on this model, the general formula resulted to a composition of $Ga_{2.81}O_{3.57}N_{0.43}$.

Besides the attempts to synthesize crystalline material, powders were also of general interest. For the first time, thick GaON-films were accessible *via* thermal nitridation of a gallium oxide precursor in the composition of $NiGa_2O_4$, under ammonia atmosphere, prepared by complexation-calcination processes (citrate method) [432]. These powders offer interesting applications as stable sensor material, based on their high sensitivity on ethanol.

In addition to the experimental work on that field, the formation of spinel-type gallium oxonitrides was theoretically investigated by Kroll *et al.* [433]. DFT calculations were performed concerning the structure formation from the binary end-members w-GaN and β-Ga_2O_3 as well as the relative stability of the product and educts. The ideal cubic spinel would exhibit the composition Ga_3O_3N (γ-galon), (Ga_2O_3 : GaN = 1 : 1). Being consistent with the constant anion model, defective spinels with vacancies on the cation sites, containing 36 mol% and 17 mol% GaN, were also investigated.

The calculations confirmed defective structures for ternary oxonitrides with vacancies only on the cation sites in accordance with the constant anion model. Additionally, a strong dependence on the GaN content was found, affecting both, lattice parameters and the

bandgaps. Interestingly, the formation enthalpy indicated that difficulties in the synthesis of gallium oxonitrides at normal pressure conditions depend strongly on the low energy of the ground state structure of monoclinic β-Ga_2O_3. Therefore, the maximal driving force to the formation of gallium oxonitrides corresponds with the $\beta \rightarrow \alpha$-transition.

On the basis of the first results for gallium oxide, nitride, and oxonitrides, the formation of spinel-type compounds was investigated, depending on the parameter pressure [434]. Starting from the end-members β-Ga_2O_3 and w-GaN, the formation of ideal Ga_3O_3N compounds (50 mol% w-GaN) and its defective variants, comprising 36 mol% and 17 mol% w-GaN in the structure, were stated to transform at pressures of 2.6 or 6 GPa, which is in good accordance with the results of Kinski *et al*. [429] and Soignard *et al*. [430]. The variation of the results depends on the treatment of the corresponding *d* electrons of gallium (as core or valence electrons). Furthermore, site occupancies in defective structures were also examined. Based on energetic differences, the tetrahedral coordinated gallium positions were energetically favored compared to octahedral sites. Therefore, defects should appear only on octahedral sites.

On the basis of these results, high-pressure / high-temperature approaches into the field of gallium oxonitrides were taken. Experiments concerning formation tendency were performed under the required high-pressure and high-temperature conditions to improve the crystallinity of the gallium oxonitride compounds.

The work on gallium oxonitrides was performed as part of a cooperation project with I. Kinski, *Fraunhofer-Institut für Keramische Technologien und Systeme*, Dresden, C. E. Zvoriste and R. Riedel, *Institut für Material- und Geowissenschaften, Technische Universität*, Darmstadt. This project was funded by the Deutsche Forschungsgemeinschaft (HU 966 / 5-1 and KI 838 / 3-1).

4.4.2 Starting Materials

As end members, hexagonal gallium nitride w-GaN and monoclinic gallium oxide β-Ga_2O_3 were applied in different molar ratios. Starting from mixtures in the molar ratio of 9 : 1 of w-GaN (99.9%, Alfa Aesar, Karlsruhe, Germany) mixed with β-Ga_2O_3 (99.9+%, Sigma Aldrich, Munich, Germany).

4.4.2.1   Gallium Oxide

For the systematic investigations on gallium oxonitrides, monoclinic gallium sesquioxide (β-Ga_2O_3) was applied as a starting material.

Gallium oxide exists in five different modifications. The monoclinic form β-Ga_2O_3 (space group $C2/m$, no. 12, $a = 1223$, $b = 304$, $c = 580$ pm, $Z = 4$) represents the thermodynamically stable ambient-pressure modification [241]. The crystal structure (Figure 4-24) contains two crystallographically different Ga-sites: Ga1, which is tetrahedrally coordinated by oxygen atoms and Ga2, which is octahedrally coordinated [435].
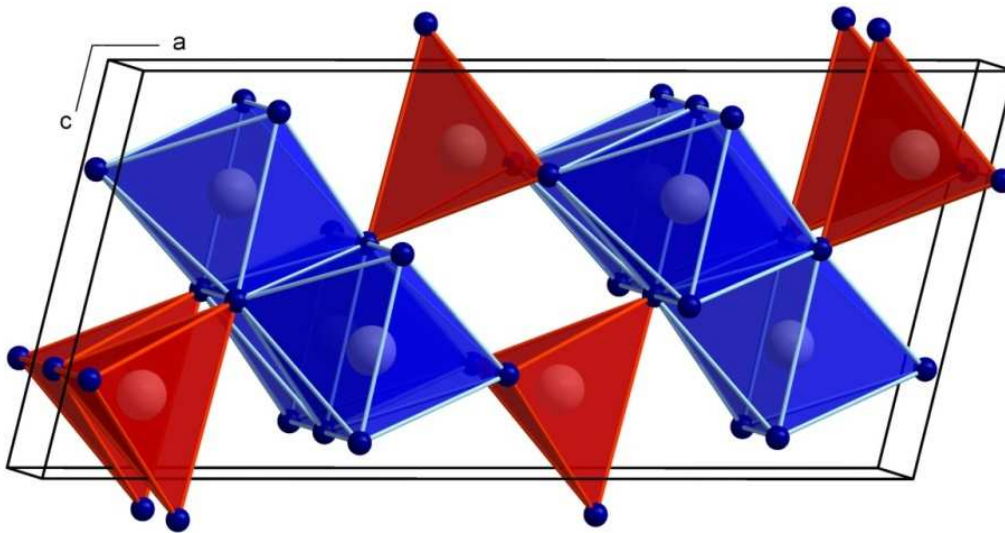
Figure 4-24. Crystal structure of monoclinic β-Ga_2O_3 ($C2/m$, no. 12), view along [0$\bar{1}$0].

The high-pressure modification of α-Ga_2O_3 can be obtained *via* high-pressure conditions applied to β-Ga_2O_3. In contrast to the β-Ga_2O_3 modification, the crystal structure of α-Ga_2O_3, consists only of GaO_6-octahedra. Figure 4-25 displays the structure [238]. The first syntheses of rhombohedral α-Ga_2O_3 (space group $R\bar{3}c$, no.167, $a = 498.25(5)$, $c = 1343.3(1)$ pm, $Z = 6$) were reported by Goldschmid *et al.* [242] and Zachariasen *et al.* [436] at ambient pressure. Foster *et al.* prepared α-Ga_2O_3 by heating up the monohydrate $Ga_2O_3 \cdot H_2O$ up to 400 °C in air [437]. Applying high-pressure / high-temperature conditions of 4.4 GPa and 1000 °C to β-Ga_2O_3, a phase transformation into the high-pressure corundum-type modification α-Ga_2O_3 occurs [238,438].

Additional results from Machon *et al.* proved that a phase transformation of β-Ga_2O_3 to α-Ga_2O_3 can be induced by applying high-pressure conditions of 20-22 GPa [439]. Interestingly,

different results show that the transformation of β-Ga_2O_3 to α-Ga_2O_3 takes already place at 19.2 GPa, when compressed without heating. Investigations in DAC-experiments led to transformed Ga_2O_3 under high-pressure / high-temperature conditions of 30 GPa and 1730 °C [440].

However, the phase stability of α-Ga_2O_3 was predicted to be in the range of 6.5 / 7 - 40 GPa [441]. Theoretical calculations of Kroll *et al*. [442] showed that a phase transformation starting from the β-modification of Ga_2O_3 to the high-pressure modification α-Ga_2O_3 might occur already at low pressures of 2.6 - 6 GPa, depending on the *d*-electron handling for the calculation.
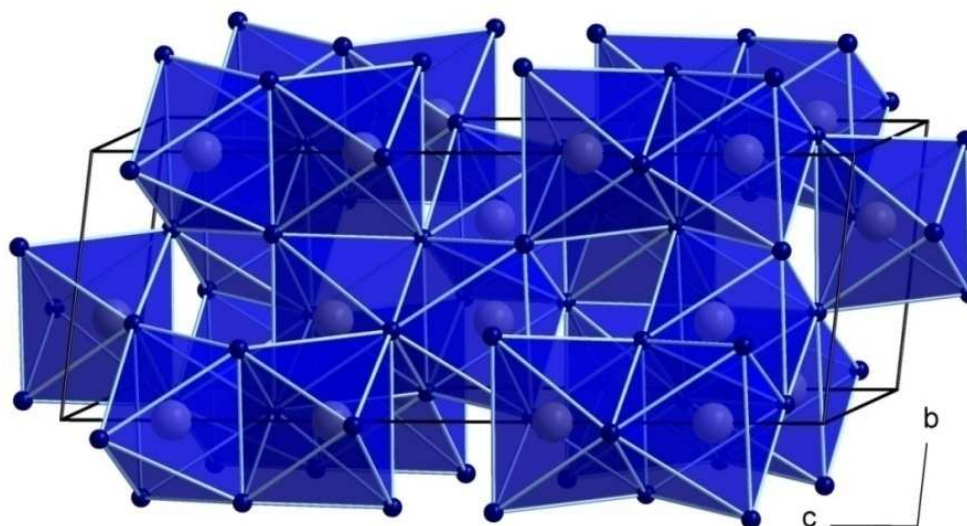
Figure 4-25. Crystal structure of α-Ga_2O_3 ($R\bar{3}c$, no.167), view along [$\bar{1}$00].

Apart from α-Ga_2O_3, other metastable modifications of gallium oxide exist. One of them is the metastable cubic spinel-type compound γ-Ga_2O_3 [443], which has a structure analogue to γ-Al_2O_3. It can be obtained by heating up gallia gels [444]. Starting from metallic Ga and nitric acid, another modification, δ-Ga_2O_3, occurs. The compound can be synthesized *via* gallium nitrate as an intermediate state and exhibits an identical structure to the cubic type C rare-earth oxides [chapter 4.1.1]. The following thermal decomposition of the nitrate leads directly to pure δ-Ga_2O_3 [445]. The last known metastable modification is ε-Ga_2O_3. The structure of ε-Ga_2O_3 is related to the structure of monoclinic β-Ga_2O_3 [445], and can be obtained by heating δ-Ga_2O_3 above 500 °C.

Besides its importance for different synthesis and transformation processes, it plays a significant role in technical applications, *e.g.* in laser facilities, due to its interesting middle bandgap or as active material for lithium ion batteries [446].

Therefore, another interesting aspect of gallium oxide relies on its conductive behavior. This property was found by Nagarajan *et al.* [447]. Non-stoichiometric amorphous $GaO_{1.2}$ on Al_2O_3-layers showed an enormous increase in conductivity when heated up to 390 °C. The driving force is a spontaneously activated crystallization of stoichiometrically correct β-Ga_2O_3 reducing the bandgap until its complete closure. This effect might provide a technical application for a permanent storage of data.

4.4.2.2   Gallium Nitride

Wurtzite-type gallium nitride, counted as a member of the III-V semiconductors, is well known for its applications in optical and electronic devices such as detectors, solid state laser facilities, or laser diodes, or due to its high potential for blue and white energy saving LEDs (light-emitting diode) [448-451]. The wide direct electronic bandgap, computed on the basis of the atomic potentials of Herman and Skillman of 3.50 eV at the Γ point [452-454], the low dielectric constants, and the strong bonding (ionic and covalent) allow applications for opto- and microelectronic devices, besides an amazing temperature resistance [455-458].

There are two different modifications known, the hexagonal wurtzite structured w-GaN and the cubic rocksalt-type gallium nitride [459,460].

The ambient pressure modification of gallium nitride, the wurtzite-type structure, crystallizes hexagonally, and can be related to the structure of hexagonal diamond. A structural shift in the ambient pressure modification of gallium nitride (space group $P6_3mc$ (no. 186), $a = 319.0$ pm, $c = 518.9$ pm, Z = 2) can be initiated by applying high pressure. Powders of w-GaN can be prepared by heating up gallium(III)nitrate salts in a constant ammonium flow at temperatures of 500 up to 1050 °C [461], or *via* reaction of metallic gallium with ammonia at 1200 °C [462].

The cubic high-pressure modification (rocksalt-structure, space group $F\bar{4}3m$ (no. 216), $a = 450.0$ pm, Z = 4) was examined with the help of computational ab initio calculations on the basis of GGA and LDA methods [463]. First results predicted that a phase transition from wurtzite to rocksalt structure would take place at pressures around 87 GPa [464], as later on, these results were corrected to lower pressures of 47 GPa [465]. The stability of gallium nitride was investigated up to a pressure of 60 GPa. Experiments showed a phase transformation of gallium nitride at 47 GPa, which was confirmed by Raman scattering and X-ray absorption spectroscopy [466]. Further experimental data collected by DAC experiments proved that the reversible structural transformation into the cubic sixfold-

coordinated rocksalt-structure starts at a pressure of 37 GPa. According to the authors, the rocksalt structure is stable up to a pressure of 70 GPa [454].

4.4.3   A Single Crystal of $Ga_xO_yN_z$

4.4.3.1   Introduction

As crystalline gallium oxonitride phases were the central question in this thesis, the examination of the formation of the spinel-type compound was performed under high-pressure / high-temperature conditions.

On the basis of the results on gallium oxonitrides from the literature, high-pressure / high-temperature experiments were arranged, starting from w-GaN and β-Ga_2O_3. Kinski *et al*. [429] and Soignard *et al*. [430] obtained both crystalline spinel-type oxonitrides and confirmed the structure by powder investigations (Rietveld refinement) as the determination of the crystal structure by single crystal data was not possible. Due to their low degree in crystallinity, the current research on crystalline phases continued.

Taking into account the theoretical results of Kroll *et al*. [433], experimental work was performed under high-pressure / high-temperature conditions, investigating the formation of crystalline gallium oxonitrides. In this work, single crystals of a spinel-type gallium oxonitride of sufficient size for collecting single crystal data could be synthesized in a high-pressure / high-temperature synthesis, starting from w-GaN and β-Ga_2O_3 in the molar ratio of 9 : 1 at 5 GPa and 1250 °C for the first time. Furthermore, the crystal structure of the spinel-type gallium oxonitride could be refined in a reasonable way, based on the determination of the mean ratio of nitrogen to oxygen N/O in the compound *via* EELS-analysis.

4.4.3.2   Synthesis of $Ga_{2.79}\square_{0.21}(O_{3.05}N_{0.76}\square_{0.19})$

For the synthesis of the crystalline spinel-type gallium oxonitrides, a mixture of hexagonal w-gallium nitride and monoclinic β-Ga_2O_3 was closely mixed together and finally filled into a hexagonal boron nitride crucible (Henze BNP GmbH, HeBoSint® S10, Kempten, Germany). The boron nitride crucible was positioned inside the center of an 18/11-assembly, which was compressed by eight tungsten carbide cubes (TSM-10 Ceratizit, Reutte, Austria). The conditions of the high-pressure / high-temperature synthesis leading to the formation of the crystalline spinel sample were a pressure of 5 GPa at a temperature of 1250 °C starting from w-gallium nitride and β-gallium oxide in a molar ratio of 9 : 1.

The assembly was compressed up to 5 GPa within 2 h, using a multianvil device, based on a Walker-type module and a 1000 t press (both devices from the company Voggenreiter, Mainleus, Germany). A detailed description of the preparation of the assembly can be found in the chapters 2.1.1 - 2.1.1, or references [103,104,111].

The sample was heated electrically with a cylindrical graphite furnace up to 1250 °C within 10 min. The temperature was kept constant for 15 min, and cooled slowly down to 850 °C with in 25 min at constant pressure. Afterwards, the sample was quenched to room temperature by switching off the resistance heating, followed by a decompression period of 6 h.
After the experiment, the cube was removed from the module, and the sample secured for analytical characterization. The sample was mechanically separated from the surrounding boron nitride of the crucible, and prepared for further analysis.

4.4.3.3   Spectroscopic and Transmission Electron Microscope Investigations on $Ga_{2.79}\square_{0.21}(O_{3.05}N_{0.76}\square_{0.19})$

The content of the gallium oxonitride was determined with different analytical methods. The qualitative content of the sample was investigated with EDX. The result of an energy dispersive X-ray spectroscopic investigation (Jeol JFM-6500F, Jeol, Ltd, Tokyo, Japan) of these crystals confirmed the presence of gallium, oxygen, and nitrogen as well as in the crystals and the bulk sample.

For a quantitative analysis of the elemental composition of the crystalline spinel-type compound, the combination of energy-dispersive X-ray spectroscopy (EDS), electron energy loss spectroscopy (EELS), and transmission electron microscopy (TEM) provides powerful means for the characterization. Especially the simultaneous use of EDS and EEL-spectroscopy allows the quantification of nitrogen and oxygen in the matrix and the characterization of their distribution in the microstructure.

The homogeneity and the nitrogen to oxygen ratio of the new spinel-type gallium oxonitride phase were determined using a transmission electron microscope (CM12, operated at 120 kV equipped with a LaB_6 cathode, FEI, Hillsboro, USA) coupled with an electron energy loss spectrometer (Gatan DigiPeels 766, parallel electron spectrometer attached to the FEI CM12) and an energy dispersive X-ray (Genesis 2000, EDAX AMETEK, Paoli, USA) spectrometer. Several series of spectra were taken from small gallium oxonitride crystals of the reaction product. In detail, different areas of one particle as well as different particles were investigated, which exhibited all the spinel structure. Additionally, the spinel structure of all analyzed particles was confirmed by selective area diffraction patterns (SAED). To avoid the loss of nitrogen during the investigation, caused by a heating process through interaction of highly accelerated electrons with the sample (ionization), a double tilt liquid nitrogen cooling stage was used (Model 613 from Gatan) for the sample holder. It is already well known that high-pressure synthesized nitrides lose nitrogen during investigation in high vacuum and under exposure to electron radiation of the type used in TEM.

Table 4-24 gives a view over the results of twelve measurements at one single crystal of the spinel gallium oxonitride phase. Each value represents a different position at the crystal. These measurements resulted in a mean value of $\overline{N/O} = 0.25\pm0.06$, representative for this single crystal (Table 4-24).

Table 4-24. EELS-measurements on the oxonitride single crystals, resulting in a mean value of N/O = 0.25±0.06.

Meas. No.	1	2	3	4	5	6
N/O	0.30±0.067	0.29±0.061	0.31±0.070	0.30±0.072	0.18±0.051	0.32±0.069

Meas. No.	7	8	9	10	11	12
N/O	0.20±0.046	0.21±0.052	0.27±0.062	0.17±0.046	0.16±0.043	0.24±0.053

Figure 4-26 shows a representative EELS spectrum, measured at single crystals of the spinel gallium oxonitride phase. All further measurements of different crystals led to similar results, definitely confirming a considerable amount of nitrogen in the investigated spinel gallium oxonitride crystals of the high-pressure sample.
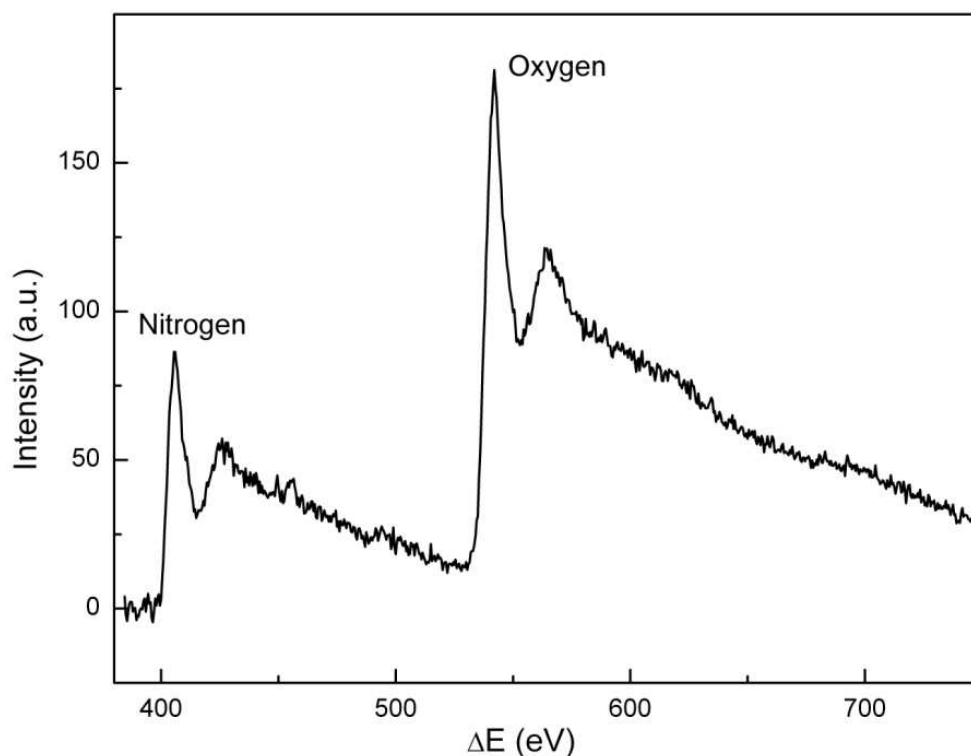
Figure 4-26. Typical EEL-spectrum from a selected area of a single crystal of the cubic spinel phase.

The ideal composition of a fully occupied spinel gallium oxonitride with the highest amount of nitrogen corresponds to Ga_3O_3N.

Taking into account the determined value of $\overline{N/O} = 0.25 \pm 0.06$, the resulting molar ratio of oxygen : nitrogen is therefore 3.05 : 0.76. Due to the results of the single crystal structure determination (*vide infra*) and that charge neutrality in the spinel must be guaranteed, the total stoichiometric composition of the spinel gallium oxonitride crystal averages to $Ga_{2.79}\square_{0.21}(O_{3.05}N_{0.76}\square_{0.19})$.

4.4.3.4   Crystal Structure Analysis of $Ga_{2.79}\square_{0.21}(O_{3.05}N_{0.76}\ _{0.19})$

The powder diffraction pattern of the reaction product was collected with a Stoe Stadi P diffractometer, using monochromatized $CuK_{\alpha1}$ ($\lambda = 154.051$ pm) radiation at ambient temperatures. Figure 4-27 gives a view of the Rietveld refinement of the measured X-ray

diffraction pattern, showing reflections resulting of the cubic spinel-type gallium oxonitride phase, beside small amounts of the educt hexagonal w-gallium nitride.
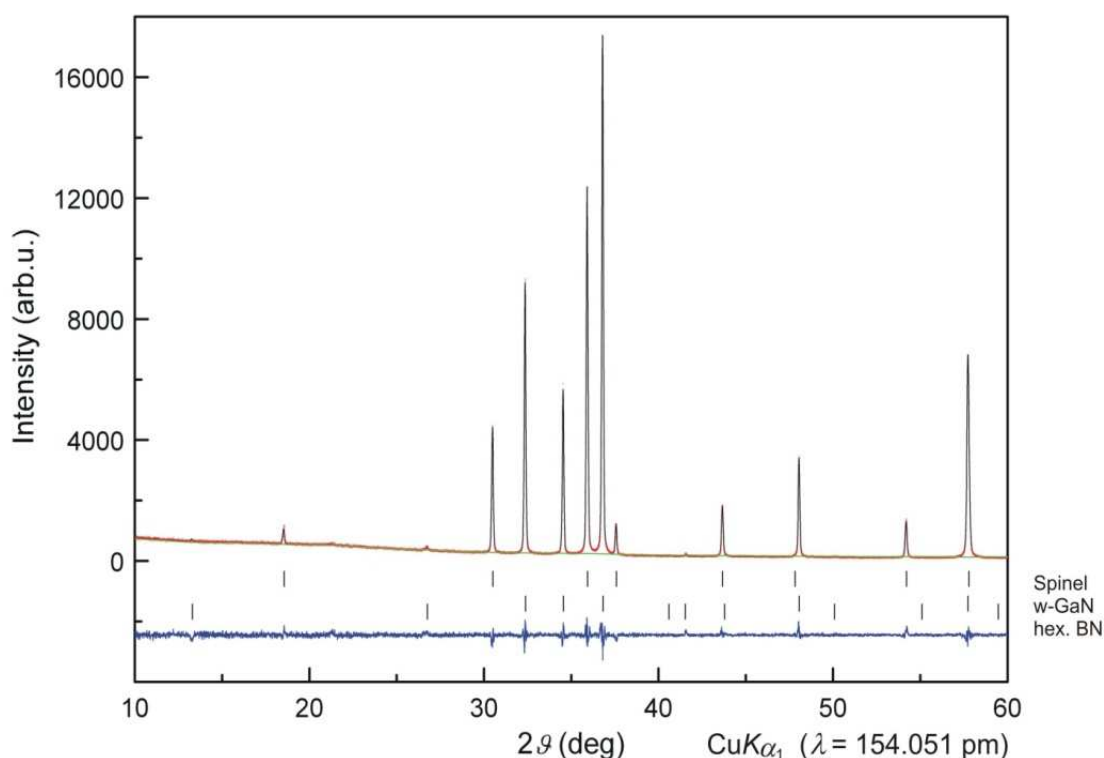
Figure 4-27. Rietveld refinement of the powder diffraction pattern of the reaction product, including the cubic spinel phase $Ga_{2.79}\square_{0.21}(O_{3.05}N_{0.76}\square_{0.19})$ and w-GaN as a by-product.

The reflections of the cubic gallium oxnitride spinel phase were indexed with the program TREOR [155-157] which is implemented in the Stoe software package. The powder diffraction pattern was refined on the basis of a cubic unit cell. The result led to a lattice parameter of a_0 = 828.0(1) pm (FullProf [467,468], Table 4-25). The comparison of the indexed result $a_0 = 828.0(1)$ pm and the lattice parameter derived from single crystal data ($a_0 = 827.8(2)$ pm) showed that both values agree well. The correct indexing of the pattern was confirmed by intensity calculations [153], taking the atomic positions from the structure refinement of $Ga_{2.79}\square_{0.21}(O_{3.05}N_{0.76}\square_{0.19})$ (Table 4-25).

Single crystal intensity data were collected at room temperature from a light-green crystal (dimensions: $0.025 \times 0.025 \times 0.020$ mm^3, Table 4-25) using an Enraf-Nonius Kappa CCD with graphite monochromatized Mo$K_{\alpha 1}$ ($\lambda = 71.073$ pm) radiation. According to the systematic extinctions $h+k = 2n$, $h+l$, $k+l = 2n$, $0kl$ with $k+l = 4n$ and $k,l = 2n$, and $h00$ with $h = 4n$, the cubic space groups $Fd\overline{3}m$ (no. 227) and $Fd\overline{3}$ (no. 203) were derived. A solution and refinement of the structure was only successful in the space group $Fd\overline{3}m$. To adjust the

obtained results to the former published data, the starting positional parameters were taken from the structural refinement of $Ga_{2.81}O_{3.57}N_{0.43}$ [429]. Therewith, Ga1 is positioned on the Wyckoff site 8*a* (⅛,⅛,⅛) while Ga2 occupies the position 16*d* (½,½,½) according to origin choice 2. The difference Fourier syntheses revealed the Wyckoff site 32*e* for the oxygen and nitrogen anions. Due to the fact that a differentiation between the amount of oxygen and nitrogen at the mixed Wyckoff site 32*e* based on X-ray data is impossible, the results of the above reported EELS measurements were used to restrain the ratio of $\overline{N/O} = 0.25\pm0.06$ in the structural refinement. In a separate series of least-squares cycles, the refinement of the occupancy parameter of the tetrahedrally coordinated gallium site (Ga1, 8*a*) showed full occupation within two standard deviations. The ideal occupancy was again assumed in the final cycles. In contrast, the octahedral gallium site (Ga2, 16*d*) exhibited a site occupation deficiency of about 10 %. To maintain charge neutrality, the occupancy of the anionic site was additionally coupled with the sum of positive charges from Ga1 and Ga2. The final least-squares cycles resulted in an occupation of 95.4(4) % for the anionic site. From these data, the nominal composition is $Ga_{2.79}(O_{3.05}N_{0.76})$, which implicates vacancies on the cationic as well as on the anionic sublattice of the structure. To summarize, all relevant details of the data collections and evaluations are listed in Table 4-25.

Structure solution and parameter refinement with anisotropic displacement parameters for all atoms (full-matrix least squares against F^2) were successfully performed by the SHELX-97 software suite [171,172]. The final difference Fourier synthesis did not reveal any significant residual peaks (results listed in Table 4-25). Additionally, the positional parameters, occupancy factors (Table 4-26), anisotropic displacement parameters (Table 4-27), interatomic distances, and angles (Table 4-28) of the spinel compound $Ga_{2.79}\square_{0.21}(O_{3.05}N_{0.76}\square_{0.19})$ are listed.

Table 4-25. Crystal data and structure refinement for $Ga_{2.79}\square_{0.21}(O_{3.05}N_{0.76}\square_{0.19})$.

Empirical formula	$Ga_{2.79}\square_{0.21}(O_{3.05}N_{0.76}\square_{0.19})$
Molar mass, g mol^{-1}	254
Crystal system	cubic
Space group	$Fd\bar{3}m$ (no. 227)
Powder diffractometer	Stoe Stadi P
Radiation	$CuK_{\alpha1}$ ($\lambda = 154.051$ pm)
Powder data	
a, pm	828.0(1)
V, nm^3	0.5682(1)
Single crystal diffractometer	Enraf-Nonius Kappa CCD
Radiation	$MoK_{\alpha1}$ ($\lambda = 71.073$ pm) (graphite monochromator)
Single crystal data	
a, pm	827.8(1)
V, nm^3	0.5673(2)
Formula units per cell	$Z = 8$
Calculated density, g cm^{-3}	5.95
Crystal size, mm^3	$0.025 \times 0.025 \times 0.020$
Temperature, K	293(2)
Detector distance, mm	40.0
Exposure time, min	110
Absorption coefficient, mm^{-1}	47.9
$F(000)$, e	930
θ range, deg	4.3 to 32.3
Range in hkl	$\pm12, \pm8, \pm7$
Reflections total / independent	171/ 69
R_{int}	0.0138
Reflections with $I \geq 2\sigma(I)$	62
R_σ	0.0152
Data / ref. parameters	69 / 10
Restraints	1
Absorption correction	multi-scan (SCALEPACK [150])
Final $R1$ / $wR2$ [$I \geq 2\sigma(I)$]	0.0171 / 0.0516
Final $R1$ / $wR2$ (all data)	0.0191 / 0.0528
Goodness-of-fit on F^2	1.153
Largest diff. peak and hole, e Å^{-3}	0.94 / -0.75

Table 4-26. Atomic coordinates, isotropic equivalent displacement parameters U_{eq} (Å^2), and site occupancy factors for $Ga_{2.79}\square_{0.21}(O_{3.05}N_{0.76}\square_{0.19})$ (space group: $Fd\bar{3}m$, no. 227). U_{eq} is defined as one third of the trace of the orthogonalized U_{ij} tensor.

Atom	Wyckoff-position	x	y	z	U_{eq}	S.O.F.
Ga1	8*a*	⅛	⅛	⅛	0.0075(3)	1
Ga2	16*d*	½	½	½	0.0114(3)	0.895(4)
O	32*e*	0.2569(2)	x	x	0.0083(7)	0.763(3)
N	32*e*	0.2569(2)	x	x	0.0083(7)	0.191(1)

Table 4-27. Anisotropic displacement parameters U_{ij} (Å^2) for $Ga_{2.79}\square_{0.21}(O_{3.05}N_{0.76}\square_{0.19})$.

Atom	U_{11}	U_{22}	U_{33}	U_{23}	U_{13}	U_{12}
Ga1	0.0075(3)	U_{11}	U_{11}	0	0	0
Ga2	0.0114(3)	U_{11}	U_{11}	-0.0017(2)	U_{23}	U_{23}
O/N	0.0083(7)	U_{11}	U_{11}	-0.0005(6)	U_{23}	U_{23}

Table 4-28. Interatomic distances (pm) and angles (deg) calculated with the single crystal lattice parameters of $Ga_{2.79}\square_{0.21}(O_{3.05}N_{0.76}\square_{0.19})$ with standard deviations in parentheses.

Ga1 – O/N	189.1(3)	4 ×
Ga2 – O/N	201.4(2)	6 ×
O/N – Ga1 – O/N	109.5	
O/N – Ga2 – O/N	180	
O/N – Ga2 – O/N	86.71(9)	
O/N – Ga2 – O/N	93.29(9)	

4.4.3.5   Crystal Structure Description of $Ga_{2.79}\square_{0.21}(O_{3.05}N_{0.76}\;_{0.19})$

The structure of the new gallium oxonitride phase $Ga_{2.79}\square_{0.21}(O_{3.05}N_{0.76}\square_{0.19})$ can be described as a defective fluorite structure. The spinel type structure crystallizes in the cubic space-group $Fd\bar{3}m$ (no. 227) exhibiting a lattice parameter of $a_0 = 827.8(2)$ pm. Commonly, vacancies occur on tetrahedral and octahedral gallium positions as well, statistically distributed in the structure. Figure 4-28 displays the structure, showing tetrahedrally (red) and octahedrally coordinated polyhedra (blue).
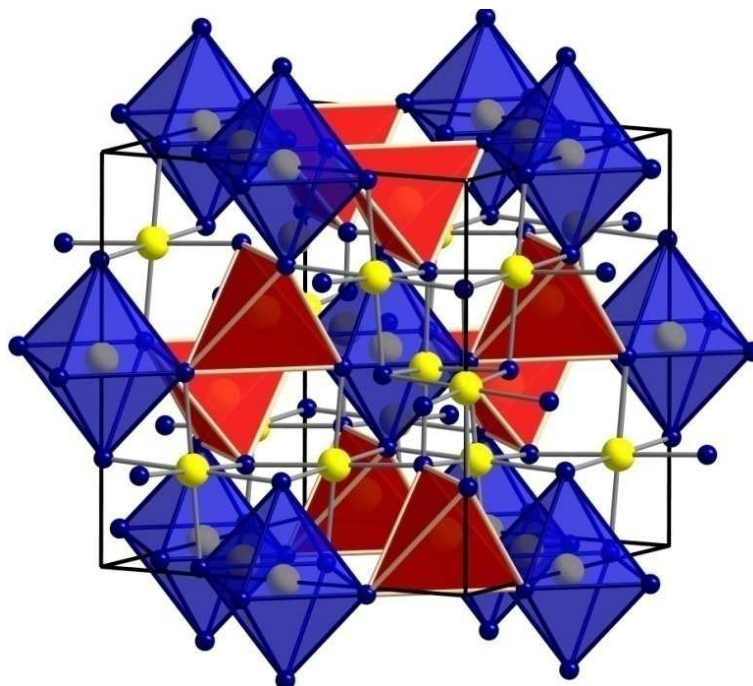
Figure 4-28. Crystal structure of a spinel-type gallium oxonitride. The tetrahedra and octahedra are displayed as red and blue polyhedra, respectively.

4.4.3.6   Results and Discussion on $Ga_{2.79}\square_{0.21}(O_{3.05}N_{0.76}\square_{0.19})$

Table 4-29 shows a comparison of the lattice parameters of γ-Ga_2O_3 [469,470] besides all known gallium oxonitrides arranged in the order of increasing ratio $\overline{N/O}$.

Table 4-29. Comparison of the lattice parameters (pm) of γ-Ga_2O_3 and gallium oxonitrides in the spinel type structure.

Phase	Ratio $\overline{N/O}$	Lattice param. a /pm	References
γ-Ga_2O_3	-	822; 823.8(6) 822.43 (GGA); 807.48 (LDA)	[469]; [470]; [433,472]
$Ga_{22}O_{30}N_2$	0.06	827.14 (GGA); 812.01 (LDA)	[433,472]
$Ga_{2.81}O_{3.57}N_{0.43}$	0.12	826.4(1)	[429]
$Ga_{2.8}O_{3.5}N_{0.5}$	0.14	820.0(7)	[427]
$Ga_{23}O_{27}N_5$	0.185	829.81 (GGA); 814.88 (LDA)	[433,472]
$Ga_{2.8}O_{3.24}N_{0.64}$	0.20	828.1(2)	[430]
$Ga_{2.79}\square_{0.21}(O_{3.05}N_{0.76}\square_{0.19})$	0.25±0.06	827.8(2) (single cryst.)	[471]
$Ga_{2.79}\square_{0.21}(O_{3.05}N_{0.76}\square_{0.19})$	0.25±0.06	828.0(1) (powder)	[471]
Ga_3O_3N	0.33	820(7); 832.61 (GGA); 817.63 (LDA)	[426]; [433,472]

In Figure 4-29 the results are shown graphically. Additionally, calculations for theoretical compounds are considered, beside experimental data sets. The results of GGA (Generalized Gradient Approximation) and LDA (Local Density Approximation) calculations of Kroll *et al*. [433,472] are displayed in Table 4-29 and Figure 4-29. The value for the lattice parameter of 820(7) pm from Lowther *et al*. [426] for a hypothetical Ga_3O_3N is not shown in the graphic due to its high standard deviation. As expected, the typical GGA and LDA calculations over- and underestimate the experimentally determined values, while all calculations are based on the constant anion model. With the exception of Puchinger´s value ($Ga_{2.8}O_{3.5}N_{0.5}$: $a_0 = 820.0(7)$ pm, determined at thin films [427]), all other experimental values can be found on or near a line plotted in Figure 4-29, which depends approximately linearly on the nitrogen to oxygen ratio in the compound.
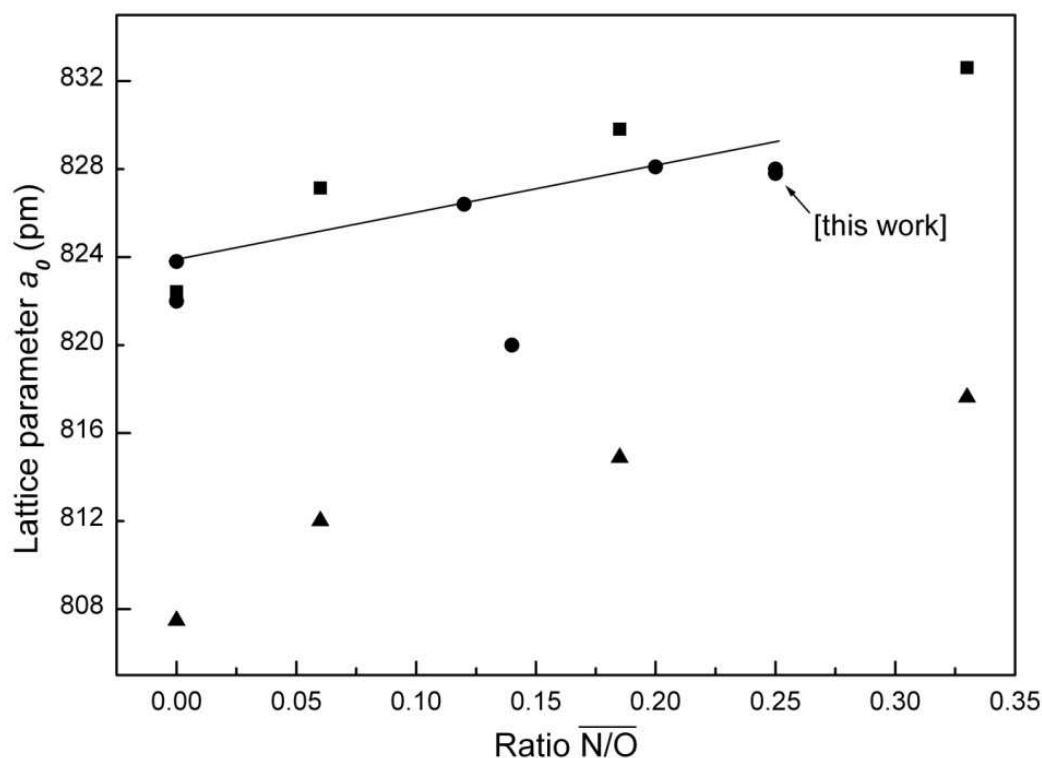
Figure 4-29. Lattice parameters of γ-Ga_2O_3 and cubic spinel-type gallium oxonitrides as a function of the ratio $\overline{N/O}$ (data see Table 4-29). The circles (●) stand for the experimental collected data, the triangles (▲) encode LDA results and the squares (■) represent lattice parameters calculated *via* GGA.

It is obvious that the determined lattice parameters given in this work (827.8(2) and 828.0(1) pm for single crystal and indexed powder data, respectively) show slightly smaller values as it would be expected from the extrapolation of the plotted line. A possible explanation for that requires a closer look at the structure.

Based on the structural refinement of the single crystal data, the bond-length between the tetrahedral gallium site (Ga1) and the mixed occupied anionic position (oxygen/nitrogen; Wyckoff position 32*e*) comes to 189.1(3) pm, while the corresponding distance from the octahedral site (Ga2) shows a slightly larger value of 201.4(2) pm.

Interestingly, the structural refinement of the single crystal data showed that the octahedral site 16*d* (Ga2) is not fully occupied. Soignard *et al.* obtained similar results during their Rietveld-refinement of the phase $Ga_{2.8}O_{3.24}N_{0.64}$ [430]. Starting the Rietveld-refinement on the powder pattern of $Ga_{2.8}O_{3.24}N_{0.64}$, the occupancies on the tetrahedral and octahedral gallium sites were refined freely. Similar to the results for $Ga_{2.79}(O_{3.05}N_{0.76})$ here, they observed that the occupancy of the tetrahedral site remained very close to unity. In contrast to that, the octahedrally coordinated gallium site was determined to be 0.90(4), resulting in the composition $Ga_{2.8}O_{3.24}N_{0.64}$ by keeping charge neutrality. These results stand in good accordance with the single crystal data refinement for the tetrahedral Ga2 positions in

$Ga_{2.79}(O_{3.05}N_{0.76})$. Though the tetrahedrally coordinated Ga site is fully occupied while the occupancy of the octahedral site comes to 0.895(4).

Investigations on the defective spinel γ-Al_2O_3 [473,474] led to similar results, though vacancies occurred also at the octahedrally coordinated cationic site. A long-standing controversy occurred, discussing the question whether the vacancies occupy the tetrahedral or the octahedral sites in the spinel structure [475-479]. One of the last investigations, based on transmission electron diffraction experiments, stated that the tetrahedral sites are fully occupied by aluminium and that the vacancies are located only at the octahedral site [480]. Furthermore, theoretical investigations based on pair-potential calculations showed that vacancies are preferred on the octahedral site. The averaged energetic difference of 3.7 eV per vacancy is in favour of the octahedral positions, in contrast to the tetrahedrally coordinated Ga sites [481]. In this context it is interesting to mention that cation vacancies in the nonstoichiometric spinel $MgAl_2O_4$ are also found at the octahedral sites [482]. The first-principles calculations of Kroll *et al.* also exhibited octahedral vacancies in the lowest energy structure of $Ga_{23}O_{27}N_5$ [433,472].

Due to the fact that the gallium oxonitride reported here exhibits a higher nitrogen content (EELS results) than the above mentioned compound of Soignard *et al.*, the total composition is necessarily calculated to $Ga_{2.79}O_{3.05}N_{0.76}$. Interestingly, this result implies vacancies on the cation site (octahedrally coordinated site 16*d*) and on the anion site 32*e* relative to the ideal spinel structure leading to the notation $Ga_{2.79}\square_{0.21}(O_{3.05}N_{0.76}\square_{0.19})$. This result differs from former models used in the structural characterization of spinel type oxonitrides. For example, the ideal structure of γ-alon Al_3O_3N would have a cubic spinel type structure (space group $Fd\bar{3}m$, No. 227) with oxygen and nitrogen atoms randomly distributed at the Wyckoff site 32*e* and the aluminium atoms at the tetrahedral (8*a*) and octahedral (16*d*) sites. The assumption of crystal defects, based on deviations from the ideal composition, led to the introduction of new structure models by Adams *et al.* [483], Lejus *et al.* [484], and McCauley [431]. The first model, designated as constant anion model, is based on aluminium vacancies and can be formulated as $Al_{(2+x/3)}\square_{Al,[(3-4x)/12]}O_{3-x}N_x$ (Adams *et al.*), $Al_{(8+x)/3}\square_{Al,[(1-x)/3]}O_{4-x}N_x$ (Lejus *et al.*; all values multiplied by 4/3 to point on the ideal spinel composition AB_2O_4), or $Al_{(64+x)/3}V_{Al,[(8-x)/3]}O_{(32-x)}N_x$ (McCauley, standardized to 32 anions inside the unit cell of the spinel type structure). The second model of McCauley is the constant cation model represented by the formula $Al_{24}O_{(72-3x)/2}N_x\square_{[(72-x)/2-32]}$, in which the cationic part of the structure is always fully occupied. Up to now, *ab initio* calculations between the constant anion and the constant cation model in the alon-systems revealed that the constant anion

model with vacancies on the Al sites is preferred, whereas a model with oxygen interstitial anions is unlikely [485]. This model was also confirmed by structure refinements based on XRD and neutron diffraction data [486]. Therewith, the AlON spinel unit cell has eight aluminium cations in tetrahedral sites and 15 Al and one vacancy in the 16 octahedral sites ($Al_8^{[4]}Al_{15}^{[6]}\square^{[6]}O_{27}N_5$) [487]. Interestingly, the normal spinel composition (N = 8) does not exist, whereas AlON (N = 5) and Φ' (N = 2) are stable phases [404].

Kroll *et al.* calculated the hypothetical structure of a spinel type gallium oxonitride with the ideal composition γ-Ga_3O_3N and showed that the lowest energy is realized in a regular distribution of the nitrogen atoms in the slightly distorted cubic substructure of the anionic part of the structure [433]. However, the estimation of the enthalpy for the formation of a spinel type gallium oxonitride is still endothermic, even when the lowest energy structures of GaN and Ga_2O_3 were used. Thus, the ternary compound is postulated to be formed at elevated temperatures with substantial entropy contributions ΔS. Further calculations on defective spinel type structures like $Ga_{23}O_{27}N_5$ and $Ga_{22}O_{30}N_2$ (both with the constant anion model) revealed a lower enthalpy of formation (still endothermic) than the calculations of the ideal γ-Ga_3O_3N. The necessary entropy terms are presumably raised from a mixing of oxygen and nitrogen in the anionic part of the structure as well as of the vacancies within the octahedral sites of the structure. Hence, Kroll *et al.* conclude that at temperatures of 1000 K all spinel type phases are thermodynamically instable with respect to the binary compounds β-Ga_2O_3 and GaN. The necessary temperatures for the formation of Ga_3O_3N, $Ga_{23}O_{27}N_5$, $Ga_{22}O_{30}N_2$, and γ-Ga_2O_3 are 1486, 1370, 1456, and 2400 K, respectively [433]. Accordingly, the formation of defective spinel type oxonitrides is always favoured over the ideal composition Ga_3O_3N.

The calculations on γ-alons as well as on the gallium oxonitrides are always based on the constant anion model with a completely filled anionic part of the structure. This model may not be the only possibility, as already noted by McCauley [404]. Based on the experimental data, which leads to the composition $Ga_{2.79}\square_{0.21}(O_{3.05}N_{0.76}\square_{0.19})$, vacancies on the cationic and anionic part of the spinel type structure are implied. Therewith, the validity of the approximation of a constant anionic part of the structure is in question. From the existing models, the formation enthalpy of the ternary oxonitride spinels comes out unfavourable relative to the low-energy structures of the oxides. Up to now, the deficiency in enthalpy can only be balanced *via* contributions, which arise from a mixing of oxygen and nitrogen in the anionic part of the structure. From our opinion, this contribution can be additionally enhanced

by the assumption of defects on the crystallographic site 32e, as found in the defect spinel type gallium oxonitride $Ga_{2.79}\square_{0.21}(O_{3.05}N_{0.76}\square_{0.19})$.

A problem for an intended reliable calculation of the enthalpy is the fact that a true distribution of oxygen and nitrogen gives a substantial contribution to the configurational entropy. Now, additional vacancies in the anionic part of the structure next to the already included cationic defects on the octahedral site have to be considered. These non-integer occupations are usually treated by the application of super-cells, complicating a computational approach.

Next to the EELS investigations, an experimental determination of the specific density of the single crystals would be desirable, to confirm the reported results *via* a second independent method. Up to now, verification by common density measurement methods such as Archimedes, pycnometer, and floating method were not possible, because the current size of the single crystals was not sufficient.

Concerning the lattice parameter (Table 4-29 and Figure 4-29), the determined vacancies in the cationic and anionic part of the structure are assumed to have a noticeable impact on the size of the unit cell, resulting in a reduction to smaller sizes than expected (see Figure 4-29). Certainly, $Ga_{2.81}O_{3.57}N_{0.43}$ and $Ga_{2.8}O_{3.24}N_{0.64}$ also exhibit vacancies but not to as extended as in $Ga_{2.79}\square_{0.21}(O_{3.05}N_{0.76}\square_{0.19})$. Therefore, a linear dependency of the lattice parameter with increasing ratio $\overline{N/O}$ is in question.

Interestingly, Pashchenko *et al.* [488] already presumed the existence of defects in both the cation and anion substructure in technologically important mono- and polycrystalline manganese-zinc ferrites, which were used for magnetic heads in video tape recorders and the transformer cores of color television sets. This assumption was based on an entire collection of experimental results with respect to the chemical inhomogeneities, which determine the quality of the manganese-zinc ferrites.

Based on the spinel-type structure, the cubic unit cell is face-centered ($Fd\overline{3}m$, no. 227) with the cations occupying the special positions 8a and 16d, while the anions are positioned on the site 32e. For a complete description of the spinel-type structure, an additional parameter designated as the "anion parameter u" [489] is required. If the value u is equal to 0.25, the anions form a perfect, cubic close packed structure, coordinating the sites 8a (point symmetry 43m) and 16d ($m3m$) in regular tetrahedra and octahedra, respectively. For the structural refinement the parameter u results to a value of 0.2569(2), which is slightly higher than the ideal value of 0.25. This causes an enlargement of the tetrahedral site at the expense

of the octahedral and a degeneration of the octahedral site symmetry to $\overline{3}m$ (displacement of the oxygen atoms along the [111] direction.

4.4.3.7   Conclusion

The data from the single crystal structure refinement of the presented spinel-type gallium oxonitride confirm a fully occupied tetrahedral gallium site beside vacancies at the octahedrally coordinated gallium positions, coupled with vacancies on the anionic site (Wyckoff position 32e). So, the composition of the characterized single crystal comes to $Ga_{2.79}\square_{0.21}(O_{3.05}N_{0.76}\square_{0.19})$, revealing anionic vacancies in a single crystal structure determination of a spinel-type structure for the first time. Theoretical calculations concerning vacancies on the cation sites in the structure must be determined in the future. More computational calculations should follow, to estimate and confirm a secure model, which allows vacancies on both cation and anion sites as well. Nevertheless, with respect to the increase of computer power, continuing calculations are planned in the near future.

Beside the theoretical work, for future investigations an analytical approach is in the focus, concerning the question of an ordering of oxygen, nitrogen, and the vacancies inside the anionic substructure. Results may be obtained *via* neutron diffraction experiments at a single crystal of acceptable size, but therefore the size of the single crystals must be improved by varying the parameters pressure and temperature in further experiments.

4.4.4   Systematic Investigations on the Formation of Gallium Oxonitrides

The conditions leading to the formation of gallium oxonitrides were systematically investigated under high-pressure / high-temperature conditions, *via* the application of varying starting mixtures of w-GaN and β-Ga_2O_3.

4.4.4.1   Introduction

On the basis of the success in synthesizing the first measurable single crystal in the GaON-system, the experimental work continued. To adress the question of anion ordering in the structure and determination of vacancies, experiments with varying pressure, temperature, and

educt ratio were arranged. The questionable model of a spinel, with vacancies on both cation and anion sites, could be confirmed by neutron scattering on suitable crystals. Therefore, the crystal size must be improved in further experimental work.

Systematic investigations on gallium oxonitrides were required for a better understanding of the formation tendency of the spinel, but also of the sample properties, like product to educt ratio, grade of crystallinity, or the mean $\overline{\text{N/O}}$ content. By varying the parameters pressure and temperature as well as the different molar ratio of the starting materials β-Ga_2O_3 and w-GaN, the ideal conditions for crystalline samples were identified.

The stability field of the gallium oxonitride spinel-type phases was investigated systematically in 65 multianvil experiments under high-pressure / high-temperature conditions. Starting at low pressure of 1 GPa and up to pressures as high as 11.5 GPa, temperatures ranging in between 500 to 1350 °C were applied with different heat treatment protocols. The mixture of the educts β-Ga_2O_3 and wurtzite-structured GaN was also varied, investigating the influence of a nitrogen-rich sample, in contrast to a mixture with an excess of β-gallium oxide. Mixtures starting from w-GaN : β-Ga_2O_3 = 9 : 1 up to the reverse mixture of w-GaN : β-Ga_2O_3 = 1 : 9 were used.

4.4.4.1 Systematic Experimental Studies into the Field of Gallium Oxonitrides

The experiments started with mixtures of fine powders of the end members wurtzite-structured gallium nitride (99.9 %, Alfa Aesar, Karlsruhe, Germany) and monoclinic β-gallium oxide (99.9 %, Sigma Aldrich, Munich, Germany). Molar ratios differed from 90 mol-% w-GaN with 10 mol-% β-Ga_2O_3 up to the reverse mixture of 90 mol-% β-Ga_2O_3 and 10 mol-% w-GaN. Column 2 of Table 4-30 shows the name of the experiment and column 3 the molar ratio of the educts used in the corresponding experiments.

The pressure conditions ranged from 1 GPa up to 11.5 GPa increased by small steps of 0.5, 1 or 2.5 GPa. For each experiment, the pressure is listed in column 4 of Table 4-30. Beside systematic pressure investigations, the influence of temperature (Table 4-30, column 5) was examined for the formation of the gallium oxonitride spinel phases, the decomposition and transformation of the educts. Therefore, the heating protocols were varied to see if there were differences in the sample formation, yield, or the degree of crystallinity of the resulting spinel phase, depending on a long or short heating protocol, slow or fast cooling, and the presence or absence of a tempering phase. Column 6 of Table 4-30 lists the exact heating protocols for each experiment. Distinctions between long-term heating periods, with heating

segments of about 1 h (*e.g.* Table 4-30, column 6, Pos. 23, SH_054; Pos. 25, SH_056; Pos. 27, SH_058; Pos. 48, SH_213) and long tempering phases of 3-5 h were made. Also shorter heating protocols were applied, with heating up times of approximately 10 min, a constant period during which the maximum temperature was held for 15-25 min, followed by a tempering phase of about half an hour (Table 4-30, column 6, *e.g.* Pos. 64, SH_06; Pos. 53, SH_020; Pos. 32, SH_031; Pos. 33, SH_034; Pos. 38, SH_045; Pos. 6, SH_077; Pos 42, SH_123). Heating phases were distinguished by heating time and temperature, but also protocols comprising several heating phases at different temperatures were applied. A special program implied two tempering phases at lower temperatures, a first one at 200 °C, then holding the temperature constant for 5-10 min, to increase it afterwards to a maximum temperature of 600-700 °C (Table 4-30, column 6, Pos. 19, SH_093; Pos. 7, 095; Pos. 2, SH_096, Pos. 20, SH_097; Pos. 21, SH_098).

The standard heating program comprised three relatively equal heating sequences, heating up in 5-10 min, holding the temperature for at least 10-20 min, and cooling down to a lower temperature (approximately 600-800 °C) within about 5-15 min.

All high-pressure / high-temperature experiments were performed using the modified multianvil technique [103-105,111]. Each experiment started with the preparation of an octahedron containing the starting mixture, which was centered in a cube consisting of eight truncated tungsten carbide cubes (TSM-10 Ceratizit, Reutte, Austria). The educts were mixed together, filled into a boron nitride crucible and closed with a BN-plate (Henze BNP GmbH, HeBoSint® S10, Kempten, Germany). The crucible was positioned in two graphite furnaces (RW430, SGL Carbon, Bonn, Germany), centered by two MgO plates (Magnorite MN 399 CX, Saint-Gobain, Industrial Ceramics, Worcester, UK) to guarantee nearly equal heating in the whole sample. After that, the sample was positioned in a zirconia sleeve (Ceramic Substrates, Newport, Isle of Wight, UK) to insulate the graphite furnace from the outer part. Finally, the cylindrical sample was positioned into a MgO octahedron doped with Cr_2O_3 (Ceramic Substrates & Components LTD., Isle of Wight, UK). To guarantee conductivity, a requirement to heat the sample, two molybdenum plates were positioned on top and bottom of the octahedron. The octahedron was positioned in the center of eight tungsten carbide cubes with truncated corners [111,112]. Pyrophyllite gaskets (Ceramic Substrates, Newport, Isle of Wight, UK) separated the cubes. Alternatively, they were laminated with cardboards (Bristolkarton, 369 g/m^3) and self-adhesive Teflon foil (Fiberflon, Konstanz, Germany and Vitaflon, Bad Kreuznach, Germany), so that every foil side lay next to a side prepared with cardboard. The assembled cube was positioned into the Walker-type

module. A hydraulic 1000 t press compressed the module (both devices from Voggenreiter, Mainleus, Germany).

The typical high-pressure / high-temperature protocol had three main parts: 1. increasing the pressure with a press load of 100 t per hour; 2. the heating period, during which the pressure stayed constant; 3. the decompression of the assembly within the threefold of the compression time. Exact information about the pressure / temperature protocols is listed in the columns 4-6 of Table 4-30. After decompression, each sample was isolated from the surrounding assembly materials and prepared for further analysis. Regularly, the samples were investigated with X-ray powder diffractometry for phase analysis and crystallinity and EDX to confirm the elemental content.

Table 4-30. Molar ratio of the starting materials, conditions of synthesis, and products of all high-pressure / high-temperature experiments performed in this work.

		Conditions of synthesis				Identified products			
Position	Sample	w-GaN : β-Ga$_2$O$_3$	p (GPa)	T (°C)	Temperature ramp	GaON-Spinel	w-GaN	β-Ga$_2$O$_3$	α-Ga$_2$O$_3$
1	SH_152	9:1	1.0	1000	↑ 10 min (1000 °C) - 15 min (**1000** °C) ↓ 10 min (600 °C)		X	X	
2	SH_096	9:1	1.5	600	↑ 5 min (200 °C) - 10 min (200 °C) ↑ 15 min (600 °C) - 5 min (**600** °C) ↓ 1 min (25°C)		X	X	
3	SH_154	9:1	2.0	1200	↑ 10 min (1200 °C) - 15 min (**1200** °C) ↓ 10 min (700 °C)		X	X	
4	SH_185	7:3	2.0	1250	↑ 10 min (1250 °C) - 15 min (**1250** °C) ↓ 10 min (650 °C)		X	X	
5	SH_155	9:1	2.0	1350	↑ 10 min (1350 °C) - 15 min (**1350**°C) ↓ 10 min (800 °C)		X	X	X**
6	SH_077	1:1	2.5	1300	↑ 10 min (1250 °C) - 15 min (**1250** °C) ↓ 25 min (650 °C)	X	X	X	X
7	SH_095	9:1	2.5	500	↑ 10 min (200 °C) - 15 min (200 °C) ↑ 10 min (500 °C) - 15 min (**500** °C) ↓ 10 min (200 °C)		X		X
8	SH_130	7:3	2.5	1250	↑ 10 min (1250 °C) - 10 min (**1250** °C) ↓ 10 min (800 °C)	X	X	X	X
9	SH_139	7:3	2.5	1300	↑ 10 min (1300 °C) - 10 min (**1300** °C) ↓ 10 min (800 °C)		X		X
10	SH_131	7:3	3.0	1000	↑ 10 min (1000 °C) - 20 min (**1000** °C) ↓15 min (800 °C)		X	X	
11	SH_176	7:3	3.0	1250	↑ 10 min (1250 °C) - 5 min (**1250** °C) ↓ 10 min (800 °C)	X	X	X	
12	SH_180	3:7	3.0	1250	↑ 10 min (1250 °C) - 15 min (**1250** °C) ↓ 10 min (800 °C)		X	X	
13	SH_182	4:6	3.0	1250	↑ 10 min (1250 °C) – 15 min (**1250** °C) ↓ 10 min (800 °C)		X	X	
14	SH_184	7:3	3.0	1250	↑ 10 min (1250 °C) - 15 min (**1250** °C) ↓ 10 min (800 °C)		X	X	
15	SH_188	3:7	3.0	1250	↑ 10 min (1250 °C) - 15 min (**1250** °C) ↓ 10 min (800 °C)		X	X	
16	SH_068	9:1	3.5	1250	↑ 10 min (1250 °C) - 20 min (**1250** °C) ↓ 15 min (850 °C)	X	X		
17	SH_138	9:1	3.5	1350	↑ 10 min (1350 °C) - 20 min (**1350** °C) ↓ 15 min (800 °C)		X	X	**
18	SH_159	6:4	4.0	800	↑ 15 min (800 °C) - 15 min (**800** °C) ↓ 10 min (400 °C)		X	X	

		Conditions of synthesis				Identified products			
Position	Sample	w-GaN : β-Ga$_2$O$_3$	p (GPa)	T (°C)	Temperature ramp	GaON-Spinel	w-GaN	β-Ga$_2$O$_3$	α-Ga$_2$O$_3$
19	SH_093	9:1	4.5	500	↑ 10 min 200 °C) - 15 min (200 °C) ↑ 10 min (500 °C) -15 min (**500** °C) ↓ 10 min (200 °C)		X		X
20	SH_097	7:3	4.5	600	↑ 10 min (200 °C) - 5 min (200 °C) ↑ 10 min (600 °C) - 15 min (**600** °C) ↓ 5 min (200 °C)		X		X
21	SH_098	9:1	4.5	700	↑ 10 min (200 °C) - 15 min (200 °C) ↑ 10 min (700 °C) - 15 min (**700** °C) ↓ 10 min (200 °C)		X	X	X
22	SH_051	1:1	4.5	1250	↑ 10 min (1250 °C) - 15 min (**1250** °C) ↓ 25 min (800 °C)	X	X		X
23	SH_054	1:1	4.5	1250	↑ 15 min (1250 ° - 60 min (**1250** °C) ↓ 300 min (500 °C)	X	X		X
24	SH_055	9:1	4.5	1250	↑ 10 min (1250 °C) - 15 min (**1250** °C) ↓ 25 min (800 °C)	X	X		
25	SH_056	9:1	4.5	1250	↑ 15 min (1250 °C) - 60 min (**1250** °C) ↓ 300 min (800 °C)	X	X		
26	SH_057	2:8	4.5	1250	↑ 10 min (1250 °C) - 15 min (**1250** °C) ↓ 25 min (800 °C)	X	X		
27	SH_058	9:1	4.5	1250	↑ 15 min (1250 °C) - 60 min (**1250** °C) ↓ 200 min (700 °C)	X	X		
28	SH_025	7:3	5.0	1200	↑ 10 min (1200 °C) - 15 min (**1200** °C) ↓ 5 min (800 °C)	X	X		
29	SH_026	1:1	5.0	1200	↑ 10 min (1200 °C) - 15 min (**1200** °C) ↓ 5 min (800 °C)	X	X	X	
30	SH_028	7:3	5.0	1200	↑ 10 min (1200 °C) - 15 min (**1200** °C) ↓ 30 min (800 °C)	X	X		
31	SH_030	9:1	5.0	1250	↑ 10 min (1250°C) - 15 min (**1250** °C) ↓ 25 min (800 °C)	X	X		
32	SH_031	3:7	5.0	1300	↑ 10 min (1300 °C) - 15 min (**1300** °C) ↓ 30 min (800 °C)	X	X	X	X
33	SH_034	4:6	5.0	1300	↑ 10 min (1300 °C) - 15 min (**1300** °C) ↓ 30 min (800 °C)	X	X		X
34	SH_035	5:5	5.0	1300	↑ 10 min (1300 °C) - 15 min (**1300** °C) ↓ 25 min (800 °C)	X	X		X
35	SH_039	8:2	5.0	1200	↑ 10 min (1200 °C) - 15 min (**1200** °C) ↓ 30 min (800 °C)	X	X		X
36	SH_041	6:4	5.0	1200	↑ 10 min (1200 °C) - 15 min (**1200** °C) ↓ 25 min (800 °C)	X	X	X	
37	SH_042	2:8	5.0	1200	↑ 10 min (1200 °C) - 15 min (**1200** °C) ↓ 25 min (800 °C)	X	X		X
38	SH_045	7:3	5.0	1200	↑ 10 min (1200 °C) - 15 min (**1200** °C) ↓ 60 min (800 °C)	X	X	X	
39	SH_046	1:9	5.0	1250	↑ 10 min (1250 °C) - 15 min (**1250** °C) ↓ 25 min (800 °C)	X			X

		Conditions of synthesis				Identified products			
Position	Sample	w-GaN : β-Ga$_2$O$_3$	p (GPa)	T (°C)	Temperature ramp	GaON-Spinel	w-GaN	β-Ga$_2$O$_3$	α-Ga$_2$O$_3$
40	SH_047	2:8	5.0	1250	↑ 10 min (1250 °C) - 15 min (**1250** °C) ↓ 30 min (800 °C)	X			X
41	SH_063	9:1	5.0	1250	↑ 10 min (1250 °C) - 15 min (**1250** °C) ↓ 10 min (800 °C)	X	X		
42	SH_123	9:1	5.0	1250	↑ 10 min (1250 °C) - 15 min (**1250** °C) ↓ 25 min (800 °C)	X	X		X
43	SH_133	6:4	5.0	1250	↑ 10 min (1250 °C) - 15 min (**1250** °C) ↓ 25 min (800 °C)	X	X		X
44	SH_134	9:1	5.0	1250	↑ 10 min (**1250** °C) - 15 min (**1250** °C) ↓ 25 min (800 °C)	X	X		
45	SH_208	6:4	5.0	1250	↑ 15 min (1250 °C) - 10 min (**1250** °C) ↓ 10 min (800 °C)		X		X
46	SH_211	6:4	5.0	1100	↑ 15 min (1100 °C) - 10 min (**1100** °C) ↓ 10 min (800 °C)				X
47	SH_212	6:4	5.0	1200	↑ 15 min (1200 °C) - 10 min (**1200** °C) ↓ 10 min (800 °C)	X			X
48	SH_213	5:5	5.0	1250	↑ 10 min (1250 °C) - 15 min (**1250** °C) ↓ 300 min (1100°C)	X	X		
49	SH_230	1:1	6.0	700	↑ 10 min (700 °C) - 15 min (**700** °C) ↓ 10 min (650 °C)		X		X
50	SH_227	9:1	6.0	800	↑ 10 min (800 °C) - 15 min (**800** °C) ↓ 10 min (650 °C)		X		X
51	SH_228	1:1	6.0	900	↑ 10 min (900 °C) - 15 min (**900** °C) ↓ 10 min (700 °C)				X
52	SH_229	1:1	6.0	1000	↑ 10 min (1000 °C) - 15 min (**1000** °C) ↓ 10 min (850 °C)	X	X		X
53	SH_020	7:3	6.0	1200	↑ 10 min (1200 °C) - 15 min (**1200** °C) ↓ 5 min (800 °C)	X	X		
54	SH_135	1:9	6.0	1250	↑ 15 min (1250 °C) - 10 min (**1250** °C) ↓ 10 min (800 °C)	X	X		X
55	SH_022	7:3	7.0	1200	↑ 10 mi n (1200 °C) - 15 min (**1200** °C) ↓ 5 min (800 °C)	X	X		X
56	SH_05	7:3	8.0	1200	↑ 10 min (1200 °C) - 10 min (**1200** °C) ↓ 5 min (800 °C)	X	X		X
57	SH_08	1:1	8.0	1200	↑ 10 min (1200 °C) - 10 min (**1200** °C) ↓ 5 min (800 °C)		X		X
58	SH_010	9:1	8.0	1200	↑ 10 min (1200 °C) - 10 min (**1200** °C) ↓ 5 min (800 °C)		X		X
59	SH_012	7:3	8.0	1200	↑ 10 min (1200 °C) - 10 min (**1200** °C) ↓ 5 min (800 °C)		X		X
60	SH_014	3:7	8.0	1100	↑ 10 min (1100 °C) - 10 min (**1100** °C) ↓ 5 min (800 °C)		X		X
61	SH_015	3:7	8.0	1150	↑ 10 min (1150 °C) - 15 min (**1150** °C) ↓ 5 min (800 °C)		X		X
62	SH_016	9:1	8.0	1100	↑ 10 min (1100 °C) - 10 min (**1100** °C) ↓ 5 min (800 °C)		X		X

		Conditions of synthesis				Identified products			
Position	**Sample**	**w-GaN : β-Ga₂O₃**	***p* (GPa)**	***T* (°C)**	**Temperature ramp**	**GaON-Spinel**	**w-GaN**	**β-Ga₂O₃**	**α-Ga₂O₃**
63	SH_017	7:3	8.0	1150	↑ 10 min (1150 °C) - 15 min (**1150** °C) ↓ 5 min (800 °C)		X		X
64	SH_06*	7:3	9.2	1300	↑ 15 min (1300 °C) - 5 min (**1300** °C) ↓ 20 min (700 °C)		X		X
65	SH_021	7:3	11.5	1200	↑ 10 min (1200 °C) - 15 min (**1200** °C) ↓ 5 min (800 °C)	X	X		X

* crucible material Mo; ** additional by-product: metallic Ga

4.4.4.2 Analytic of Spinel-type Gallium Oxonitrides

Small parts of the sample were ground and prepared for X-ray powder diffractometry, using STOE Stadi P diffractometers (Stoe & Cie, Darmstadt, Germany) with monochromatized $CuK_{\alpha 1}$ ($\lambda = 154.051$ pm) or $MoK_{\alpha 1}$ ($\lambda = 71.073$ pm) radiation.

All X-ray powder diffractograms were handled with the Stoe program package [153,154]. The programs TREOR [155-157], ITO [158], DICVOL [159], and THEO [160] allowed the indexing and handling of the diffractograms. The JCPDS / ICDD-database [162] served for the phase analysis. To mark the starting materials, products, by-products, or impurities from assembly materials, the references of the ICDD-database with the corresponding PDF numbers are shown in Table 4-31. The cubic gallium oxonitride spinel phase was compared to the powder pattern of the spinel phase $Ga_{2.81}O_{3.57}N_{0.43}$, found by Kinski *et al.* [429] (lattice parameter: $a = 826.4(1)$ pm), and the single crystal data of Huppertz *et al.* of the compound $Ga_{2.79}\square_{0.21}(O_{3.05}N_{0.76}\square_{0.19})$ [471].

Furthermore, GSAS [163] and EXPGUI [164] were used for the Rietveld refinements, confirming the spinel-type compound, and the product to educt ratio in the sample.

Further analysis was done with an EDS device (*E*nergy *D*ispersive X-ray *S*pectroscopy) (JSM-6500F with field emission source, Jeol, USA), which allowed a qualitative and semi-quantitative analysis of the composition, based on the characteristical X-ray emission of the elements (EDX detector: 7418 Oxford Instruments, Abingdon, Oxfordshire, OX13 5QX, UK). However, the main focus lied on the synthetic investigations concerning the formation of the spinel-type gallium oxonitrides.

Table 4-31. Identified phases of the HP / HT-experiments with ICDD-reference numbers.

Category	Substance	PDF-number
Product	Spinel gallium oxonitride	Kinski [429]; Huppertz [471]
Educts	w-GaN (hexagonal)	00-076-0703
	β-Ga$_2$O$_3$ (monoclinic)	00-087-1901
By-products	α-Ga$_2$O$_3$ (rhombohedral)	00-074-1610
	Ga (orthorhombic)	00-005-0601
Assembly materials	BN (hexagonal)	00-085-1068
	Graphite (rhombohedral)	00-005-0444

4.4.4.3   Thermal Behavior of Spinel-type Gallium Oxonitrides

Additionally, the thermal stability of the spinel phase was examined by a Stoe Stadi P powder diffractometer with monochromatized radiation Mo$K_{\alpha 1}$ ($\lambda = 71.073$ pm) equipped with a computer-controlled Stoe furnace. The sample was filled into a silica glass capillary (silica glass capillary, Hilgenberg, Malsfeld, Germany, Ø$_{ext.}$ 0.1–0.5 mm) and measured in Debye-Scherrer geometry. The sample was heated electrically and fixed with respect to the scattering plane of a graphite tube. The unobstructed pathways for the primary beam of the molybdenum radiation source and for the scattered radiation were granted through wells in the graphite tube. The temperature was measured by an integrated thermocouple in the graphite tube and was found to vary within 0.2 °C.

Figure 4-30 shows the powder diffraction diagram recorded with a Stoe Stadi P diffractometer with Cu$K_{\alpha 1}$ ($\lambda = 154.051$ pm) radiation of the crystalline sample, resulting from a mixture in the molar ratio of w-GaN : β-Ga$_2$O$_3$ = 1 : 1 and synthesized under high-pressure / high-temperature conditions of 4.5 GPa and 1250 °C (Table 4-30, Pos. 23, SH_054, column 6, Figure 4-30). The sample was analyzed with the Rietveld method, exhibiting a product to educt ratio of spinel 45 % : 15 % w-GaN.
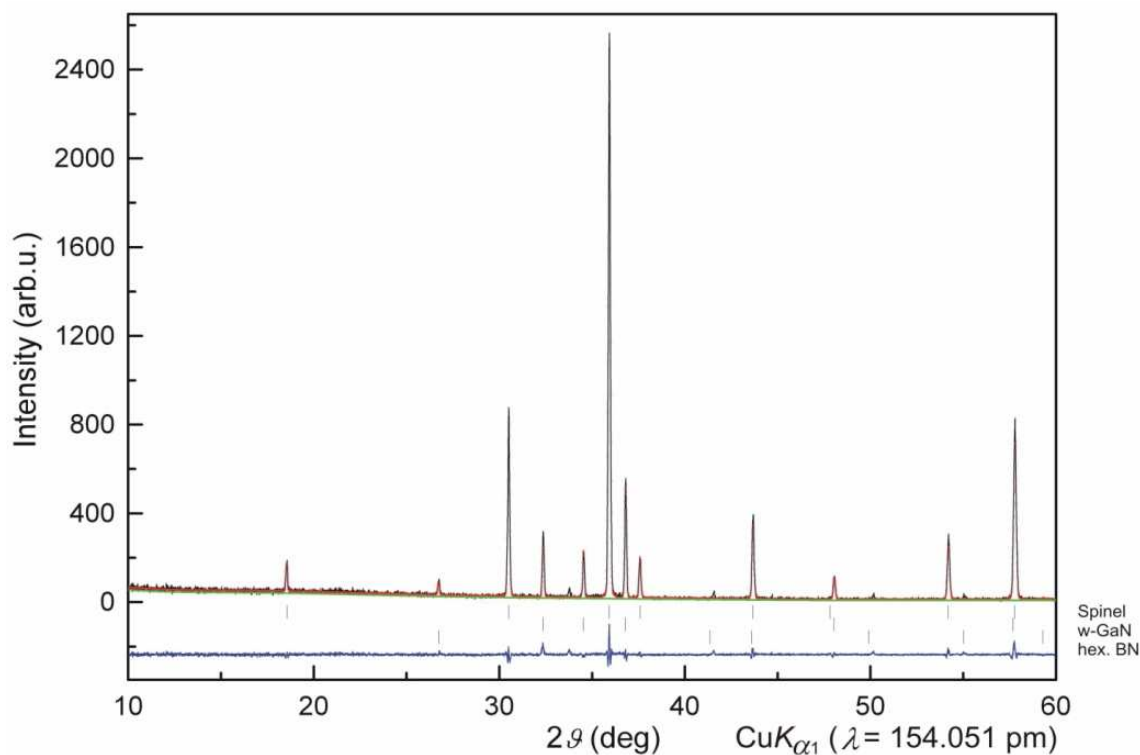
Figure 4-30. Rietveld fit of SH_054 (Pos. 23); starting mixture w-GaN : β-Ga$_2$O$_3$ = 1 : 1 (molar ratio), 4.5 GPa, 1250 °C, displaying spinel-type gallium oxonitride (45 %), w-GaN (15 %), and hex. BN (from the crucible).

The thermal stability was tested by an *in-situ* high temperature X-ray powder diffraction experiment. The powdered sample was heated up from room temperature to 1100 °C in steps of 50 °C (Figure 4-31). Cooling down the sample to room temperature was also done in steps of 50 °C. Each temperature was kept constant for at least 10 minutes, before the measurement started.
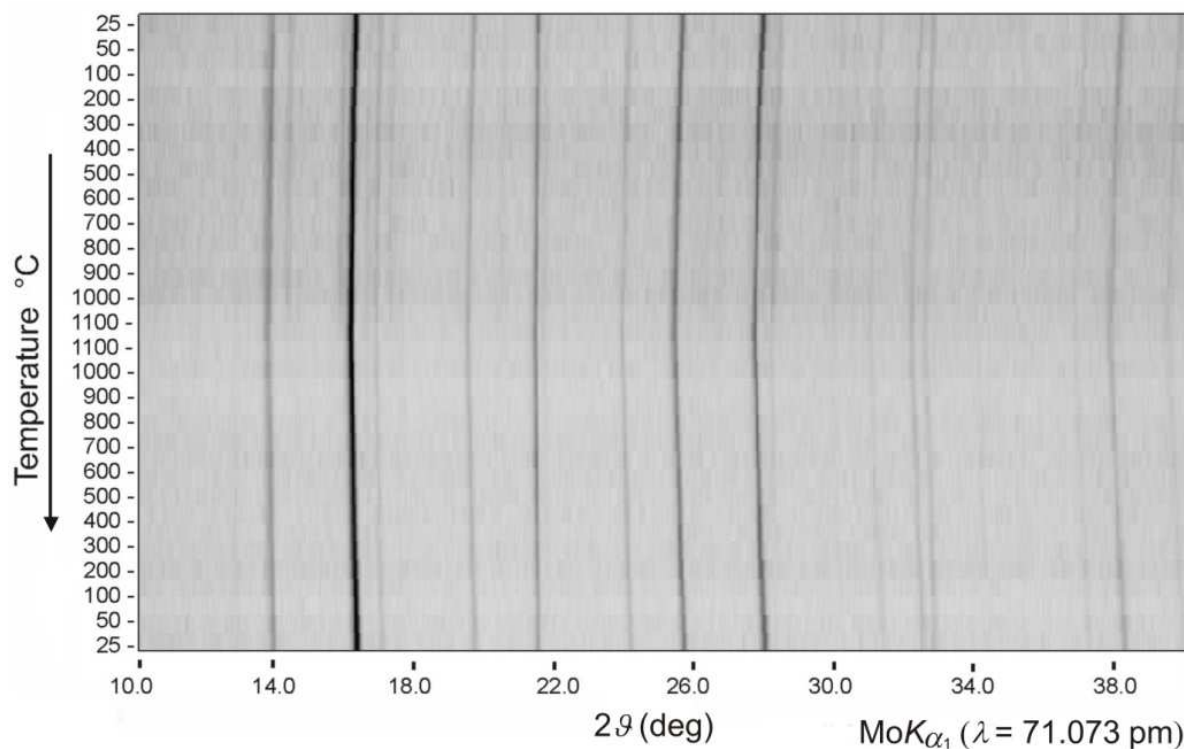
Figure 4-31. *In-situ* temperature-programmed X-ray powder diffraction patterns (radiation: Mo$K_{\alpha1}$, $\lambda = 71.073$ pm), showing the thermal behavior of the spinel-type gallium oxonitride sample SH_054 (Table 4-30, Pos. 23).

Figure 4-31 shows that successive heating of the product led to a shift of the reflections of the gallium oxonitride phase towards larger *d*-values (larger cell volume), while the reflections of w-GaN disappeared at a temperature of 1000 °C. No decomposition of the spinel-type gallium oxonitride could be observed up to a temperature of 1100 °C.

4.4.4.4   Results and Discussion on Spinel-type Gallium Oxonitrides

The mixtures of the end members of the binary phase diagram wurtzite-structured gallium nitride and β-gallium oxide were systematically examined under high-pressure / high-temperature conditions, applied in different molar ratios (w-GaN : β-Ga$_2$O$_3$ = 9 : 1 - 1 : 9).
65 experiments were performed under different high-pressure / high-temperature conditions while the parameters pressure, temperature, and the applied molar ratio of the starting mixtures were varied. The applied temperature protocols included a variation of the heating, tempering, and cooling periods. Figure 4-32 shows the identified product mixtures of the experiments, depending on the conditions of pressure and temperature. The data of the

reactions, which led additionally to metallic gallium (Table 4-30, Pos. 5, SH_155; Pos. 17, SH_138), are not shown in Figure 4-32.
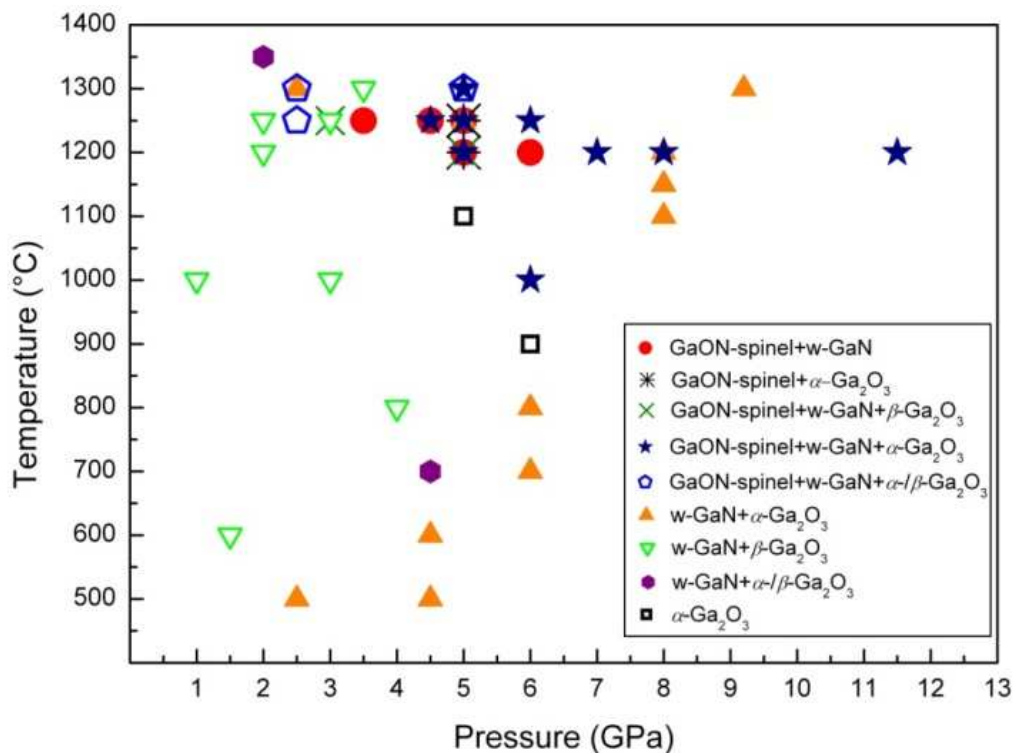
Figure 4-32. Survey of the products, obtained under specified pressure and temperature conditions with varying starting mixtures.

Searching for the minimum of the high-pressure / high-temperature conditions required for the formation of the spinel, the optimum values of 2.5 GPa and 1000 °C (different experiments) were established.

The comparison between the different experiments and the high-pressure / high-temperature protocols (Table 4-30) showed the onset of the reaction of the two end members to form the high-pressure spinel-type gallium oxonitride phase and transformed α-Ga_2O_3 already at a pressure of 2.5 GPa and a temperature of 1250 °C (Table 4-30, Pos. 8, SH_130).

The lowest synthetic temperature of 1000 °C necessary for the formation of the spinel phase could be found at a pressure of 6 GPa (Table 4-30, Pos. 52, SH_229) if lowering the temperature higher pressures are required to form the spinel. Apart of the desired crystalline gallium oxonitride, the sample contained w-GaN and α-Ga_2O_3 still not having fully reacted.

The process of the spinel formation could be traced from the experiments at a pressure condition of 6 GPa, for which Figure 4-32 (Table 4-30) shows three experiments at 700 (▲), 900 (□), and 1000 °C (★), which started all from the same starting mixtures of w-GaN and β-Ga_2O_3 in a molar ratio of 1 : 1. After the high-pressure / high-temperature reaction, the first

experiment at 700 °C (▲) revealed the starting materials w-GaN and gallium oxide, the latter already being transformed into the α-modification (specific conditions can be found in Table 4-30, Pos. 49, SH_230). Upon increasing the temperature up to 900 °C (■), the XRD pattern exhibited only α-Ga_2O_3 (Table 4-30, Pos. 51, SH_228). As none of the reactants could leave the crucible, a transition state of the reaction appears, in which w-GaN and gallium oxide form an amorphous intermediate phase on their way to a crystalline gallium oxonitride compound. Only part of the gallium oxide can be detected *via* the XRD pattern in form of crystalline α-Ga_2O_3. Furthermore, increasing the synthesis temperature up to 1000 °C (Table 4-30, Pos. 52, SH_229), the crystalline spinel-type gallium oxonitride phase can be observed (Figure 4-32, ★) next to unreacted w-GaN and α-Ga_2O_3. These results confirm the formation of the spinel-type gallium oxonitride compound, *via* an intermediate state of an amorphous oxonitride compound. Although the required pressure and temperature conditions can be limited, only at an applied temperature of 1000 °C the formation is fully detectable, while lowering the synthetic temperature leads to almost unreacted compounds. So, decreasing the initial temperature below 1000 °C at all pressures (Table 4-30) led to samples consisting of the educts w-GaN, β-Ga_2O_3, or the high-pressure modification α-Ga_2O_3.

On the other hand, at experiments with temperatures exceeding 1300 °C, but pressures as low as 2 and 3.5 GPa, metallic gallium was formed as a decomposition product of wurtzite structured gallium nitride, and no spinel-structured gallium oxonitride could be detected with X-ray powder diffractometry (Table 4-30, Pos. 5, SH_155; Pos. 17, SH_138). Therefore we can state that ideal temperatures leading to crystalline samples lie around 1100-1250 °C.

Not only pressure and temperature influences the formation of the spinel. A comparison of the experiments showed, that the different temperature protocols had a remarkable influence on the fraction of the spinel phase. The degree of crystallinity could be improved by high heating rates and short holding times, for example heating the mixture up in 10 minutes to 1250 °C, holding the temperature there for 15 minutes, and cooling it down to 800 °C within 25 minutes (*e.g*. Table 4-30, Pos. 22, SH_051). Beside short heating segments, also long tempering phases (5-12 h) at temperatures of 700-800 °C helped to obtain highly crystalline samples with a high fraction of the spinel-type gallium oxonitride (Table 4-30, Pos 25, SH_056).

Next to the issue of the necessary synthetic conditions of pressure and temperature for the formation of spinel-type structured gallium oxonitrides, the question of the starting ratio w-GaN : β-Ga_2O_3 was in the focus. Having an ideal composition of spinel-type gallium oxonitride Ga_3O_3N in mind, with the theoretically highest possible nitrogen / oxygen ratio of

N/O = 0.33, the synthesis of nitrogen-rich samples had priority. Using w-GaN and β-Ga$_2$O$_3$ for the high-pressure / high-temperature experiments, the stoichiometrically required starting material to form a compound with the ideal composition Ga$_3$O$_3$N is a mixture of w-GaN : β-Ga$_2$O$_3$ in the molar ratio 1 : 1. Aiming at nitrogen-rich phases in the spinel structure, it was favourable to use starting mixtures of w-GaN and β-Ga$_2$O$_3$ in the molar ratio of 9 : 1 (high excess of w-GaN). However, the ratio of the starting mixture in the investigated system clearly was not decisive for the formation of the spinel-type structure, because both experiments, starting from the molar ratios of w-GaN : β-Ga$_2$O$_3$ = 9 : 1 and 1 : 9, resulted in the formation of the spinel-structured phases, obtained by experiments which were performed under identical conditions (Table 4-30, column 3, Pos. 31, SH_030 and Pos. 39, SH_046). Figure 4-33 and Figure 4-34 show the Rietveld refinements of the two experiments, synthesized with an identical experimental protocol (p = 5 GPa, T$_{max.}$ = 1250 °C, heating protocol: 10 min up to 1250 °C, 15 min at 1250 °C, within 25 min down to 800 °C).
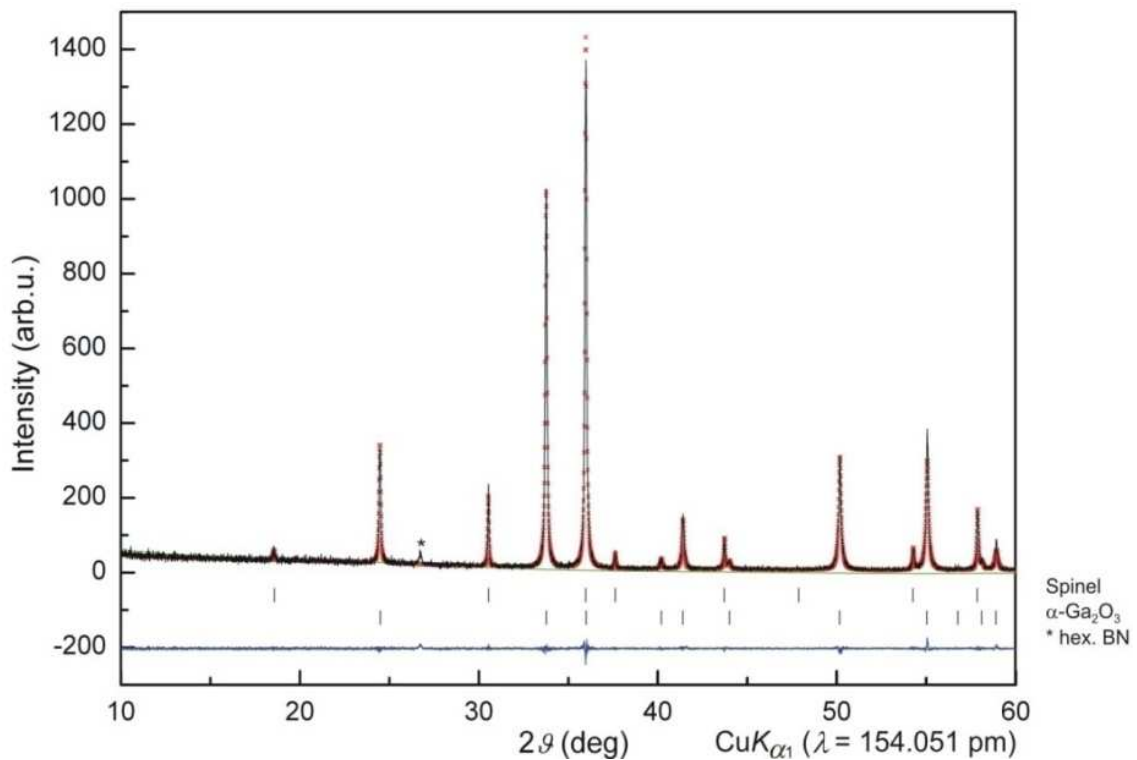
Figure 4-33. Rietveld fit of SH_046 (Pos. 39); starting mixture w-GaN : β-Ga$_2$O$_3$ = 1 : 9 (molar ratio), 5 GPa, 1250 °C displaying spinel-type gallium oxonitride (17 %), α-Ga$_2$O$_3$ (40 %), and hex. BN (from the crucible).
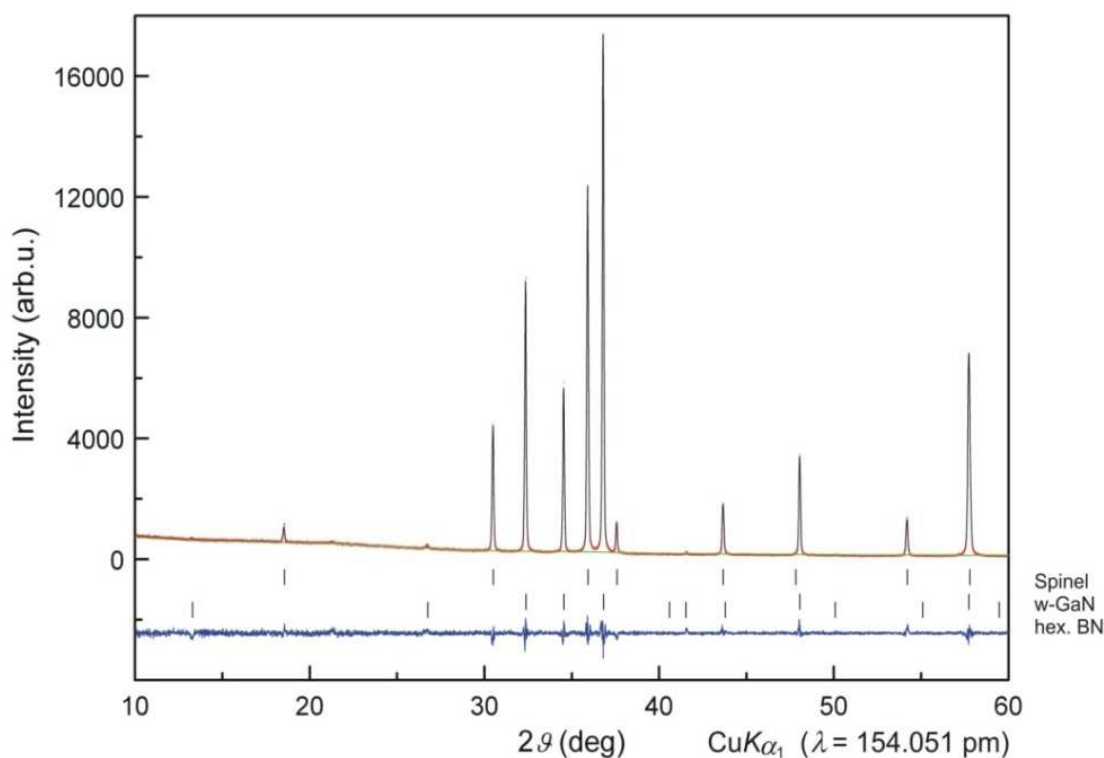
Figure 4-34. Rietveld fit of SH_030 (Pos. 31); starting mixture w-GaN : β-Ga$_2$O$_3$ = 9 : 1 (molar ratio), 5 GPa, 1250 °C, displaying spinel-type gallium oxonitride (40 %), w-GaN (56 %), and hex. BN (from the crucible).

The comparison of both figures clearly indicates that the formation of the spinel-structured phase is much more favoured, when the starting mixture contains a higher amount of w-GaN. In detail, the Rietveld refinements of SH_030 (Table 4-30, Pos. 31) and SH_046 (Table 4-30, Pos. 39) showed a fraction of 40 and 17 % of the spinel-type gallium oxonitride phases, respectively.

In general, the samples derived from a molar ratio of 9 : 1 of wurtzite-structured gallium nitride to β-gallium oxide gave the best results to produce nitrogen-rich spinel-type gallium oxonitrides, so far. Commonly, oxide-rich starting mixtures led to products with a low fraction of the gallium oxonitride spinel phase. Nevertheless, even the lowest fraction of w-GaN in the starting mixture (10 mol-%) led to the formation of the spinel-structured material. This raised the question whether the application of identical experimental parameters could transform pure β-Ga$_2$O$_3$ into a gallium oxide crystallizing in the spinel structure (γ-Ga$_2$O$_3$ [470,490]). Up to now, high-pressure / high-temperature experiments have only led to the high-pressure modification α-Ga$_2$O$_3$ [238,491-493], but not to the desired spinel-type compound γ-Ga$_2$O$_3$ [470,490]. Monoclinic β-Ga$_2$O$_3$ (rel. density: δ = 5.94 g/cm^{-3} [491]) has equal amounts of Ga^{3+} ions on tetrahedral and octahedral positions, while α-Ga$_2$O$_3$ (rel. density: δ = 6.48 g/cm^{-3} [491]; corundum-type structure) exhibits Ga^{3+} exclusively in octahedral coordination. So, in principle, pressure could raise the fraction of six-fold

coordinated Ga^{3+} at the expense of four-fold coordinated cations, leading to a spinel-structured γ-Ga_2O_3. But up to now, a small amount of catalytic gallium nitride is still essential for the formation of a spinel-type structured material, which corresponds to the results of McCauley, obtained and established in 2001 for the alon-system [404]. Therefore, the corresponding nitride plays a decisive role as an additive to form the respective spinel-type structured materials.

The colors of the products are determined by the starting materials. Compounds resulting from a mixture with an excess of nitride always revealed a dark greenish/grey color. Samples synthesized with less nitride showed a brighter color (light-green to yellow) than samples derived from nitride-rich starting mixtures.

Figure 4-35 gives a survey of the experiments which led to spinel-type gallium oxonitrides. The graphic illustrates the effect of the synthesis parameters pressure, temperature, and molar ratio of the starting mixture. The left side of Figure 4-35 provides a view over the pressure and temperature conditions; while the right side shows the same results, turned by 90°, to expose the corresponding molar ratios of the starting mixtures. Figure 4-35 does not include information about heating protocols, remaining educts (w-GaN and β-Ga_2O_3), or transformed α-Ga_2O_3. Such information is available from Table 4-30 and Figure 4-32.
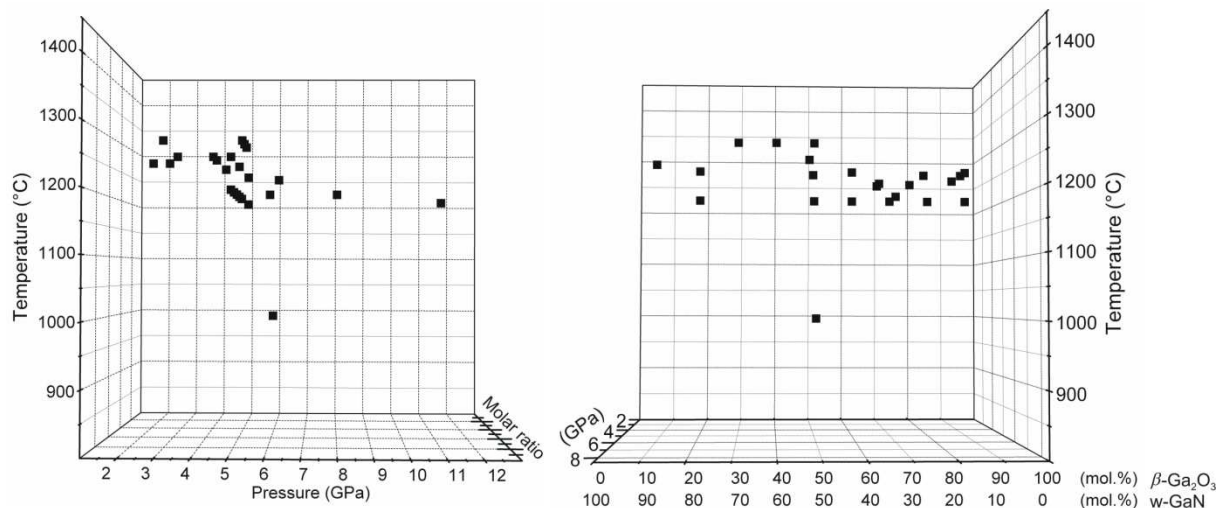
Figure 4-35. Survey of the experiments leading to the cubic spinel-type gallium oxonitrides in dependence of pressure, temperature, and molar ratio w-GaN : β-Ga_2O_3 of the starting mixture.

Figure 4-35 shows clearly that ideal synthesis conditions for the spinel formation lie in the region of 1000-1300 °C while applying pressures in the range of 2.5 up to 11.5 GPa.

All in all, a minimum pressure of 2.5 GPa and an initial temperature of 1250 °C (Table 1, Pos. 8, SH_130) are required to form the crystalline spinel-type gallium oxonitrides. Also experiments performed at higher pressure (>8 GPa) produce the spinel phase, but the degree

of crystallinity of the products decreases dramatically. Presumably, a shift to higher temperatures (>1350 °C) might lead to better results (faster kinetics). The observation that cubic spinel-type gallium oxonitrides can be synthesized at pressures ≥ 2.5 GPa is of high industrial interest, because this pressure can be realized on a commercial scale. So far, the lowest pressure reported by Soignard *et al.* was still 5 GPa at 1700 °C [430], starting from a mixture of α- / β-Ga_2O_3 with w-GaN in the molar ratio of 1 : 1.

This result corresponds with that of recent DAC investigations, confirming the presence of a spinel type material at a pressure of 3 GPa and a temperature of around 1300 °C [494]. Further information is available in chapter 4.4.7.

4.4.5   Conclusion

This work describes a systematic investigation of the formation of cubic spinel-type gallium oxonitrides under high-pressure / high-temperature conditions, starting from mixtures of w-GaN and β-Ga_2O_3 in different molar ratios using the multianvil technique. Starting at high-pressure / high-temperature conditions of 2.5 GPa and 1250 °C (Table 4-30, Pos. 8, SH_130), the formation of the gallium oxonitride spinel can be observed up to pressures of 8 GPa and at a temperature of 1200 °C (Table 4-30, Pos. 56, SH_05). The increase of pressure up to 11.5 GPa at this temperature led to samples containing cubic spinel-type material with a low degree of crystallinity (Table 4-30, Pos. 65, SH_021). Depending on the mixture of the starting materials (w-GaN and β-Ga_2O_3 in the different molar ratios of 9 : 1 up to 1 : 9), the results varied, *e.g.* a high amount of nitride led to spinel-type gallium oxonitrides with a high degree of crystallinity in good yield. *In-situ* X-ray powder diffraction experiments revealed that the cubic gallium oxonitride spinel phase is stable up to temperatures of 1100 °C, without decomposition or cell distortion.

4.4.6   High-pressure Investigations on β-Ga$_2$O$_3$

Within the systematic investigations on the formation on gallium oxonitrides, the phase transformation of β-Ga$_2$O$_3$ to α-Ga$_2$O$_3$ occurred under different high-pressure / high-temperature conditions. The formation of the α-modification of Ga$_2$O$_3$ was already observed at 4.4 GPa / 1000 °C [438], while theoretical calculations on the phase transformation of β-Ga$_2$O$_3$ estimated the necessary pressure to 2.6 or 6 GPa for the transformation (depending on the d-electron handling [442].

4.4.6.1   High-pressure / High-temperature Experiments on the Phase Stability of β-Ga$_2$O$_3$

For the experiments leading to the transformed high-pressure modification of α-Ga$_2$O$_3$, synthesis was carried out in analogy to experiments in the GaON-system.

Monoclinic β-Ga$_2$O$_3$ was filled into a hexagonal boron nitride crucible (Henze BNP GmbH, HeBoSint® S10, Kempten, Germany), positioned inside the center of an 18/11-assembly, and compressed by eight tungsten carbide cubes (TSM-10 Ceratizit, Reutte, Austria).

The assembly was compressed up to 6 GPa within 2.5 h, using a multianvil device, based on a Walker-type module and a 1000 t press (both devices from the company Voggenreiter, Mainleus, Germany). A detailed description of the preparation of the assembly can be found in chapters 2.1.1 - 2.1.1, or references [103,104,111].

In addition to that, several experiments were performed, resulting in the transformed α-compound. The high-pressure / high-temperature conditions and the exact heating protocols can be found in Table 4-30.

The sample was heated electrically in a cylindrical graphite furnace up to 1200 °C in 5 min, temperature was kept constant for 20 min, and cooled slowly down to 850 °C in 100 min at constant pressure. Afterwards, the sample was quenched to room temperature by switching off the resistance heating, followed by a decompression period of 7 h.

After the experiment, the cube was removed from the module, and the sample secured for analytical characterization. The sample was mechanically separated from the surrounding boron nitride of the crucible, and prepared for further powder diffractometry.

4.4.6.2 Analytic on *β*-Ga₂O₃

The samples were analyzed *via* powder diffractometry, applying a Stoe Stadi P device equipped with Cu*K*$_{\alpha 1}$ radiation. Figure 4-36 shows the powder diffraction pattern of the sample, derived from high-pressure / high-temperature experiments at 6 GPa and 1200 °C. Characterization of the powder pattern revealed small impurities of rhombohedral GaBO₃ [495] as by product and BN from the crucible.
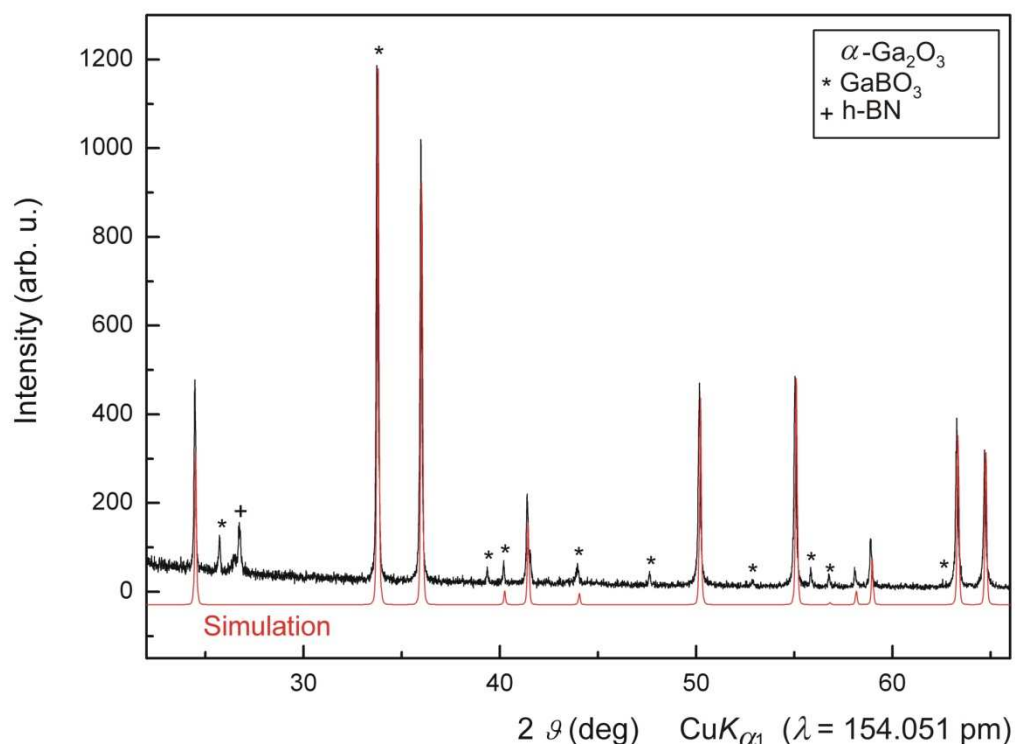
Figure 4-36. Powder diffraction pattern of *α*-Ga₂O₃, transformed at 6 GPa, 1200 °C, displaying *α*-Ga₂O₃, w-GaN, GaBO₃, and hex. BN (from the crucible).

4.4.6.3 Results and Discussion on *β*-Ga₂O₃

Within the investigations in the binary phase diagram of w-GaN and *β*-Ga₂O₃ the transformed high-pressure modification of *α*-Ga₂O₃ occurred at different high-pressure / high-temperature conditions. A successful transformation of *β*-Ga₂O₃ into *α*-Ga₂O₃ was observed, starting at low pressures of 2 GPa, at 1350 °C up to pressures of 11.5 GPa at 1200 °C. Table 4-32 shows the high-pressure / high-temperature conditions for a successful formation of the high-pressure modification of *α*-Ga₂O₃.

Table 4-32. Observed $\beta \rightarrow \alpha$ transformation in high-pressure / high-temperature experiments.

Pressure [GPa]	Temperature range [°C]	Pressure [GPa]	Temperature range [°C]
2	1200	7	1200
2.5	500-1300	8	1100-1200
4.5	500-1250	9.2	1300
5	1100-1300	11.5	1200
6	700-1250		

4.4.6.4   Conclusion

The phase transformation of β-Ga_2O_3 into the α-modification of gallium oxide was observed at pressures ranging in between 2 GPa and 11.5 GPa in the presence of w-GaN. Scanning the literature, the lowest pressure reported so far was estimated *via* theoretical calculations to pressures of 2.6 and 6 GPa, respectively, for the transformation (depending on the *d*-electron handling [442]). From these results we can assert that the phase transformation of β-Ga_2O_3 into α-Ga_2O_3 in the presence of w-GaN already starts at pressures of 2 GPa (at high temperatures; 1350 °C).

4.4.7   Diamond Anvil Cell Investigation on Gallium Oxonitrides

The investigations on gallium oxonitrides, using a diamond anvil cell, were performed by C. Zvoriste and L. Dubrovinsky in the high-pressure facilites in Bayreuth.

These high-pressure / high-temperature investigations using laser heated diamond anvil cells led to the successful synthesis of spinel-type gallium oxonitrides. The *in-situ* investigations were performed in addition to the multianvil syntheses. Applied were mixtures of w-GaN : β-Ga_2O_3 in the molar ratio of 3 : 2. Additionally, high-pressure experiments were performed using gallium oxonitride ceramics derived from pyrolysis processes, starting from a molecular single source precursor $(Ga(O^tBu)_2NMe_2)_2)$ [428]. In these experiments, we tried to limit the required high-pressure / high-temperature conditions to a minimum, while obtaining crystalline compounds.

4.4.7.1   DAC Experiments on Gallium Oxonitrides

Different starting mixtures in different molar ratio of β-Ga$_2$O$_3$ (99.9 %, Sigma Aldrich, Munich, Germany) and w-GaN (99.9 %, Alfa Aesar, Karlsruhe, Germany) in the molar ratio of 6 : 4 were applied., The starting mixtures, applied as fine powders, were ball milled and compacted, to grant homogeneity of the samples, before used in the experiment.

The high-pressure experiments were performed in a modified Merril-Basset type (four-pin opposite-plate type) diamond anvil cell, equipped with a laser-heating facility using a cw Nd:YLF laser with a maximum power of 50 W (λ = 1064 nm, Quantronix Inc., USA), heating the cells from both sides. During the experiment, laser scans were arranged, varying between 10 to 20 min, depending on the experiment. Temperature was controlled spectroradiometrically, while the pressure was measured at ambient temperatures with the ruby fluorescence method. Nitrogen was added as pressure medium, compressed by 0.14 GPa, while rhenium foil was applied as gasket material. The culet sizes of the mounted diamonds ranged between 300 to 500 μm.

In-situ powder diffraction pattern were recorded using a rotating anode X-ray diffractometer with a FR-D high-brilliance source (RIGAKU Corporation; with Mo$K_{\alpha1}$ (λ = 71.073 pm) radiation) OSMIC Inc. Confocal Max-Flux optics, and a SMART APEX 4K CCD area detector were used.

For experiments starting from gallium oxonitride ceramics, LiF was used as pressure transmitter, beside the pressure standard [496]. The dimension of the diamond anvil cell culet resulted to 400 nm, applied with rhenium gaskets. The actual pressure was determined by adding ruby chips to the sample and detecting the resulting fluorescence spectrum.

4.4.7.2   Results and Discussion for Gallium Oxonitrides

The formation of spinel-type gallium oxontrides was investigated using a laser-heated diamond anvil cell (LH-DAC). In addition to the multianvil experiments, starting mixtures of w-GaN and β-Ga$_2$O$_3$ were applied, to provide insights into the formation region of gallium oxonitrides by filling gaps in the binary phase diagram of w-GaN and β-Ga$_2$O$_3$. In contrast to

that, the precursor approach leads potentially to phase-pure spinel-type compounds under less extreme conditions.

The compressibility of gallium oxonitrides was investigated to determine the corresponding bulk modulus. Therefore, compression-decompression runs were performed applying the precursor-derived amorphous gallium oxonitride ceramic. Loading the spinel-compound next to a thin pellet of LiF into a DAC, the compression was started and experiments were performed up to pressures of 9 GPa. Crystallization of the amorphous compound was observed at pressures of 1 GPa initiated *via* laser heating. Figure 4-37 shows the results of the Rietveld refinement, proving the formation of the spinel-compound, next to LiF.
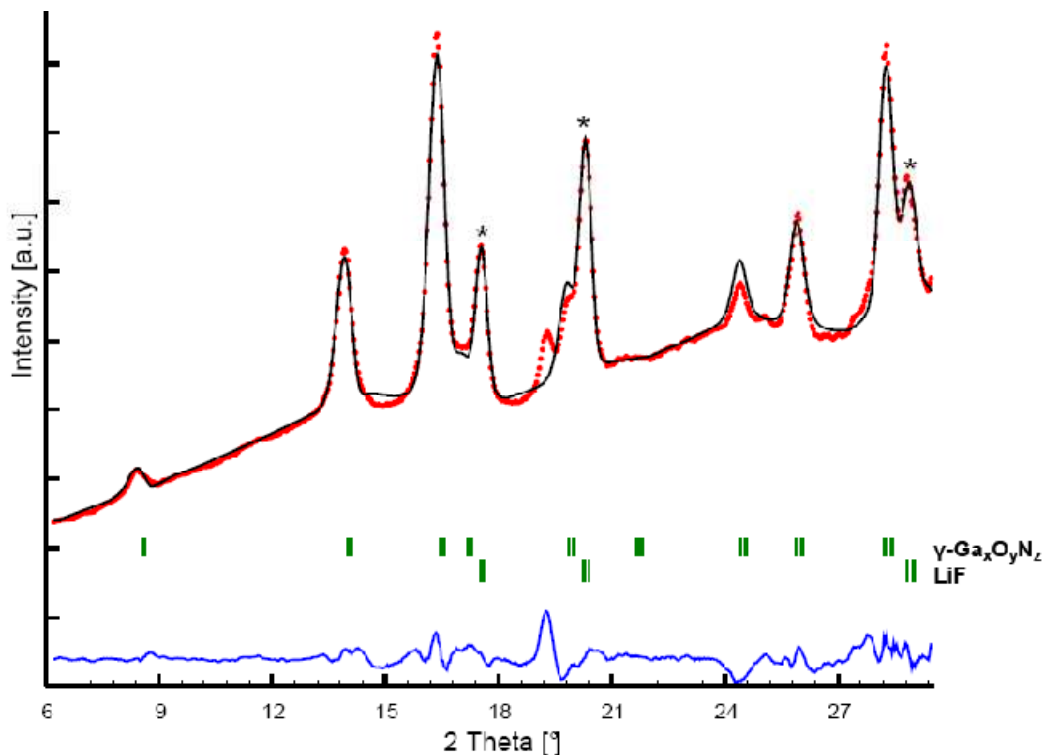
Figure 4-37. Rietveld refinement of a X-ray diffraction pattern showing the spinel-type gallium oxonitride (first phase) and LiF (second phase), data collected from an *in-situ* LH-DAC synthesis (0.7 GPa, 1300 °C). The experimental data points are shown as a dotted line and the fit to the data with a solid line. The * mark stands for the LiF reflections. The reflection at 2θ 19.3 is attributed to Re, the gasket material.

The reflections were related to a spinel-type compound, exhibiting the space group ($Fd\bar{3}m$, 227) beside the LiF reflections, derived from the pressure transmitting medium. Figure 4-38 shows the powder diffraction pattern, depending on the applied pressure, confirming pressure stability up to 9 GPa.
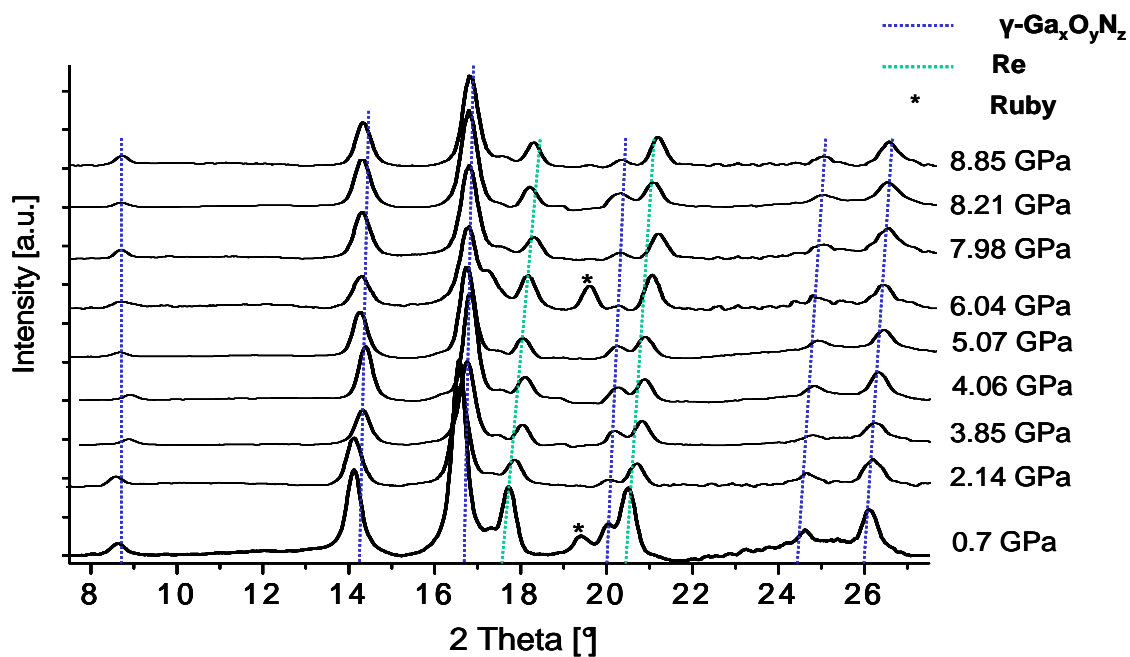
Figure 4-38. XRD patterns from the compressed diamond anvil cell containing as starting material the gallium oxonitride ceramic which was completely transformed into the spinel $Ga_xO_yN_z$ from 0.7 GPa. Up to 8.85 GPa no other by-products were observed

In Figure 4-39 the function P-V is shown. The results of measuring the pressure in dependence of the unit cell volume for a precursor-derived gallium oxonitride sample, synthesized at 0.7 GPa at 1300 °C, are shown.
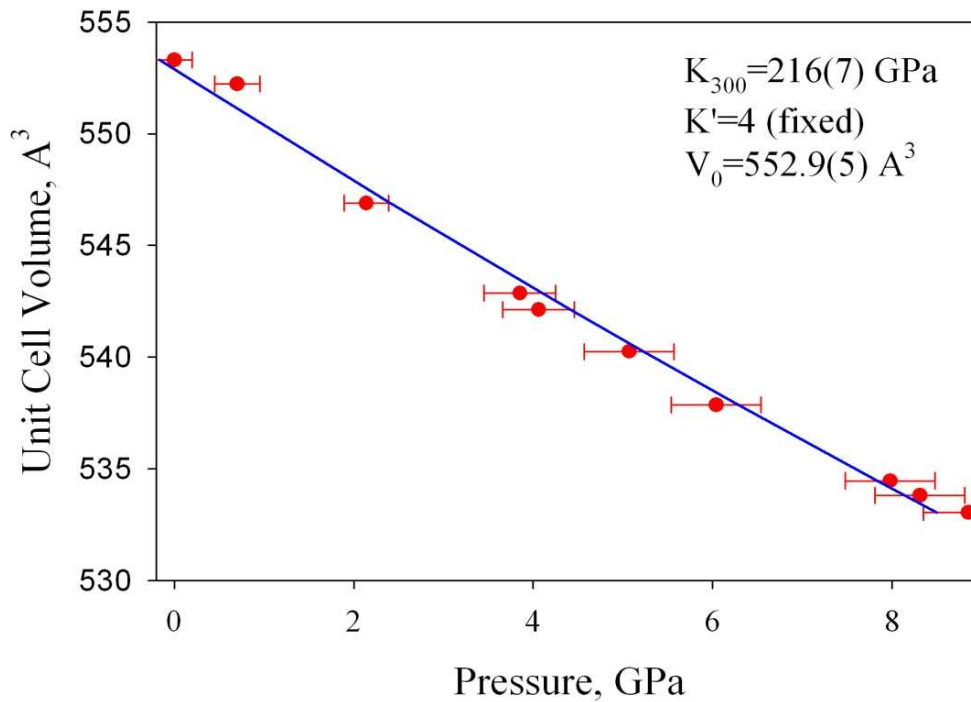
Figure 4-39. Unit cell volume of the spinel-type $Ga_xO_yN_z$ as a function of pressure. The experimental data are shown by solid circles. The error-bars of the unit cell volume are within symbols. The solid line represents the least-squares fit of the second-order Birch-Murnaghan EOS to the experimental data. The fit yielded K_{300}=216(7) GPa having K' fixed to 4.

The bulk modulus K was estimated to 216(7) GPa leading to a volume at zero pressure of $V_0 = 552.9(5)$ Å^3, by data fitting accomplished with second order Birch-Murnaghan equation EOS (K' = 4). A comparison of the results with data known from the literature shows that both, experimental and thereoretical data stand in good accordance to our results (Table 4-33).

Table 4-33. Experimental and calculated bulk modulus for the spinel-type gallium oxonitride.

$Ga_xO_yN_z$ (this work)	Ga_3O_3N cal. [497]	Ga_3O_3N exp. [430]	γ-Si_3N_4 exp. [498]	Si_2AlON_3 cal. [499] normal/inversed
216(7)	232 (177) LDA (GGA)	234	302(6) (K'=4)	260 / 271

The results for the bulk moduli vary with the applied experimental conditions. Therefore, the data should be handled carefully, though considerable influences can also be caused by the applied pressure medium. Nevertheless, spinel-type gallium oxonitrides show a considerable

hardness with a calculated bulk modulus of >200 GPa, compared to γ-Si$_3$N$_4$ [498] (302(6) GPa).

4.4.7.3 Conclusion

Experiments using mixtures of w-GaN and β-Ga$_2$O$_3$ or alternatively amorphous precursor-derived gallium oxonitride ceramics (mean N/O-ratio 1.02) were performed at different pressures. The lowest pressure for a gallium oxonitride spinel formation was determined to 3 GPa, starting from w-GaN and β-Ga$_2$O$_3$. Applying the ceramic, however, synthesis was successful at 0.7 GPa performed in a laser heated diamond anvil cell. Calculation of the bulk modulus and comparison to the known compounds of high hardness, such as γ-Si$_3$N$_4$, leads to the assumption that the spinel-type compounds can be counted as materials of high hardness. Moreover, spinel-type gallium oxonitride was found to be stable on compression to at least ~9 GPa and to have a bulk modulus K of 216(7) GPa (with fixed K' = 4).

5 Prospects

Rare-earth Gallates

Research on rare-earth gallates is still in the scientific focus, as they show interesting properties, *e.g.* paramagnetism, ferrimagnetism, ferromagnetism, or antiferromagnetism, which is used for industrial applications. Different rare-earth gallates are known in diverse stoichiometric compositions, like RE_3GaO_6, $RE_3Ga_5O_{12}$, $RE_4Ga_2O_9$, or $REGaO_3$. Research on gallates was started by Menzer and Weidenborner with the composition $RE_3Ga_5O_{12}$ [195-197]. Their work led finally to compounds in the stoichiometric ratio of $REGaO_3$. Within the chemistry of rare-earth gallates, analogue compounds equipped with different central metal ions are also known, *e.g.* in $REMO_3$ (M = Cr, Mn, Fe, Al, Ga) [215]. Only a few rare-earth gallium compounds with the composition $REGaO_3$ (RE = La, Pr, Nd, Gd, Ho) [219,225-228] could be obtained as single crystals so far. Mostly the compounds were obtained as fine powders. Therefore experimental conditions were extended into high-pressure / high-temperature chemistry. The application of high-pressure conditions helped Marezio *et al.* to obtain crystalline $REGaO_3$ compounds (RE = La, Pr, Nd, Sm-Lu) [217]. But as the single crystals were still too small for single crystal data collection, the orthorhombic structures were determined by powder refinement.

Within our high-pressure investigations on rare-earth gallates, we tried to enlarge the existing compositions of the different rare-earth gallates under high-pressure / high-temperature conditions, by using a variation of different rare-earth oxides (RE = La, Ce, Tb, Dy, Ho, Er, Tm, Yb, Lu) applied in different molar ratios, while scanning the high-pressure range. Unfortunately, the experiments did not lead to new compounds up to now. Instead of, we obtained several crystalline samples in different stoichiometric compositions of diverse rare-earth gallates, wherefrom single crystal structure determination was possible for the first time.

Our access to these crystalline samples started from the corresponding rare-earth oxides (RE = Dy, Ho, Tm) and β-Ga_2O_3 in different molar ratios. The pressure conditions ranged in between 5-12 GPa, while the applied temperatures were varied within 800-1300 °C.

Elevated high-pressure / high-temperature conditions of 7.5 GPa and 1250 °C, starting from the binary oxides, allowed to synthesize measurable single crystals of REGaO$_3$ (RE = Ho, Dy) for the first time.

The comparison of the single crystal data for HoGaO$_3$ and DyGaO$_3$ were in good accordance to the already existing powder data from Marezio *et al*. The single crystal data for HoGaO$_3$ ($a = 553.0(2)$, $b = 753.6(2)$, $c = 525.4(2)$ pm [228] and DyGaO$_3$ ($a = 552.5(2)$, $b = 754.4(2)$, $c = 527.7(2)$ pm (standard setting: *Pnma*) correspond well to the original values of Marezio *et al*. (HoGaO$_3$: $a = 525.1(2)$, $b = 553.1(2)$, $c = 753.6(2)$ pm and DyGaO$_3$: $a = 528.2(2)$, $b = 553.4(2)$, $c = 755.6(2)$ pm (setting: *Pbnm*) [216]).

For further investigations, increasing the applied high-pressure / high-temperature conditions might give access to new compounds. Up to know, the high-pressure route into rare-earth manganites, ferrites, and aluminium compounds were not tried. Maybe, here we can enlarge the existing different compositions.

Rare-earth Borates

Various different borates of rare-earth, transition metal, alkali metal, alkaline earth metal, and main metal borates were synthesized under high-pressure / high-temperature conditions. Due to the great efforts of Huppertz and his co-workers, a multitude of different borates, exhibiting a great structural diversity, were synthesized. Although more than 500 different borates are known, rare-earth borates with an exceeding amount of rare-earth element in the structure are still rare.

Within this thesis, the first compound of the stoichiometric composition Ho$_{31}$O$_{27}$(BO$_3$)$_3$(BO$_4$)$_6$ was synthesized. The ratio of Ho : B results in a value of 3.44, as it exhibits a quite high amount of rare-earth in the structure. The high-pressure / high-temperature synthesis started from boron oxide and holmium oxide and required high-pressure / high-temperature conditions of 7.5-11.5 GPa at 1250 °C.

The interesting compound Ho$_{31}$O$_{27}$(BO$_3$)$_3$(BO$_4$)$_6$ offers a new structure, exhibiting isolated BO$_3$-units next to isolated BO$_4$-groups, imbedded in a network of holmium-polyhedra. This structure is particularly amazing, as in accordance with the pressure coordination rule, coordination numbers normally increase, influenced by extreme conditions. However, here the three-fold coordinated boron atoms remain stable.

Due to the exceptional structure, experiments starting from other rare-earth elements (*RE* = La, Tb, Dy, Tm, Yb, Lu) were performed, but the results have not led to the designated composition, yet. Variations of the required pressure and temperature conditions, as well as heating and cooling protocols are needed, to obtain finally the analogue compounds.

As it is the first compound showing this composition within the row of rare-earth oxoborates, future work should concentrate on the syntheses of analogue structures scanning the row of late rare-earth elements.

Recently, a new borate occurred as side product, showing the typical apatite structure. At this point, we can confirm, that the compound crystallizes hexagonal in the space group *P*63/*m* (no.176). Further investigations are necessary, to prove the indicated property of oxygen conductivity due to the structure. More experimental work has to be done in order to confirm the structure and learn more about the specific physical properties.

Phase Transformations

Due to several working groups, the system of rare earth sesquioxides is well known. Hoekstra investigated the conditions, which led to metastable modifications. According to the ionic radii, the three groups of rare-earth oxides, type A, B, and C adopt the corresponding structures. While the early oxides crystallize hexagonally, the monoclinic structure is subjected to the rare-earth elements starting from *RE* = Sm - Tb. The late rare-earth oxides are found in the cubic C-type structure.

Under elevated temperatures or pressures, phase transformations to the monoclinic structure were achieved. Several experiments of Hoekstra and Foex [267,268,271] showed that the transformation is catalyzed by adding CaO, SrO, and other oxides to the educt.

These investigations stand in good accordance to our results. Although well investigated, the structure of these compounds could not be confirmed by single crystal data up to now. High-pressure / high-temperature investigations led to the monoclinic compound B-Ho_2O_3 which was obtained as crystalline sample, wherefrom a single crystal structure determination was possible for the first time. The comparison to theoretical investigations on B-RE_2O_3 of Wu *et al*. [247] showed that both results stand in good accordance with each other.

Investigations on the synthesis conditions showed that for the transformation high-pressure / high-temperature conditions of 11.5 GPa and 1250 °C led to highly crystalline

samples. The reduction of the pressure (7.5 GPa and 1250 °C) resulted in a crystalline material with a lower degree of crystallinity. This observation is often seen in the field of borates and other compounds. Further experiments, concerning the catalytic influence on the reaction, confirmed the results of Foex [271]. Successful transformations were carried out by adding some additives to the educts. The experimental work showed that the addition of β-Ga_2O_3, h-BN, or a mixture of h-BN and B_2O_3 help to transform the compounds.

In analogy to monoclinic B-Ho_2O_3 other rare-earth oxides were investigated. Recently, the transformed compound B-Dy_2O_3 was synthesized under high-pressure / high-temperature conditions of 7.5 GPa and 1100 °C. The reaction was carried out by adding a small amount of hex. BN, which helped to transform the compound. Unfortunately, the crystal size was too small for collecting single crystals for further structural investigations. The transformation occurred also in the case of Tm_2O_3. For future investigations, the experiments on phase transformations of the rare-earth oxides should be continued, to obtain also the monoclinic phases of other late rare-earth sesquioxides. In addition to that, the influence of the flux should also be explained, as it might be interesting for future investigations on rare-earth compounds.

Gallium Oxonitrides

Certain oxides, nitrides, and oxonitrides are in the scientific focus, due to their interesting optoelectronic and mechanical properties. These compounds offer interesting chances for industrial purposes, due to high temperature stability and extreme hardness [500]. Due to the success of Alon materials, research on gallium oxonitrides was commenced. Although the binary phase system of Al_2O_3 and AlN is well investigated, the corresponding phase diagram of Ga_2O_3 and GaN was still not accessible.

As only scarce information on gallium oxonitride is available, systematic high-pressure / high-temperature investigations on gallium oxonitrides were in the focus of this work. Experiments were performed under variation of the applied pressures (1-11.5 GPa) and temperatures (500-1350 °C), as well as of the molar ratio of the starting materials β-Ga_2O_3 and w-GaN (w-GaN : β-Ga_2O_3 = 9 : 1 - 1 : 9). The systematic approach starting from the binary compounds into the stability field of gallium oxonitrides enlightened the formation region for a gallium oxonitride compound synthesized under high-pressure / high-temperature conditions. Crystalline compounds were obtained at the lowest pressure of 2.5 GPa at

1250 °C. The synthesis temperature could be reduced to a minimum of 1000 °C at 6 GPa. The ideal conditions for highly crystalline samples was determined to 5 GPa and 1250 °C, resulting in measurable single crystals, wherefrom the cubic spinel-type structure was confirmed on single crystal data for the first time, which stands in good accordance with theoretical calculations.

As it is important to obtain phase-pure samples, the synthetic conditions have to be improved to avoid by-products or residuals of starting materials in the sample. Within the variation of the molar ratio of the starting materials, a small amount of β-gallium oxide or w-gallium nitride was always detected in the sample, wherefore the determination of the density of the spinel compounds had to be deferred.

A different high-pressure / high-temperature approach into gallium oxonitrides started from gallium ceramics. A new precursor-route was taken, providing a single source molecular precursor, which offered gallium simultaneously bonded to nitrogen and oxygen. After heat-treatment, the compound $Ga_{2.81}O_{3.57}N_{0.43}$ was synthesized under high-pressure / high-temperature conditions of 7 GPa and 1100 °C. *In-situ* investigations on the formation of a precursor-derived spinel compound were conducted using the diamond anvil cell. The phase-pure compound occurred at the lowest conditions of 1 GPa at 1300 °C.

In the near future, investigations on phase stability, optical, and mechanical properties are important for possible technical applications on industrial intentions.

Indium Oxonitrides

Scanning the literature on group III oxonitrides, there are only a few different aluminium and gallium oxonitrides known so far. As for indium oxonitrides only little information is available, several working groups commenced to work on the indium oxonitride system. The first working group reported about thin films, containing indium besides oxygen and nitrogen in a nonstoichiometric ratio [501]. As research on indium oxonitrides continued, thin InON-films derived from different synthesis methods, such as reactive radio-frequency (RF) sputtering [502,503], or *via* chemisorbed oxygen on radio frequency derived indiumnitride films were reported [504]. Even though, an access onto indium oxonitride compounds was found, the compounds suffered always from a low degree of crystallinity as they occurred only as thin films. The task, to synthese crystalline InON-compounds is interesting not only because of promising industrial applications, but also to learn more about the phase stability

of the InN-In$_2$O$_3$ system. Here, a phase diagram is still missing, although the educts are well investigated. Calculations showed that a phase transformation starting from w-InN to the semiconducting rocksalt structure should occur at pressures of 12.1 or 21.6 GPa [505,506], which is of high interest based on the demands for electrical and optical devices. Experimental work confirmed the predicted pressure range, as the transformation of w-InN into the rocksalt structure occurred at 10-12 GPa, depending on the heating [507].

In order to provide the improvement of high phase stability, relations between different structures of indium oxide (bixbyite- and corundum-type structure) were investigated. As both structures are widely known, the metastability of indium oxide polymorphs was investigated theoretically, as well as experimentally. The working group of Riedel reported on phase transitions starting from the cubic bixbyite-structure (obtained under ambient pressure conditions by the sol-gel method) and the transformation under high-pressure / high-temperature conditions (13.5 GPa) into the corundum-type indium oxonitride. Another phase transition into the Rh$_2$O$_3$-II-type is predicted at pressures exceeding 15 GPa [508].

Based on the successes on aluminium and gallium oxonitride compounds, research enlarged into the field of indium oxonitrides. Though applying high-pressure / high-temperature conditions into the GaN-Ga$_2$O$_3$ system led to new compounds, we transferred our knowledge to the InN-In$_2$O$_3$ system. Different high-pressure / high-temperature conditions were applied. Pressure was varied between 3 up to 11.5 GPa at temperatures ranging in between 550 and 1100 °C, using different heating protocols. The variation of the starting material comprised application in different molar ratios (InN : In$_2$O$_3$ = 1 : 9 up to 9 : 1) besides different educts. The experiments were started from w-InN and rhombohedral In$_2$O$_3$, besides syntheses using w-InN mixed with metallic indium (tetragonal), or a mixture of InN, In$_2$O$_3$, and metallic indium. To increase the nitrogen content, ammonium azide was added to the reaction mixture to enforce the formation of an indium oxonitride in nitrogen atmosphere *via* careful decomposition of the azide into ammonia and nitrogen. EDX measurements confirmed the elements In, O, and N in nanocrystalline indium oxonitride particles, which were far too small for a single crystal data collection. Although various experiments were performed, the degree of crystallinity could not be increased, so far.

For experiments starting from metallic indium instead of indium oxide, ammonium azide was added as nitrogen source, to form highly reactive indium nitride inside the sample. EDX data confirmed the formation of indium nitride, but reactions leading to oxonitrides

were not observed. Therefore, research must continue, exceeding the applied pressure conditions under variation of the temperatures, as well as heat-treatment protocols.

A different approach into InON-compounds was tried *via* normal pressure synthesis. Mixtures of w-InN and rhombohedral In_2O_3 mixed with ammonium azide were filled into silica glass ampoules, welded and heated in tube furnaces up to 1000 °C, applying long heating and tempering phases. Although the product showed under EDX analysis the presence of the elements In, O, and N, the resulting powder could not be characterized up to now.

These samples could be used as a precursor material for high-pressure synthesis. Variations of the temperatures including different heating and tempering phases could also improve the reaction product.

In order to apply for better results, further normal pressure and high-pressure experiments should follow, trying to localize the ideal conditions and formation region of crystalline compounds in good yield and without by-products. In lack of a precise phase diagram of the binary compounds InN and In_2O_3, more experiments leading to new compounds must be provided. In addition to high-pressure / high-temperature experiments performed in Walker-type multianvil devices, high-pressure experiments using diamond anvil cells would be helpful for the determination of the exact formation tendencies, not only to define the required pressure conditions but also to confirm the phase transformation of the starting materials and formation of the indium oxonitride compound *via in-situ* X-ray powder diffraction.

A successful approach into gallium oxonitrides applied a single-source molecular precursor in high-pressure experiments conducted in a Walker-type multianvil device as well as in diamond anvil cells. Obviously, starting from an indium ceramic could lead also to crystalline indium oxonitrides *via* a ceramic precursor. Therefore, synthesis of the analogue indium compound, starting from a dimethylamine adduct of indium tris-(t-butoxide) $In(O^tBu_3) \cdot HNMe_2$, would lead to a molecular precursor and finally *via* pyrolysis processes to the ceramic compound. An important point would be to retain control on the oxygen to nitrogen content in the compound.

As it is widely known, chlorides are highly reactive. Under variation of different high-pressure / high-temperature conditions experiments starting from the corresponding indium(III)chloride mixed with indium nitride in different molar ratios were performed. Preparation of the experiment required handling of the compounds in a glove box under argon atmosphere. After high-pressure / high-temperature synthesis, the compound was still sensitive against air and moisture. An unidentified phase occurred with a low degree of

crystallinity, which could not be characterized yet. Based on these first results, we see that it could be a successful route to crystalline indium oxonitride compounds, obtained with small amounts of chlorine-by-products.

Gallium Indium Oxonitrides

Besides our investigations in the systems Ga-O-N and In-O-N, we tried to synthesize mixed oxonitride compounds with gallium and indium in the system.

In the literature only a few mixed oxide-compounds are known, one published by Goldschmidt *et al.* [242] derived from starting mixtures of In_2O_3 and Ga_2O_3 resulting in different compositions and structures. He investigated the system and received different oxidic compounds crystallizing in the cubic type C rare-earth structure, or the crystal structure of α- alumina and β-gallia, depending on the synthesis temperature.

A new phase of the composition $(In,Ga)_2O_3$ in a structure similar to κ-alumina was obtained by Schneider *et al.* [214]. This structure was confirmed later on by MacDonald *et al.* who considered this phase as a monoclinic structure with an equivalent 1:1-composition [509]. Finally, confirmed by Cava *et al.* [510], the monoclinic $InGaO_3$ compound was derived from the corresponding oxides and can be considered as the β-phase in correspondence to the β-Ga_2O_3 structure.

Alongside, hexagonal $InGaO_3$-II was found by Shannon *et al.* It is considered as a high-pressure modification of $InGaO_3$, which can be synthesized under an applied pressure of 6.5 GPa at temperatures of 1200 °C [511].

But not only experimental work was done on the indium and gallium oxides. Also theoretical calculations concerning the stability of the sphalerite structured alloys in the composition $Ga_xIn_{1-x}N$ were performed by Saib *via* ab initio-methods [512].

Our systematic investigations under high-pressure / high-temperature conditions started from mixtures of Ga_2O_3 / In_2O_3, Ga_2O_3 / InN, and In_2O_3 / GaN in different molar ratios. Various different heat-treatment protocols were applied, scanning a pressure range between 1 GPa up to 12 GPa, at temperatures of 400 up to 1350 °C. Typically, we obtained the high-pressure modification of $InGaO_3$ but did not succeed in synthesizing new compounds, so far. As a matter of routine, the samples were investigated with powder diffractometry, which resulted often in unknown reflections in the pattern, but as the samples suffered always from crystallinity, a distinct assignment of the reflections was not possible.

Here, the addition of chlorine-compounds might be helpful, to increase the reactivity of the starting materials. A lot more experimental work must be done, to continue these first steps into the new system under elevated temperatures (for oxides) and addition of a nitrogen source (ammonium azide).

Mixed Oxonitrides with Aluminium and Gallium

Following the results for aluminium oxonitrides, research on mixed compounds was also started. In the literature, only two Al-Ga-N-compounds are known, $Al_{0.8}Ga_{0.2}N$ and $Al_{0.5}Ga_{0.5}N$ [513,514], which were obtained as thin films, while Al-Ga-O-N-compounds are not known yet. The analogue Al-In-system is also scarcely investigated. Doping of aluminium oxide with indium resulted in the compound $Al_{11}In_{1.23}O_{17}$. It crystallizes in the "β-alumina" structure and was obtained in form of single crystals, wherefrom a single crystal determination was possible [515].

Synthesis started from mixtures of AlN with Ga_2O_3, AlN with GaN, and AlN with In_2O_3, besides AlN mixed with InN in different molar ratios under high-pressure conditions of 5-8 GPa and temperatures of 600-1200 °C. Due to the strong chemical affinity of aluminium to oxygen, we obtained only Al_2O_3 and the corresponding oxides of gallium and indium in small amounts.

The first steps are made, now more experiments must follow. In order to learn more about the behavior of the educts under extreme conditions, systematic investigations are required. Under variation of the applied pressures and temperatures, influences of heat-treatment protocols should also be examined.

6 Summary

6.1   High-pressure / High-temperature Syntheses

High-pressure / high-temperature conditions provide the possibility to synthesize new metastable compounds, which are not accessible under normal pressure.

Various different chemical fields were investigated by now, leading to new structures and compounds. Interesting results for industrial purposes, advanced materials, and improvement of still existing materials are the driving force in high-pressure chemistry. According to the pressure coordination rule, coordination numbers increase under pressure as often seen in the field of borates [277], as boron often forms tetrahedrally coordinated BO_4-groups under elevated pressure.

The parameter pressure enables also crystallization. Gallium oxonitrides require elevated pressure to form crystalline compounds to resolve the high stability of galliumoxide, which is energetically and kinetically favoured. Theoretical results show that high pressures and high temperatures at the same time are required to provide crystalline gallium oxonitride compounds.

The stability investigations on gallium oxonitrides were all performed under high-pressure, to localize the ideal conditions for the formation of the spinel-type material. Initiated by extreme conditions, phase transformations of educts are observed. As often used for pressure calibration sets, changes in the structure can be caused at these conditions. As by-product different transformed compounds occurred, always in high crystallinity.

Since the first artificial diamond was synthesized, several different high-pressure devices were constructed. Starting with the belt apparatus, followed by the tetrahedral arrangement, the technological progress led to the multianvil Walker-type device, which works with eight equal anvils. The pressure conditions were improved with every technical step, taken towards the apparatus used today.

The 1000 t presses are equipped with multianvil Walker-type moduls working with an octahedral cavity for the sample. The experimental work in this thesis reflects the prospects which are provided by this method. This offers the best possibilities for high-pressure

chemistry, combining reasonable costs, large sample volumes, and extreme pressure and temperature conditions, at the same time.

6.2   Rare-earth Gallates

DyGaO$_3$

The structure of the orthorhombic rare-earth gallate DyGaO$_3$ was already known from the literature, but only powdered samples were obtained, so far. Single crystal data exists only for the following rare-earth orthogallates REGaO$_3$ (RE = La, Pr, Nd, Gd, Ho) [219,225-228].

High-pressure / high-temperature experiments led to single crystals suitable for a single crystal data collection.

The orthorhombic DyGaO$_3$ crystallizes in the space group *Pnma* (no. 62) (Z = 4) with the parameters a = 553.0(2), b = 753.6(2), c = 525.4(2) pm, $R1$ = 0.0222, and $wR2$ = 0.0303 (all data).

The structure of the orthorhombic DyGaO$_3$ can be described as isostructural with the rare-earth

Figure 6-1. Crystal structure of DyGaO$_3$.

orthoferrites, possessing an orthorhombic perovskite-like structure in the GdFeO$_3$-type. It consists of slightly distorted GaO$_6$-polyhedrons, connected *via* corner-sharing, forming traces through the structure. Therefore, every corner is connected with another corner of a near GaO$_6$-octahedron. The Dy^{3+}-cations build up displaced layers, with the cations positioned among the GaO$_6$-octahedrons in the resulting channels (Figure 6-1).

The comparison of the different lattice parameters a, b, and c of all known rare-earth gallates, standard setting (space group: *Pnma*) including the values of DyGaO$_3$, shows an exceptional behavior: while the b and c parameters smoothly decrease in going from La to Lu, the parameter a exhibits an unexpected behavior, showing a maximum approximately at Gd (Figure 6-2). Marezio *et al.* observed for the rare-earth gallates (powder data [216]) the same increasement, as Eibschütz did for the corresponding orthoferrites [230].

This effect is commonly interpreted as consequence of the size of the rare-earth cations: as the size of the RE^{3+} decreases, the average RE^{3+}-O distance of the first nearest

oxygen atoms decreases as well (first effect), whereas the average RE^{3+}-O of the second nearest oxygen atoms increases (second effect). Only parameter a is affected by this double effect, leading to an increasement within the row of rare-earth elements, starting from La to Gd. In this region, the second effect is the predominant one, whereas it decreases within the series from Gd to Lu, because here the first effect is predominant compared to the second effect. This rather unsatisfying explanation has to be checked in the future, when the missing single crystal data in the whole rare-earth gallates series will be available. Similar observations were described by Berkowski *et al.*, who investigated single crystals of the solid solution $La_{1-x}Nd_xGaO_3$ [516]. It was found that the volume of unit cell decreases linearly in correlation with an increasing Nd concentration according to Vegard´s law. This agrees with the general behavior of all ternary rare-earth gallates, showing decreasing volumes due to the lanthanide contraction (Figure 6-2).
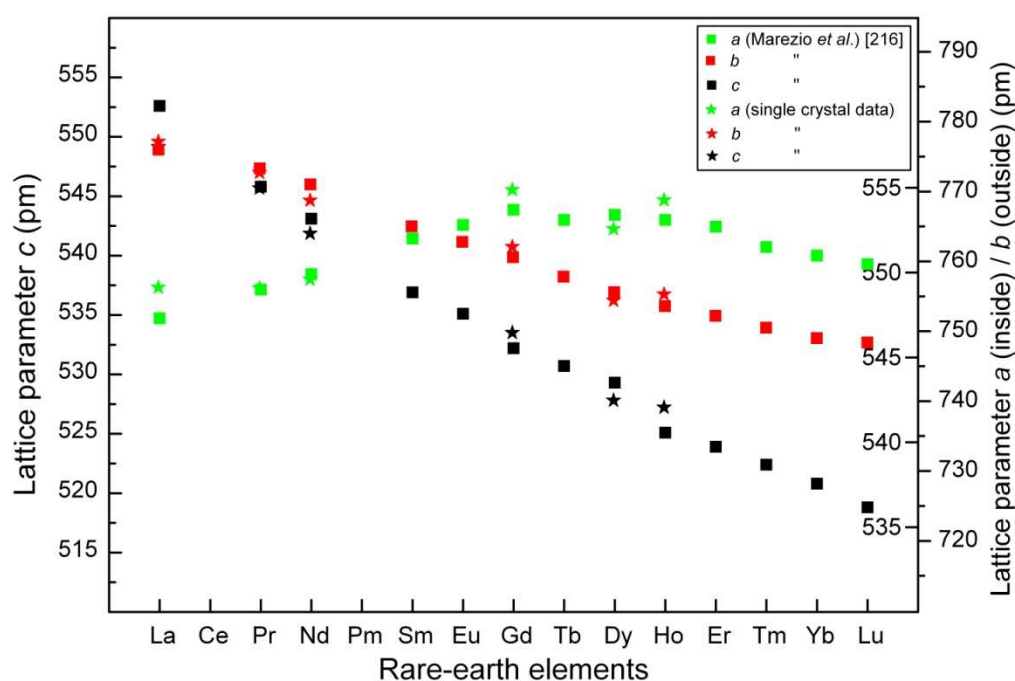
Figure 6-2. Lattice parameters a, b, and c of the different rare-earth gallates REGaO$_3$ (RE = La, Pr, Nd, Sm - Lu; standard setting *Pnma*).

6.3   Rare-earth Borates

$Ho_{31}O_{27}(BO_3)_3(BO_4)_6$

Although there are a multitude of different rare-earth oxoborates, we recently managed to synthesize a new compound with the composition $Ho_{31}O_{27}(BO_3)_3(BO_4)_6$.

The new rare-earth oxide borate $Ho_{31}O_{27}(BO_3)_3(BO_4)_6$ was synthesized in a Walker-type module under high-pressure / high-temperature conditions of 7.5-11.5 GPa and 1200 °C. It crystallizes in the space group $R\bar{3}$ (no. 148) with the lattice parameters $a = 2657.8(8)$ pm and $c = 1146.9(2)$ pm $(Z = 6)$. Refinement of the single crystal data led to final values of $R1 = 0.0319$ besides $wR2 = 0.0526$.

Figure 6-3. Crystal structure of $Ho_{31}O_{27}(BO_3)_3(BO_4)_6$.

Exceptional is the elemental ratio of the elemental composition $Ho_{31}O_{27}(BO_3)_3(BO_4)_6$, which represents a ratio of $RE : B = 3.44$ (31 : 9). As only oxide borates with less content of rare-earth in the structure are known, $Ho_{31}O_{27}(BO_3)_3(BO_4)_6$ represents the rare-earth richest rare-earth oxoborate known to date.

The crystal structure is shown in Figure 6-3. For a better view only the isolated BO_4- and BO_3-units are displayed, integrated in the network of Ho-polyhedra. Although, synthesized under high-pressure / high-temperature conditions, the three-fold coordination of boron partly remained. Remarkably, the three and six crystallographically independent BO_3-units and BO_4-groups are isolated without any linkage among each other.

For a better understanding of the arrangement, Figure 6-4 displays only the BO_3- and BO_4-units, showing the corrugated sequences.

Figure 6-4. Arrangement of the isolated BO_3- and BO_4-units in $Ho_{31}O_{27}(BO_3)_3(BO_4)_6$.

Besides the exceptional bonding situation of boron, the structure exhibits 11 crystallographically different Ho^{3+}-cations. The holmium network consists of $(HoO)_x$-polyhedra (x = 7 - 9), connected *via* corner, edge, and face sharing to each other. In this network, the trigonal BO_3-units and the BO_4-tetrahedra are embedded.

6.4   Phase Transformations

B-Ho_2O_3

High-pressure / high-temperature experiments performed at 11.5 GPa and 1250 °C led to the

phase transformation of cubic C-Ho_2O_3 into monoclinic B-Ho_2O_3. As the compound was obtained as highly crystalline sample, the crystal structure was determined by single-crystal X-ray diffraction data, collected at room temperature.

Figure 6-5. Crystal structure of monoclinic B-Ho_2O_3.
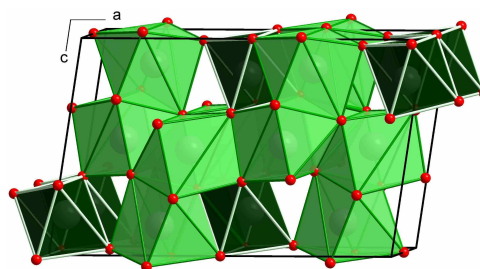
The monoclinic B-holmium oxide crystallizes in the space group $C2/m$ (no. 12) with the lattice parameters $a = 1394.7(3)$, $b = 350.83(7)$, $c = 865.6(2)$ pm, $\beta = 100.23(3)°$, $R1 = 0.0517$, and $wR2 = 0.1130$ (all data).

The structure was already solved by powder methods [267,268], as well as investigated theoretically [280], but the single crystal data of the compound was still missing. Now, for the first time, the crystals were suitable for single crystal determination, wherefrom the structure was determined and compared with the powder and calculated data.

The crystal structure of B-Ho_2O_3 is shown in Figure 6-5. Two different types of polyhedra are found in the structure: distorted octahedrally coordinated Ho^{3+}-ions next to sevenfold coordinated Ho^{3+}-cations forming capped trigonal prisms.

α-Ga_2O_3

Within the investigations of gallium oxonitrides, the phase transformation of β-Ga_2O_3 to α-Ga_2O_3 occurred at different high-pressure / high-temperature conditions. The phase transformation is reported to start at pressure conditions around 6 GPa, based on theoretical results. We observed the transformation already at lower pressures, starting at 2 GPa, up to 11.5 GPa. The required pressure for the transformation can be reduced to a minimum in the presence of w-GaN. While compressing samples consisting only of β-Ga_2O_3, the required pressure for a successful transformation increased.

6.5   Gallium Oxonitrides

6.5.1   Single Crystal of $Ga_{2.79}\square_{0.21}(O_{3.05}N_{0.76}\ _{0.19})$

Systematic investigations under high-pressure / high-temperature conditions into the formation of gallium oxonitrides, starting from the binary compounds β-Ga_2O_3 and w-GaN were performed using a multianvil high-pressure device.

The crystalline gallium oxonitride phase $Ga_{2.79}\square_{0.21}(O_{3.05}N_{0.76}\square_{0.19})$ was synthesized under high-pressure / high-temperature conditions of 5 GPa and 1250 °C. For the first time, the

crystal structure of a crystalline spinel-type gallium oxonitride was determined on the basis of single crystal X-ray diffraction data. The cubic spinel-type gallium oxonitride crystallizes in the space group $Fd\overline{3}m$ (no. 227) with a lattice parameter of $a = 827.8(2)$ pm.

Single crystal structure determination led to final values of $R1 = 0.0191$ and $wR2 = 0.0528$ (all data). The combination of energy-dispersive X-ray spectroscopy (EDS) with electron energy-loss spectroscopy (EELS) allowed the quantification of nitrogen and oxygen for the structural refinement, resulting in a mean value of $\overline{N/O} = 0.25\pm0.06$, therefore the molar ratio of
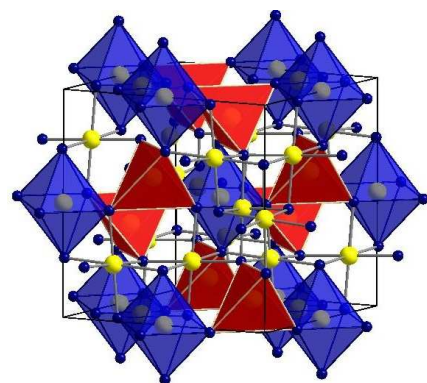
Figure   6-6.   Crystal   structure   of $Ga_{2.79}\square_{0.21}(O_{3.05}N_{0.76}\square_{0.19})$.

oxygen : nitrogen comes to $3.20 : 0.80$. The stoichiometric composition was determined to $Ga_{2.79}\square_{0.21}(O_{3.05}N_{0.76}\square_{0.19})$ ($\square$ = vacancy). The crystal structure is shown in Figure 6-6.

6.5.2   Systematic Investigations on the Formation of Gallium Oxonitrides

The systematic high-pressure / high-temperature investigations on the formation of the gallium oxonitride spinel phase were performed using a Walker-type module and 1000 t presses. Under variation of pressure (1-11.5 GPa), temperature (500-1350 °C), and molar ratio of the starting materials (w-GaN : β-Ga$_2$O$_3$ = 9 : 1 - 1 : 9), the formation region of gallium oxonitrides under high-pressure / high-temperature conditions was investigated.

Based on these investigations, the formation of the spinel-type gallium oxonitride phase starts at a lowest pressure of 2.5 GPa and 1250 °C, while the formation can be observed up to pressures of 8 GPa at a temperature of 1200 °C. Increasing the pressure up to 11.5 GPa resulted still in the spinel-phase, but with a low degree of crystallinity. The lowest reaction temperature for a successful formation of the gallium oxonitride-compound could be determined to 1000 °C, as further decrease showed no reaction of the educts at all.

From these results, initial conditions of 2.5-11.5 GPa at temperatures between 1000-1300 °C can be stated as leading to the formation of cubic, spinel-type gallium oxonitride phases.
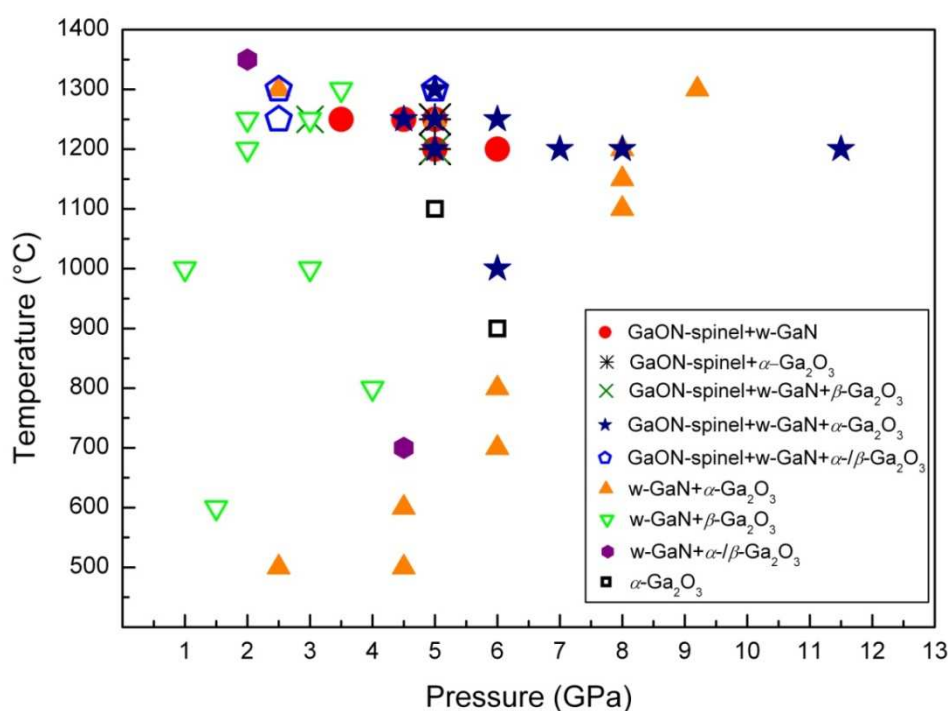
Figure 6-7. Survey of the products, obtained under specified pressure and temperature conditions with varying starting mixtures.

Figure 6-7 shows the different high-pressure / high-temperature experiments leading to different compounds in dependence of the applied pressure, temperature.

The variation of the mixture starting materials (w-GaN and β-Ga$_2$O$_3$ in the different molar ratios of 9 : 1 up to 1 : 9) showed a remarkable influence on the spinels crystallinity and yield. The results are shown in Figure 6-8. As a high amount of w-gallium nitride in the educt mixture led to spinel-type gallium oxonitrides with a high degree of crystallinity in good yield, oxide-rich samples suffered from low crystallinity beside small fractions of spinel-type gallium oxonitride in the compound.

These samples mostly showed high fractions of transformed α-Ga$_2$O$_3$ in high crystallinity. Taking a closer look at the phase transformation, the transformation was observed in the presence of w-GaN even at a minimum pressure of 2 GPa.

To estimate the temperature-resistivity of the compound, high-temperature X-ray diffraction patterns were measured. The sample was heated in a cylindrical graphite furnace up to 1100 °C in steps of 50 or 100 °C, respectively. Examination of the HT-powder diffraction pattern revealed temperature resistance, as the spinel-structured gallium oxonitride phase stayed stable without decomposition or cell distortion. The phase is almost unaffected, except for a light increase of the lattice parameter.
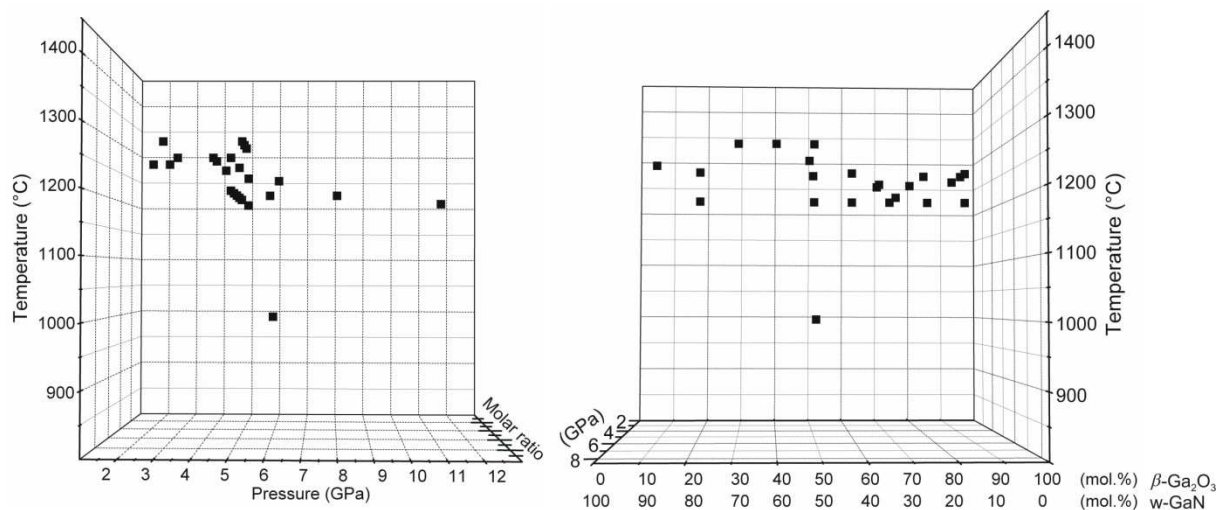
Figure 6-8. Survey of the experiments leading to the cubic spinel-type gallium oxonitrides in dependence of pressure, temperature, and molar ratio w-GaN : β-Ga$_2$O$_3$ of the starting mixture.

6.5.3   DAC Experiments on Spinel-type Gallium Oxonitrides

In contrast to the systematic investigations using a multianvil high-pressure device, diamond anvil syntheses were performed using molecular precursors as well as w-GaN and β-Ga_2O_3 as starting materials. Spinel-type gallium oxonitrides were obtained at pressures of 3 GPa and temperatures of 1300 °C, while application of molecular precursors reduced the required pressure conditions for a successful synthesis down to 0.7 GPa. Additionally, the bulk modulus $K = 216(7)$ GPa with K' fixed to 4 and a volume at zero pressure $V_0 = 552.9(5)$ $Å^3$ was determined.

7 Appendix

7.1 Abbreviations

Å	Ångström	LED	Light Emitting Diode
∅	Average	LT	Low Temperature
η	Asymmetry parameter	M	Magnetization
atm.	atmosphere	χ	Magnetic susceptibility
ca./~	Circa	μ_B	Effective Bohr magneton
°C	Degree in Celsius	μm	Micrometer
CCD	Charge Coupled Device	min	Minute
CN	Coordination number	mg	Milligrams
cm^{-1}	Wavenumber	mm	Millimeter
CVD	Chemical Vapor Deposition	NLO	Non Linear Optic
δ	Chemical shift parameter	NP	Normal-Pressure
d	Distance	Pa	Pascal
DAC	Diamond Anvil Cell	PSD	Position Sensitive Detector
DFT	Density Functional Theory	pm	Picometer
EDX	Energy Dispersive Analysis of X-rays	ppm	Parts per million
EELS	Electron Loss Spectroscopy	PPMS	Physical Property Measurement System
et al.	Et alii	PTFE	Polytetrafluorethylene
e.g.	Exempli gratia	PET	Polyethylenterephtalat
eq.	Equation	R_C	Rockwell hardness
eV	Electron Volt	*RE*	Rare-Earth
Fa.	Firma, engl. company	RT	Room Temperature
FBB	Fundamental Building Block	SAED	Selected-Area Electron Diffraction
GGA	Generalized Gradient Approximation	SAD	Selected-Area Diffraction
GooF	Goodness of Fit	σ	Standard deviation
H	Field	sec	Second
h	hour	sof	Site occupation factor
HP	High-Pressure	t	Tons
HT	High Temperature	T	Tesla
ICSD	Inorganic Crystal Structure Database	T	Temperature
IR	Infrared	TEM	Transmission Electron Microscope
JCPDS	Joint Committee on Powder Diffraction Standards	V	Volume
J	Joule	W	Watt
K	Kelvin	λ	Wave length
LDA	Local Density Approximation	Z	Formula units

7.2 Curriculum Vitae

Personal Information	
	Stefanie Alexandra Hering
12/01/1980	Rosenheim, Bavaria, Germany Nationality: german
Education	
06/2000 1994-2000 1986-1994	Abitur: Luitpold Gymnasium, Wasserburg a. Inn Luitpold Gymnasium, Wasserburg a. Inn Freie Waldorfschule, Prien a. Chiemsee
Scientific career	
12/2009	Internship at the IP law firm Stolmár Scheele & Partner
06/2007-10/2009	PhD studies in the group of Univ. - Prof. Dr. H. Huppertz, Ludwig-Maximilians University, Department of Chemistry, Munich PhD thesis: "*Synthetic Investigations in Rare-Earth Borates, Gallates, Oxides, and Gallium Oxonitrides at Extreme Conditions*"
06/2007	Diploma thesis: *Hochdruck-/ Hochtemperatur-Synthese, Struktur und Charakterisierung des neuen Galliumoxonitrides Ga_3O_3N sowie Untersuchungen und Analytik zur Synthese neuer Seltenerd-Gallate unter Hochdruck-/ Hochtemperatur-Bedingungen*
10/2000-05/2007	Chemistry study (diploma) at the Ludwig-Maximilians University, Munich
Awards	
2004	John Loesch Sponsorship
2003	Oskar-Karl-Forster-Scholarship

7.3 Publications

1. High-Pressure Synthesis, Electron Energy-Loss Spectroscopy Investigations, and Single Crystal Structure Determination of a Spinel-Type Gallium Oxonitride $Ga_{2.79}\square_{0.21}(O_{3.05}N_{0.76}\square_{0.19})$, *Chem. Mater.* **2009**, *21*, 2101.

2. High-Pressure Syntheses and Crystal Structures of Monoclinic B-Ho_2O_3 and Orthorhombic $HoGaO_3$, *Z. Naturforsch. B* **2009**, *64*, 1032.

3. A Systematic Investigation of the Stability Field of Spinel-type Gallium Oxonitrides, *Z. Naturforsch. B* **2009**, *64*, 1115.

4. Diamond anvil cell syntheses and compressability studies of the spinel-structured gallium oxonitride, *High-press. Res.* **2009**, *29(3)*, 389.

5. High-pressure Synthesis and Crystal Structure of the new holmium oxide borate $Ho_{31}O_{27}(BO_3)_3(BO_4)_6$, *J. Solid State Chem.* **2010**, *in preparation*.

6. High-pressure Synthesis and Crystal Structure of the Orthorhombic Rare-Earth Gallate $DyGaO_3$, *Z. Naturforsch. B* **2010**, *in preparation*.

7.4 CSD-Numbers

The CIF-files (Crystallographic Information File) of the following compounds were deposited at the Fachinformationszentrum Karlsruhe, 76344 Eggenstein Leopoldshafen, Germany.

$Ga_{2.79}\square_{0.21}(O_{3.05}N_{0.76}\square_{0.19})$ CSD-419664

B-Ho_2O_3 CSD-420710

7.5 References

[1]   Lu, F. X.; Tang, W. Z.; Tong, Y. M.; Miao, J. Q.; He, L. F.; Li, C. M.; Chen, G. C. *Diamond Rel. Mat.* **2006**, *15*, 2039.

[2]   Cruz, R.; Rao, J.; Rose, T.; Lawson, K.; Nicholls, J. R. *Diamond Rel. Mat.* **2006**, *15*, 2055.

[3]   http://www.mindat.org.

[4]   Wei, L.; Kuo, P. K.; Thomas, R. L. *Phys. Rev. Lett.* **1993**, *70*, 3764.

[5]   Walker, J. *Rep. Prog. Phys.* **1979**, *42*, 1605

[6]   http://www.goldschmiede-leypoldt.de/rohdiamant.jpg, **09.2009**.

[7]   http://www.design-technology.net/s/cc_images/cache_997181612.jpg, **09.2009**.

[8]   http://uploads.inkscape-forum.de/2007/09/Diamant.png, **09.2009**.

[9]   http://www.diamanten-diamant.de/bilder/farbige-diamanten.jpg, **09.2009**.

[10]   Wise, R. W. *Secrets Of The Gem Trade, The Connoisseur's Guide To Precious Gemstones* Brunswick House Press, Lenox, USA, **2001**.

[11]   Hounsome, L. S.; Jones, R. *Phys. Rev. B* **2006**, *73*, 125203.

[12]   Knittle, E.; Kaner, R. B.; Jeanloz, R.; Cohen, M. L. *Phys. Rev. B*: *Condens. Matter* **1995**, *51*, 12149.

[13]   Erlich, E. I.; Dan Hausel, W. *Diamond Deposits*, Society for Mining, Metallurgy, and Exploration, Blackwell Publishing, 2nd Ed., Malden, USA, **2002**.

[14]   Hazen, R. M. *The diamond makers*, Cambridge University Press; Rev Ed., GB, **1999**.

[15]   Bundy, F. P.; Hall, H. T.; Strong, H. M.; Wentorf, R. H. *Nature* **1955**, *176*, 51.

[16]   Bovenkerk, H. P.; Bundy, F. P.; Hall, H. T.; Strong, H. M.; Wentorf, R. H. *Nature* **1959**, *184*, 1094.

[17]   Hall, H. T. *Rev. Sci. Instr.* **1960**, *31*, 125.

[18]   Yarnell, A. *Chem. Engin. News* **2004**, *82*, 26.

[19]   Sappok, R. *Chemie in unserer Zeit* **1970**, *4*, 145.

[20]   Shigley, J. E.; Abbaschian, R.; Clarke, C. *Gems & Gemology* **2002**, *38*, 301.

[21]   Werner, M.; Locher, R. *Rep. Progr. Phys.* **1998**, *61*, 1665.

[22]   Varnin, V. P.; Laptev, V. A.; Ralchenko, V. G. *Inorg. Mater.* **2006**, *42*, 1.

[23]   http://4.bp.blogspot.com/_IoU3bEFUwWc/SJGqnLLwBcI/AAAAAAAAChY/ZWyr9NQdJnQ/s320/H. +Tracy+Hall.jpg, **09.2009**.

[24]   Ito, E.; Schubert. G. Multianvil cells and high-pressure experimental methods, in Treatise of Geophysics. 2. Ed., Elsevier, Amsterdam, The Netherlands, **2007**.

[25]   Hall, H. T. *Science* **1958**, *128*, 445.

[26]   Loshak, M. G.; Alexandrova, L. I. *Int. J. Ref. Met. Hard Mater.* **2001**, *19*, 5.

[27]   Todd, R. H.; Allen, D. K. *Manufacturing Processes Reference Guide*. Industrial Press Inc., New York, USA, **1994**.

[28]   Iwakuma, T.; Toge, N.; Tanii, S. JP Patent 2008073784, **2008**.

[29]   Adamovskii, A. A.; Zyukin, N. S.; Evdokimov, V. A. *Adgeziya Rasplavov i Paika Materialov* **2008**, *41*, 91.

[30]   Guo, Y. D.; Yang, X. D.; Li, X. B.; Song, X. S.; Cheng, X. L. *Diamond Rel. Mater.* **2008**, *17*, 1.

[31] Taniguchi, T.; Kimoto, K.; Tansho, M.; Horiuchi, S.; Yamaoka, S. *Chem. Mater.* **2003**, *15*, 2744.

[32] Kawai, N.; Yokoo, M.; Kondo, K.-I.; Taniguchi, T.; Saito, F. *J. Appl. Phys.* **2009**, *106*, 033508.

[33] Petrusha, I. A. *Diamond Rel. Mater.* **2000**, *9*, 1487.

[34] Hall, D. R.; Crockett, R.; Waldron, J. S.; Fox, J. U.S. Patent 7575425, **2009**.

[35] Hubert, H.; Garvie, L. A. J.; Buseck, P. R.; Petuskey, W. T.; McMillan, P. F. *J. Solid State Chem.* **1997**, *133*, 356.

[36] Garvie, L. A. J.; Hubert, H.; Petuskey, W. T.; McMillan, P. F.; Buseck, P. R. *J. Solid State Chem.* **1997,** *133*, 365.

[37] Hubert, H.; Devouard, B.; Garvie, L. A. J.; O'Keeffe, M.; Buseck, P. R.; Petuskey, W. T.; McMillan, P. F. *Nature* **1998**, *391*, 376.

[38] Hubert, H.; Garvie, L. A. J.; Devouard, B.; Buseck, P. R.; Petuskey, W. T.; McMillan, P. F. *Chem. Mater.* **1998**, *10*, 1530.

[39] Guo, Y. D.; Yang, X. D.; Li, X. B.; Song, X. S.; Cheng, X. L. *Diamond Rel. Mater.* **2008**, *17(1)*, 1.

[40] Solozhenko, V. L.; Andrault, D.; Fiquet, G.; Mezouar, M.; Rubie, D. C. *Appl. Phys. Lett.* **2001**, *78*, 1385.

[41] Lundstrom, T.; Andreev, Y. G. *Mater. Sci. Eng. Microstr. Proc.* **1996**, *209*, 16.

[42] He, J. L.; Tian, Y. J.; Yu, D. L.; Wang, T. S.; Liu, S. M.; Guo, L. C.; Li, D. C.; Jia, X. P.; Chen, L. X.; Zou, G. T.; Yanagisawa, O. *Chem. Phys. Lett.* **2001**, *340*, 431.

[43] Liu, A. Y.; Cohen, M. L. *Science* **1989**, *245*, 841.

[44] Teter, D. M.; Hemley, R. J. *Science* **1996**, *271*, 53.

[45] Mori-Sanchez, P.; Marques, M.; Beltran, A.; Jiang, J. Z.; Gerward, L.; Recio, J. M. *Phys. Rev. B* **2003** *68*, 064115.

[46] Solozhenko, V. L.; Dub, S. N.; Novikov, N. V. *Diamond Rel. Mater.* **2001**, *10*, 228.

[47] Zerr, A.; Miehe, G.; Serghiou, G.; Schwarz, M.; Kroke, E.; Riedel, R.; Fuess, H.; Kroll, P.; Boehler, R. *Nature* **1999**, *400*, 340.

[48] Soignard, E.; Somayazulu, M.; Dong, J.; Sankey, O. F.; McMillan, P. F. *J. Phys. B*: *Condens. Matter* **2001**, *13*, 557.

[49] Schnick, W. *Angew. Chem.* **1999**, *111*, 3511; *Angew. Chem. Int. Ed. Engl.* **1999**, *38*, 3309.

[50] He, H.; Sekine, T.; Kobayashi, T.; Hirosaki, H.; Suzuki, I. *Phys. Rev. B* **2000**, *62*, 11412.

[51] Landskron, K.; Huppertz, H.; Senker, J.; Schnick, W. *Angew. Chem.* **2001**, *113*, 2713; *Angew. Chem. Int. Ed. Engl.* **2001**, *40*, 2643.

[52] Kroll, P.; Schnick, W. *Chem. Eur. J.* **2002**, *8*, 3530.

[53] Schnick W.; Lücke, J. *Z. Anorg. Allg. Chem.* **2004**, *588(1)*, 19.

[54] Schnick, W.; Lücke, J. *J. Solid State Chem.* **1990**, *87*, 101.

[55] Karau, F.; Schnick, W. *Angew. Chem.* **2006**, *118*, 4617; *Angew. Chem. Int. Ed. Engl.* **2006**, *632*, 2093.

[56] West, A. R. *Basic Solid State Chemistry*, John Wiley & Sons Ltd, 2. Ed., Chichester, UK, **1999**.

[57] Nguyen, P. T.; Sleight, A. W.; Roberts, N.; Warren, W. W. *J. Solid State Chem.* **1996**, *122*, 259.

[58] Rao C. N. R.; Gopalakrishnan, J. *New directions in solid state chemistry*, Cambridge University Press, 2. Ed., Cambridge, GB, **1986**.

[59] Bierlein J. D.; Vanherzeele, H. *J. Opt. Soc. Am. B* **1989**, *6*, 622.

[60]   Sedlmaier, S.; Schmedt auf der Günne, J.; Schnick, W. *Dalton Trans*. **2009**, 4081.

[61]   Higashi, I.; Kobayashi, K.; Takabatake, T.; Kasaya, M. *J. Alloys Compd*. **1993**, *193*, 300.

[62]   Routsi, C.; Yakinthos, J. K.; Gamari-Seale, E. *J. Magn. Magn. Mater*. **1992**, *110*, 137.

[63]   Pöttgen, R. *Z. Naturforsch. B* **1996**, *51*, 806.

[64]   Sakurai, J.; Kegai, K.; Kuwai, T.; Isikawa, Y.; Nishimura, K.; Mori, K. *J. Magn. Magn. Mater*. **1995**, *140-144*, 875.

[65]   Canepa, F.; Cirafici, S. *J. Alloys Compd*. **1996**, *232*, 71.

[66]   Heymann, G. *PhD Thesis*, Ludwig-Maximilians-Universität München, **2007**.

[67]   Skolozdra, R. V.; Koretskaya, O. E.; Gorelenko, Y. K. *Inorg. Mater*. **1984**, *20*, 604.

[68]   Takabatake, T.; Teshima, F.; Fujii, H.; Nishigori, S.; Suzuki, T.; Fujita, T.; Yamaguchi, Y.; Sakurai, J.; Jaccard, D. *Phys. Rev. B*. **1990**, *41*, 9607.

[69]   Krypyakevich, P. I.; Markiv, V. Y.; Melnyk, E. V. *Dopov. Akad. Nauk. Ukr. RSR Ser A* **1967**, 750.

[70]   Zumdick, M. F.; Hoffmann, R.-D.; Pöttgen, R. *Z. Naturforsch. B* **1999**, *54*, 45.

[71]   Dwight, A. E.; Mueller, M. H.; Conner, R. A. (Jr.); Downey, J. W.; Knott, H. *Trans. Met. Soc. AIME* **1968**, *242*, 2075.

[72]   Riecken, J. F.; Heymann, G.; Soltner, T.; Hoffmann, R.-D.; Huppertz, H.; Johrendt, D.; Pöttgen, R. *Z. Naturforsch. B* **2005**, *60*, 821.

[73]   Heymann, G.; Rayaprol, S.; Riecken, J. F.; Hoffmann, R.-D.; Rodewald, U. C.; Huppertz, H.; Pöttgen, R. *Solid State Sci*. **2006**, *8*, 1258.

[74]   Riecken, J. F.; Rodewald, U. C.; Heymann, G.; Rayaprol, S.; Huppertz, H.; Hoffmann, R.-D.; Pöttgen, R. *Z. Naturforsch. B* **2006**, *61*, 1477.

[75]   Heymann, G.; Riecken, J. F.; Rayaprol, S.; Christian, S.; Pöttgen, R.; Huppertz, H. *Z. Anorg. Allg. Chem*. **2007**, *633*, 77.

[76]   Shoemaker, C. B; Shoemaker, D. P. *Acta Cryst.***1965**, *18*, 900.

[77]   Huppertz, H.; von der Eltz, B. *J. Am. Chem. Soc*. **2002**, *124*, 9376.

[78]   Huppertz, H. *Z. Naturforsch. B* **2003**, *58*, 278.

[79]   Huppertz, H.; Emme, H. *J. Phys. Condens. Matter* **2004**, *16*, S1283.

[80]   Knyrim, J. S.; Huppertz, H. *J. Solid State Chem*. **2007**, *180*, 742.

[81]   Knyrim, J. S.; Huppertz, H. *Z. Naturforsch. B* **2008**, *63*, 707.

[82]   Huppertz, H.; Heymann, G. *J. Solid State Chem*. **2003**, *5*, 281.

[83]   Knyrim, J. S.; Huppertz, H. *J. Solid State Chem*. **2008**, *181*, 2092.

[84]   Knyrim, J. S.; Roeßner, F.: Jakob, S.: Johrendt, D.; Kinski, I.; Glaum, R.; Huppertz, H. *Angew. Chem.* **2007**, *119*, 9256; *Angew. Chem. Int. Ed*. **2007**, *46*, 9097.

[85]   Robinson, P. D.; Fang, J. H. *Am. Mineral*. **1977**, *62*, 167.

[86]   Knyrim, J. S.; Becker, P.; Johrendt, D.; Huppertz, H. *Angew. Chem*. **2006**, *118*, 8419; *Angew. Chem. Int. Ed. Engl*. **2006**, *45*, 8239.

[87]   Haberer, A.; Huppertz, H. *J. Solid State Chem*. **2009**, *182*, 888.

[88]   Haberer, A.; Kaindl, R.; Huppertz, H. *J. Solid State Chem*. **2010**, *in press*.

[89]   Haberer, A.; Huppertz, H. **2010**, *Solid State Sci., in press.*

[90]   http://www.gemini-licht.com/files/led-vorteile05.jpg, **09.2009**.

[91]   http://www.electronicsweekly.com/blogs/electronics-weekly-blog/02apr08LuxeonK2.jpg, **09.2009**.

[92]   Mueller-Mach, R.; Mueller, G.; Krames, M. R.; Höppe, H. A.; Stadler, F.; Schnick, W.; Juestel, T.; Schmidt, P. *Phys. Stat. Sol. A* **2005**, *202(9)*, 1727.

[93]   Zeuner, M.; Hintze, F.; Schnick, W. *Chem. Mater.* **2009**, *21*, 336.

[94]   Zeuner, M.; Schmidt, P. J.; Schnick, W. *Chem. Mater.* **2009**, *21*, 2467.

[95]   Kechele, J. A.; Oeckler, O.; Stadler, F.; Schnick, W. *Solid State Sci.* **2009**, *11*, 537.

[96]   Bachmann, V.; Ronda, C.; Oeckler, O.; Schnick, W.; Meijerink, A. *Chem. Mater.* **2009**, *21*, 316.

[97]   Hecht, C.; Stadler, F.; Schmidt, P. J.; Schmedt auf der Günne, J.; Baumann, V.; Schnick, W. *Chem. Mater.* **2009**, *21*, 1595.

[98]   Oeckler, O.; Kechele, J. A.; Koss, H.; Schmidt, P. J.; Schnick, W. *Chem. Eur. J.* **2009**, *15*, 5311.

[99]   Nakamura, S.; Mukai, T.; Senoh, M. *Appl. Phys. Lett.* **1994**, *64*, 1687.

[100]   Mukai, T.; Nagahama, S.; Iwasa, N.; Senoh, M.; Yamada, T. *J. Phys.: Condens. Matter* **2001** *13*, 7089.

[101]   Chang, S. J.; Chen, W. S.; Shei, S. C.; Shen, C. F.; Ko, T. K.; Tsai, J. M.; Lai, W. C.; Sheu, J. K.; Lin, A. J.; Hung, S. C. *J. Sel. Quant. Electr.* **2009**, *15(4)*, 1287.

[102]   Bisping, D.; Pucicki, D.; Fischer, M.; Koeth, J.; Zimmermann, C.; Weinmann, P.; Hofling, S.; Kamp, M.; Forchel, A. *Sel. J. Topics Quantum Electronics*, IEEE, **2009**, *15*, 968.

[103]   Walker, D.; Carpenter, M. A.; Hitch, C. M. *Am. Mineral.* **1990**, *75*, 1020.

[104]   Walker, D. *Am. Mineral.* **1991**, *76*, 1092.

[105]   Frost, D. J. Pers. Commumications.

[106]   Frost, D. J.; Poe, B. T.; Trønnes, R. G.; Liebske, C.; Duba, A.; Rubie, C. *Phys. Earth Planet. Interiors* **2004**, *143*, 507.

[107]   Wünschheim, W.; Huppertz, H. "PRESSCONTROL I" – *A Program for Communication, Calibration and Surveillance of a Hydraulic Press with Heating Device via RS232C Interfaces*, Ludwig-Maximilians-Universität München, **1999-2003**.

[108]   Wünschheim, W.; Huppertz, H. PRESSCONTROL II – *A Program for Communication, Calibration and Surveillance of a Hydraulic Press with Heating Device*, Ludwig-Maximilians-Universität, München, **2008**.

[109]   Huppertz, H. *Habilitationsschrift*, Ludwig-Maximilians-Universität München, **2003**.

[110]   Takahashi, E.; Yamada, H.; Ito, E. *Geophys. Res. Lett.* **1982**, *9*, 805.

[111]   Huppertz, H. *Z. Kristallogr.* **2004**, *219*, 330.

[112]   Ohtani, E.; Irifune, T.; Hibberson, W. O.; Ringwood, A. E. *High-Temp.-High Press.* **1987**, *19*, 523.

[113]   Getting, L. C.; Chen, G. L.; Brown, J. A. *Pure Appl. Geopys.* **1993**, *141*, 545.

[114]   Bridgman, P. W. *Phys. Rev.* **1935**, *48*, 825.

[115]   Bean, V. E.; Akimoto, S.; Bell, P. M.; Block, S.; Holzapfel, W. B.; Manghnani, M. H.; Nicol, M. F.; Stishov, S. M. *Physica* **1986**, *139 & 140B*, 52.

[116]   Bundy, F. P. *Natl. Bur. Stand. Sp. Publ.* **1971**, *326*, 263.

[117]   Bridgman, P. W. *Phys. Rev.* **1935**, *48*, 893.

[118]   Giardini, A. A.; Samara, G. A. *J. Phys. Chem. Solids* **1965**, *26*, 1523.

[119]   Duggin, M. J. *J. Phys. Chem. Solids* **1972**, *33*, 1267.

[120]   Yoneda, A.; Endo, S. *J. Appl. Phys.* **1980**, *51*, 3216.

[121]   Chen, J. H.; Iwasaki, H.; Kikegawa, T. *High Press. Res.* **1996**, *15*, 143.

[122]   Lloyd, E. C.; Becket, C. W.; Boyd, F. R. (Jr.); *Accurate Characterization of the High-Pressure Environment*, ed. Lloyd, E. C., Washington, DC: *Natl. Bur. Stand. (US) Sp. Publ.*, **1971**, *326*, 1.

[123]   Drickamer, H. G. *Rev. Sci. Instr.* **1970**, *41*, 1667.

[124]   Homan, C. G. *J. Phys. Chem. Solids* **1975**, *36*, 1249.

[125]   McMahon, M. I.; Degtyareva, O.; Nelmes, R. *J. Phys. Rev. Let.* **2000**, *85*, 4896.

[126]   Kusaba, K.; Galoisy, L.; Wang, Y.; Vaughan, M. T.; Weidner, D. *J. Pure Appl. Geophys.* **1993**, *141*, 643.

[127]   Camacho, J.; Loa, I.; Cantarero, A.; Syassen, K. *J. Phys.: Condens. Matter* **2002**, *14*, 739.

[128]   Miguel, A. S.; Polian, A.; Gautier, M.; Itie, J. P. *Phys. Rev. B* **1993**, *48*, 8683.

[129]   Nelmes, R. J.; McMahon, M. I.; Wright, N. G.; Allan, D. R. *J. Phys. Chem. Solids* **1995**, *56*, 545.

[130]   Nelmes, R. J.; McMahon, M. I.; Wright, N. G.; Allan, D. R. *Phys. Rev. Lett.* **1994**, *73*, 1805.

[131]   Herman, R.; Swenson, C. A. *J. Chem. Phys.* **1958**, *29*, 398.

[132]   Singh, A. K. *High Temp.-High Pressures* **1980**, *12*, 47.

[133]   Stager, R. A.; Drickamer, H. G. *Phys. Rev. B* **1964**, *133*, A830.

[134]   Vereshchagin, L. F.; Zubova, E. V.; Stupnikov, V. A. *High Temp.-High Pressures* **1975**, *7*, 149.

[135]   Balchan, A. S.; Drickamer, H. G. *Rev. Sci. Instr.* **1961**, *32*, 308.

[136]   Stager, R. A.; Drickamer, H. G. *Phys. Rev.* **1963**, *131*, 2524.

[137]   Akimoto, S.; Yagi, T.; Ida, Y.; Inoue, K. *High Temp.-High Pressures* **1975**, *7*, 287.

[138]   Chen, X.-R.; Li, X.-F.; Cai, L.-C.; Zhu, J. *Solid State Comm.* **2006**, *139(5)*, 246.

[139]   Pan, Y.-W.; Qu, S.-C.; Gao, C.-X.; Han, Y.-H.; Luo, J.-F.; Cui, Q.-L.; Liu, J.; Zou, G.-T. *Chinese Phys. Lett.* **2004**, *21*, 67.

[140]   Jyoti, G.; Joshi, K. D.; Gupta, Satish C. *Solid State Phys. (India)* **2000**, *43*, 372.

[141]   Qteish, A.; Munoz, A. *Phys. Stat. Solidi B* **2001**, *223(2)*, 417.

[142]   Desgreniers, S.; Beaulieu, L.; Lepage, I. *Phys. Rev. B* **2000**, *61(13),* 8726.

[143]   Walter, M. J.; Thibault, Y.; Wei, K.; Luth, R. W. *Can. J. Phys.* **1995**, *73*, 273.

[144]   Kleber, W. *Einführung in die Kristallographie*, 17th Ed., Verlag Technik Berlin, Germany, **1990**.

[145]   Massa, W. *Kristallstrukturbestimmung*, 4. Auflage, B. G. Teubner, Stuttgart, Germany, **2005**.

[146]   Giacovazzo, C.; Monaco, H. L.; Artioli, G.; Viterbo, D.; Ferraris, G.; Gilli, G.; Zanotti, G.; Catti, M.; *Fundamentals of Crystallography*, IUCr Texts on Crystallography, 2nd Ed., Oxford University Press, New York, USA, **2002**.

[147]   Karle, J. *Angew. Chem.* **1986**, *98*, 611; *Angew. Chem. Int. Ed. Engl.* **1986**, *25*, 614.

[148]   Hauptman, H. *Angew. Chem.* **1986,** *98*, 600; *Angew. Chem. Int. Ed. Engl.* **1986**, *25*, 603.

[149]   Amemiya, Y.; Miyahara, J. *Nature* **1988**, *336*, 89.

[150]   Otwinowski, Z.; Minor, W. *Methods Enzymol.* **1997**, *276*, 307.

[151]   Basread, Raytest Isotopenmessgeräte GmbH, Straubenhardt.

[152]   TINA, v2.10g, Raytest Isotopenmessgeräte GmbH, Straubenhardt, **1993**.

[153]   STOE & CIE GmbH, WinXPOW Software: Darmstadt, Germany, **1998**.

[154]   STOE WinXPOW, v1.2, STOE & CIE GmbH, Darmstadt, Germany, **2001**.

[155]   Werner, P.-E. *TREOR90*, Universität Stockholm, **1990**.

[156] Werner, P.-E. *Z. Kristallogr.* **1964**, *120*, 375.

[157] Werner, P.-E.; Errikson, L.; Westdahl, M. *J. Appl Crystallogr.* **1985**, *18*, 367.

[158] Visser, J. W. *J. Appl. Crystallogr.* **1969**, *2*, 89.

[159] Boultif, A.; Louër, D. *J. Appl. Crystallogr.* **1991**, *24*, 987.

[160] STOE WinXPOW THEO, Version 1.18, **2000**.

[161] WinXPOW Search, v1.22, **1999**.

[162] JCPDS, International Center for Diffraction Data, Swathmore, USA, **1992**.

[163] Larson, A. C.; Von Dreele, R. B.; General Structure Analysis System (GSAS), Los Alamos National Laboratory Report LAUR 86-748, **2000**.

[164] Toby, B. H. *J. Appl. Crystallogr.* **2001**, *34*, 210.

[165] STOE X-RED, Version 1.19, *STOE Data Reduction Programm,* STOE & Cie GmbH, Darmstadt, **1999**.

[166] STOE X-SHAPE, Version 1.06, *Crystal Optimisation for Numerical Absorption Correction,* STOE & Cie GmbH, Darmstadt, **1999**.

[167] Herrendorf, W.; Bärnighausen, H. HABITUS - *Program for Numerical Absorption Correction*, University of Karlsruhe / Giessen, Germany, **1993/1997**.

[168] Sheldrick, G. M. XPREP, *Data Preparation & Reciprocal Space Exploration,* v6.12, Siemens Analytical X-ray Instruments, **1996**.

[169] Sheldrick, G. M. SHELXS-97, *Program for the Solution of Crystal Structures*, Universität Göttingen, **1997**.

[170] Burla, M. C.; Caliandro, R.; Camalli, M.; Carrozzini, B.; Cascarano, G. L.; Caro, L. D.; Giacovazzo, C.; Polidori, G.; Spagna, R.; SIR2004, **2004**.

[171] Sheldrick, G. M. SHELXL-97, *Program for Crystal Structure Refinement*, Universität Göttingen, **1997**.

[172] Sheldrick, G. M. *Acta Cryst*. A **2008**, *64*, 112.

[173] X-STEP32, Revision 1.05b, STOE + Cie GmbH, **1999**.

[174] Farrugia, L. J. *J. Appl. Cryst.* **1999**, *32*, 837.

[175] WinGX, v1.70.01, **2005**.

[176] Speck, A. L. PLATON, *A Multipurpose Crystallographic Tool*, Utrecht University, Utrecht, **2003**.

[177] Brandenburg, K. DIAMOND, *Program for X-ray Structure Analysis*, v3.0d, Crystal Impact GbR, Bonn, **2005**.

[178] INCA, v4.02, Oxford Instruments Analytical Limited, **1998–2002**.

[179] Reimer, L.; Kohl, H. *Transmission electron microscopy: physics of image formation*, 5. Ed., Springer, Berlin, Germany, **2008**.

[180] Ahn, C. C. *Transmission electron energy loss spectrometry in material science and the EELS Atlas*, Wiley, Weinheim, Germany, **2004**.

[181] Cerenkov, P. A. *Doklady Akad. Nauk SSSR* **1934**, *2*, 451.

[182] Egerton, R. F. *Rep. Prog. Phys.* **2009**, *72*, 016502.

[183] Hoppe, R. *Angew. Chem.* **1966**, *78*, 52; *Angew. Chem. Int. Ed.*, **1966**, *5*, 95.

[184] Hoppe, R. *Angew. Chem.* **1970**, *82*, 7; *Angew. Chem. Int. Ed.*, **1966**, *9*, 25.

[185] Hübenthal, R. MAPLE- *Program for the Calculation of* MAPLE- *Values*, Vers. 4, University of Giessen, Germany, **1993**.

[186]   Pauling, L. *J. Am. Chem. Soc.* **1947**, *69*, 542.

[187]   Brown, I. D.; Altermatt, D. *Acta Cryst.***1985**, *B41*, 244.

[188]   Brese, N. E.; O`Keeffe, M. *Acta Cryst.***1991**, *B47*, 192.

[189]   Trzesowska, A.; Kruszynski, R.; Bartczak, T. J. *Acta Cryst.***2004**, *B60*, 174.

[190]   Hoppe, R.; Voigt, S.; Glaum, H.; Kissel, J.; Müller, H. P.; Bernet, K. J.; *J. Less-Common Met.* **1989**, *156*, 105.

[191]   Hoppe, R. *Z. Kristallogr.* **1979**, *150*, 23.

[192]   Liu, F. S.; Liu, Q. L.; Lang, J. K.; Lang, L. T.; Song, G. B.; Luo, J.; Rao, G. H. *J. Solid. State Chem.* **2004**, *177*, 1796.

[193]   Antic-Fidancev, E.; Lemaitre-Blaise, M.; Latroche, M.; Porcher, P.; Coutures, J.; Coutures, J. P. *J. Alloys Compd.* **1997**, *250*, 342.

[194]   Nicholas, J.; Coutures, J.; Coutures, J. P.; Boudot, B. *J. Solid. State Chem.* **1984**, *52*, 101.

[195]   Menzer, G. *Z. Kristallogr.* **1926**, *63*, 157.

[196]   Menzer, G. *Z. Kristallogr.* **1926**, *69*, 300.

[197]   Weidenborner, J. E. *Acta Cryst.***1961**, *14*, 1051.

[198]   Linares, R. C. *Solid State Commun.* **1964**, *2*, 229.

[199]   Euler, F.; Bruce, J. A. *Acta Cryst.***1965**, *19*, 971.

[200]   Brandle, C. D.; Brans, R. L. *J. Cryst. Growth* **1974**, *26*, 169.

[201]   Sawada, H. *J. Solid. State Chem.* **1997**, *132*, 300.

[202]   Patzke, G.; Wartchow, R.; Binnewies, M. *Z. Kristallogr. - New Cryst. Struct.* **1999**, *214*, 143.

[203]   Czochralski, J. *Z. Phys. Chem.* **1917**, *92*, 219.

[204]   Carruthers, J. R.; Kokta, M.; Barns, R. L.; Grasso, M. *J. Cryst. Growth* **1973**, *19*, 204.

[205]   Kim, J. C.; Kim, M.-H.; Lim, J.-B.; Nahm, S.; Paik, J.-H.; Kim, J.-H. *J. Am. Ceram. Soc.* **2007**, *90(2)*, 641.

[206]   Abrahams, S. C.; Geller, S. *Acta Cryst.* **1958**, *11*, 437.

[207]   Strunz, H. *Naturwissenschaften* **1965**, *52*, 493.

[208]   Belov, K. P.; Mill, B. V.; Sokolov, V. I.; Chien, T. D. *Fiz. Metal. Metalloved.* **1969**, *27(4)*, 616614.

[209]   Suchow, L.; Kokta, M. *J. Solid State Chem.* **1972**, *5*, 85.

[210]   Kestigian, M.; Smith, A. B.; Bekebrede, W. R. *J. Appl. Phys.* **1979**, *50*, 2161.

[211]   Kolmakova, N. P.; Levitin, R. Z.; Orlov, V. N.; Vedernikov, N. F. *J. Magn. Magn. Matter.* **1990**, *87*, 218.

[212]   Yamane, H.; Ogawara, K.; Omori, M.; Hirai, T. *J. Am. Chem. Soc.* **1995**, *78*, 2385.

[213]   Gesing, T. M.; Uecker, R.; Buhl, J. C. *Z. Kristallogr. - New Cryst. Struct.* **1999**, *214*, 431.

[214]   Schneider, S. J.; Roth, R. S.; Waring, J. L. *J. Res. Natl. Bur. Std.* **1961**, *65a*, 345.

[215]   Geller, G. *Z. Kristallogr.* **1967**, *125*, 1.

[216]   Marezio, M.; Remeika, J. P.; Dernier, P. D. *Inorg. Chem.* **1968**, *9*, 1337.

[217]   Marezio, M.; Remeika, J. P.; Dernier, P. D. *Inorg Mater. Res. Bull.* **1966**, *1*, 247.

[218]   Brandle, C. D.; Steinfink, H. *Inorg. Chem.* **1969**, *8*, 1320.

[219]   Geller, S.; Curlander, P. J.; Ruse, G. F. *Mater. Res. Bull.* **1974**, *9*, 637.

[220]   Guitel, J. C.; Marezio, M.; Mareschal, J. *Mat. Res. Bull.* **1976**, *11*, 739.

[221]   Brandle, C. D.; Miller, D. C.; Nielsen, J. W. *J. Cryst. Growth*. **1972**, *12*, 195.

[222]   Sallavuard, G.; Szabo, G.; Paris, R. A. *C. R. Seances Acad. Sci. (Ser. C)* **1969**, *268*, 1050.

[223]   Schäfer, M. W.; Roy, R. *J. Amer. Ceram. Soc*. **1959**, *42*, 563.

[224]   Geller, S. *Acta Cryst.***1957**, *10*, 243.

[225]   Angel, R. J.; Zhao, J.; Ross, N. L.; Jakeways, C. V.; Redfern, S. A. T.; Berkowski, M. *J. Solid State Chem*. **2007**, *180*, 3408.

[226]   Vasylechko, L.; Pivak, Ye.; Senyshyn, A.; Savytskii, D.; Berkowski, M.; Borrmann, H.; Knapp, M.; Paulmann, C. *J. Solid. State Chem*. **2005**, *178*, 270.

[227]   Vasylechko, L.; Akselrud, L.; Morgenroth, W.; Bismayer, U.; Matkovskii, A.; Savytskii, D. *J. Alloys Compd*. **2000**, *297*, 46.

[228]   Hering, S. A.; Huppertz, H. *Z. Naturforsch. B* **2009**, *64*, 1032.

[229]   Geller, S. *J. Chem. Phys*. **1956**, *24*, 1236.

[230]   Eibschütz, M. *Acta Cryst.***1965**, *19*, 337.

[231]   Geller, S.; Gilleo, M. A. *Acta Cryst*. **1957**, *10*, 239.

[232]   Batt, A.; Post, B. *Acta Cryst.***1962**, *10*, 1268.

[233]   Hering, S. A.; Huppertz, H. *Z. Naturforsch. B* **2009**, *in preparation*.

[234]   Coppens, P.; Eibschütz, M. *Acta Cryst.***1965**, *19*, 524.

[235]   Geller, S.; Wood, E. A. *Acta Cryst.***1956**, *9*, 563.

[236]   Will, G. *Naturwissenschaften*, **1966**, *53*, 609.

[237]   Marezio, M.; Remeika, J. P.; Dernier, P. D. *Acta Cryst. B* **1970**, *26*, 2008.

[238]   Marezio, M.; Remeika, J. P. *J. Chem. Phys*. **1967**, *46*, 1862.

[239]   Åhman, J.; Svensson, G.; Albertsson, J. *Acta Cryst. C* **1996**, *52*, 1336.

[240]   Berkowski, M.; Fink-Finowicki, J.; Piekarczyk, W.; Perchuć, L.; Byszewski, P.; Vasylechko, L. O.; Savytskij, D. I.; Mazur, K.; Sass, J.; Kowalska, E.; Kapuśniak, J. *J. Cryst. Growth* **2000**, *209*, 75.

[241]   Geller, S. *J. Chem. Phys*. **1960**, *33*, 676.

[242]   Goldschmidt, V. M.; Barth, T.; Lunde, G. *Mat.-Nat. Kl*. **1925**, *7*, 59.

[243]   Iandelli, A. *Gazz. Chim. Ital*. **1947**, *77*, 312.

[244]   Foex, M.; Traverse, J.-P. *Bull. Soc. Minér. Crist*. **1966**, *89*, 184.

[245]   Shafer, M. W.; Roy, R. *J. Amer. Ceram. Soc*. **1959**, *42*, 563.

[246]   Greis, O.; Ziel, R.; Breidenstein, B.; Haase, A.; Petzel, T. *J. Alloys Compd*. **1994**, *216*, 255.

[247]   Wu, B.; Zinkevich, M.; Aldinger, F.; Wen, D.; Chen, L. *J. Solid State Chem*. **2007**, *180*, 3280.

[248]   Sawyer, J. O.; Hyde, B. G.; Eyring, L. *Inorg. Chem*. **1965**, *4*, 426.

[249]   Hirosaki, N.; Ogata, S.; Kocer, C. *J. Alloys Compd*. **2003**, *351*, 31.

[250]   Boulesteix, C.; Caro, P. E.; Gasgnier, M.; Henry La Blanchetais, Ch.; Pardo, B.; Schiffmacher, G. *Phys. Stat. Sol. A* **1974**, *23*, 597.

[251]   Trovarelli, A. *Catal. Rev. Sci. Eng*. **1996**, *38*, 439.

[252]   Trovarelli, A. *Catalysis by Ceria and Related Materials*, Imperial Collegc Press, **2002**.

[253]   Yamamoto, T.; Momida, H.; Hamada, T.; Uda, T.; Ohno, T. *Thin Solid Film*. **2005**, *486*, 1 36.

[254]   Haberer, A.; Huppertz, H. *Z. Anorg. Allg. Chem*. **2009**, *in press*.

[255]   Eyring, L.; Holmberg, B. *Adv. Chem. Ser*. **1963**, *39*, 46.

[256]   Hase, W. *Phase Transition*, **1992**, *38*, 127.

[257]   Lohberg, K. Z. *Phys. Chem.* **1935**, *28b*, 402.

[258]   Maslen, E. N.; Streltsov, V. A.; Ishizawa, N. *Acta Cryst.* **1996**, *B52*, 414.

[259]   Coutures, J. P.; Coutures, J.; Renard, R.; Benezech, G. *C. R. Seances Acad. Sci. C* **1972**, 275.

[260]   Shevchenko, A. V.; Zaitseva, Z. A.; Lopato, L. M. *Inorg. Mater.* **1986**, *22*, 686.

[261]   German, V. N.; Podurets, A. M. *Inorg. Mater.* **1982**, *18*, 1492.

[262]   Meyer, C.; Sanchez, J. P.; Thomasson, J.; Itié, J.P. *Phys. Rev. B: Condens. Matter* **1995**, *51*, 12187.

[263]   Hubbert-Paletta, E.; Müller-Buschbaum, H. K. Z. *Anorg. Allg. Chem.* **1968**, *363*, 145.

[264]   Gouteron, J.; Michel, D.; Lejus; A. M.; Zarembowitch, J. *J. Solid State Chem.* **1981**, *38*, 288.

[265]   Chikalla, T. D.; McNeilly, C. E.; Roberts, F. P. *J. Am. Ceram. Soc.* **1972**, *55*, 428.

[266]   Daire, M.; Willer, B. *C. R. Seances Acad. Sci. Ser. C* **1968**, 266.

[267]   Hoekstra, H. R. *Science* **1964**, *164*, 1163.

[268]   Hoekstra, H. R. *Inorg. Chem.* **1965**, *5*, 754.

[269]   Hall, H. T. *Sci. Instr.* **1958**, *29*, 267.

[270]   Cromer, D. T. *J. Phys. Chem.* **1957**, *61*, 753.

[271]   Foex, M. *Bull. Soc. Minér. Crist.* **1965**, *88*, 521.

[272]   Warshaw, I.; Roy, R. *J. Phys. Chem.* **1961**, *65*, 2048.

[273]   Foex, M. Z. *Anorg. Allg. Chem.* **1965**, *337*, 313.

[274]   Farok, M. H.; Saunders, G. A.; Lambsom, W. A.; Krüger, R.; Senin, H. B.; Bartlett, S.; Takel, S. *Phys. Chem. Glasses* **1996**, *37*, 125.

[275]   Schmetzer, K. *Naturwissenschaften* **1978**, *65*, 592.

[276]   Schubert, J. *Physikalische Effekte - Anwendungen*, *Beschreibungen*, *Tabellen*, 2. Aufl., Physik Verlag, Weinheim, Germany, **1984**.

[277]   Knyrim, J. S.; Schappacher, F. M.; Pöttgen, R.; Schmedt auf der Günne, J.; Johrendt, D.; Huppertz, H. *Chem. Mater.* **2007**, *19*, 254.

[278]   Schleid, T.; Meyer, G. *J. Less-Common Met.* **1989**, *149*, 73.

[279]   Yakel, H. L. *Acta Cryst.B* **1979**, *35*, 564.

[280]   Wu, B.; Zinkevich, M.; Aldinger, F.; Wen, D.; Chen, L. *J. Solid. State Chem.* **2007**, *180*, 3280.

[281]   Pagano, S.; Lupart, S.; Zeuner, M.; Schnick, W. *Angew. Chem.* **2009**, *121*, 6453; *Angew. Chem. Int. Ed. Engl.* **2009**, *48*, 6335.

[282]   Li, G. *Faming Zhuanli Shenqing Gongkai Shuomingshu* **2009**, 12.

[283]   http://www.asahi-net.or.jp/~UG7S-KTU/kernit.jpg, **09.2009**.

[284]   http://www.minerals.net/mineral/borates/ulexite/ulexite2.jpg, **09.2009**.

[285]   http://www.dioptaskristall.de/mediac/400_0/media/DIR_49801/DIR_141601/DIR_160601/ff3104c800 38c86effff820dac144225.jpg, **09.2009**.

[286]   Anthony, J. W.; Bideaux, R. A.; Bladh, K. W.; Nichols, M. C. *Handbook of Mineralogy: Borates, Carbonates, Sulfates*: *5*, Mineral Data Publishing, Tucson, USA, **2003**.

[287]   Liebertz, J.; Stähr, S. Z. *Kristallogr.* **1983**, *165*, 91.

[288]   Chen, C.; Wu, B.; Jiang, A.; You, G. *Sci. Sin. B* **1985**, *28*, 235.

[289]   Mazzetti, C.; Carli, F. D. *Chim. Ital.* **1926**, *56*, 23.

[290]   Sastry, B. S. R.; Hummel, F. A. *J. Am. Ceram. Soc*. **1958**, *41*, 7.

[291]   König, H.; Hoppe, R. *Z. Anorg. Allg. Chem.* **1978**, *41*, 7.

[292]   Chen, C.; Wu, B.; Jiang, A.; Xou, G.; Li, R.; Lin, S. *J. Opt. Soc. Am. B* **1989**, *6*, 616.

[293]   Liebertz, J. *Z. Kristallogr.* **1982**, *158*, 319.

[294]   Fröhlich, R.; Bohatý, L.; Liebertz, J. *Acta Cryst.C* **1984**, *40*, 343.

[295]   Becker, P.; Liebertz, J.; Bohatý, L. *J. Cryst. Growth* **1999**, *203*, 149.

[296]   Mori, Y.; Kuroda, I.; Nakajiama, S.; Sasaki, T.; Nakai, S. *Appl. Phys. Lett.* **1995**, *67*, 1818.

[297]   Ryu, G.; Yoon, C. S.; Han, T. P. J.; Gallagher, H. G. *J. Cryst. Growth* **1998**, *191*, 492.

[298]   Mori, Y.; Yap, Y. K.; Kamimura, T.; Yoshimura, M. *J. Nonlinear Opt. Phys. Mater.* **2001**, *2*, 249.

[299]   Sasaki, T.; Mori, Y.; Yoshimura, M. J. *Nonlinear Opt. Phys. Mater.* **2001**, *2*, 249.

[300]   Becker, P. *Adv. Mater.* **1998**, *10*, 979.

[301]   Keszler, D. A. *Solid State Mater. Sci.* **1999**, *4*, 155.

[302]   Heller, G. *Top. Curr. Chem.* **1986**, *131*, 42.

[303]   Christ, C. L.; Clark, J. R. *Phys. Chem. Minerals* **1977**, *2*, 59.

[304]   Neuhaus, A. *Chimia* **1964**, *18*, 93.

[305]   Effenberger, H.; Lengauer, C. L.; Parthé, E. *Monatshefte für Chemie* **2001**, *132*, 1515.

[306]   Prewitt, C. T., Shannon, R. D.; *Acta Cryst.* **1968**, *B24*, 869.

[307]   Edwards, J. O.; Ross, V. F. J. *Inorg. Nucl. Chem.* **1960**, *15*, 329. (b) Christ, C. L. *Am. Mineral.* **1960**, *45*, 334. (c) Tennyson, C. *Fortschr. Mineral.* **1963**, *41*, 64. (d) Ross, V. F.; Edwards, J. O. *The Structural Chemistry of the Borates. In The Chemistry of Boron and its Compounds*; Wiley: New York, **1967**. (e) Heller, G. *Fortschr. Chem. Forsch.* **1970**, *15*, 206. (f) Christ, C. L.; Clark, J. R. *Phys. Chem. Miner.* **1977**, *2*, 59.

[308]   (a) Burns, P. C.; Grice, J. D.; Hawthorne, F. C. *Can. Mineral.* **1995**, *33*, 1131. (b) Grice, J. D.; Burns, P. C.; Hawthorne, F. C. *Can. Mineral.* **1999**, *37*, 731.

[309]   Filatov, S. K.; Bubnova, R. S. *Phys. Chem. Glasses* **2000**, *41(5)*, 216.

[310]   (a) Meyer, H. J. *Naturwissenschaften* **1969**, *56*, 458. (b) Meyer, H. J.; Skokan, A. *Naturwissenschaften* **1971**, *58*, 566. (c) Meyer, H. J. *Naturwissenschaften* **1972**, *59*, 215.

[311]   Hawthorne, F. C.; Burns, P. C.; Grice, J. D. *Boron: Mineralogy, Petrology, and Geochemistry*, Chapter 2, Reviews in Mineralogy 33, Mineralogical Society of America, Washington, USA, **1996**.

[312]   Sasaki, T.; Mori, Y.; Yoshimura, M.; Yap, Y. K.; Kamimura, T. *Mater. Sci. Eng.* **2000**, *30*, 1.

[313]   Keszler, D. A. *Solid State Mater. Sci.* **1996**, *1*, 204.

[314]   Huppertz, H. *Z. Naturforsch. B* **2003**, *58*, 257.

[315]   Knyrim, J. S.; Römer, S. R.; Schnick, W.; Huppertz, H. *Solid State Sci.* **2009**, *11*, 343.

[316]   Huppertz, H.; Heymann, G. *Solid State Sci.* **2003**, *5*, 281.

[317]   Emme, H.; Weil, M.; Huppertz, H. *Z. Naturforsch. B* **2005**, *60*, 815.

[318]   Knyrim, J. S.; Friedrichs, J; Neumair, S.; Roeßner, F.; Floredo, Y.; Jakob, S.; Johrendt, D.; Glaum, R.; Huppertz, H. *Solid State Sci.* **2008**, *10*, 168.

[319]   Haberer, A.; Huppertz, H. *Z. Naturforsch. B* **2008**, *63*, 713.

[320]   Knyrim, J. S.; Emme, H.; Döblinger, M.; Oeckler, O.; Weil, M. *Chem. Eur. J.* **2008**, *19*, 6149.

[321]   Neumair, S. C.; Glaum, R.; Huppertz, H. *Z. Naturforsch. B* **2009**, *64*, 883.

[322]   Haberer, A.; Huppertz, H. *J. Solid State Chem.* **2009**, *182*, 484.

[323]   Neumair, S. C.; Knyrim, J. S.; Glaum, R.; Huppertz, H. *Z. Anorg. Allg. Chem.* **2009**, *635*, 2002.

[324]   Gmelin, *Handbook of Inorganic and Organometallic Chemistry* C11b**,** 8th edition, Springer Verlag, Berlin, Germany, **1991**.

[325]   Levin, E. M.; Roth, R. S.; Martin, J. B. *Am. Mineral.* **1961**, *46*, 1030.

[326]   Bradley, W. F.; Graf, D. L.; Roth, R. S. *Acta Cryst.***1966**, *20*, 283.

[327]   Henry, J.-Y. *Mat. Res. Bull.* **1976**, *11*, 577.

[328]   Newnham, R. E.; Redman, M. J.; Santoro, R. P.; *J. Am. Ceram. Soc.* **1963**, *46*, 253.

[329]   Roth, R. S.; Waring, J. L.; Levin, E. M.; Proc. 3rd Conf. *Rare-earth Res.*, Clearwater, Fla. **1963**, *153*, 1030.

[330]   Morgan, P. E. D.; Carroll, P. J.; Lange, F. F. *Mat. Res. Bull.* **1977**, *12*, 251.

[331]   Chadeyron, G.; El-Ghozzi, M.; Mahiou, R.; Arbus, A.; Cousseins, J. C. *J. Solid State Chem.* **1997**, *128*, 261.

[332]   Ren, M.; Lin, J. H.; Dong, Y.; Yang, L. Q.; Su, M. Z.; You, L. P. *Chem. Mater.* **1999**, *11*, 1576.

[333]   Palkina, K. K.; Kuznetsov, V. G.; Butman, L. A.; Dzhurinskii, B. F. *Acad. Sci. USSR* **1976**, *2*, 286.

[334]   Meyer, H. J. *Naturwissenschaften* **1969,** *56*, 458.

[335]   Meyer, H. J.; Skokan, A. *Naturwissenschaften* **1971**, *58*, 566.

[336]   Meyer, H. J. *Naturwissenschaften* **1972**, *59*, 215.

[337]   Cohen-Adad, M. Th.; Aloui-Lebbou, O.; Goutaudier, C.; Panczer, G.; Dujardin, C.; Pedrini, C.; Florian, P.; Massiot, D.; Gerard, F.; Kappenstein, Ch. *J. Solid State Chem.* **2000**, *154*, 204.

[338]   Keszler, D. A.; Sun, H. *Acta Cryst.C* **1988**, *44*, 1505. ,

[339]   Abrahams, S. C.; Bernstein, J. L.; Keve, E. T. *J. Appl. Crystallogr.* **1971**, *4*, 284.

[340]   Huppertz, H. *Z. Naturforsch. B* **2001**, *56*, 697.

[341]   Corbel, G.; Leblanc, M.; Antic-Fidancev, E.; Lemaître-Blaise, M.; Krupa, J. C. *J. Alloys Comp.* **1999**, *287*, 71.

[342]   Böhlhoff, R.; Bambauer, H. U.; Hoffmann, W. *Z. Kristallogr. Krist.* **1971**, *133*, 386.

[343]   Böhlhoff, R.; Bambauer, H. U.; Hoffmann, W. *Naturwissenschaften* **1970**, *57*, 129.

[344]   Lemanceau, S.; Bertrand-Chadeyron, G.; Mahiou, R.; El-Ghozzi, M.; Cousseins, J. C.; Conflant, P.; Vannier, R. N. *J. Solid State Chem.* **1999**, *148*, 229.

[345]   Weidelt, J.; Bambauer, H. U. *Naturwissenschaften* **1968**, *55*, 342.

[346]   Abdullaev, G. K.; Mamedov, Kh. S.; Dzhafarov, G. G. *Azerbaidzhanskii Khimicheskii Zhurnal* **1976**, 117.

[347]   Hosokawa, S.; Tanaka, Y.; Iwamoto, S.; Inoue, M. *J. Mater. Sci.* **2008**, *43*, 2276.

[348]   Noirault, S.; Joubert, O.; Caldes, M. T.; Piffard, Y. *Acta Cryst.E* **2006**, *62*, i228.

[349]   Emme, H.; Huppertz, H. *Acta Cryst.C* **2004**, *60*, i117.

[350]   Goubin, F.; Montardi, Y.; Deniard, P.; Rocquefelte, X.; Brec, R.; Jobic, S. *J. Solid State Chem.* **2004**, *177*, 89.

[351]   Müller-Bunz, H.; Nikelski, T.; Schleid, Th. *Z. Naturforsch. B* **2003**, *58*, 375.

[352]   Huppertz, H.; von der Eltz, B.; Hoffmann, R.-D.; Piotrowski, H. *J. Solid State Chem.* **2002**, *166*, 203.

[353]   Hoffmann, R.-D.; Huppertz, H. unpublished results.

[354]   Bambauer, H. U.; Weidelt, J.; Ysker, J.-St. *Z. Kristallogr.* **1969**, *130*, 207.

[355]   Bambauer, H. U.; Weidelt, J.; Ysker, J.-St. *Naturwissenschaften* **1968**, *55*, 81.

[356]   Ysker, J. St.; Hoffmann, W. *Naturwissenschaften* **1970**, *57*, 129.

[357]   Abdullaev, G. K.; Mamedov, Kh. S.; Dzhafarov, G. G.; *Sov. Phys. Crystallogr.* **1981**, *26*, 473.

[358]   Goriounova, A.; Held, P.; Becker, P.; Bohatý, L. *Acta Cryst.E* **2004**, *60*, i134.

[359]   Goriounova, A.; P. Held,; Becker, P.; Bohatý, L. *Acta Cryst.E* **2004**, *60*, i131.

[360]   Goriounova, A.; Held, P.; Becker, P.; Bohatý, L. *Acta Cryst.E* **2003**, *59*, i83.

[361]   Canneri, G. *Gazz. Chim. Ital.* **1926**, *56*, 450.

[362]   Becker, P.; Fröhlich, R. *Cryst. Res. Technol.* **2008**, *43*, 1240.

[363]   Weidelt, J. *Z. Anorg. Allg. Chem.* **1970**, *374*, 26.

[364]   Tananaev, I. V.; Dzhurinskii, B. F.; Belyakov, I. M. *Izv. Akad. Nauk SSSR Neorgan. Materialy* **1966**, *2*, 1791.

[365]   Tananaev, I. V.; Dzhurinskii, B. F.; Chistova, B. F. *Izv. Akad. Nauk SSSR Neorgan. Materialy* **1975**, *11*, 165.

[366]   Abdullaev, G. K.; Mamedov, Kh. S.; Dzhafarov, G. G.; *Sov. Phys. Crystallogr.* **1975**, *20*, 161.

[367]   Sieke, C.; Nikelski, T.; Schleid, Th. *Z. Anorg. Allg. Chem.* **2002**, *628*, 819.

[368]   Emme, H.; C. Despotopoulou, Huppertz, H. *Z. Anorg. Allg. Chem.* **2004**, *630*, 1717.

[369]   Emme, H.; C. Despotopoulou, Huppertz, H. *Z. Anorg. Allg. Chem.* **2004**, *630*, 2450.

[370]   Heymann, G.; Soltner, T.; Huppertz, H. *Solid State Sci.* **2006**, *8*, 821.

[371]   Haberer, A.; G. Heymann, Huppertz, H. *Z. Naturforsch. B* **2007**, *62*, 759.

[372]   Pakhomov, V. I.; Sil´nitskaya, G. B.; Medvedev, A. V.; Dzhurinskii, B. F. *Inorg. Mater.* **1972**, *8*, 1107.

[373]   Emme, H.; G. Heymann, Haberer, A.; Huppertz, H. *Z. Naturforsch. B* **2007**, *62*, 765.

[374]   Nikelski, T.; Schleid, Th. *Z. Anorg. Allg. Chem.* **2003**, *629*, 1017.

[375]   Nikelski, T.; Schäfer, M. C.; Huppertz, H.; Schleid, Th. *Z. Kristallogr.* **2008**, *223*, 177.

[376]   Emme, H.; T. Nikelski, Th. Schleid, R. Pöttgen, M. H. Möller, Huppertz, H. *Z. Naturforsch. B* **2004**, *59*, 202.

[377]   Leskelä, M.; Niinistö, L. *Handbook on the Physics and Chemistry of Rare-Earth*, K. A. Gschneider, Jr., L. Eyring, Ed.), Elsevier Science, Amsterdam, The Netherlands, **1986**.

[378]   Lin, J. H.; Su, M. Z.; Wurst, K.; Schweda, E. *J. Solid State Chem.* **1996**, *126*, 287.

[379]   Noirault, S.; Celerier, S.; Joubert, O.; Caldes, M. T.; Piffard, Y. *Inorg. Chem.* **2007**, *46*, 9961.

[380]   Lin, J. H.; Zhou, S.; Yang, L. Q.; Yao, G. Q.; Su, M. Z.; You, L. P. *J. Solid State Chem.* **1997**, *134*, 158.

[381]   Lin, J. H., You, L. P.; Lu, G. X.; Yang, L. Q.; Su, M. Z. *J. Mater. Chem.* **1998**, *8*, 1051.

[382]   Dzhurinskii, B. F.; Ilyukhin, A. B. *Crystallogr. Rep.* **2002**, *47*, 397.

[383]   Li, L.; Lu, P.; Wang, Y.; Jin, X.; Li, G.; Wang, Y.; You, L.; Lin, J. *Chem. Mater.* **2002**, *14*, 4963.

[384]   Li, L.; Jin, X.; Li, G.; Wang, Y.; Liao, F.; Yao, G.; Lin, J. *Chem. Mater.* **2003**, *15*, 2253.

[385]   Nikelski, T.; Schäfer, M. C.; Schleid, Th. *Z. Anorg. Allg. Chem.* **2008**, *634*, 49.

[386]   Emme, H.; Huppertz, H. *Z. Anorg. Allg. Chem.* **2002**, *628*, 2165.

[387]   Emme, H.; Huppertz, H. *Chem. Eur. J.* **2003**, *9*, 3623.

[388]   Huppertz, H.; Altmannshofer, S.; Heymann, G. *J. Solid State Chem.* **2003**, *170*, 320.

[389]   Emme, H.; Huppertz, H. *Acta Cryst.C* **2005**, *61*, i23

[390]   Emme, H.; Valldor, M.; Pöttgen, R.; Huppertz, H. *Chem. Mater.* **2005**, *17*, 2707.

[391]   Haberer, A.; Heymann, G.; Huppertz, H. *J. Solid State Chem.* **2007**, *180*, 1595.

[392]   Haberer, A.; Heymann, G.; Huppertz, H. *Z. Anorg. Allg. Chem.* **2006**, *632*, 2079.

[393]   Bonazzi, P.; Menchetti, S.; *N. Jahrb. Mineral. Monatsh.* **1989**, *69.*

[394]   Fang, J. H.; Newnham, R. E. *Mineral Mag.* **1965**, *35*, 196.

[395]   Clark, J. R. *Am. Mineral.* **1964**, *49*, 1549.

[396]   Ghose, S.; Wan, C. *Am. Mineral.* **1977**, *62*, 979.

[397]   Negro, A. D.; Ungaretti, L. *Am. Mineral.* **1971**, *56*, 1553.

[398]   Zobetz, E. *Z. Kristallogr.* **1982**, *160*, 81.

[399]   Neuhaus, A. *Chimia* **1964**, *18*, 93.

[400]   Laperches, J. P.; Tarte, P. *Spectrochim. Acta* **1966**, *22*, 1201.

[401]   Ren, M.; Lin, J. H.; Dong, Y.; Yang, L. Q.; Su, M. Z.; Xou, L. P. *Chem. Mater.* **1999**, *11*, 1576.

[402]   Steele, W. C.; Decius, J. C. *J. Chem. Phys.* **1956**, *25*, 1184.

[403]   Bartos, A.; Lieb, K. P.; Uhrmacher, M.; Wiarda, D. *Acta Cryst. B* **1993**, *49*, 165.

[404]   McCauley, J. W. Structure and Properties of AlN and AlON Ceramics. Elsevier´s Encyclopedia of *Materials: Science and Technology*, Elsevier Science Ltd., New York, USA, **2001**.

[405]   McCauley, J. W.; Corbin, N. D. *Progress in Nitrogen Ceramics*, ed. Riley, F. L., Martinus Nijhoff Pub., The Netherlands, **1983**.

[406]   Sakai, T. *Mater. Sci. Monogr.*, **1981**, *14*, 591.

[407]   Kollemberg, E.; Ryman-Lipinska, E. *Keramische Zeitschrift*, **1992**, *44(8)*, 520.

[408]   Wang, X.; Wang, F.; Li, W. *Mater. Sci. Eng. A* **2003**, *342(1/2)*, 245.

[409]   Merdrignac, O.; Guyader, J.; Verdier, P.; Colin, Y.; Laurent, Y. *Fr. Demande EPA*, FR2638527*, **1990***.

[410]   Yoshida, K.; Sasaki, M. *Jpn. Kokai Tokkyo Koho*, JP 07142404, **1995**.

[411]   Kovalgin, A. Y.; Lermontova, N. A. *Proc. Electrochem. Soc.* **1997**, *97*, 701.

[412]   Wolter, S. D.; Luther, B. P.; Waltemyer, D. L.; Onneby, C.; Mohney, S. E.; Molnar, R. J. *Appl. Phys. Lett.* **1997**, *70*, 2156.

[413]   Schmitz, G.; Eumann, M.; Stapel, D.; Franchy, R. *Surf. Sci.* **1999**, *427*, 91.

[414]   Tsuruoka, T.; Kawasaki, M.; Ushioda, S.; Franchy, R.; Naoi, Y.; Sugahara, T.; Sakai, S.; Shintani, Y. *Surf. Sci.* **1999**, *257*, 427.

[415]   Verdier, P.; Marchand, R. *Revue de chimie minérale* **1976**, *13*, 145.

[416]   Grekov, F. F.; Demidov, D. M.; Zykov, A. M. *Zh. Prikl. Khim.* **1979**, *52(6)*, 1394.

[417]   Nishizawa, J.; Shiota, I. U.S. Patent 4331737, **1982**,

[418]   Shiota, I.; Miyamoto, N.; Nishizawa, J. *Surf. Sci.* **1979**, *86*, 272.

[419]   Shiota, I.; Nishizawa, J. *Surf. Interface Anal.* **1979**, *1(6)*, 185.

[420]   Merdrignac, O.; Guyader, J.; Verdier, P.; Colin, Y.; Laurent, Y. *Fr. Demande* **1990**, *2638527*, 16.

[421]   Yoshida, K.; Sasaki, M. *Jpn. Kokai Tokkyo Koho* **1995**, 5.

[422]   Kovalgin, A. Y.; Lermontova, N. A. *Proc. Electrochem. Soc.* **1997**, *97-25*, 701.

[423]   Wolter, S. D.; Luther, B. P.; Waltemyer, D. L.; Onneby, C.; Mohney, S. E.; Molnar, R. J. *Appl. Phys. Lett.* **1997**, *70*, 2156.

[424]   Tsuruoka, T.; Kawasaki, M.; Ushioda, S.; Franchy, R.; Naoi, Y.; Sugahara, T.; Sakai, S.; Shintani, Y.

Surf. Sci. **1999**, *427-428*, 257.

[425]   Schmitz, G.; Eumann, M.; Stapel, D.; Franchy, R. *Surf. Sci*. **1999**, *427-428*, 91.

[426]   Lowther, J. E.; Wagner, T.; Kinski, I.; Riedel, R. *J. Alloys Compd.* **2004**, *376*, 1.

[427]   Puchinger, M.; Kisailus, D. J.; Lange, F. F.; Wagner, T. *J. Cryst. Growth* **2002**, *245*, 219.

[428]   Kinski, I.; Scheiba, F.; Riedel, R. *Adv. Eng. Ma*t. **2005**, *7*, 921.

[429]   Kinski, I; Miehe, G.; Heymann, G.; Theissmann, R.; Riedel, R.; Huppertz, H. *Z. Naturforsch*. **2005,** *60b*, 831.

[430]   Soignard, E.; Machon, D.; McMillan, P. F.; Dong, J.; Xu, B.; Leinenweber, K. *Chem. Mater.* **2005,** *17*, 5465.

[431]   McCauley, J. W.; *J. Amer. Ceram. Soc*. **1978**, *61*, 372.

[432]   Kerlau, M.; Merdrignac-Conanec, O.; Reichel, P.; Bârsan, N.; Weimar, U. *Sens. Act. B* **2006**, *111*, 4.

[433]   Kroll, P.; Dronskowski, R.; Martin, M. *J. Mater. Chem.* **2005**, *15*, 3296.

[434]   Kroll, P. *Phys. Rev. B* **2005**, *72*, 144407.

[435]   Geller, S. *J. Chem. Phys*. **1960**, *33*, 676.

[436]   Zachariasen, W. H. *Mat. Nat. Kl.* **1928**, *7*, 165.

[437]   Foster, L. M.; Stumpf, H. C. *J. Am. Chem. Soc*. **1951**, *73*, 1590.

[438]   Remeika, J. P.; Marezio, M. *Appl. Phys. Lett*. **1966**, *8*, 87.

[439]   Machon, D.; McMillan, P. F.; Xu, B.; Dong, J. *Phys. Rev. B* **2006**, *73*, 094125.

[440]   Yan-Mej, M.; Hai-Yong, C.; Kai-Feng, Y.; Min, L.; Qi-Liang, C.; Jing, L.; Guang-Tian, Z. *Chin. Phys. Lett*. **2008**, *25*, 1603.

[441]   Lipinska-Kalita, K. E.; Kalita, P. E.; Hemmers, O. A.; Hartmann, T. *Phys. Rev. B* **2008**, *77*, 094123.

[442]   Kroll, P. *Phys. Rev. B* **2005**, *72*, 144407.

[443]   Zinkevich, M.; Morales, F. M.; Nitsche, H.; Ahrens, M.; Ruehle, M.; Aldinger, F. *Z. Metallkunde* **2004**, *95*, 756.

[444]   Böhm, J. *Angew. Chem*. **1940**, *53*, 131.

[445]   Roy, R.; Hill, V. G.; Osborne, E. R. *J. Am. Chem. Soc*. **1952**, *74*, 719.

[446]   Young-Jin, C.; Ho-Suk, R.; Gyu-Bong, C.; Kwon-Koo, C.; Kwang-Sun, R.; Ki-Won, K. *J. Kor. Electrochem. Soc*. **2009**, *12(2)*, 189.

[447]   Nagarajan, L.; De Souza, R. A.; Samuelis, D.; Valov, I.; Börger, A.; Janek, J.; Becker, K.-D.; Schmidt, P. C.; Martin, M. *Nat. Mater*. **2008**, *7*, 391.

[448]   Nakamura, S.; Fasol, G. *The Blue Laser Diode: GaN Based Light Emitters and Lasers*, Springer, Berlin, Germany, **1997**.

[449]   Shur, M. S.; Khan, M. A. *MRS Bull*. **1997**, *22*, 44.

[450]   Amano, H.; Kito, M.; Hiramatsu, X.; Akasaki, I. *Jpn. J. Appl. Phys*. **1989**, *28*, L2112.

[451]   Nakamura, S.; Mukai, T.; Senoh, M. *Jpn. J. Appl. Phys*. **1991**, *30*, L1998.

[452]   Bourne, J.; Jacobs, R. L. *J. Phys. C: Solid State Phys*. **1972**, *5*, 3462.

[453]   Berry, P. B.; Rutz, R. F. *Appl. Phys. Lett*. **1978**, *33*, 319.

[454]   Xia, H.; Xia, Q.; Ruoff, A. L. *Phys. Rev. B* **1993**, *47*, 12925.

[455]   Edgar, J. H. *Properties of Group III Nitrides*, Institution of Electrical Engineerings, London, GB, **1994**.

[456]   Vurgaftman, I.; Meyer, J. R. *J. Appl. Phys*. **2003**, *94*, 3675.

[457]   Ortin, J. W.; Foxon, C. T. *Rep. Prog. Phys*. **1998**, *61*, 1.

[458]   Jain, S. C.; Willander, M.; Narayan, J.; Van Overstraeten, R. *J. Appl. Phys*. **2000**, *87*, 965.

[459]   Ramos, L. E.; Teles, L. K.; Scolfaro, L. M. R.; Castineira, J. L. P.; Ros, A. L.; Leite, J. R. *Phys. Rev. B* **2001**, *63*, 165210.

[460]   Stampfl. C.; Van de Walle, C. G. *Phys. Rev. B* **1999**, *59*, 5521.

[461]   Jung, W. S. *Bull. Korean Chem. Soc*. **2004**, *25*, 51.

[462]   Juza, R.; Hahn, H. *Z. Anorg. Allg. Chem*. **1938**, *239*, 282.

[463]   Saib, S.; Bouarissa, N. *Optoelectronics*, **2006**, *153*, 179.

[464]   Van Vechten, J. A. *Phys. Rev*. **1969**, *182*, 891.

[465]   Perlin, P.; Jauberthie-Carillon, C.; Itie, J.-P.; San Miguel, A.; Grzegory, I.; Polian, A. *Phys. Rev. B* **1992**, *45*, 83.

[466]   Perlin, P.; Jauberthie-Carillon, C.; Itie, J. P.; San Miguel, A.; Grzegory, I.; Polian, A. *Phys. Rev. B* **1992**, *45*, 83.

[467]   Rodriguez-Carvajal, J. *Physica B* **1993**, *192*, 55.

[468]   Rodriguez-Carvajal, J. *Short Reference Guide of the FullProf. Prog*., Laboratory Leon Brillouin (CEA-CNRS): Saclay, France, Version July, **2001**.

[469]   Pohl, K. *Naturwissenschaften* **1968**, *55*, 82.

[470]   Zinkevich, M.; Morales, F. M.; Nitsche, H.; Ahrens, M.; Rühle, M.; Aldinger, F. *Z. Metallk.* **2004**, *95*, 756.

[471]   Huppertz, H.; Hering, S. A.; Zvoriste, C. E.; Lauterbach, S.; Oeckler, O.; Riedel, R.; Kinski, I. *Chem. Mater.* **2009**, *21*, 2101.

[472]   Kroll, P., personal communication.

[473]   Verwey, E. J. W. *Z. Kristallogr.* **1935**, *91*, 317.

[474]   Bragg, S. L.; Claringbull, G. F.; Taylor, W. H.; *Crystal Structures of Minerals*, Cornell University Press, Ithaca, New York, **1965**.

[475]   Sinha, K. P.; Sinha, A. P. B.; *J. Phys. Chem.* **1957**, *61*, 758.

[476]   Jagodzinski, H.; Saalfed, H.; *Z. Kristallogr.* **1958**, *110*, 197.

[477]   Saalfed, H.; Mehrotra, B. B. *Ber. Dtsch. Keram. Ges.* **1965**, *42*, 161.

[478]   Dupree, R.; Farnan, I.; Forty, A. J.; El-Mashri, S.; Bottyan, L. *J. Phys. C* (*Paris*) **1985**, *8*, 113.

[479]   Jayaram, V.; Levi, C. G. *Acta Metall.* **1989**, *37*, 569.

[480]   Ealet, B.; Elyakhloufi, M. H.; Gillert, E.; Ricci, M. *Thin Solid Films*, **1994**, *250*, 92.

[481]   Mo, S.-D.; Xu, Y.-N.; Ching, W.-Y. *J. Am. Ceram. Soc.* **1997**, *80*, 1193.

[482]   Dupree, R.; Lewis, M. H.; Smith, M. E. *Philos. Mag. A* **1986**, *53*, L17.

[483]   Adams, I.; AuCoin, T. R.; Wolff, G. A. *J. Electrochem. Soc.* **1962**, *109*, 1050.

[484]   Lejus, A. M. *Rev. Hautes Temp. Réfract.* **1964**, *1*, 53

[485]   Fang, C. M.; Metselaar, R.; Hintzen, H. T.; de With, G. *J. Am. Ceram. Soc.* **2001**, *84*, 2633.

[486]   Tabary, P.; Servant, C. *J. Appl. Cryst.* **1999**, *32*, 241.

[487]   McCauley, J. W.; Patel, P.; Chen, M.; Glide, G.; Strassburger, E.; Paliwal, B.; Ramesh, K. T.; Dandekar, D. P. *J. Eur. Ceram. Soc.* **2008**, doi:10.1016/j.jeurceramsoc.2008.03.046.

[488]   Pashchenko, V. P.; Nesterov, A. M.; Drigibka, Ya. G.; Potapov, G. A.; Khapalyuk, E. A.; Shemyakov,

A. A.; Berezhnaya, V. P. *Powder Metall. Met. Cer.* **1994**, *33*, 300.

[489]   O´Neill, H. St. C.; Navrotsky, A. *Am. Mineral.* **1983**, *68*, 181.

[490]   Böhm, J. *Angew. Chem.* **1940**, *53*, 131.

[491]   Remeika, J. P.; Marezio, M. *Appl. Phys. Lett.* **1966**, *8*, 87.

[492]   Foster, L. M.; Stumpf, H. C. *J. Am. Chem. Soc.* **1951**, *73*, 1590.

[493]   Machon, D;. McMillan, P. F.; Xu, B.; Dong, J. *Phys. Rev. B* **2006**, *73*, 094125.

[494]   Zvoriste, C. E.; Dubrovinsky, L.; Hering, S. A.; Huppertz, H.; Riedel, R.; Kinski, I. *High-Press. Res.* **2009**, *29(3)*, 389.

[495]   Bither, T. A.; Young, H. S. *J. Solid State Chem.* **1973**, *6*, 502.

[496]   Liu, J.; Dubrovinsky, L.; Boffa Ballaran, T.; Chrichton, W. *High-Press. Res.* **2007**, *27*, 483.

[497]   Okeke, O. U.; Lowther, J. E. *Phys. Rev. B* **2008**, *77*, 094129.

[498]   Zerr, A.; Kempf, M.; Schwarz, M.; Kroke, E.; Göken, M.; Riedel, R. *J. Am. Ceram. Soc.* **2002**, *85*, 86.

[499]   Lowther, J. E.; Schwarz, M.; Kroke, E.; Riedel, R. *J. Solid State Chem.* **2003**, *176*, 549.

[500]   Salmang, H.; Scholze, H. *Keramik*, 7. Ed., Springer-Verlag, Berlin Heidelberg, Germany, **2007.**

[501]   Izaki, R.; Kaiwa, N. *Int. Conf. Thermoelectrics*, **2004**, 23rd.

[502]   Yamaguchi, S.; Izaki, R.; Kaiwa, N.; Sugimura, S.; Yamamoto A.; EEIE, *Mat. Res. Soci. Symp. Proc.*, **2004**, 798.

[503]   Yodo, Nakamura, Konyama, *Phys. Stat. Solidi C* **2005**, *2(7)*, 2305.

[504]   Motlan; Goldys, E. M; Tranley, T. L. *J. Cryst. Growth* **2002**, *241*, 165.

[505]   Saib, S.; Bouarissa, N. *Physica B* **2007**, *387*, 377.

[506]   Christensen, N. E.; Gorczyca, I. *Phys. Rev. B* **1994**, *7*, 4397.

[507]   Saitoh, H.; Utsumi, W.; Kaneko, H.; Aoki, A. *J. Cryst. Growth.* **2007**, *300*, 26.

[508]   Gurlo, A.; Kroll, P.; Riedel, R. *Chem. Eur. J.* **2008**, *14*, 3306.

[509]   MacDonald, J.; Gard, J. A.; Glasser, F. P. *J. Inorg. Nucl. Chem.* **1967**, *29*, 661.

[510]   Cava, R. J.; Phillips, J. M.; Kwo, J.; Thomas, G. A.; van Dover, R. P.; Carter, S. A.; Krajewski, J. J.; Peck, W. F.; Marshall, J. H.; Rapkine, D. H. *Appl. Phys. Lett.* **1994**, *64(16)*, 2071.

[511]   Shannon, R. D.; Prewitt, C. T. *J. Inorg. Nucl. Chem.* **1968**, *30*, 1389.

[512]   Saib, S. *J. Phys. Condens. Matter* **2007**, *19*, 486 209.

[513]   Domagala, J.; Leszczynski, M.; Prystawko, P.; Suski, T.; Langer, R.; Barski, A.; Bremser M. *J. Alloys Compd.* **1999**, *286*, 284.

[514]   Yoshida, S.; Misawa, S.; Gonda, S. *J. Appl. Phys.* **1982**, *53*, 6844.

[515]   Pitt, M. G.; Fray, D. J. *J. Solid State Chem.* **1982**, *43*, 227.

[516]   Berkowski, M.; Fink-Finowicki, J.; Piekarczyk, W.; Perchuć, L.; Byszewski, P.; Vasylechko, L. O.; Savytskij, D. I.; Mazur, K.; Sass, J.; Kowalska, E.; Kapuśniak, J. *J. Cryst. Growth* **2000**, *209*, 75.